

TECHNISCHE UNIVERSITÄT MÜNCHEN

Lehrstuhl für Numerische Mechanik

Residual-based variational multiscale methods for turbulent flows and fluid-structure interaction

Peter Gamnitzer

Vollständiger Abdruck der von der Fakultät für Maschinenwesen der Technischen Universität München zur Erlangung des akademischen Grades eines

Doktor-Ingenieurs (Dr.-Ing.)

genehmigten Dissertation.

Vorsitzender: Univ.-Prof. Wolfgang H. Polifke, Ph. D. (CCNY)

Prüfer der Dissertation:

1. Univ.-Prof. Dr.-Ing. Wolfgang A. Wall

2. Prof. Assad A. Oberai, Ph. D.

Rensselaer Polytechnic Institute, Troy, NY/USA

Die Dissertation wurde am 14. April 2010 bei der Technischen Universität München eingereicht und durch die Fakultät für Maschinenwesen am 21. Juni 2010 angenommen.

Abstract

Many physical problems are characterised by a two-way interaction of fluid flow and elastic structural deformation. Such fluid-structure interaction (FSI) problems cannot be split into two independent subproblems but rather have to be treated as a coupled system. This is the case for instance for vortex shedding of flexible bodies or for wind-excited thin-walled structures. Many FSI applications of engineering interest will involve fully turbulent, incompressible flow.

The simulation framework established in the present work was developed with respect to an application in this important subclass. Thus, one challenge faced in this thesis is the combination of a multiscale component introduced by turbulence and a multiphysics part related to the coupling of fluid and elastic solid. The emphasis is on the multiscale part, i.e. on the turbulent flow subproblem. Due to the enormous range of scales involved in high REYNOLDS number turbulence, a resolution of all scales is not feasible.

Within the present thesis, this problem is overcome using large-eddy simulation (LES). In this approach, the large scales are resolved while the more universal, small scales are modelled. The multiphysics component is treated by an adaptation of the powerful block-preconditioned monolithic solution algorithms for coupled problems, which are available in the in-house research code BACI. All subdomain problems in the proposed simulation framework are stated using finite element (FE) discretisations of weak forms. In the FE approach, the spatially discrete problem is obtained by a restriction of trial and weighting function spaces to finite dimensional subspaces. These ‘resolved’ subspaces introduce a natural two-scale partitioning of the fluid subproblem, separating large, resolved scales from small, unresolved scales. The required closure for the unresolved scales is introduced by residual-based model terms in the equation for the resolved scales. This is done based on local algebraic scalings, a procedure that is adapted from stabilised methods. Within the present work, this functional LES approach is formulated in an Arbitrary-LAGRANGEan-EULERian setting, i.e. for deforming domains.

It is studied thoroughly, especially with respect to the time-dependency of the unresolved scales. Regarding resolved-scale quantities, these investigations do not indicate a positive effect of a consideration of the time-dependency of the unresolved scales. Nevertheless unresolved-scale velocities are represented robustly for such an approach, while the corresponding quantities in the conventional approach exhibit a dependency on the time step size. In addition, the numerical dissipation of model terms is analysed. An explanation for the robustness of the resolved scales in the conventional approach is given based on the model’s energy budget. For small time steps, the dissipation related to the least-squares incompressibility stabilisation compensates the diminishing terms related to the unresolved-scale velocities. It is shown that the well-known improved performance of the isogeometric, i.e. NURBS shape function based, approach with respect to the resolved-scale results comes along with a more pronounced representation of the unresolved scales. Furthermore, for a turbulent flow around a square cylinder, a weak imposition of the no-slip boundary conditions is shown to improve the approximation of the drag value at the cost of increased computational expenses.

Implications of these observations are that the conventional residual-based approach is sufficient to serve as an LES model in the turbulent FSI context and that it is recommendable to employ an isogeometric approach if possible. The feasibility of the combination of the two methods is proven in one example, showing clearly the potential of the established framework for turbulent FSI.

Zusammenfassung

Physikalische Probleme können gleichzeitig eine strömungsmechanische und eine strukturmechanische Komponente besitzen. Sind diese beiden Teilprobleme aufgrund gegenseitiger Wechselwirkung nicht unabhängig voneinander, so müssen sie ganzheitlich als gekoppeltes System behandelt werden. Man spricht dann von Fluid-Struktur-Interaktion (FSI). Dies ist zum Beispiel bei Wirbelablösungen an flexiblen Körpern oder bei von Wind angeregten, dünnwandigen Strukturen der Fall. Viele ingenieurwissenschaftlich relevante FSI Anwendungen sind solche mit turbulenten, inkompressiblen Strömungen.

Die vorliegende Arbeit beschäftigt sich mit der Simulation von Vorgängen aus dieser bedeutenden Klasse. Sie behandelt demnach zwei grundlegende Problemstellungen: Zum einen muss die Mehrskalennatur der turbulenten Strömung berücksichtigt werden und gleichzeitig muss die Mehrfeldeigenschaft, die von der Kopplung zwischen Strömung und elastischer Struktur herrührt, beachtet werden. Der Schwerpunkt der Arbeit liegt auf dem strömungsmechanischen Teil des Problems. Dieser stellt eine besondere Herausforderung dar, da aufgrund der enormen Bandbreite an Größenskalen, die in einer turbulenten Strömung bei hoher REYNOLDSzahl enthalten sind, eine Auflösung aller Skalen in einer Simulation in der Praxis nicht möglich ist.

Um dieser Problematik zu begegnen wird hier auf den „Large-Eddy“ Simulationsansatz (LES) zurückgegriffen. Er basiert auf der Idee, die größeren Skalen aufzulösen und den fehlenden Beitrag der universelleren, kleinen Skalen durch ein Modell zu ersetzen. Die effiziente Behandlung der Mehrfeldproblematik erfolgt im Rahmen dieser Arbeit durch eine geeignete Anpassung der leistungsfähigen blockweise vorkonditionierten monolithischen Lösungsalgorithmen aus dem lehrstuhleigenen Forschungsprogramm BACI. In dem vorgestellten ganzheitlichen Simulationskonzept werden alle Felder mit Hilfe von Finite Element (FE) Ansätzen diskretisiert. In einem FE Ansatz wird die räumliche Diskretisierung durch eine Einschränkung der in der schwachen Form verwendeten Funktionenräume auf endlich dimensionale Teilräume vorgenommen. Dies erzeugt eine natürliche Partition des Strömungsproblems in große, aufgelöste Skalen aus den endlich dimensionalen Teilräumen und kleine, nicht aufgelöste Skalen aus deren Komplement. Aus dem LES Ansatz resultiert ein Schließungsproblem für die nicht aufgelösten Terme in der Gleichung für die aufgelösten Skalen. Die Schließung erfolgt durch eine Approximation, die auf dem Residuum der großen Skalen basiert. Diese Approximation ist durch ein ähnliches Vorgehen im Rahmen von stabilisierten finiten Elementen motiviert und beruht auf lokalen, algebraischen Skalierungsargumenten. Um eine Anwendung im Zusammenhang mit FSI zu ermöglichen, wird dieser Ansatz in einem Arbitrary-LAGRANGEan-EULERian Kontext formuliert, das heißt für bewegte Gebiete.

Der verwendete Ansatz wird für Testprobleme validiert und eingehend untersucht. Dies gilt insbesondere für die Auswirkungen der Zeitabhängigkeit der nicht aufgelösten Skalen und den Einfluß einer isogeometrischen, d.h. NURBS basierten, Wahl der Ansatzfunktionen. Aus diesen Untersuchungen kann auf keinen positiven Effekt einer Berücksichtigung der Zeitabhängigkeit der nicht aufgelösten Skalen im Bezug auf das Ergebnis für die aufgelösten Skalen geschlossen werden. Trotzdem führt ein solches Vorgehen im Vergleich zum traditionellen Ansatz, der die zeitliche Entwicklung der nicht aufgelösten Skalen unberücksichtigt läßt, zu einer robusteren, zeitschrittunabhängigen Darstellung nicht aufgelöster, d.h. modellierter, Geschwindigkeiten. Eine Erklärung für die überraschende Robustheit der aufgelösten Skalen im traditionellen Ansatz wird in dieser Arbeit aus der Untersuchung der numerischen Dissipation der Modell-

terme abgeleitet. Für kleine Zeitschrittweiten übernimmt der Stabilisierungsterm aus der Kontinuitätsstabilisierung die zurückgehenden Beiträge der anderen Terme. Weiter wird gezeigt, dass die vom isogeometrischen Ansatz erzeugte verbesserte Darstellung aufgelöster Größen mit einer stärker ausgeprägten Modellierung der nicht aufgelösten Skalen einher geht. Schließlich wird auch noch am Beispiel einer turbulenten Umströmung eines rechteckigen Zylinders gezeigt, daß eine schwache Aufbringung der Haftbedingung den berechneten Widerstandsbeiwert reduzieren kann und damit zum Preis eines erhöhten Rechenaufwands eine bessere Approximation erreicht wird.

Eine wesentliche Folgerung aus den Ergebnissen dieser Arbeit ist, dass die traditionelle Herangehensweise ohne Berücksichtigung der Zeitabhängigkeit der nicht aufgelösten Skalen für die betrachteten FSI Problemstellungen ausreicht. Der Einsatz von isogeometrischen Ansatzfunktionen wird, sofern möglich, aus Genauigkeits- und Effizienzgründen empfohlen. Das Potential einer Kombination dieser beiden Ansätze wird durch eine Beispielsimulation verdeutlicht.

Danksagung

Zu Beginn dieser Arbeit möchte ich noch einmal meine Dankbarkeit an alle zum Ausdruck bringen, die mich während dieser langen Jahre der intensiven Arbeit so tatkräftig unterstützt haben. Angefangen bei Herrn Prof. Wolfgang A. Wall und Herrn Dr.-Ing. Volker Gravemeier, deren Betreuung und das von ihnen geschaffene Umfeld aus dem Lehrstuhl für Numerische Mechanik und der Emmy-Noether Gruppe „Computational Multiscale Methods for Turbulent Combustion in Complex Geometries“ mir diese Arbeit erst ermöglicht haben.

Ein ganz besonderes Dankeschön geht auch an meine Kollegen, von denen ich viel gelernt habe. Sie haben für mich meine Promotionszeit zu einem Lebensabschnitt gemacht, an den ich mich auch in Zukunft noch gerne erinnern werde. Das selbe gilt auch für alle „Texaner“ am ICES in Austin, die mich dort während meines Forschungsaufenthaltes ausnahmslos herzlich aufgenommen haben.

Weiter möchte ich meinen Eltern und meiner Schwester danken, die mich schon mein Leben lang unterstützt haben. Ein Teil meines Erfolges ist sicherlich auch ihnen geschuldet. Genauso gilt mein Dank meiner Freundin Julia für ihre nicht endende Geduld mit mir und meiner Arbeit.

Ihnen allen sowie meinen zahlreichen Korrekturlesern und den weiteren Mitgliedern der Prüfungskommission, Herrn Prof. Assad A. Oberai und Herrn Prof. Wolfgang H. Polifke, ein herzliches vergelt's Gott!

München, 30. September 2010

Peter Gamnitzer

Contents

| | | |
|----------|---|-----------|
| 1 | Introduction | 1 |
| 1.1 | Motivation | 1 |
| 1.2 | Scope and objectives | 2 |
| 1.3 | Overview | 2 |
| 2 | Principles of turbulent incompressible flows | 5 |
| 2.1 | Continuum mechanical description of incompressible flows | 5 |
| 2.1.1 | Flow kinematics and transport in flows | 5 |
| 2.1.2 | Kinetics | 13 |
| 2.1.3 | Constitutive equation | 16 |
| 2.1.4 | The arising system of nonlinear partial differential equations | 17 |
| 2.1.5 | The initial and boundary value problem | 19 |
| 2.2 | The nature of turbulence | 20 |
| 2.2.1 | Turbulent flow characteristics | 21 |
| 2.2.2 | REYNOLDS-averaged NAVIER-STOKES equations | 22 |
| 2.2.3 | The multiscale character of turbulence | 24 |
| 2.2.4 | Energy spectra | 26 |
| 2.2.5 | Wall-bounded turbulent channel flow | 28 |
| 3 | Finite elements for incompressible flows — base algorithm | 35 |
| 3.1 | Implicit time integration | 36 |
| 3.1.1 | Generalised-alpha time integration | 37 |
| 3.1.2 | Application to the incompressible NAVIER-STOKES equations | 42 |
| 3.2 | Weak form of the semi-discrete problem | 44 |
| 3.2.1 | ALE and convective EULERian formulation | 46 |
| 3.2.2 | Conservative EULERian version | 46 |
| 3.2.3 | Abstract notation | 47 |
| 3.3 | Geometry approximation | 47 |
| 3.3.1 | Introduction to NURBS | 48 |
| 3.3.2 | Finite element geometry representation | 53 |
| 3.4 | Spatial approximation of the solution | 57 |
| 3.4.1 | Restriction to finite dimensional subspaces | 58 |
| 3.4.2 | Isoparametric concept, basis representations and degrees of freedom | 58 |
| 3.4.3 | Time derivatives of discretised degrees of freedom | 61 |
| 3.4.4 | Resulting nonlinear system and solution process | 61 |
| 3.4.5 | LAGRANGEan and isogeometric finite elements | 66 |
| 3.5 | Residual-based stabilisation techniques | 69 |

| | | |
|----------|--|------------|
| 3.5.1 | PSPG, SUPG and LSIC stabilisation | 69 |
| 3.5.2 | Stabilisation parameters | 71 |
| 3.6 | Imposition of initial conditions | 78 |
| 3.7 | Basic boundary conditions | 79 |
| 3.7.1 | DIRICHLET boundary conditions | 79 |
| 3.7.2 | NEUMANN (traction) boundary conditions | 80 |
| 3.7.3 | A consistency term for conservative formulations | 81 |
| 3.7.4 | Stabilised outflow boundary conditions | 81 |
| 3.7.5 | Periodic boundary conditions | 81 |
| 4 | Turbulence modelling with a focus on residual-based LES | 85 |
| 4.1 | Limitations of direct numerical simulation | 86 |
| 4.2 | Approaches for modelling turbulence | 86 |
| 4.2.1 | RANS closures | 88 |
| 4.2.2 | Large-eddy simulation | 89 |
| 4.3 | The original formulation of VMM in turbulence modelling | 93 |
| 4.3.1 | Two-scale separation with explicit solution or approximation of the un-resolved-scale equation | 93 |
| 4.3.2 | Three-scale approaches keeping consistency on the large resolved scales | 97 |
| 4.4 | Residual-based modelling of turbulence | 98 |
| 4.4.1 | Subgrid closures | 99 |
| 4.4.2 | The resolved-scale continuity equation | 102 |
| 4.4.3 | Resolved-scale equation in advective ALE form | 102 |
| 4.4.4 | A comment on the nonlinear character of the time-dependent subgrid-scale approximation | 105 |
| 4.4.5 | Conservative EULERian resolved-scale equation | 107 |
| 4.4.6 | Implementation | 107 |
| 4.5 | Weak DIRICHLET boundary conditions in residual-based VMM | 108 |
| 4.5.1 | Required extensions to the weak form | 109 |
| 4.5.2 | Definition of τ_B | 110 |
| 4.5.3 | Nonlinearity, implementation issues | 111 |
| 5 | Time-dependent subgrid-scale modelling of plane channel turbulence | 113 |
| 5.1 | Problem setup | 113 |
| 5.2 | Averaging procedures | 115 |
| 5.2.1 | Time averages | 115 |
| 5.2.2 | Spatial averaging for resolved-scale quantities | 116 |
| 5.2.3 | Spatial averaging for unresolved-scale related data | 117 |
| 5.3 | Size and sparsity of system matrices in residual-based VMM | 117 |
| 5.3.1 | Matrix structure | 118 |
| 5.3.2 | Resolved-scale results for the investigated discretisations | 119 |
| 5.4 | Benefits of a time-dependent subgrid representation | 119 |
| 5.4.1 | Mean resolved-scale quantities | 120 |
| 5.4.2 | Averaged unresolved-scale quantities | 121 |
| 5.5 | Influence of stabilisation parameter and element length definition | 124 |

| | | |
|----------|--|------------|
| 5.6 | Modelled turbulent dissipation | 127 |
| 5.6.1 | Investigations for a series of time step sizes | 129 |
| 5.6.2 | Influence of isogeometric representation on subgrid dissipation | 129 |
| 6 | Further examples of turbulent flow computations | 133 |
| 6.1 | TAYLOR-COUETTE flow | 133 |
| 6.1.1 | Computations for selected REYNOLDS numbers | 135 |
| 6.1.2 | Advantages of a KRYLOV-projection-based solution method | 138 |
| 6.2 | Turbulent flow around a square-section cylinder | 139 |
| 6.2.1 | Setup | 140 |
| 6.2.2 | Mean streamwise velocity distributions | 144 |
| 6.2.3 | Mean pressure on the cylinder's surface | 145 |
| 6.2.4 | Lift and drag | 146 |
| 7 | Isogeometric residual-based VMM for modelling turbulence in FSI | 151 |
| 7.1 | Additional subproblems in fluid-structure interaction | 151 |
| 7.1.1 | Structure | 151 |
| 7.1.2 | Mesh motion | 153 |
| 7.2 | Fluid-structure interaction: coupled problem and solution methods | 153 |
| 7.3 | Preliminary study of residual-based VMM on a deforming channel | 154 |
| 7.4 | Fluid-structure interaction for a turbulent pipe flow with a flexible wall | 156 |
| 7.4.1 | Computational setup | 156 |
| 7.4.2 | Results | 158 |
| 8 | Summary and outlook | 161 |
| A | Mathematical tools and proofs for the description of flows | 163 |
| A.1 | REYNOLDS transport theorem | 163 |
| A.2 | ALE mass conservation in spatial representation — a proof | 164 |
| A.3 | Statistical description of turbulent flows | 167 |
| A.4 | Fundamental function spaces | 171 |
| B | Additional information on non-uniform rational B-splines | 173 |
| B.1 | Knot insertion and order elevation for B-splines | 173 |
| B.2 | Construction of a circle segment using NURBS — an example | 179 |
| C | A dynamic SMAGORINSKY implementation for comparison | 181 |
| C.1 | The (dynamic) SMAGORINSKY model | 181 |
| C.1.1 | Eddy-viscosity subgrid models | 181 |
| C.1.2 | GERMANO model | 182 |
| C.2 | Finite element implementation | 185 |
| C.3 | Averaged distribution of effective viscosity in a turbulent channel flow | 186 |
| D | Linearisation schemes for residual-based VMM | 189 |
| D.1 | Convective ALE form | 189 |
| D.2 | Conservative EULERian form | 195 |

| | | |
|----------|---|------------|
| E | Iterative solution of the linear problem | 201 |
| E.1 | A preconditioned GMRES procedure | 202 |
| E.1.1 | The GMRES method | 202 |
| E.1.2 | Preconditioned version | 204 |
| E.2 | Treatment of singular systems with known kernel | 205 |
| E.2.1 | Choices for the weight vector | 207 |
| E.2.2 | Projector definitions | 208 |
| E.2.3 | Projected system of equations | 209 |

Nomenclature

General styles for scalars, vectors and tensors

| | |
|---|--|
| q | style for a scalar value |
| $\mathbf{v}, \boldsymbol{\sigma}$ | style for vectors and tensors in 3D-space |
| \mathbf{A} | style for matrices |
| $\underline{q}^h, \underline{\mathbf{v}}^h$ | coordinate representation of a spatially discretised scalar and vector-valued quantity |

Mappings, domains, boundaries

| | |
|---------------------------------|---|
| φ | particle mapping |
| Φ | mesh mapping |
| Ψ^{-1} | particle motion modulo domain deformation |
| \mathbf{R} | orthogonal matrix used to define a rigid-body mesh rotation |
| Υ | a generic particle mapping |
| Ω_0 | initial domain |
| $\Omega_{\mathbf{x}}(t)$ | deformed domain at time t |
| $\Omega_{\xi}(t)$ | reference domain at time t |
| $\Omega(t_0)$ | initial control volume |
| $\Omega(t)$ | current control volume/computational domain at time t |
| $\Gamma(t) = \partial\Omega(t)$ | boundary of current control volume, time t |
| $\Gamma_N(t)$ | NEUMANN part of the boundary |
| $\Gamma_D(t)$ | DIRICHLET part of the boundary |
| $\Gamma_{D,\text{weak}}(t)$ | part of the boundary with weakly imposed DIRICHLET conditions |
| Γ_{outflow} | outflow part of boundary |

Frames of reference and functional dependencies

| | |
|--|---|
| q^0, q, q^{ref} | quantity q in material, current and referential frame of reference |
| $f _{\mathbf{x}}, f _{\xi}, f _{\mathbf{x}}$ | function f , expressed as a function on $\Omega_0, \Omega_{\mathbf{x}}(t)$ or $\Omega_{\xi}(t)$ |

Spaces, inner products and norms

| | |
|--------------------------------------|---|
| $\mathbb{N}, \mathbb{R}, \mathbb{C}$ | natural, real and complex numbers |
| $H^1(\Omega), H^2(\Omega)$ | SOBOLEV-spaces on a domain Ω |
| $H_0^1(\Omega)$ | functions from $H^1(\Omega)$ that vanish on the domain boundary |
| $\mathcal{L}^2(\Omega), L^2(\Omega)$ | spaces of square-integrable functions on Ω |
| $[H^1(\Omega)]^3, [L^2(\Omega)]^3$ | generalised CARTESIAN product spaces |
| $\Gamma^{-\frac{1}{2}}$ | trace space on $\partial\Omega$ |

| | |
|--------------------------------|--|
| $\mathcal{S}_u, \mathcal{S}_p$ | spaces of trial functions for velocity and pressure |
| $\mathcal{T}_u, \mathcal{T}_p$ | spaces of weighting functions for velocity and pressure |
| $(\cdot, \cdot)_\Omega$ | inner product of $L^2(\Omega)$ |
| $(\cdot; \cdot)_\Omega$ | inner product of $[L^2(\Omega)]^3$ |
| $(\cdot : \cdot)_\Omega$ | $L^2(\Omega)$ -inner product for tensor-valued functions |
| $(\cdot, \cdot)_{H^1(\Omega)}$ | inner product of $H^1(\Omega)$ |
| $\ \cdot\ _{L^2}$ | L^2 -norm induced by respective scalar product |
| $\ \cdot\ _{H^1}$ | H^1 -norm induced by scalar product |
| $\ \cdot\ _E$ | energy norm |

General mathematical operators and symbols

| | |
|---|---|
| $O(\cdot)$ | asymptotic notation, ‘is order of \cdot ’ |
| ∇v | JACOBIan of a vector-valued function v |
| ∇q | gradient of a scalar function q |
| Δ | LAPLACE operator |
| $\nabla \cdot$ | divergence of a vector-valued function. For tensor-valued functions, the operator is applied to each row of the tensor. |
| \det | determinant |
| tr | trace operator |
| area, vol | area and volume operators |
| \dim | operator determining the dimension of a space |
| δ_{ij} | KRONECKER-delta |
| \sim | proportional to |
| $\frac{\partial}{\partial t}$ | partial time derivative. analogously for partial spatial derivatives |
| $\dot{f} = \frac{\partial f _{\mathbf{x}}}{\partial t}$ | short form of a partial time derivative of a function f in current configuration |
| $\dot{f}^\circ = \frac{\partial f _{\boldsymbol{\xi}}}{\partial t}$ | short form of a partial time derivative of a function f in reference configuration |
| \mathbb{I} | identity mapping |
| $\mathbf{1}$ | identity tensor |
| \mathbf{e}_d | unit vector in direction d |
| \mathbf{n} | unit normal pointing outwards |
| $\{\cdot\}_-$ | function that is zero on the part of the expected outflow that is in effect an outflow and non-zero elsewhere |
| $\mathcal{P}_{yz}(\cdot)$ | an operator that projects a vector into the yz -plane |

General dimensionless parameters

| | |
|----|-----------------|
| Re | REYNOLDS number |
| Pe | PECLET number |

Basic physical quantities

| | |
|---|--|
| ρ | fluid density |
| μ, ν | dynamic and kinematic viscosity |
| \mathbf{a} | fluid acceleration |
| \mathbf{u}, \mathbf{v} | fluid velocity and associated weighting function |
| \mathbf{u}_G | grid velocity |
| \mathbf{c} | ALE convective velocity |
| p, q | pressure and corresponding weighting function |
| \mathbf{d} | displacement |
| \mathbf{d}_G | mesh displacement |
| $\boldsymbol{\varepsilon}$ | rate-of-strain tensor for fluid |
| $\boldsymbol{\sigma}$ | CAUCHY stress tensor |
| $\boldsymbol{\tau}$ | viscous stresses |
| $\boldsymbol{\tau}_{\text{rey}}$ | REYNOLDS stress tensor |
| $\boldsymbol{\tau}_{\text{rey}}^{\text{dev}}$ | deviatoric part of $\boldsymbol{\tau}_{\text{rey}}$ |
| \mathbf{t} | traction |
| \mathbf{b} | volume force per unit mass |
| \mathbf{S} | second PIOLA-KIRCHHOFF stress tensor |
| \mathbf{E} | GREEN-LAGRANGE strain tensor |
| ρ_S | structure density |
| λ_S, μ_S | LAMÉ constants |
| ν_S | POISSON'S ratio |
| E_S | YOUNG'S modulus |
| $\kappa, \boldsymbol{\kappa}, \ell_\kappa$ | wave number wave vector and associated length scale |
| k | turbulent kinetic energy |
| ϵ | rate of dissipation |
| Θ | velocity spectrum tensor |
| ε | diffusion constant in a convection-diffusion model problem |

Characteristic scales in turbulent flows

| | |
|---|---|
| $\mathcal{L}, \mathcal{T}, \mathcal{U}$ | characteristic length, time and velocity scales of large-scale motions |
| η, t_η, u_η | characteristic length, time and velocity scales for the smallest eddies |

Important notations for (simulation of) wall-bounded/channel flows

| | |
|------------------------------------|---|
| δ | channel half-height |
| b | channel width |
| L | channel length |
| $\ell_x, \ell_y = 2\delta, \ell_z$ | size of the periodic domain used for computations |
| \bar{u} | bulk velocity |
| τ_w | mean wall shear stress |
| u_{τ_w} | friction velocity |

| | |
|---|---|
| Re_τ | REYNOLDS number based on friction velocity |
| \cdot^+ | wall units |
| y^+ | distance to the wall measured in wall units |
| y_{first}^+ | distance of first grid point to the wall measured in wall units |
| δ_ν | viscous length scale |
| p_w | pressure on the wall |
| $\mathcal{F}, \mathcal{F}^{\text{inner}}$ | universal non-dimensional functions |
| $\kappa_{\text{log-law}}$ | VON KÁRMÁN constant |
| $B_{\text{log-law}}$ | log-law parameter |
| C_{stretch} | mesh-stretching constant |
| ε_X | element-averaged modelled rate of turbulent dissipation for term X |
| Δp | pressure drop along channel |
| p^*, \mathbf{b}^* | modified pressure and body force per unit mass used for the application of periodic boundary conditions |

Statistics and averages

| | |
|---|--|
| $\langle q \rangle$ | averaged value or (in the limit) expected value of a quantity q |
| $\langle q \rangle_{\text{time}}, \langle q \rangle_{\text{space}}$ | time and space average of a quantity q |
| $\langle q \rangle_{\text{plane}}$ | average of a quantity q in a homogeneous plane |
| $\langle q \rangle_{\text{space,time}}$ | combined space-time average of a quantity q |
| S | sample space |
| Σ | sigma-algebra of possible events |
| $P(E)$ | probability of an event E |
| U, \mathbf{U} | scalar and vector-valued random variables |
| \bar{U}^n | arithmetic mean of a random variable |
| \underline{U} | fluctuations of a random variable |
| P_U | (cumulative) probability distribution of a random variable U |
| p_U | associated probability density function |
| ϖ | mean value |
| σ | standard deviation |
| Var, Cov | variance and covariance |
| \mathbf{R} | two-point, one-time autocovariance |
| C_t | two-time covariance function for general random processes |
| C_t^{stat} | two-time covariance function for statistically stationary random processes and statistically homogeneous random fields |
| $t_{\text{cor}}, \ell_{\text{cor}}$ | correlation time and length |

Time integration

| | |
|------------------------------|------------------------------|
| Δt | time step size |
| t_0 | initial time |
| $n_{\Delta t}$ | number of time steps |
| $\alpha_F, \alpha_M, \gamma$ | generalised-alpha parameters |

| | |
|--|--|
| β | additional generalised-alpha parameter for structural time integration |
| A | Amplification matrix |
| ρ_∞ | spectral radius of an infinite time step |
| $(\lambda\Delta t)^{\text{rootloc}}$ | root locus curve |
| $\wp^{\lambda\Delta t}(\zeta)$ | characteristic polynomial of the associated linear difference equation |
| $(\cdot)^{n+1}, (\cdot)^n, (\cdot)^{n-1}$ | value at current, most recent and old time step |
| $(\cdot)^{n+\alpha_F}, (\cdot)^{n-1+\alpha_F}$ | quantity at intermediate time levels $t^{n+\alpha_F}$ and $t^{n-1+\alpha_F}$ |
| $(\cdot)^{n+\alpha_M}, (\cdot)^{n-1+\alpha_M}$ | quantity at intermediate time level $t^{n+\alpha_M}, t^{n-1+\alpha_M}$ |

Parts of the time-discrete weak form of the NAVIER-STOKES equations

| | |
|-------------------|--|
| $B(\cdot, \cdot)$ | momentum part which is depending at least linearly on velocity |
| $G(\cdot, \cdot)$ | bilinear form including all contributions of pressure |
| $D(\cdot, \cdot)$ | bilinear form containing contributions of continuity |
| $F(\cdot)$ | linear form containing surface traction and body force effects as well as contributions from previous time steps |

Finite elements

| | |
|--|--|
| $(\cdot)^h$ | entity associated with a finite-dimensional trial or weighting subspace |
| $n_u^{\text{dof}}, n_p^{\text{dof}}, n^{\text{dof}}$ | number of velocity, pressure and total degrees of freedom (dofs) |
| $\bar{n}_u^{\text{dof}}, \bar{n}^{\text{dof}}$ | numbers of dofs plus number of dofs blocked by a DIRICHLET condition |
| R_u, R_p | Residual of weak form of discretised momentum and continuity equation, including stabilisation, subgrid and boundary terms |
| R_u^{Gal} | GALERKIN part of weak form of momentum equation |
| $\underline{R}_{u,\delta}, \underline{R}_{p,\kappa}$ | Residuals of weak form evaluated for basis functions δ (velocity dof) and κ (pressure dof) |
| n_{np} | number of nodes/control points |
| n_{ele} | number of elements |
| n_{np}^e | number of nonzero basis functions on element e |
| ien | mapping from element local number to global index |
| $n_{e,\text{adj}}(\iota)$ | number of elements adjacent to a node ι |
| Ω_e | element domain in space |
| χ_e | mapping from element to reference element |
| ξ_1, ξ_2, ξ_3 | coordinates in reference element |
| ξ_{Gp} | location of GAUSSpoint in reference element |
| N_ι | basis function for finite element geometry representation associated with node/control point ι |
| S_I^e | element shape function associated with element local node I |
| $\mathbf{N}_\delta^{S_u^h}, \mathbf{N}_\delta^{T_u^h}$ | basis functions for finite dimensional trial and weighting function spaces (velocity) |

| | |
|--|---|
| $N_{\kappa}^{S_p^h}, N_{\kappa}^{T_p^h}$ | basis functions for finite dimensional trial and weighting function spaces (pressure) |
| HEX8 | trilinear volume elements |
| HEX20 | 20-noded serendipity volume elements |
| NURBS27 | second order NURBS volume elements |

Non-uniform rational B-splines

| | |
|---|---|
| N_i^p | i -th NURBS basis function of degree p |
| B_i^p | i -th B-spline basis function of degree p |
| l | number of B-spline basis functions in patch |
| u, v, w | knot values |
| n_{patch} | index of patch |
| offset (n_{patch}) | number of elements contained in patches with an index smaller than n_{patch} |
| \mathbf{X}^B | B-spline control point |
| \mathbf{X} | NURBS control point |
| ω | NURBS weight |
| $\mathbf{V}^{\text{B-spline}}, \mathbf{V}^{\text{NURBS}}$ | B-spline or NURBS volumes (similar for curves C and surfaces S) |
| \overline{B}_i^p | B-spline basis function refined by knot insertion or order elevation. Corresponding knot and control points are also denoted by an overbar. |

Stabilisation and (residual-based) variational multiscale modelling

| | |
|---|--|
| τ_M, τ_{Mp} | stabilisation parameters (SUPG,PSPG) |
| τ_C | stabilisation parameters (LSIC) |
| \mathbf{r}_M^h | residual of strong advective form of momentum equation |
| \mathbf{r}_C^h | residual of strong form of continuity equation |
| m_e, C_{inv} | constants from inverse estimate |
| h_e, \mathbf{d}_{∇} | choices for element lengths |
| \mathbf{g}, \mathbf{G} | metric vector and metric tensor |
| $\tau_M^{\text{VX}\oplus\Delta t}, \tau_M^{\text{VX}\ominus\Delta t}$ | stabilisation parameter variants $X = 1, 2, 3$ (momentum) |
| $\tau_C^{\text{VX}\oplus\Delta t}, \tau_C^{\text{VX}\ominus\Delta t}$ | stabilisation parameter variants $X = 1, 2, 3$ (continuity) |
| IP | index for quantities evaluated at an integration point |
| \mathbb{P} | projection into finite dimensional solution subspace |
| \mathfrak{S}_a^b | operator separating scales a and b |
| \mathfrak{P}_a^b | prolongation operator |
| \mathfrak{R}_a^b | restriction operator |
| (\cdot) | unresolved scale quantities |
| $(\cdot)^H$ | large resolved scales |
| $(\cdot)^{\delta h}$ | small resolved scales |
| $B_1(\cdot, \cdot, \cdot)$ | part of $B(\cdot, \cdot)$ that contains products of resolved and unresolved velocities |
| $B_2(\cdot, \cdot)$ | part of $B(\cdot, \cdot)$ depending only on unresolved velocities |

| | |
|------------------------|--|
| γ_{wdbc} | constant that defines the adjoint consistent/inconsistent approach |
| τ_B | element-specific stability parameter for weak DIRICHLET conditions |
| C_B | a positive constant related to the local boundary inverse estimate |
| h_B | element length in the direction normal to the boundary |

RANS modelling and large-eddy simulation

| | |
|--|---|
| ℓ_{mix} | ‘mixing length’ scale |
| u_{tur} | velocity scale required in turbulent viscosity approaches |
| ν_{tur} | turbulent viscosity |
| k_{cutoff} | cutoff wave number |
| C_{Smag} | SMAGORINSKY’s constant |
| $\ell_{\text{S,mix}}$ | SMAGORINSKY length scale |
| C_{Dyn} | counterpart to C_{Smag} in the GERMANO approach |
| $\nu_{\text{S,tur}}$ | subgrid viscosity |
| ν_{eff} | effective viscosity |
| $\overline{G}, \widehat{G}, \widehat{\widehat{G}}$ | filter, coarser filter, combined filter |
| $\overline{\Delta}, \widehat{\Delta}, \widehat{\widehat{\Delta}}$ | filter widths |
| α_{Δ} | filter width ratio |
| $\overline{(\cdot)}, \widehat{(\cdot)}, \widehat{\widehat{(\cdot)}}$ | the three filters applied to a quantity (\cdot) |
| $\overline{p}^{\text{dev}}$ | filtered pressure including trace of subgrid stress tensor |
| $\tau_{\Delta}^{\text{res}}, \tau_{\widehat{\Delta}}^{\text{res,dev}}$ | subgrid stress for filter \overline{G} and its deviatoric part |
| L, L^{dev} | resolved (deviatoric) part of $\tau_{\widehat{\Delta}}^{\text{res}}$ |
| M | \widehat{G} unresolved but \overline{G} resolved part of modelled stress (normalised) |

Symbols used in linearisation schemes

| | |
|-------------|--|
| J | JACOBIan of velocities in integration point (IP), most recent non-linear iteration value |
| c | most recent nonlinear iteration value of ALE convective velocity in IP |
| u | most recent nonlinear iteration value of velocity in IP |
| \tilde{u} | most recent nonlinear iteration value of subgrid velocity in IP |

Iterative solution of the linear problem

| | |
|-----------------|---------------------|
| \underline{w} | weight vector |
| \underline{c} | kernel basis vector |
| span | linear span |

| | |
|-----------|---|
| K^i | KRYLOV subspace of order i |
| H | HESSENBERG matrix |
| \hat{H} | extended HESSENBERG matrix |
| M | preconditioner |
| P, P^T | discrete projectors used for the solution of purely DIRICHLET constraint problems |

Abbreviations

| | |
|-------|--|
| LES | large-eddy simulation |
| RANS | REYNOLDS-averaged NAVIER-STOKES |
| DNS | direct numerical simulation |
| VMM | variational multiscale method |
| FSI | fluid-structure interaction |
| PSPG | pressure-stabilising PETROV-GALERKIN |
| SUPG | streamline upwind PETROV-GALERKIN |
| LSIC | least-squares incompressibility constraint stabilisation |
| USFEM | unusual stabilised finite element method |
| GLS | GALERKIN-least-squares |
| NURBS | non-uniform rational B-splines |
| ALE | Arbitrary-LAGRANGEAN-EULERian |
| GMRES | generalised minimal residual |
| CAD | computer aided design |
| BDF2 | second order backward differentiation formula |
| LBB | LADYSHENSKAYA-BABUŠKA-BREZZI |
| rms | root-mean-square value |
| rV | conventional residual-based subgrid closure |
| td | time-dependent subgrid closure |

1 Introduction

1.1 Motivation

The application of finite elements in simulation of fluid-structure interaction has been under intensive research for many years now. Significant progress has been made in this field, allowing impressive simulations of complex biological systems like tracheobronchial trees or aortic aneurysms as they can be found in KÜTTLER et al. [149]. Nevertheless, fluid-structure interaction involving turbulent flow is still an open research topic because of the additional complexity introduced by the multiscale character of turbulence. The fact that the turbulent regime is characteristic for many applications of engineering interest shows that further developments in this direction are necessary. Examples for such applications can be found, for instance, in aircraft engineering or civil engineering where air-flow induced forces interact with aeroplanes, buildings, bridges, wind turbines and so on.

An experimental investigation of such problems is not straightforward and would involve costly experimental setups like wind tunnels. Numerical simulation allows to reduce these costs and to obtain detailed information in a very convenient way. Nevertheless, it should be pointed out that numerical simulation cannot make experiments obsolete. It is rather necessary to check thoroughly the results of each numerical method against experiments or known solutions.

Finite elements are well established as the preferred method for problems based on self-adjoint elliptic or parabolic partial differential operators, which can be found for instance in heat conduction and structural mechanics. Among other things, users of the finite element method appreciate the easy and accurate representation of complex geometries, the natural way differential type boundary equations can be included and furthermore the convenient framework for an implementation. In computational fluid dynamics, usage of finite elements is not as widespread yet. Nevertheless, since the introduction of stabilised methods, finite elements have constantly been gaining popularity also in this field.

A characteristic feature of finite elements is that the approximation theory behind this method is based on weak forms and function spaces. Thus, discrete numerical solutions correspond not only to point values but to functions that are defined on the whole computational domain. The concept of function spaces opens a door to a ‘natural’ way of scale separation allowing turbulence modelling approaches that are embedded in the general concept of finite elements. The main topic of this thesis is located in the overlap region between turbulent flows and finite elements. Methodologies are developed in particular with regard to applications in fluid-structure interaction, but they can be applied to other multiphysics problems like turbulent combustion as well.

1.2 Scope and objectives

Within this work, a complete framework for residual-based large eddy simulation on deformable domains is provided, which can be used for the simulation of fluid-structure interaction involving turbulent, incompressible flow. This framework consists of many elements: Spatial discretisation using LAGRANGEan, serendipity and isogeometric finite elements, numerical treatment of time derivatives of resolved and unresolved, i.e. modelled, quantities and residual-based subgrid approximations.

The residual-based variational multiscale method (residual-based VMM) arising from these building blocks is investigated in detail. Special attention is given to an investigation of a time-dependent treatment of the subgrid scales. Furthermore, the impact of an isogeometric element choice on unresolved scales is analysed. Numerical dissipation rates associated with the model terms arising from residual-based approximation of the unresolved scales are evaluated, providing further insight into the mechanisms behind residual-based approaches. Other integral parts of this thesis are a careful evaluation of weak boundary conditions with respect to forces imposed on structures in turbulent flows, and a brief discussion of the efficiency of isogeometric approaches in comparison to serendipity-based finite elements. Furthermore, the impact of element length definitions in boundary layer meshes is clarified, and a consistent way for computing spatial averages of finite element solution functions is provided.

In addition, the practicability of the presented framework for fluid-structure interaction is illustrated based on two examples: turbulent channel flow on a mesh that is deformed according to a prescribed mesh motion and turbulent flow through a deforming pipe. The latter incorporates residual-based variational multiscale modelling and isogeometric finite elements for turbulent fluid-structure interaction in a monolithic framework.

1.3 Overview

This thesis addresses a variety of different subjects. Physical requirements are discussed as well as numerical algorithms. The computational approaches are investigated, validated and combined with other algorithms in order to generate a method which can be successfully applied to turbulent fluid-structure interaction problems. Although everything is directed towards this application, the main focus of the thesis remains on the fluid part. In order to simplify navigation through the thesis and to help the reader to recognise the connections between the individual chapters, their contents are summarised briefly in the following.

In chapter 2, governing equations for flows on deforming domains are provided. Furthermore, an introduction to turbulence is given. Some basic knowledge on this topic is required to understand the methods and results that are presented later on.

The governing equations form the base of the numerical algorithm described in chapter 3. Its main topic is a stabilised finite element method for the solution of flow problems. Issues of time integration are addressed, including an advanced linear stability analysis for the generalised-alpha method yielding an explicit formula for root-locus curves. In addition, the incorporation of isogeometric finite element approaches is discussed and the solution process is outlined.

The residual-based variational multiscale modelling of turbulence presented in chapter 4 is closely related to the numerical algorithm introduced in chapter 3. It can be interpreted as a

large-eddy simulation approach, establishing a connection between numerics and physics of turbulence.

Chapter 5 provides some detailed investigations of residual-based large-eddy simulation approaches for the well-documented canonical flow example of turbulent plane channel flow. The behaviour of different subgrid models is studied, especially with respect to the time-dependency of subgrid scales and their relation to the spatial discretisation approach.

Further examples for applications of the method to more complex turbulent flow examples are contained in chapter 6. Among other things, these examples include investigations of the advantages of KRYLOV-projection-based solver techniques for a purely DIRICHLET bounded flow problem, the TAYLOR-COUETTE flow, and investigations of the performance of weak DIRICHLET boundary conditions with respect to lift and drag values obtained for a turbulent flow around a square cylinder.

In chapter 7, the residual-based large-eddy simulation including the advantageous isogeometric representation is incorporated into a monolithic fluid-structure interaction framework. First numerical examples show the feasibility of the combined approach in a turbulent regime.

The scope of chapter 8 is to summarise the main achievements of this work, to draw conclusions and to provide directions for future work.

Several appendices come along with this thesis. They have been included for various reasons. Appendix A is intended to provide additional details on the derivation of the kinematic formulation that is used to develop the governing equations on moving meshes. Furthermore, a number of mathematical tools for the statistical description of turbulent flows and for the statement of a weak form are collected in that appendix.

The purpose of appendix B is to provide a small extension to the very brief introduction of non-uniform rational B-splines contained in chapter 3. The content does not exceed what can be obtained from standard literature. However, readers not familiar with isogeometric finite element approaches or non-uniform rational B-splines will possibly appreciate this small collection.

Appendix C, in turn, provides a detailed description of a finite element-based dynamic SMAGORINSKY implementation. This more traditional approach is used for comparison to the residual-based variational multiscale approach in several places in the present thesis.

The next appendix, D, contains a detailed listing of all matrix contributions arising from the residual-based variational multiscale approach formulated in chapter 4. It clarifies some statements on the treatment of nonlinearity and provides an implementation-ready version of the element-matrix part of the algorithm.

Finally, in appendix E, an efficient solution procedure is provided for linear systems corresponding to problems for which the pressure level is defined only up to a constant. Although similar approaches are already used by some groups, the impact of such an approach is often underestimated. For this reason, an implementation of a solution method for the projected system is included. Additionally, numerical tests for the method are contained in the TAYLOR-COUETTE flow example already mentioned above.

2 Principles of turbulent incompressible flows

This chapter is intended to provide a short introduction to important basic principles of turbulent flows. The first section is about continuum mechanics, containing governing equations for incompressible flow of a NEWTONian fluid. The second section focuses on the topic of turbulence. Main features of turbulent flows are highlighted and ways to describe them using stochastic calculus are discussed. Afterwards, the nature of turbulence is dealt with in the discussion of energy spectra and wall-bounded turbulence.

2.1 Continuum mechanical description of incompressible flows

In this section, continuum mechanical basics for the description of flows will be provided. For general textbooks on continuum mechanics, the reader is referred to the books by GURTIN [105] or TRUESDELL and NOLL [210]. Beside this general literature on continuum mechanics, there are a number of textbooks dealing with the application of continuum mechanic principles to flows. An example is the book by TRUESDELL and RAJOPAL [211], containing a mathematically profound introduction. Furthermore, a wide range of books on fluid mechanics in general, like the books by BATCHELOR [10], GRANGER [93] or PANTON [169], is available. Among other things, the books by GRANGER [93] and PANTON [169] include remarkable illustrations of flow patterns. Another well-known reference is LANDAU and LIFSCHITZ [152], a book that emphasises the relationship of hydromechanics to other branches of physics. Further information on the description of flows on deformable domains using the Arbitrary-LAGRANGEan-EULERian (ALE) approach, a name introduced by HIRT [113] in 1974, can be obtained from the book by DONEA and HUERTA [64] or the chapter by DONEA et al. in [65]. Finally, for a description of continuum mechanical principles in the interdisciplinary context of fluid-structure interaction, the reader is encouraged to consult the thesis by WALL [215].

This section starts with the kinematic description of flows. The causes for fluid motion are discussed in the subsection on kinetics and finally, a connection between kinematics and kinetics is established by a constitutive equation. The section is concluded with a summary of all equations and a short description of initial and boundary conditions.

2.1.1 Flow kinematics and transport in flows

In this subsection, tools for the description of fluid motion are provided. In addition, restrictions on the fluid motion are discussed which arise from the incompressibility requirement. Neverthe-

less, causes for this motion will not be considered yet. In the first part, all motions are described using suitable mappings between initial, reference and current domain. Control volumes are introduced as the regions in which the flow is under investigation. Several ways to observe physical quantities in flows are discussed. An example for these quantities are displacements and velocities, which can be deduced from the motion mappings. In addition, densities are introduced and the transport of density, i.e. the mass conservation, is studied using the REYNOLDS transport theorem. The subsection will be closed by a discussion of the impact of incompressibility on the equation of mass conservation.

Domains, motions and control volumes

At time $t = t_0$, the fluid under observation covers an initial domain Ω_0 . The motion of the fluid in time is described by a particle motion mapping, i.e. the current position of all infinitesimal fluid volumes associated with points in Ω_0 can be obtained for every time t according to the following map:

$$\begin{aligned} \varphi(\cdot, t) : \Omega_0 &\rightarrow \Omega_x(t) \quad , \quad \mathbf{X} \mapsto \varphi(\mathbf{X}, t) \\ &\text{with} \\ \det \left(\frac{\partial \varphi}{\partial \mathbf{X}} \right) (\mathbf{X}, t) &> 0 \quad \forall \quad \mathbf{X} \in \Omega_0, \quad t \geq t_0 \\ \varphi(\mathbf{X}, t_0) &= \mathbf{X} \quad \forall \quad \mathbf{X} \in \Omega_0. \end{aligned} \quad (2.1)$$

For fixed t , the range $\Omega_x(t)$ of the particle motion mapping $\varphi(\cdot, t)$ describes the domain currently covered by the fluid. In practice we are not interested in the extremely large deformation of the whole fluid domain but only in the flow through a ‘control volume’ $\Omega(t)$ in space. This is visualised in the upper half of Figure 2.1. If this control volume deforms in time, the introduction of a reference domain $\Omega_\xi(t)$ via a mapping

$$\begin{aligned} \Phi(\cdot, t) : \Omega_\xi(t) &\rightarrow \Omega_x(t) \quad , \quad \xi \mapsto \Phi(\xi, t) \\ &\text{with} \\ \det \left(\frac{\partial \Phi}{\partial \xi} \right) (\xi, t) &> 0 \quad \forall \quad \xi \in \Omega_\xi(t), \quad t \geq t_0 \\ \Phi(\xi, t_0) &= \xi \quad \forall \quad \xi \in \Omega_\xi(t_0) = \Omega_x(t_0) = \Omega_0 \end{aligned} \quad (2.2)$$

is beneficial. This mapping is chosen such that it represents the deformation from the initial control volume $\Omega(t_0)$ to the control volume $\Omega(t)$. Since, in the framework of finite elements, the mesh can be associated with the control volume, this mapping will be referred to as the mesh motion mapping. Note that this special choice for the mapping is not mandatory. Any other motion mapping from a possible physical state, a so-called configuration, to the current configuration would be applicable as well. Nevertheless, in most of the cases, the constant control volume in the reference domain is a desirable property for practical reasons.

Both particle motion mapping and mesh motion mapping are invertible. Thus, a third mapping is defined via

$$\begin{aligned} \Psi^{-1}(\cdot, t) &:= (\Phi^{-1} \circ \varphi)(\cdot, t) : \Omega_0 \rightarrow \Omega_\xi(t), \\ \mathbf{X} &\mapsto \Psi^{-1}(\mathbf{X}, t) := \Phi^{-1}(\varphi(\mathbf{X}, t), t). \end{aligned} \quad (2.3)$$

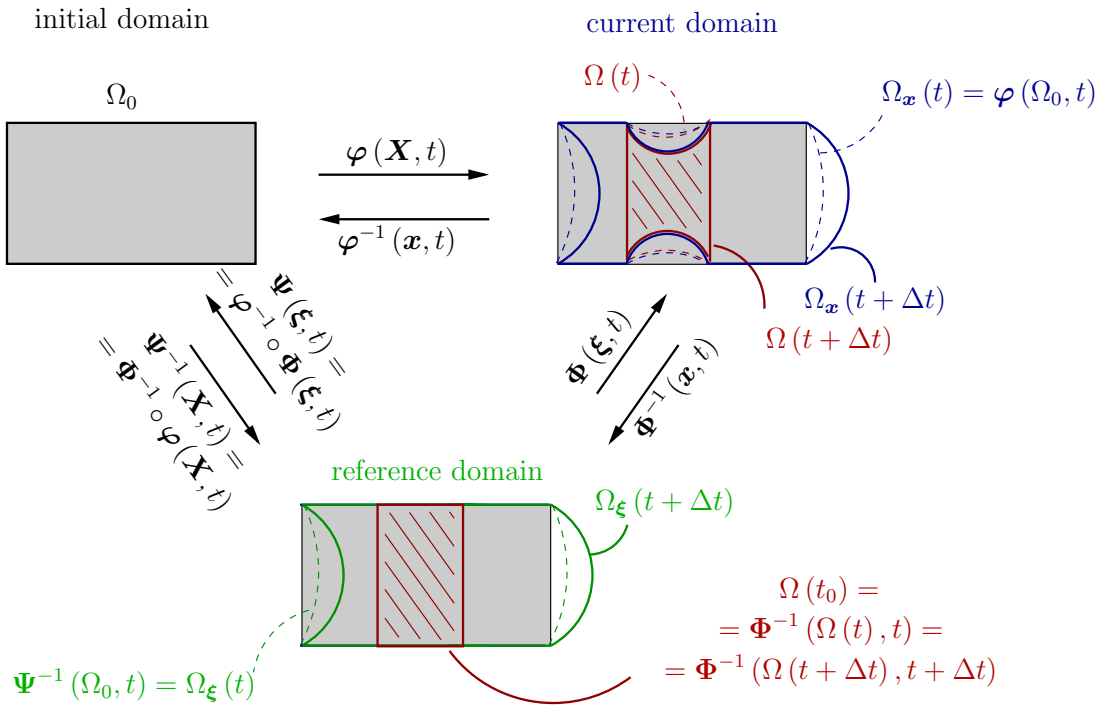


Figure 2.1: Initial domain (grey), current domain (blue), reference domain (green). The mappings are defined by the fluid motion and the deformation of the control volume (red).

This mapping represents the motion of infinitesimal fluid volumes modulo the deformation of the control volume. See Figure 2.1 for the complete interrelationship between the three mappings and domains.

Observing physical quantities

An arbitrary physical quantity f can be measured by different observers that operate on the domains introduced above:

- LAGRANGEan observers measure quantities in an infinitesimal volume element with initial position $\mathbf{X} \in \Omega_0$, i.e. they track a quantity along the infinitesimal volume's trajectory.

$$\mathbf{f} = \mathbf{f}|_{\mathbf{X}}(\mathbf{X}, t) \quad (2.4)$$

- EULERian observers measure quantities floating through an infinitesimal volume element at position $\mathbf{x} \in \Omega_{\mathbf{x}}(t)$ in the current configuration.

$$\mathbf{f} = \mathbf{f}|_{\mathbf{x}}(\mathbf{x}, t) \quad (2.5)$$

- Arbitrary-LAGRANGEan-EULERian observers measure a quantity floating through an infinitesimal volume element at a fixed point $\xi \in \Omega_\xi(t)$ in the reference configuration.

$$\mathbf{f} = \mathbf{f}|_{\xi}(\xi, t) \quad (2.6)$$

At every time t , a quantity determined by one observer in one point can be obtained by all other observers in appropriate points as well:

$$\begin{aligned} \mathbf{f}|_{\mathbf{x}}(\mathbf{x}, t) &= (\mathbf{f}|_{\mathbf{X}} \circ \varphi^{-1})(\mathbf{x}, t) = \mathbf{f}|_{\mathbf{X}}(\varphi^{-1}(\mathbf{x}, t), t) = \\ &= (\mathbf{f}|_{\xi} \circ \Phi^{-1})(\mathbf{x}, t) = \mathbf{f}|_{\xi}(\Phi^{-1}(\mathbf{x}, t), t) \end{aligned} \quad (2.7)$$

$$\begin{aligned} \mathbf{f}|_{\xi}(\xi, t) &= (\mathbf{f}|_{\mathbf{x}} \circ \Phi)(\xi, t) = \mathbf{f}|_{\mathbf{x}}(\Phi(\xi, t), t) = \\ &= (\mathbf{f}|_{\mathbf{X}} \circ \Psi)(\xi, t) = \mathbf{f}|_{\mathbf{X}}(\Psi(\xi, t), t) \end{aligned} \quad (2.8)$$

$$\begin{aligned} \mathbf{f}|_{\mathbf{X}}(\mathbf{X}, t) &= (\mathbf{f}|_{\xi} \circ \Psi^{-1})(\mathbf{X}, t) = \mathbf{f}|_{\xi}(\Psi^{-1}(\mathbf{X}, t), t) = \\ &= (\mathbf{f}|_{\mathbf{x}} \circ \varphi)(\mathbf{X}, t) = \mathbf{f}|_{\mathbf{x}}(\varphi(\mathbf{X}, t), t) \end{aligned} \quad (2.9)$$

Note that for the other observers in equations (2.7)–(2.9) not only the position of measurement changes in time but also that infinitesimal volume elements are deformed according to the motion mappings. This point will be dealt with in detail when introducing densities later in this section. In fluid mechanics, the EULERian point of view is predominant. Nevertheless, as we will see later on, the Arbitrary-LAGRANGEan-EULERian observer is very useful for the description of fluid flows on deforming domains since, by construction, this observer can make use of control volumes that do not deform in time.

Displacements

The motion mappings can be represented equivalently using displacements, i.e. the distances between current and initial positions. For example, a particle displacement is defined by

$$\mathbf{d}|_{\mathbf{X}}(\mathbf{X}, t) := \varphi(\mathbf{X}, t) - \varphi(\mathbf{X}, t_0) = \varphi(\mathbf{X}, t) - \mathbf{X} \quad (2.10)$$

and a mesh displacement is given by

$$\mathbf{d}_G|_{\xi}(\xi, t) := \Phi(\xi, t) - \Phi(\xi, t_0) = \Phi(\xi, t) - \xi. \quad (2.11)$$

Velocities

The three motion mappings give rise to the definition of several velocities by time differentiation of the motion mapping. At time t , the velocity of a particle with initial position $\mathbf{X} \in \Omega_0$ can be obtained as

$$\mathbf{u}|_{\mathbf{X}}(\mathbf{X}, t) := \frac{d\varphi}{dt}(\mathbf{X}, t) = \frac{d(\mathbf{d}|_{\mathbf{X}})}{dt}(\mathbf{X}, t) \quad (2.12)$$

The ‘grid’ velocity generated from the mesh motion mapping is defined as

$$\mathbf{u}_G|_{\xi}(\xi, t) := \frac{d\Phi}{dt}(\xi, t) = \frac{d(\mathbf{d}_G|_{\xi})}{dt}(\xi, t) \quad (2.13)$$

and the combined mapping Ψ^{-1} defines

$$\mathbf{w}|_{\mathbf{X}}(\mathbf{X}, t) := \frac{d\Psi^{-1}}{dt}(\mathbf{X}, t). \quad (2.14)$$

The following equation,

$$\begin{aligned}
 \mathbf{u}|_{\mathbf{X}}(\mathbf{X}, t) &= \frac{d\Phi(\Psi^{-1}(\mathbf{X}, t), t)}{dt} = \frac{\partial\Phi}{\partial t}(\Psi^{-1}(\mathbf{X}, t), t) + \\
 &\quad + \frac{\partial\Phi}{\partial\xi}(\Psi^{-1}(\mathbf{X}, t), t) \cdot \frac{\partial\Psi^{-1}(\mathbf{X}, t)}{\partial t} = \\
 &= \mathbf{u}_G|_{\xi}(\Psi^{-1}(\mathbf{X}, t), t) + \\
 &\quad + \frac{\partial\Phi}{\partial\xi}(\Psi^{-1}(\mathbf{X}, t), t) \cdot \mathbf{w}|_{\mathbf{X}}(\mathbf{X}, t), \tag{2.15}
 \end{aligned}$$

shows that these three velocities are related and it allows for an interpretation of the ALE convective velocity

$$\mathbf{c}|_{\mathbf{X}}(\mathbf{X}, t) := \frac{\partial\Phi}{\partial\xi}(\Psi^{-1}(\mathbf{X}, t), t) \cdot \mathbf{w}|_{\mathbf{X}}(\mathbf{X}, t) \tag{2.16}$$

as the relative velocity between particles and deforming domain:

$$\mathbf{c}|_{\mathbf{X}}(\mathbf{X}, t) = \mathbf{u}|_{\mathbf{X}}(\mathbf{X}, t) - \mathbf{u}_G|_{\mathbf{X}}(\mathbf{X}, t) \tag{2.17}$$

Note that in equations (2.12)–(2.14), total and partial time derivatives are equivalent since the first arguments are not time dependent. Figure 2.2 shows velocity and ALE convective velocity vectors in a simple example. The definition of a particle acceleration is straightforward. As usual, it is defined as the second derivative of the particle map in time.

Densities

In the current configuration, every volume $V \subset \Omega_{\mathbf{x}}(t)$ can be associated with a unique mass $m(V)$. Based on this mass, a mass density can be obtained as the limit of the ratio between mass m and volume vol for infinitesimally small volumes for each configuration. Thus, we define the current density by

$$\rho|_{\mathbf{x}}(\mathbf{x}, t) := \lim_{\text{vol}(V) \rightarrow 0} \frac{m(V)}{\text{vol}(V)}, \quad \mathbf{x} \in V \subset \Omega_{\mathbf{x}}(t), \tag{2.18}$$

the material density by

$$\rho^0|_{\mathbf{X}}(\mathbf{X}, t) := \lim_{\text{vol}(V^0) \rightarrow 0} \frac{m(\varphi(V^0, t))}{\text{vol}(V^0)}, \quad \mathbf{X} \in V^0 \subset \Omega_0, \tag{2.19}$$

and the reference density by

$$\rho^{\text{ref}}|_{\xi}(\xi, t) := \lim_{\text{vol}(V^{\text{ref}}) \rightarrow 0} \frac{m(\Phi(V^{\text{ref}}, t))}{\text{vol}(V^{\text{ref}})}, \quad \xi \in V^{\text{ref}} \subset \Omega_{\xi}(t). \tag{2.20}$$

The three densities are separate quantities, but they are not independent since they are related via the motion mappings:

$$\begin{aligned}
 \rho^{\text{ref}}|_{\xi}(\xi, t) &= \rho|_{\mathbf{x}}(\Phi(\xi, t), t) \cdot \det\left(\frac{\partial\Phi}{\partial\xi}\right)(\xi, t) = \\
 &= \rho^0|_{\mathbf{X}}(\Psi(\xi, t), t) \cdot \det\left(\frac{\partial\Psi}{\partial\xi}\right)(\xi, t) \tag{2.21}
 \end{aligned}$$

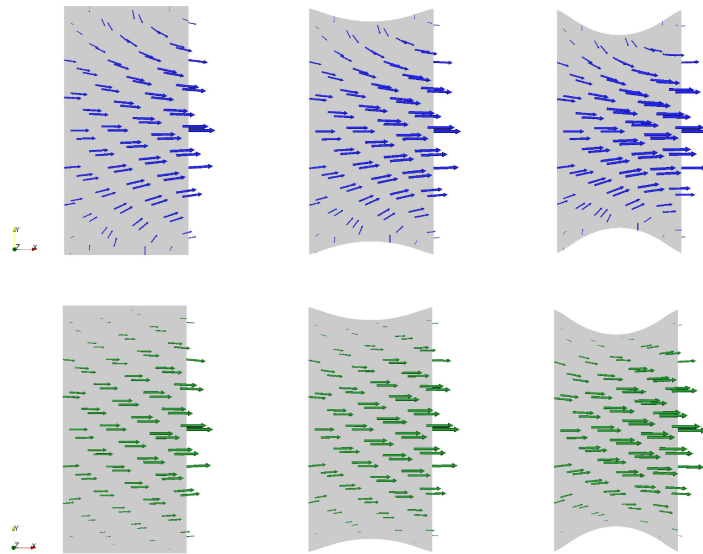


Figure 2.2: Flow from left to right through a plane channel segment $\Omega(t)$ with deforming top and bottom wall. The motion of the wall is such that the channel is narrowing as indicated by the control volumes in the sketch in Figure 2.1, the current control volume is shown for three consecutive points in time. Visualised are velocity vectors (top) and ALE convective velocity vectors (bottom). Due to the non-slip condition at the surface, in contrast to the ALE convective velocity, the velocity vectors do not vanish on the deforming walls but represent the velocity of the domain deformation.

In this formula, the JACOBIAN determinant takes into account the volume change of an infinitesimal element caused by the motion mapping, see Figure 2.3 for an illustration.

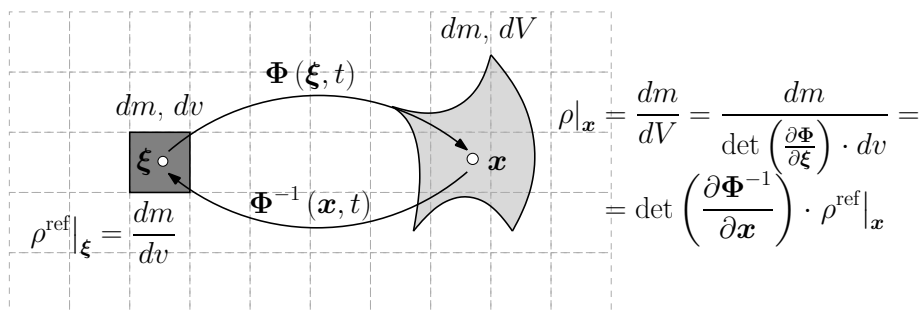


Figure 2.3: Definition of an associated density via a motion mapping.

According to the transformation theorem, see textbooks on analysis like the book by KÖNIGSBERGER [145], relation (2.21) expresses the fact that the total mass $m(\Phi(V, t))$ in an arbitrary

volume V in the reference configuration can be computed in all three configurations, i.e.

$$\begin{aligned} m(\Phi(V, t)) &:= \int_{\Phi(V, t)} \rho|_{\mathbf{x}}(\mathbf{x}, t) d\mathbf{x} = \int_V \rho^{\text{ref}}|_{\boldsymbol{\xi}}(\boldsymbol{\xi}, t) d\boldsymbol{\xi} = \\ &= \int_{\Psi(V, t)} \rho^0|_{\mathbf{X}}(\mathbf{X}, t) d\mathbf{X}. \end{aligned} \quad (2.22)$$

Substantial time derivative of moving domain integrals — a transport theorem

In appendix A.1, the REYNOLDS transport theorem is derived for an arbitrary motion mapping Υ with a positive JACOBIAN determinant. From this general form of the theorem, the following implications can be derived easily:

- The choice $\Upsilon \equiv \Psi^{-1}$ results in the ALE REYNOLDS transport theorem in reference representation

$$\begin{aligned} \frac{d}{dt} \int_{V(t)} \mathbf{f}|_{\boldsymbol{\xi}}(\boldsymbol{\xi}, t) d\boldsymbol{\xi} &= \\ &= \int_{V(t)} \left(\frac{\partial \mathbf{f}|_{\boldsymbol{\xi}}}{\partial t}(\boldsymbol{\xi}, t) + \sum_j \frac{\partial}{\partial \boldsymbol{\xi}_j} \left((\mathbf{w}|_{\boldsymbol{\xi}})_j(\boldsymbol{\xi}, t) \cdot \mathbf{f}|_{\boldsymbol{\xi}}(\boldsymbol{\xi}, t) \right) \right) d\boldsymbol{\xi} \end{aligned} \quad (2.23)$$

This version will be used later on to derive conservation laws on deforming control volumes in the current configuration.

- Choosing $\Upsilon \equiv \varphi$ immediately results in the EULERIAN version of the REYNOLDS transport theorem in spatial representation:

$$\begin{aligned} \frac{d}{dt} \int_{V(t)} \mathbf{f}|_{\mathbf{x}}(\mathbf{x}, t) d\mathbf{x} &= \\ &= \int_{V(t)} \left(\frac{\partial \mathbf{f}|_{\mathbf{x}}}{\partial t}(\mathbf{x}, t) + \sum_j \frac{\partial}{\partial \mathbf{x}_j} \left((\mathbf{u}|_{\mathbf{x}})_j(\mathbf{x}, t) \cdot \mathbf{f}|_{\mathbf{x}}(\mathbf{x}, t) \right) \right) d\mathbf{x} \end{aligned} \quad (2.24)$$

This is the formulation normally used to derive the NAVIER-STOKES equations for incompressible flow on non-deforming control volumes. Note that (2.24) is just a special case of (2.23) with the choice of the mesh mapping equal to the identity $\Phi = \mathbf{I}$.

Keeping in mind the picture of Figure 2.1, we can now understand why the ALE point of view, with a mesh motion mapping as introduced above, is so profitable. A numerical approximation of the local time derivative in equations (2.23) and (2.24) requires the evaluation of the transported quantity $\mathbf{f}|_{\mathbf{x}}$ and accordingly $\mathbf{f}|_{\boldsymbol{\xi}}$ for at least two points in time, t and $t + \Delta t$. For an EULERIAN observer, points may enter or leave the control volume in the time interval $[t, t + \Delta t]$. Thus, for this observer, such an approximation of the local time derivative in these points is not computable. In contrast, the constant control volume in the ALE point of view allows an approximation of the time derivative even for deforming meshes.

Mass conservation

In incompressible flows, mass conservation acts as a constraint on the fluid velocities. Strictly speaking, mass conservation is not a ‘kinematic’ restriction. Nevertheless, it is convenient to derive this conservation equation here, since all necessary ingredients like densities and transport theorems have already been introduced. Conservation of mass implies that the mass contained in a transported balance volume $V(t) = \varphi(V(t_0), t)$ is constant. Expressed in the reference configuration, this balance volume can be written as $V^{\text{ref}}(t) = \Psi^{-1}(V(t_0), t)$ and thus, using the ALE REYNOLDS transport theorem (2.23), we arrive at the following integral version of the ALE mass conservation equation in reference representation:

$$\begin{aligned} \frac{dm(V(t))}{dt} &= \frac{d}{dt} \int_{V^{\text{ref}}(t)} \rho^{\text{ref}}|_{\xi}(\xi, t) d\xi = \int_{V^{\text{ref}}(t)} \left(\frac{\partial \rho^{\text{ref}}|_{\xi}}{\partial t}(\xi, t) + \right. \\ &\quad \left. + \sum_j \frac{\partial}{\partial \xi_j} \left((w|_{\xi})_j(\xi, t) \cdot \rho^{\text{ref}}|_{\xi}(\xi, t) \right) \right) d\xi = 0 \end{aligned} \quad (2.25)$$

Since the balance volume was chosen arbitrarily, the equation has to hold pointwise as well and the differential form of the ALE mass conservation equation in reference representation is obtained:

$$0 = \frac{\partial \rho^{\text{ref}}|_{\xi}}{\partial t}(\xi, t) + \sum_j \frac{\partial}{\partial \xi_j} \left(\rho^{\text{ref}}|_{\xi}(\xi, t) \cdot (w|_{\xi})_j(\xi, t) \right) \quad (2.26)$$

This ALE mass conservation equation, also known as the ALE version of the continuity equation, can be rewritten in spatial representation as well. At point $\mathbf{x} = \Phi(\xi, t)$, it reads as follows:

$$\begin{aligned} 0 &= \frac{\partial \rho|_{\xi}}{\partial t}(\Phi^{-1}(\mathbf{x}, t), t) + \sum_i (c|_{\mathbf{x}})_i(\mathbf{x}, t) \cdot \frac{\partial \rho|_{\mathbf{x}}}{\partial x_i}(\mathbf{x}, t) + \\ &\quad + \rho|_{\mathbf{x}}(\mathbf{x}, t) \cdot \sum_l \frac{\partial (u|_{\mathbf{x}})_l}{\partial x_l}(\mathbf{x}, t) \end{aligned} \quad (2.27)$$

In order to emphasise that equation (2.27) is obtained from the ALE point of view and not from the EULERian point of view, the proof of the equivalence of (2.27) and (2.26) will be given in appendix A.2.

Incompressibility

A fluid is said to behave incompressibly if the density of an element of fluid is not affected by the pressure. Such behaviour can be assumed in all low MACH number applications, i.e. in flows with a flow velocity which is significantly smaller than the speed of sound in the fluid. Hence, incompressibility is not a material but rather a flow property. Examples of fluids behaving incompressibly are air in car aerodynamics, water in rivers or blood in arteries to name a few. Nevertheless, it is obvious for instance that air flow has to be considered compressible in other applications like aircraft aerodynamics.

Assuming incompressibility, the ALE version of the continuity equation in spatial representation (2.27) shortens to

$$0 = \sum_l \frac{\partial (\mathbf{u}|_{\mathbf{x}})_l}{\partial x_l}(\mathbf{x}, t). \quad (2.28)$$

A very common special case, the only one considered in this thesis, is a fluid with a constant density independent of space and time. For such a fluid, equation (2.28) could be derived from equation (2.27) directly. For incompressible flows, the EULERian and Arbitrary-LAGRANGEan-EULERian point of view result in an identical continuity equation.

2.1.2 Kinetics

This subsection establishes the relationship between fluid motion and surface and volume forces, the causes of the flow. This is done based on a continuum mechanical extension of NEWTON's second law, which states that for every balance volume the change of linear momentum is equal to the resulting force on the balance volume. First, the change of linear momentum in a balance volume is studied as it is observed from an ALE point of view using the ALE version of the REYNOLDS transport theorem. The result is restated in spatial representation, allowing to express the momentum equation in the current configuration. CAUCHY stresses are introduced and are used to rewrite the integral equation in a differential form.

Transport of linear momentum

The components of the vector of linear momentum associated with a transported balance volume $V(t) = \varphi(V(t_0), t)$ are computable in all configurations:

$$\begin{aligned} \mathbf{P}_k(V(t)) &:= \int_{V(t_0)} \rho^0|_{\mathbf{X}}(\mathbf{X}, t) \cdot (\mathbf{u}|_{\mathbf{X}})_k(\mathbf{X}, t) d\mathbf{X} = \\ &= \int_{V^{\text{ref}}(t)} \rho^{\text{ref}}|_{\boldsymbol{\xi}}(\boldsymbol{\xi}, t) \cdot (\mathbf{u}|_{\boldsymbol{\xi}})_k(\boldsymbol{\xi}, t) d\boldsymbol{\xi} = \\ &= \int_{V(t)} \rho|_{\mathbf{x}}(\mathbf{x}, t) \cdot (\mathbf{u}|_{\mathbf{x}})_k(\mathbf{x}, t) d\mathbf{x}, \quad k = 1, 2, 3. \end{aligned} \quad (2.29)$$

Once more, $V^{\text{ref}}(t) = \boldsymbol{\Psi}^{-1}(V(t_0), t)$ denotes the representation of the transported balance volume in the reference configuration. According to the ALE REYNOLDS transport theorem in reference representation (2.23), the change of linear momentum in this balance volume is given by the following equation:

$$\begin{aligned} \frac{d\mathbf{P}_k(V(t))}{dt} &= \int_{V^{\text{ref}}(t)} \left[\frac{\partial (\rho^{\text{ref}}|_{\boldsymbol{\xi}} \cdot (\mathbf{u}|_{\boldsymbol{\xi}})_k)}{\partial t}(\boldsymbol{\xi}, t) + \right. \\ &\quad \left. + \sum_j \frac{\partial}{\partial \boldsymbol{\xi}_j} \left((\mathbf{w}|_{\boldsymbol{\xi}})_j(\boldsymbol{\xi}, t) \cdot \rho^{\text{ref}}|_{\boldsymbol{\xi}}(\boldsymbol{\xi}, t) \cdot (\mathbf{u}|_{\boldsymbol{\xi}})_k(\boldsymbol{\xi}, t) \right) \right] d\boldsymbol{\xi} \end{aligned} \quad (2.30)$$

Application of the product rule and subsequent usage of the ALE mass conservation equation in reference representation (2.26) results in

$$\frac{d\mathbf{P}_k(V(t))}{dt} = \int_{V^{\text{ref}}(t)} \rho^{\text{ref}}|_{\xi}(\xi, t) \cdot \left[\frac{\partial (\mathbf{u}|_{\xi})_k}{\partial t}(\xi, t) + \sum_j (\mathbf{w}|_{\xi})_j(\xi, t) \cdot \frac{\partial (\mathbf{u}|_{\xi})_k}{\partial \xi_j}(\xi, t) \right] d\xi \quad (2.31)$$

A spatial representation of this equation can be easily obtained using

$$\begin{aligned} \sum_j (\mathbf{w}|_{\xi})_j(\xi, t) \cdot \frac{\partial (\mathbf{u}|_{\xi})_k}{\partial \xi_j}(\xi, t) &= \sum_{j,l} (\mathbf{w}|_{\xi})_j(\xi, t) \cdot \frac{\partial \Phi_l}{\partial \xi_j}(\xi, t) \cdot \frac{\partial (\mathbf{u}|_{\mathbf{x}})_k}{\partial \mathbf{x}_l}(\Phi(\xi, t), t) = \\ &= \sum_l (\mathbf{c}|_{\mathbf{x}})_l(\Phi(\xi, t), t) \cdot \frac{\partial (\mathbf{u}|_{\mathbf{x}})_k}{\partial \mathbf{x}_l}(\Phi(\xi, t), t) \end{aligned} \quad (2.32)$$

and the transformation theorem. The result is the spatial representation of the total change of linear momentum in a balance volume $V(t) = \Phi(V^{\text{ref}}(t), t)$ in the current configuration:

$$\begin{aligned} \frac{d\mathbf{P}_k(V(t))}{dt} &= \int_{V(t)} \rho|_{\mathbf{x}}(\mathbf{x}, t) \cdot \left[\frac{\partial (\mathbf{u}|_{\mathbf{x}})_k}{\partial t}(\Phi^{-1}(\mathbf{x}, t), t) + \right. \\ &\quad \left. + \sum_j (\mathbf{c}|_{\mathbf{x}})_j(\mathbf{x}, t) \cdot \frac{\partial (\mathbf{u}|_{\mathbf{x}})_k}{\partial \mathbf{x}_j}(\mathbf{x}, t) \right] d\mathbf{x} \end{aligned} \quad (2.33)$$

Integral formulation of the conservation of linear momentum

External forces on a balance volume can be either of surface or volume type. Forces of surface type can be expressed using the surface traction vector. This vector is associated with the current configuration. It is defined as the limit of the quotient between the resulting force $\mathbf{R}(a)$ on the surface element and the surface element area for infinitesimally small surface elements a :

$$\mathbf{t}|_{\mathbf{x}}(\mathbf{x}, t; \mathbf{n}|_{\mathbf{x}}) = \lim_{\text{area}(a) \rightarrow 0} \frac{\mathbf{R}(a)}{\text{area}(a)}, \quad \mathbf{x} \in a \subset \partial V(t) \quad (2.34)$$

The third parameter, the surface's unit normal vector $\mathbf{n}|_{\mathbf{x}}$ in spatial representation, indicates that this surface traction depends on the orientation of the surface element in space, i.e. a different balance volume containing the same point \mathbf{x} on its surface at time t might lead to a different surface traction if it possesses a different unit normal vector. Forces of volume type can be expressed using $\mathbf{b}|_{\mathbf{x}}$, the spatial representation of the body force per unit mass. Based on these two types of external forces, the generalisation of NEWTON's second law reads:

$$\frac{d\mathbf{P}(V(t))}{dt} = \int_{V(t)} \rho|_{\mathbf{x}}(\mathbf{x}, t) \cdot \mathbf{b}|_{\mathbf{x}}(\mathbf{x}, t) d\mathbf{x} + \int_{\partial V(t)} \mathbf{t}|_{\mathbf{x}}(\mathbf{x}, t) da \quad (2.35)$$

Using the spatial representation of the total change of linear momentum in a balance volume from equation (2.33), the generalisation of NEWTON's second law is equivalent to the three equations ($k = 1, 2, 3$) of integral momentum conservation in spatial representation:

$$\begin{aligned} \int_{V(t)} \rho|_{\mathbf{x}}(\mathbf{x}, t) \cdot \left[\frac{\partial (\mathbf{u}|_{\xi})_k}{\partial t} (\Phi^{-1}(\mathbf{x}, t), t) + \sum_j (\mathbf{c}|_{\mathbf{x}})_j(\mathbf{x}, t) \cdot \frac{\partial (\mathbf{u}|_{\mathbf{x}})_k}{\partial \mathbf{x}_j}(\mathbf{x}, t) \right] d\mathbf{x} = \\ = \int_{V(t)} \rho|_{\mathbf{x}}(\mathbf{x}, t) \cdot (\mathbf{b}|_{\mathbf{x}})_k(\mathbf{x}, t) d\mathbf{x} + \int_{\partial V(t)} (\mathbf{t}|_{\mathbf{x}})_k(\mathbf{x}, t) da \end{aligned} \quad (2.36)$$

CAUCHY stresses and the differential form

According to CAUCHY's fundamental lemma, tractions are generated by a unique — due to the conservation of angular momentum — symmetric tensor field $\boldsymbol{\sigma}$, the CAUCHY stress, with a spatial representation

$$\boldsymbol{\sigma}|_{\mathbf{x}}(\mathbf{x}, t) = \begin{pmatrix} (\boldsymbol{\sigma}|_{\mathbf{x}})_{11}(\mathbf{x}, t) & (\boldsymbol{\sigma}|_{\mathbf{x}})_{12}(\mathbf{x}, t) & (\boldsymbol{\sigma}|_{\mathbf{x}})_{13}(\mathbf{x}, t) \\ (\boldsymbol{\sigma}|_{\mathbf{x}})_{12}(\mathbf{x}, t) & (\boldsymbol{\sigma}|_{\mathbf{x}})_{22}(\mathbf{x}, t) & (\boldsymbol{\sigma}|_{\mathbf{x}})_{23}(\mathbf{x}, t) \\ (\boldsymbol{\sigma}|_{\mathbf{x}})_{13}(\mathbf{x}, t) & (\boldsymbol{\sigma}|_{\mathbf{x}})_{23}(\mathbf{x}, t) & (\boldsymbol{\sigma}|_{\mathbf{x}})_{33}(\mathbf{x}, t) \end{pmatrix}. \quad (2.37)$$

The traction's spatial representation is computable using the respective representation of the CAUCHY stresses, see MARS DEN and HUGHES [158]:

$$\mathbf{t}|_{\mathbf{x}}(\mathbf{x}, t) = \boldsymbol{\sigma}|_{\mathbf{x}}(\mathbf{x}, t) \cdot \mathbf{n}|_{\mathbf{x}}(\mathbf{x}, t) \quad (2.38)$$

This equation holds in every point on the boundary of any balance volume, i.e. pointwise in the whole current domain. Thus, the integral momentum conservation equation in spatial representation (2.36) can be rewritten as follows:

$$\begin{aligned} \int_{V(t)} \rho|_{\mathbf{x}}(\mathbf{x}, t) \cdot \left[\frac{\partial (\mathbf{u}|_{\xi})_k}{\partial t} (\Phi^{-1}(\mathbf{x}, t), t) + \sum_j (\mathbf{c}|_{\mathbf{x}})_j(\mathbf{x}, t) \cdot \frac{\partial (\mathbf{u}|_{\mathbf{x}})_k}{\partial \mathbf{x}_j}(\mathbf{x}, t) \right] d\mathbf{x} = \\ = \int_{V(t)} \left[\rho|_{\mathbf{x}}(\mathbf{x}, t) \cdot (\mathbf{b}|_{\mathbf{x}})_k(\mathbf{x}, t) + \sum_j \frac{\partial (\boldsymbol{\sigma}|_{\mathbf{x}})_{kj}}{\partial \mathbf{x}_j}(\mathbf{x}, t) \right] d\mathbf{x} \end{aligned} \quad (2.39)$$

Here, GAUSS's divergence theorem, as it can be found for example in KÖNIGSBERGER [145], was used to transform the surface integral into a volume integral. Equation (2.39) holds for every choice of the reference balance volume $V(t)$ and hence is equivalent to the differential version of the ALE linear momentum conservation equation in spatial representation:

$$\begin{aligned} \rho|_{\mathbf{x}}(\mathbf{x}, t) \cdot \left[\frac{\partial (\mathbf{u}|_{\xi})_k}{\partial t} (\Phi^{-1}(\mathbf{x}, t), t) + \sum_j (\mathbf{c}|_{\mathbf{x}})_j(\mathbf{x}, t) \cdot \frac{\partial (\mathbf{u}|_{\mathbf{x}})_k}{\partial \mathbf{x}_j}(\mathbf{x}, t) \right] = \\ = \rho|_{\mathbf{x}}(\mathbf{x}, t) \cdot (\mathbf{b}|_{\mathbf{x}})_k(\mathbf{x}, t) + \sum_j \frac{\partial (\boldsymbol{\sigma}|_{\mathbf{x}})_{kj}}{\partial \mathbf{x}_j}(\mathbf{x}, t) \quad \text{for } k = 1, 2, 3 \end{aligned} \quad (2.40)$$

2.1.3 Constitutive equation

To establish the connection between kinetics and kinematics, a constitutive model has to be introduced, relating the stress tensor and the fluid motion. One of the characteristics of fluids is that they are unable to support shear stress in static equilibrium. Nevertheless, it is well known from hydrostatics that fluids are able to support a hydrostatic stress state at rest. Hence, it is reasonable to separate the hydrostatic stress state from the CAUCHY stress tensor, introducing the fluid pressure and a trace-free, deviatoric part. This will be done in the first paragraph. Afterwards, a constitutive equation for this deviatoric part will be provided.

Hydrostatic stress contribution and viscous stresses

The ‘mechanical’ fluid pressure is defined by

$$p|_{\mathbf{x}}(\mathbf{x}, t) := -\operatorname{tr}(\boldsymbol{\sigma}|_{\mathbf{x}}(\mathbf{x}, t)). \quad (2.41)$$

In compressible flows, this mechanical fluid pressure is usually assumed to be identical to the thermodynamic pressure. This is referred to as the STOKES assumption. For incompressible flows, there is no such interpretation. The negative fluid pressure can only be understood as the averaged normal surface forces on an infinitesimal element. Using the pressure, the hydrostatic stress state can be separated from the CAUCHY stress tensor, resulting in

$$\boldsymbol{\sigma}|_{\mathbf{x}}(\mathbf{x}, t) = -p|_{\mathbf{x}}(\mathbf{x}, t) \cdot \mathbf{1} + \boldsymbol{\tau}|_{\mathbf{x}}(\mathbf{x}, t) \quad (2.42)$$

The so-called viscous stress $\boldsymbol{\tau}|_{\mathbf{x}}(\mathbf{x}, t)$ denotes the trace-free, deviatoric part of the CAUCHY stress tensor. It is a reasonable requirement that this viscous stress tensor is invariant under rigid body rotations. Note that the part of the traction caused by the hydrostatic part $-p|_{\mathbf{x}}(\mathbf{x}, t) \cdot \mathbf{1}$ of the stress tensor is the same for all surface orientations.

NEWTONian fluids

For a NEWTONian fluid, it is assumed that the viscous stress tensor depends linearly on the symmetric part of the velocity gradient, the rate-of-strain tensor

$$(\boldsymbol{\varepsilon}|_{\mathbf{x}}(\mathbf{u}|_{\mathbf{x}}))_{ij}(\mathbf{x}, t) := \frac{1}{2} \cdot \left(\frac{\partial (\mathbf{u}|_{\mathbf{x}})_i}{\partial \mathbf{x}_j}(\mathbf{x}, t) + \frac{\partial (\mathbf{u}|_{\mathbf{x}})_j}{\partial \mathbf{x}_i}(\mathbf{x}, t) \right) \quad (2.43)$$

where $i, j = 1, 2, 3$. Using this rate-of-strain tensor, the constitutive equation of a NEWTONian fluid compatible to the STOKES assumption reads:

$$\boldsymbol{\tau}|_{\mathbf{x}}(\mathbf{x}, t) = 2\mu \cdot (\boldsymbol{\varepsilon}|_{\mathbf{x}}(\mathbf{u}|_{\mathbf{x}}))(\mathbf{x}, t) - \frac{2}{3}\mu \cdot \operatorname{tr}((\boldsymbol{\varepsilon}|_{\mathbf{x}}(\mathbf{u}|_{\mathbf{x}}))(\mathbf{x}, t)) \cdot \mathbf{1} \quad (2.44)$$

The quantity μ , called dynamic viscosity, is a material parameter. According to this law, the viscous stress in NEWTONian fluids is defined instantaneously by the rate-of-strain tensor, i.e. there is no dependence on the past of the flow. Furthermore, for NEWTONian fluids the viscous stress is local, i.e. its value at one point depends only on the rate-of-strain tensor at this point.

For incompressible flows, the trace of the rate-of-strain tensor, which is identical to the divergence of the velocity, vanishes. Thus, the constitutive equation for the viscous stress in the incompressible case is simplified to

$$\boldsymbol{\tau}|_{\mathbf{x}}(\mathbf{x}, t) = 2\mu \cdot (\boldsymbol{\varepsilon}|_{\mathbf{x}}(\mathbf{u}|_{\mathbf{x}}))(\mathbf{x}, t). \quad (2.45)$$

In practice, many fluids like air, water or mineral oil can be considered NEWTONian. Nevertheless, fluids that exhibit a viscoelastic or nonlinear behaviour cannot be described properly by the NEWTONian law. This is the case for instance for polymer melts or blood. The interested reader is referred to BIRD and WIEST [30] for a review of constitutive equations for polymeric liquids and the textbook by BÖHME [35] for an introduction to non-NEWTONian fluids.

2.1.4 The arising system of nonlinear partial differential equations

For incompressible flows of NEWTONian fluids with constant current density ρ , the continuity equation (2.28), the momentum equation (2.40) and the constitutive law (2.42) incorporating (2.45), amount to a nonlinear system of partial differential equations in the primary variables velocity $\mathbf{u}|_{\mathbf{x}}$ and pressure $p|_{\mathbf{x}}$. In this subsection, this system of equations will be summarised in the ALE version of the NAVIER-STOKES equations. An important special case, i.e. the EULERian version for non-deformable control volumes will be presented.

All of the following equations will be formulated in spatial representation, i.e. all quantities will be expressed as measured by an EULERian observer in an appropriate point. Hence, for ease of notation, the index $\cdot|_{\mathbf{x}}$ indicating the EULERian observer will be dropped in the symbolic short forms and the remaining sections and chapters of this thesis.

ALE version of the NAVIER-STOKES equations

Summing up the results from the previous sections, the ALE momentum and continuity equations are given as follows:

$$\begin{aligned} & \frac{\partial (\mathbf{u}|_{\mathbf{x} \circ \Phi})_k}{\partial t}(\Phi^{-1}(\mathbf{x}, t), t) + \sum_j \left((\mathbf{u}|_{\mathbf{x}})_j(\mathbf{x}, t) - (\mathbf{u}_G|_{\mathbf{x}})_j(\mathbf{x}, t) \right) \cdot \frac{\partial (\mathbf{u}|_{\mathbf{x}})_k}{\partial \mathbf{x}_j}(\mathbf{x}, t) + \\ & + \frac{1}{\rho} \cdot \frac{\partial p|_{\mathbf{x}}}{\partial \mathbf{x}_k}(\mathbf{x}, t) - 2\nu \cdot \sum_j \frac{\partial (\boldsymbol{\varepsilon}|_{\mathbf{x}}(\mathbf{u}|_{\mathbf{x}}))_{kj}}{\partial \mathbf{x}_j}(\mathbf{x}, t) = (\mathbf{b}|_{\mathbf{x}})_k(\mathbf{x}, t) \text{ for } k = 1, 2, 3 \\ \\ & \sum_j \frac{\partial (\mathbf{u}|_{\mathbf{x}})_j}{\partial \mathbf{x}_j}(\mathbf{x}, t) = 0 \end{aligned} \quad (2.46)$$

The equation has been normalised by the constant density. The constant $\nu = \frac{\mu}{\rho}$, introduced for convenience, is called kinematic viscosity. Note that the time derivative is not evaluated in the current configuration but is obtained by an ALE observer in the reference domain. Furthermore, the convective term is based on the ALE convective velocity. For a rigid-body mesh rotation $\Phi(\boldsymbol{\xi}, t) = \mathbf{R}(t)\boldsymbol{\xi}$, defined with an orthogonal rotation matrix \mathbf{R} , equation (2.46) can be used to derive the NAVIER-STOKES equations in a rotating frame of reference, see GAMNITZER and

WALL [87]. The short form of equation (2.46) employing symbolic operators and omitting the index $\cdot|_{\mathbf{x}}$ is:

$$\begin{aligned} \frac{\partial(\mathbf{u} \circ \Phi)}{\partial t} \circ \Phi^{-1} + ((\mathbf{u} - \mathbf{u}_G) \cdot \nabla) \mathbf{u} + \frac{1}{\rho} \nabla p - 2\nu \nabla \cdot \boldsymbol{\varepsilon}(\mathbf{u}) = \mathbf{b} \\ \nabla \cdot \mathbf{u} = 0 \end{aligned} \quad (2.47)$$

EULERian formulation, convective form

For the special choice $\Phi(\boldsymbol{\xi}, t) = \boldsymbol{\xi}$, equation (2.46) is equivalent to the EULERian form of the NAVIER-STOKES equations in convective form:

$$\begin{aligned} \frac{\partial(\mathbf{u}|_{\mathbf{x}})_k}{\partial t}(\mathbf{x}, t) + \sum_j (\mathbf{u}|_{\mathbf{x}})_j(\mathbf{x}, t) \cdot \frac{\partial(\mathbf{u}|_{\mathbf{x}})_k}{\partial \mathbf{x}_j}(\mathbf{x}, t) + \frac{1}{\rho} \cdot \frac{\partial p|_{\mathbf{x}}}{\partial \mathbf{x}_k}(\mathbf{x}, t) - \\ - 2\nu \cdot \sum_j \frac{\partial(\boldsymbol{\varepsilon}|_{\mathbf{x}}(\mathbf{u}|_{\mathbf{x}}))_{kj}}{\partial \mathbf{x}_j}(\mathbf{x}, t) = (\mathbf{b}|_{\mathbf{x}})_k(\mathbf{x}, t) \quad \text{for } k = 1, 2, 3 \\ \sum_j \frac{\partial(\mathbf{u}|_{\mathbf{x}})_j}{\partial \mathbf{x}_j}(\mathbf{x}, t) = 0 \end{aligned} \quad (2.48)$$

In this case, the convective velocity is just the fluid velocity. The corresponding short form of this equation using symbolic operators and neglecting the index $\cdot|_{\mathbf{x}}$ is:

$$\begin{aligned} \frac{\partial \mathbf{u}}{\partial t} + (\mathbf{u} \cdot \nabla) \mathbf{u} + \frac{1}{\rho} \nabla p - 2\nu \nabla \cdot \boldsymbol{\varepsilon}(\mathbf{u}) = \mathbf{b} \\ \nabla \cdot \mathbf{u} = 0 \end{aligned} \quad (2.49)$$

EULERian formulation, conservative equations

Generalised conservation laws are equations of the form

$$\frac{\partial f}{\partial t} + \sum_j \frac{\partial \mathbf{F}_j}{\partial \mathbf{x}_j} = s. \quad (2.50)$$

Here, f is the conserved quantity, \mathbf{F} the so-called flux and s is a source term. Using the incompressibility constraint, the convective form of the EULERian formulation of the NAVIER-STOKES equations can be restated as such a generalised conservation law:

$$\begin{aligned} \frac{\partial(\mathbf{u}|_{\mathbf{x}})_k}{\partial t}(\mathbf{x}, t) + \sum_j \frac{\partial}{\partial \mathbf{x}_j} \left((\mathbf{u}|_{\mathbf{x}})_j(\mathbf{x}, t) \cdot (\mathbf{u}|_{\mathbf{x}})_k(\mathbf{x}, t) + \frac{p|_{\mathbf{x}}(\mathbf{x}, t)}{\rho} \cdot \delta_{jk} - \right. \\ \left. - 2\nu \cdot (\boldsymbol{\varepsilon}|_{\mathbf{x}}(\mathbf{u}|_{\mathbf{x}}))_{kj}(\mathbf{x}, t) \right) = (\mathbf{b}|_{\mathbf{x}})_k(\mathbf{x}, t) \quad \text{for } k = 1, 2, 3 \\ \sum_j \frac{\partial(\mathbf{u}|_{\mathbf{x}})_j}{\partial \mathbf{x}_j}(\mathbf{x}, t) = 0 \end{aligned} \quad (2.51)$$

Here, δ_{jk} stands for the KRONECKER-delta. In this momentum equation, the conserved quantity is the linear momentum normalised by the density. The flux of linear momentum is assembled from a convective, a pressure, and a viscous part. The source term corresponds to the body force acting on the fluid. The continuity equation can be understood as a generalised conservation law for the mass as well. A symbolic short form is given by:

$$\begin{aligned} \frac{\partial \mathbf{u}}{\partial t} + \nabla \cdot \left(\mathbf{u} \otimes \mathbf{u} + \frac{p}{\rho} \cdot \mathbf{1} - 2\nu \boldsymbol{\varepsilon}(\mathbf{u}) \right) &= \mathbf{b} \\ \nabla \cdot \mathbf{u} &= 0 \end{aligned} \quad (2.52)$$

Once more, the index $\cdot|_{\mathbf{x}}$ indicating the EULERian observer has been dropped in this equation.

2.1.5 The initial and boundary value problem

Equation system (2.48) and the corresponding special cases contain a time derivative of the velocity. Hence, a complete problem statement requires initial conditions for the velocity field:

$$\mathbf{u}|_{\mathbf{x}}(\mathbf{x}, t_0) = \mathbf{u}_0|_{\mathbf{x}}(\mathbf{x}) \quad (2.53)$$

For a well-posed problem, this initial field has to satisfy the incompressibility constraint, i.e. the equation

$$\sum_j \frac{\partial (\mathbf{u}_0|_{\mathbf{x}})_j}{\partial x_j}(\mathbf{x}) = 0 \quad (2.54)$$

must hold.

Furthermore, the equation system under consideration has to be completed by suitable boundary conditions. The usage of a control volume, as it was described in subsection 2.1.1, introduces an additional difficulty at this point. The EULERian and quasi-EULERian way, as the ALE approach is aptly named in BELYTSCHKO et al. [25], to define control volumes introduces ‘artificial’ boundaries $\partial\Omega(t)$ in the fluid domain $\Omega_{\mathbf{x}}(t)$. The price to pay for the advantages gained from the fact that one is actually dealing only with a small part of the fluid motion is that one has to prescribe suitable boundary conditions on $\partial\Omega(t)$. This is not straightforward in general, see for instance the discussions in section 3.7.1 and section 6.2.1.

The simplest boundary conditions that can be imposed are of DIRICHLET type

$$\mathbf{u}|_{\mathbf{x}}(\mathbf{x}, t) = \mathbf{u}_D|_{\mathbf{x}}(\mathbf{x}, t) \quad \text{on DIRICHLET boundaries } \Gamma_D(t) \quad (2.55)$$

or NEUMANN type

$$\boldsymbol{\sigma}|_{\mathbf{x}}(\mathbf{x}, t) \cdot \mathbf{n}|_{\mathbf{x}}(\mathbf{x}, t) = \mathbf{t}|_{\mathbf{x}}(\mathbf{x}, t) \quad \text{on NEUMANN boundaries } \Gamma_N(t). \quad (2.56)$$

Examples for these types of boundary conditions are the well-known no-slip condition, a zero-DIRICHLET boundary condition, and the do-nothing boundary condition, imposing zero traction on a NEUMANN boundary. In practice, the range of suitable boundary conditions is closely related to the numerical approach used to solve the system of equations. For this reason, a more detailed discussion of possible boundary conditions will follow later in section 3.7.

An important special case are solely DIRICHLET bounded problems with $\Gamma_D(t) \equiv \partial\Omega(t)$. The continuity equation requires the following equation

$$\int_{\partial\Omega(t)} \mathbf{u}_D|_{\mathbf{x}}(\mathbf{x}, t) \cdot \mathbf{n}|_{\mathbf{x}}(\mathbf{x}, t) da = \int_{\Omega(t)} \sum_j \frac{\partial(\mathbf{u}|_{\mathbf{x}})_j}{\partial \mathbf{x}_j}(\mathbf{x}, t) d\mathbf{x} = 0 \quad (2.57)$$

to hold in order to keep the problem well-posed. Furthermore, in this case, the pressure is only defined up to a constant.

In general, statements on the existence and uniqueness of strong long-time solutions of the NAVIER-STOKES equations in three dimensions are not available. Nevertheless, existence and uniqueness of strong solutions have been proven locally in time, or globally in time for two dimensions or under a small-data assumption, see for instance LADYZHENSKAYA and SOLONNIKOV [151] for a typical result. Weak solutions are known to exist in two and three dimensions, but uniqueness is not guaranteed in the three-dimensional case. These results can be found for instance in TEMAM [203] or the comprehensive state of the art review by DOERING [63], which also describes the relationship between the vortex stretching mechanism in turbulent flows and the mathematical difficulties in the three-dimensional NAVIER-STOKES equations.

2.2 The nature of turbulence

For the description of the nature of turbulent flows, it is important to acknowledge that turbulent flows are not all alike. The following canonical turbulent flows should give a rough impression of the variety of possible flows. An example is isotropic grid turbulence, which exists without a preference for direction. It is not self-sustaining, but without a constant supply of energy it will decay in time. As an approximation of ideal homogeneous isotropic turbulence, it is perfectly suited to study dissipation and energy transfer in turbulent flows, see subsection 2.2.4. Another example, free-shear layer or mixing layer turbulence, includes for example jets and wakes. In these flows, turbulence is constantly produced by mean-velocity differences. A self-similar behaviour can be expected for these flows in a certain distance from the origin of the turbulence. Finally, there is wall-bounded turbulence, as it exists for example in turbulent channel or pipe flow. For those flows, the wall is governing the processes that produce turbulence. As we will see in subsection 2.2.5, we can expect a similar near-wall behaviour in every fully developed wall-bounded turbulent flow.

Nevertheless, all turbulent flows have common characteristic features. These will be reviewed in subsection 2.2.1. The fact that turbulent flows can be described using statistical methods is exploited in the next subsection 2.2.2 for the statement of the REYNOLDS-averaged NAVIER-STOKES equations. A better understanding of the nature of turbulence can be deduced from KOLMOGOROV's hypotheses. The pioneering work by KOLMOGOROV in 1941, [144, 143], still contributes a lot to the state-of-the-art knowledge about turbulence, see for example the book by FRISCH [84]. Important consequences are listed in a subsection on the multiscale character of turbulence 2.2.3 and the subsequent section on energy spectra in turbulent flows 2.2.4. Finally, this section will conclude by a brief discussion of turbulent flows near walls in the example of turbulent plane channel flow in subsection 2.2.5. Many of the turbulent flow computations contained in this thesis are of this type, therefore a detailed consideration of this class of turbulent flows is justified.

For general literature on the topic of turbulent flows, the reader is referred to an excellent textbook by POPE [174]. Supplementary details can be found for example in the books by MATHIEU and SCOTT [159] or the classic reference by TENNEKES and LUMLEY [204].

2.2.1 Turbulent flow characteristics

According to TENNEKES and LUMLEY [204], the best way to describe the physical phenomenon ‘turbulence’, i.e. to show the common features of all turbulent flows, is to list several important characteristics of turbulent flows.

Turbulence is a continuum phenomenon

Turbulent flows are controlled by the same laws of continuum mechanics as every flow. Even though turbulent flow structures, often referred to as ‘eddies’, can be very small, they are still large compared to the molecular length scales. Turbulence is not a material property, but a flow property. Similar to the MACH number for incompressibility, the REYNOLDS number is a dimensionless parameter which can be used to classify flow regimes. Using a characteristic length \mathcal{L} , the kinematic viscosity ν and a characteristic velocity \mathcal{U} , it is defined by

$$\text{Re} := \frac{\mathcal{L} \cdot \mathcal{U}}{\nu} . \quad (2.58)$$

For a low REYNOLDS number, the flow is diffusion dominated, i.e. the elliptic part of the NAVIER-STOKES equations is dominant. In this regime, the flow is clearly laminar. For a sufficiently large REYNOLDS number, the flow will be convection dominated and will exhibit all characteristics of a turbulent flow. In between these two regimes, a transition range exists. The critical REYNOLDS numbers indicating the end of the laminar and the beginning of the fully turbulent regime vary from problem to problem and depend furthermore on the definition of the characteristic scales which is not unique. In pipe-flow, for example, using a REYNOLDS number based on the diameter and the mean velocity, the flow remains laminar for REYNOLDS numbers smaller than 2300. A fully turbulent pipe-flow can be expected at a value of 4000 or higher.

Irregularity, three-dimensionality and diffusivity

Wall-bounded turbulence in a channel flow will now be used to highlight several properties of turbulence. Figure 2.4 shows the setup for this example. The fluid velocity at the wall is zero, the transition to the core region of the flow is characterised by a sharp boundary layer. A more precise description of the mean flow profile will follow later on in subsection 2.2.5. By looking at a snapshot of the absolute velocity, as it can be seen in Figure 2.4, it becomes obvious that even though two homogeneous directions exist in this example, turbulence includes a certain amount of spatial disorder and irregularity. For two points P_1 and P_2 as introduced in Figure 2.4, the time history of all three components of the velocity is given in Figure 2.5. Again, an oscillating, irregular behaviour is observed. Nevertheless, well-defined statistical quantities like mean values can be determined using an appropriate averaging procedure. Furthermore, even though the averaged solution is essentially a one-dimensional function of the wall-normal coordinate in the channel, a three-dimensional behaviour of turbulence can be observed, see the oscillations in

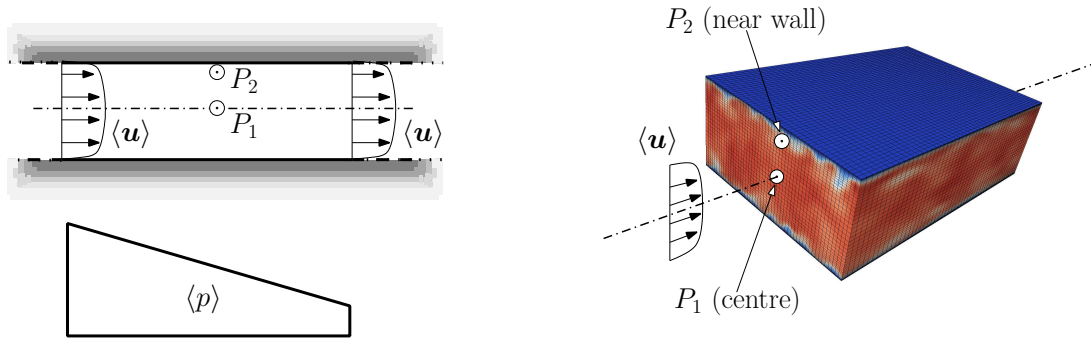


Figure 2.4: Illustrative example: Turbulent flow in a plane channel. In the picture on the left, a cut through the channel is depicted. The cutting plane is spanned by the main, streamwise, flow direction and the wall normal. The channel is infinitely extended, both in streamwise and spanwise direction normal to the cutting plane. A constant mean pressure gradient $\nabla \langle p \rangle$ results in a statistically steady state featuring a mean velocity profile $\langle \mathbf{u} \rangle$. The channel segment on the right, coloured by the instantaneous absolute value of the velocity field, demonstrates the irregularity of turbulent flows. Furthermore, two points P_1 and P_2 are introduced for which temporal functions of the velocity will be presented in Figure 2.5.

the wall-normal and spanwise components of the velocity in Figure 2.5. This three-dimensional behaviour is the basis for an important vorticity-maintenance mechanism called vortex stretching, and thus an additional necessary feature of turbulence. Another striking feature of turbulent flows is their diffusivity. The fluctuating behaviour of turbulent flows facilitates the transport of flow properties like momentum or energy and the mixing of scalar quantities. The transport rates in turbulent flows are orders of magnitude higher than molecular transport rates.

2.2.2 REYNOLDS-averaged NAVIER-STOKES equations

As already indicated above, quantities like velocities or pressure in turbulent flows can be described using statistical tools as they can be found in appendix A.3. The statistical description allows to derive equations for the expected quantities, the REYNOLDS-averaged NAVIER-STOKES equations. They will be presented here for the conservative version of the NAVIER-STOKES equations (2.52) on fixed domains.

Taking into account that the computation of expected values commutes with time- and spatial differentiation, the mean value of equation (2.52) is equivalent to

$$\begin{aligned} \frac{\partial \langle \mathbf{u} \rangle}{\partial t} + \nabla \cdot \left(\langle \mathbf{u} \otimes \mathbf{u} \rangle + \frac{\langle p \rangle}{\rho} \cdot \mathbf{1} - 2\nu \varepsilon(\langle \mathbf{u} \rangle) \right) &= \langle \mathbf{b} \rangle \\ \nabla \cdot \langle \mathbf{u} \rangle &= 0. \end{aligned} \quad (2.59)$$

Using a decomposition of the velocity into mean velocity and velocity fluctuations,

$$\mathbf{u} = \langle \mathbf{u} \rangle + \underline{\underline{\mathbf{u}}}, \quad (2.60)$$

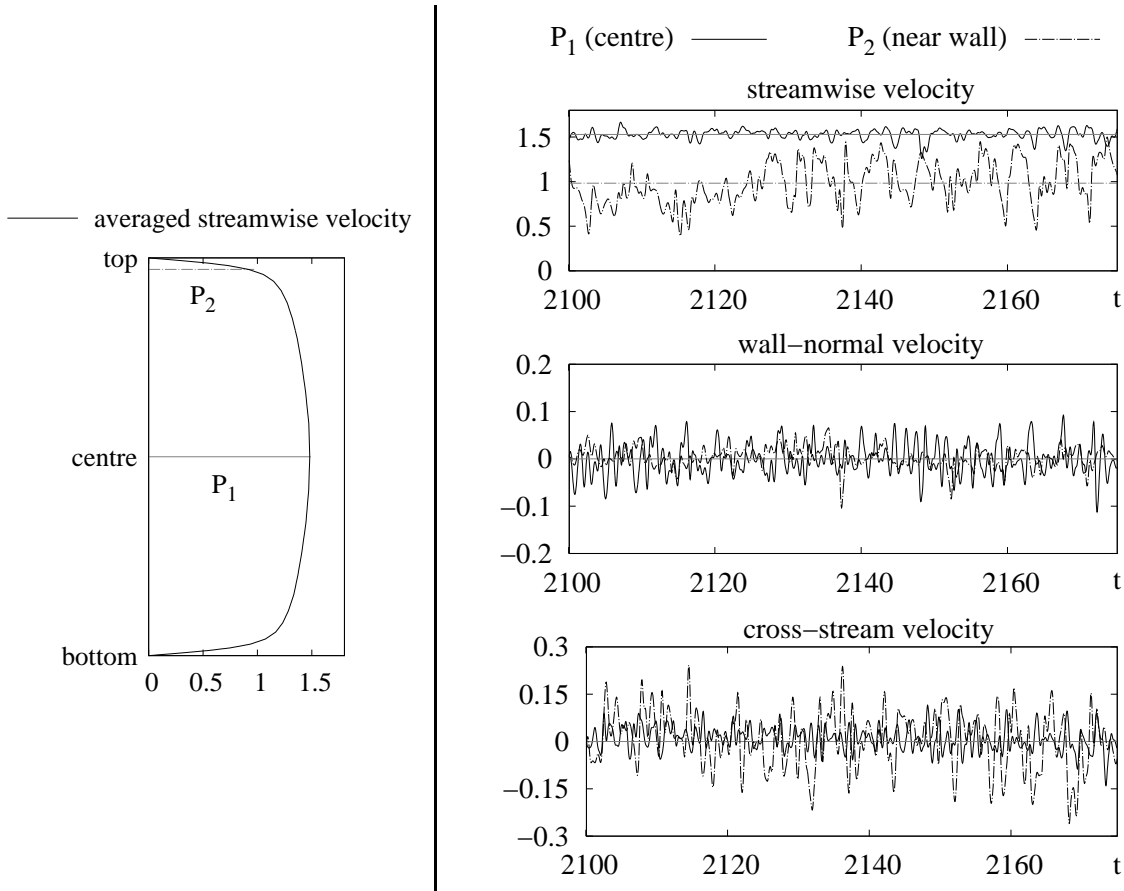


Figure 2.5: Time history of streamwise, wall-normal and spanwise velocity in two points of the channel (right). The averaged values of these quantities, indicated by the constant lines in the graphs on the right, give rise to a distribution of the averaged velocity over the height of the channel. This is displayed in the corresponding graph (left).

the mean of the nonlinear convective term can be expanded as

$$\begin{aligned} \langle \mathbf{u} \otimes \mathbf{u} \rangle &= \langle (\langle \mathbf{u} \rangle + \underline{\mathbf{u}}) \otimes (\langle \mathbf{u} \rangle + \underline{\mathbf{u}}) \rangle = \langle \mathbf{u} \rangle \otimes \langle \mathbf{u} \rangle + \langle \mathbf{u} \rangle \otimes \langle \underline{\mathbf{u}} \rangle + \langle \underline{\mathbf{u}} \rangle \otimes \langle \mathbf{u} \rangle + \langle \underline{\mathbf{u}} \otimes \underline{\mathbf{u}} \rangle = \\ &= \langle \mathbf{u} \rangle \otimes \langle \mathbf{u} \rangle + \langle \underline{\mathbf{u}} \otimes \underline{\mathbf{u}} \rangle. \end{aligned} \quad (2.61)$$

Here, the linearity of the mean-value computation and the properties

$$\langle \langle \mathbf{u} \rangle \rangle = \langle \mathbf{u} \rangle, \quad \langle \underline{\mathbf{u}} \rangle = \langle \mathbf{u} - \langle \mathbf{u} \rangle \rangle = \langle \mathbf{u} \rangle - \langle \langle \mathbf{u} \rangle \rangle = \mathbf{0} \quad (2.62)$$

have been used. The combination of equations (2.59) and (2.61) results in the REYNOLDS-averaged NAVIER-STOKES equations for the mean quantities:

$$\begin{aligned} \frac{\partial \langle \mathbf{u} \rangle}{\partial t} + \nabla \cdot \left(\langle \mathbf{u} \rangle \otimes \langle \mathbf{u} \rangle + \langle \underline{\mathbf{u}} \otimes \underline{\mathbf{u}} \rangle + \frac{\langle p \rangle}{\rho} \cdot \mathbf{1} - 2\nu \varepsilon (\langle \mathbf{u} \rangle) \right) - \langle \mathbf{b} \rangle &= \mathbf{0} \\ \nabla \cdot \langle \mathbf{u} \rangle &= 0 \end{aligned} \quad (2.63)$$

It still contains the unclosed symmetric REYNOLDS-stress tensor

$$\boldsymbol{\tau}_{\text{rey}} := \rho \cdot \langle \underline{\mathbf{u}} \otimes \underline{\mathbf{u}} \rangle = \rho \cdot \begin{pmatrix} \langle \underline{u}_1 \underline{u}_1 \rangle & \langle \underline{u}_1 \underline{u}_2 \rangle & \langle \underline{u}_1 \underline{u}_3 \rangle \\ \langle \underline{u}_2 \underline{u}_1 \rangle & \langle \underline{u}_2 \underline{u}_2 \rangle & \langle \underline{u}_2 \underline{u}_3 \rangle \\ \langle \underline{u}_3 \underline{u}_1 \rangle & \langle \underline{u}_3 \underline{u}_2 \rangle & \langle \underline{u}_3 \underline{u}_3 \rangle \end{pmatrix}, \quad (2.64)$$

representing the flux of momentum due to the turbulent fluctuations. To be able to solve the REYNOLDS-averaged NAVIER-STOKES equations, a closure for the six unknown components of the REYNOLDS-stress tensor has to be provided by a turbulence model, see subsection 4.2.1 for a discussion. The combination of the viscous stress tensor and the REYNOLDS stress tensor, $\rho \cdot (\boldsymbol{\tau}_{\text{rey}} - 2\nu\boldsymbol{\varepsilon}(\langle \underline{\mathbf{u}} \rangle))$, will be referred to as the effective stress tensor.

A generalisation of this approach to the ALE version of the NAVIER-STOKES equations in the context of fluid-structure interaction problems is not straightforward since the grid velocity has to be considered as a fluctuating quantity as well. Thus, it introduces a further unclosed term in the equation.

2.2.3 The multiscale character of turbulence

RICHARDSON's energy cascade [179] describes turbulence as being composed of 'eddies', i.e. turbulent structures of different sizes. In this model, it is assumed that the largest eddies are driven by the mean flow field. These eddies break up, passing on their energy to smaller and smaller eddies in a cascade-like process. This cascade ends as soon as the eddies are small enough so that their energy is converted into thermal energy by viscous processes. Figure 2.6 illustrates this process in a symbolic way. Significant differences between eddies of different

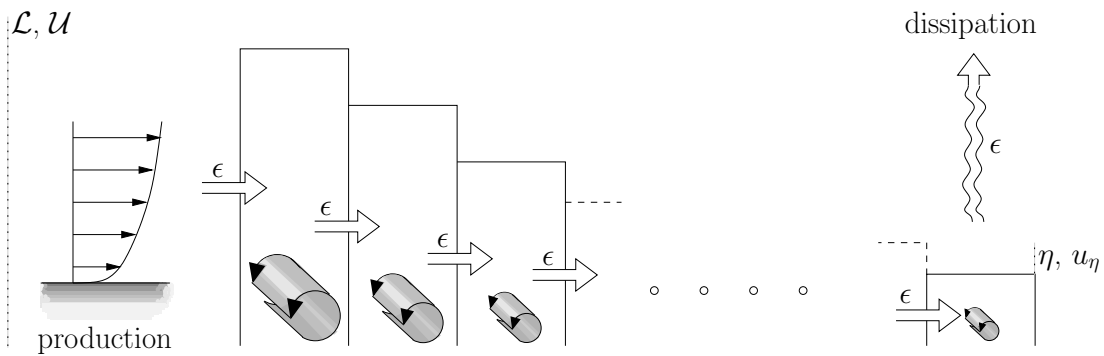


Figure 2.6: Illustration of RICHARDSON's energy cascade. Energy is extracted from the mean flow field and enters the cascade at the largest eddies associated with the characteristic scales \mathcal{L} and \mathcal{U} . During the cascade process, larger eddies continuously pass on this energy to smaller eddies. The rate of dissipation ϵ at the end of the process, associated with the smallest eddies of characteristic scales η and u_η , is determined by the input at the beginning of the cascade.

scales were recognised early. Large eddies are always influenced by boundary conditions as well as mean flow properties and thus are in general anisotropic and problem-specific. In contrast, for large REYNOLDS number flows, the small scales exhibit a more universal character. This was

summarised in 1941 by KOLMOGOROV in his hypothesis of local isotropy [144]. Following the depiction in POPE [174], this hypothesis states that at a sufficiently high REYNOLDS number the small-scale turbulent motions are statistically isotropic. Keeping in mind the picture of the energy cascade, this means that all directional information in the large eddies is lost during the scale-reduction process. This universal nature of the small scales will be an important point when discussing the idea of large eddy simulation in chapter 4.

Figure 2.6 already introduced velocity and length scales for the smallest eddies in a turbulent flow. The size of these smallest eddies will now be estimated using KOLMOGOROV's first similarity hypothesis. Approximately, the first similarity assumption states that for every flow at a sufficiently high REYNOLDS number, the statistics of the universal small-scale motions are determined uniquely by the rate of dissipation $\epsilon \left[\frac{\text{m}^2}{\text{s}^3} \right]$ and the kinematic fluid viscosity $\nu \left[\frac{\text{m}^2}{\text{s}} \right]$. Simple dimensional analysis leads to the KOLMOGOROV scales associated with these smallest eddies. They are depicted in Table 2.1.

| length scale | velocity scale | time scale |
|--|--|--|
| $\eta = \left(\frac{\nu^3}{\epsilon} \right)^{\frac{1}{4}}$ | $u_\eta = (\nu\epsilon)^{\frac{1}{4}}$ | $t_\eta = \left(\frac{\nu}{\epsilon} \right)^{\frac{1}{2}}$ |

Table 2.1: Characteristic length, time and velocity scales for the smallest eddies.

The assumption that energy originating from the large scales is transferred in the energy cascade over a wide range of scales without dissipation was condensed by KOLMOGOROV in his second similarity hypothesis. In the version presented by POPE [174], it reads as follows: In every turbulent flow at a sufficiently high REYNOLDS number, the statistics of the motion of scales, sufficiently smaller than the largest scales \mathcal{L} and sufficiently larger than the smallest scales η , have a universal form that is uniquely determined by ϵ , independent of ν . An immediate consequence of this conception is that the energy dissipation, taking place at the smallest scales, is determined by the energy input on the largest scales. Let \mathcal{L} be a characteristic length and \mathcal{U} a characteristic velocity of the large-scale motion. Then \mathcal{U}^2 is of the order of magnitude of energy per mass unit contained in these large-scale eddies and $\mathcal{T} := \frac{\mathcal{L}}{\mathcal{U}}$ is a characteristic time-scale for large-scale eddies. It follows that the rate of dissipation per mass unit ϵ scales as

$$\epsilon \sim \frac{\mathcal{U}^2}{\mathcal{T}} = \frac{\mathcal{U}^3}{\mathcal{L}}. \quad (2.65)$$

Since the dissipation rate is directly related to the large scales as presented in equation (2.65), the ratio between the smallest and largest scales can be expressed as in Table 2.2 using the REYNOLDS number. These scale ratios reveal the multiscale character of turbulence. For flows of engineering interest, values of the REYNOLDS number up to 10^9 are common. This results in an extremely wide range of scales involved in turbulent flow. Table 2.3, partially based on REYNOLDS numbers taken from FLETCHER [77], quantifies these scale ratios. Looking for example at the numbers for the length-scale ratios and keeping in mind that turbulence is inherently three-dimensional, it becomes obvious that in practice the numerical resolution of all turbulent scales will not be possible.

| Scale ratios | | |
|---|---|---|
| $\frac{\mathcal{L}}{\eta} \sim \text{Re}^{\frac{3}{4}}$ | $\frac{\mathcal{U}}{u_\eta} \sim \text{Re}^{\frac{1}{4}}$ | $\frac{\mathcal{T}}{t_\eta} \sim \text{Re}^{\frac{1}{2}}$ |

Table 2.2: The REYNOLDS number dependence of the range of eddy sizes.

| Water flowing at $2 \frac{\text{m}}{\text{s}}$ through a 10cm pipe | | | |
|--|---|---|---|
| $\text{Re} = 2 \times 10^5$ | $\frac{\mathcal{L}}{\eta} \sim 9.5 \times 10^3$ | $\frac{\mathcal{U}}{u_\eta} \sim 2.1 \times 10^1$ | $\frac{\mathcal{T}}{t_\eta} \sim 4.5 \times 10^2$ |
| Large jet transport aircraft at cruise altitude | | | |
| $\text{Re} = 7 \times 10^7$ | $\frac{\mathcal{L}}{\eta} \sim 7.7 \times 10^5$ | $\frac{\mathcal{U}}{u_\eta} \sim 9.2 \times 10^1$ | $\frac{\mathcal{T}}{t_\eta} \sim 8.4 \times 10^3$ |
| Ship, 300m long at $15 \frac{\text{m}}{\text{s}}$ | | | |
| $\text{Re} = 4.5 \times 10^9$ | $\frac{\mathcal{L}}{\eta} \sim 1.7 \times 10^7$ | $\frac{\mathcal{U}}{u_\eta} \sim 2.6 \times 10^2$ | $\frac{\mathcal{T}}{t_\eta} \sim 6.7 \times 10^4$ |

Table 2.3: Typical REYNOLDS numbers and scale ratios for flows of engineering interest.

2.2.4 Energy spectra

Up to now, only the transfer of energy between the scales was quantified. In this subsection, additional information on the energy content of the scales will be given in order to provide a better insight into the nature of turbulence. This is done most easily for ideal statistically stationary homogeneous isotropic turbulence.

In this case, the averaged velocity is independent of the position in space and hence, with an appropriate choice of frame, it can be assumed to be zero. Statements concerning the spatial structure of homogeneous turbulence can be made using the so-called two-point, one-time autocovariance, a generalisation of equation (A.36):

$$\mathbf{R}_{ij}(\mathbf{d}) := \left\langle \underline{u}_i(\mathbf{x}_0) \cdot \underline{u}_j(\mathbf{x}_0 + \mathbf{d}) \right\rangle \quad (2.66)$$

Once more, due to the homogeneity of the flow, the definition of the two-point, one-time autocovariance does not depend on the particular choice of \mathbf{x}_0 . The total turbulent kinetic energy per unit mass E can be computed independent of \mathbf{x}_0 from the two-point correlation (2.66) using

$$E := \frac{1}{2} \sum_{i=1}^3 \left\langle \underline{u}_i(\mathbf{x}_0) \cdot \underline{u}_i(\mathbf{x}_0) \right\rangle = \frac{1}{2} \sum_{i=1}^3 \mathbf{R}_{ii}(0). \quad (2.67)$$

In order to be able to extract information about the scale-distribution of this energy, the FOURIER-transform of the two-point, one-time autocovariance is introduced:

$$\Theta_{ij}(\boldsymbol{\kappa}) := \frac{1}{(2\pi)^3} \int_{-\infty}^{\infty} \int_{-\infty}^{\infty} \int_{-\infty}^{\infty} e^{-\mathbf{r} \cdot \boldsymbol{\kappa}} \cdot \mathbf{R}_{ij}(\mathbf{r}) d\mathbf{r} \quad (2.68)$$

Θ is called velocity spectrum tensor. The FOURIER-transformation can be inverted recovering the two-point, one-time autocovariance:

$$\mathbf{R}_{ij}(\mathbf{r}) = \int_{-\infty}^{\infty} \int_{-\infty}^{\infty} \int_{-\infty}^{\infty} e^{\mathbf{r} \cdot \boldsymbol{\kappa}} \cdot \Theta_{ij}(\boldsymbol{\kappa}) d\boldsymbol{\kappa} \quad (2.69)$$

Thus, the energy per mass volume from equation (2.67) can be restated using the velocity spectrum tensor by

$$E = \frac{1}{2} \sum_{i=1}^3 \mathbf{R}_{ii}(\mathbf{0}) = \frac{1}{2} \sum_{i=1}^3 \int_{-\infty}^{\infty} \int_{-\infty}^{\infty} \int_{-\infty}^{\infty} \Theta_{ii}(\boldsymbol{\kappa}) d\boldsymbol{\kappa}. \quad (2.70)$$

Collecting the energy contribution of all wave vectors $\boldsymbol{\kappa}$ of norm κ yields a spectral energy density

$$E(\kappa) = \frac{1}{2} \sum_{i=1}^3 \int_{-\infty}^{\infty} \int_{-\infty}^{\infty} \int_{-\infty}^{\infty} \Theta_{ii}(\boldsymbol{\kappa}) \cdot \delta(\|\boldsymbol{\kappa}\| - \kappa) d\boldsymbol{\kappa}. \quad (2.71)$$

$E(\kappa)$ is the contribution to turbulent kinetic energy of wave numbers in the range between κ and $\kappa + d\kappa$, i.e.

$$E = \int_{-\infty}^{\infty} E(\kappa) d\kappa. \quad (2.72)$$

This spectral energy density $E(\kappa)$ defines the energy content of scales of size

$$\ell_{\kappa} = \frac{2\pi}{\kappa}. \quad (2.73)$$

According to KOLMOGOROV's second similarity hypothesis, the spectral energy density in high REYNOLDS number flow for scales sufficiently smaller than the largest scales \mathcal{L} and sufficiently larger than the smallest scales η has a universal form that is exclusively determined by ϵ . Dimensional analysis immediately results in the following power law spectrum for wave numbers corresponding to these length scales:

$$E(\kappa) = C\epsilon^{\frac{2}{3}}\kappa^{-\frac{5}{3}} \quad (2.74)$$

For wave numbers corresponding to length scales below the inertial sub-range, KOLMOGOROV's first similarity hypothesis indicates an additional dependence of the spectral energy density on the viscosity. The corresponding range of wave numbers or length scales is called dissipation range. Keeping in mind KOLMOGOROV's hypothesis of local isotropy, these statements remain true for any kind of turbulent flow. Only the spectral energy density of length scales above the inertial sub-range is governed by the special flow. The corresponding range contains most of the energy and is therefore called the energy containing range. Figure 2.7 contains an example energy spectrum of turbulence, showing the characteristic behaviour described above. For more detailed information on energy spectra, the reader is once more referred to POPE's book [174].

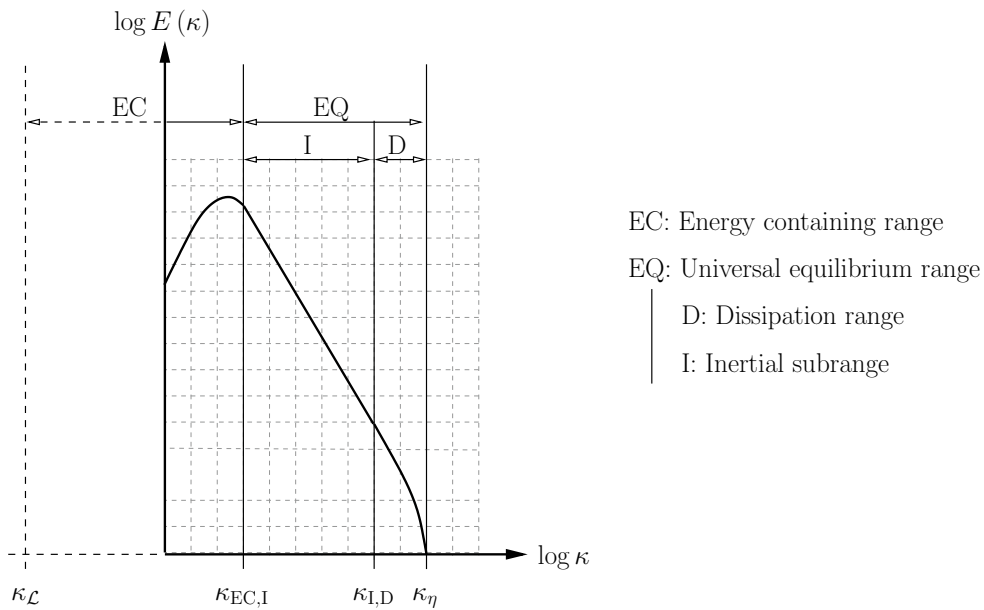


Figure 2.7: Double logarithmic plot of an energy spectrum in wave number space

2.2.5 Wall-bounded turbulent channel flow

Turbulent plane channel flow was already utilised in subsection 2.2.1 to highlight several characteristics of turbulence. In this subsection, more detailed information about this flow will be given, including a discussion of the form of mean velocity profiles.

Channel flow setup, mean flow equations and REYNOLDS numbers

The problem under consideration is statistically stationary flow through a rectangular duct as described in Figure 2.8. It is assumed that the control volume, in which the flow is investigated,

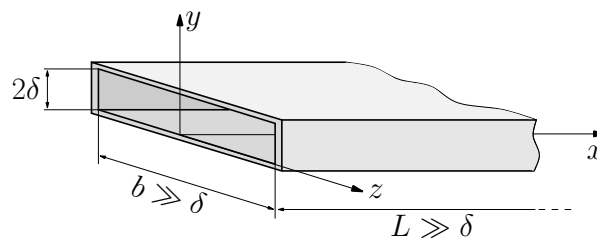


Figure 2.8: Setup for a plane channel flow aligned with the x axis. The height of the channel is 2δ . Channel length L and width b are assumed to be very large in comparison to the height so that the channel can be assumed to be extended infinitely in streamwise (x) and spanwise (z) direction.

is sufficiently far from the entry and the side walls of the duct so that the flow can be considered fully developed and homogeneous in the streamwise and spanwise direction. Hence, the velocity

statistics can be assumed to be independent of x , z and t . Furthermore, it is assumed that the mean flow is in the xy -plane and that the mean pressure is independent of z . The flow statistics can be expected to be symmetric under reflection in the midplanes at $y = \delta$ and $z = 0$. In this subsection, u , v and w will indicate the velocities in the x -, y - and z -direction respectively. The notation of means and fluctuations will make use of this assignment as well.

For the fully developed channel flow, a bulk velocity \bar{u} can be defined as the mean streamwise velocity $\langle u \rangle$ averaged over the channel height:

$$\bar{u} := \frac{1}{\delta} \int_{y=0}^{\delta} \langle u \rangle dy \quad (2.75)$$

Based on this bulk velocity, the kinematic viscosity ν and the channel height 2δ a REYNOLDS number can be defined:

$$\text{Re} := \frac{\bar{u} \cdot 2\delta}{\nu} \quad (2.76)$$

The flow in the channel is laminar up to $\text{Re} = 1350$, a fully turbulent flow can be expected for $\text{Re} > 1800$, see the book by POPE [174] and references therein.

The symmetry and homogeneity in z -direction implies vanishing REYNOLDS stresses $\langle \underline{uw} \rangle$ and $\langle \underline{vw} \rangle$. Due to homogeneity, stationarity and symmetry, the REYNOLDS-averaged NAVIER-STOKES equations reduce to the two momentum equations

$$\frac{\partial}{\partial y} \left(\langle \underline{uw} \rangle - \nu \frac{\partial \langle u \rangle}{\partial y} \right) + \frac{1}{\rho} \frac{\partial \langle p \rangle}{\partial x} = 0 \quad (2.77)$$

$$\frac{\partial}{\partial y} \left(\langle \underline{v^2} \rangle - \nu \frac{\partial \langle v \rangle}{\partial y} \right) + \frac{1}{\rho} \frac{\partial \langle p \rangle}{\partial y} = 0 \quad (2.78)$$

and the continuity equation

$$\frac{\partial \langle v \rangle}{\partial y} = 0. \quad (2.79)$$

Combining equations (2.78) and (2.79) implies

$$\frac{\partial}{\partial y} \left(\langle \underline{v^2} \rangle + \frac{\langle p \rangle}{\rho} \right) = 0 \quad (2.80)$$

and so the term in brackets depends only on x . Furthermore, since $\underline{v^2}$ vanishes on the wall, the term can be expressed using the pressure on the wall p_w :

$$\langle \underline{v^2} \rangle + \frac{\langle p \rangle}{\rho} = \frac{p_w}{\rho} \quad (2.81)$$

The REYNOLDS stress $\langle \underline{v^2} \rangle$ is independent of x . Thus, the gradient of the averaged pressure in streamwise direction is completely governed by the pressure on the wall, i.e.

$$\frac{\partial \langle p \rangle}{\partial x} = \frac{\partial p_w}{\partial x}. \quad (2.82)$$

Integration of the averaged balance of momentum (2.77) along the y axis using equation (2.82) results in

$$\left(\rho \langle \underline{uw} \rangle - \rho \nu \frac{\partial \langle u \rangle}{\partial y} \right)_{y=0}^{y=2\delta} = -2\delta \cdot \frac{\partial p_w}{\partial x}. \quad (2.83)$$

Due to the no-slip condition on the walls, the REYNOLDS stress contribution vanishes in (2.83). Thus, the mean wall shear stress τ_w can be related to the viscous part in (2.83). Using the symmetry about the midplane at $y = \delta$, it reads

$$\tau_w = \rho\nu \left(\frac{\partial \langle u \rangle}{\partial y} \right)_{y=0} = -\rho\nu \left(\frac{\partial \langle u \rangle}{\partial y} \right)_{y=2\delta}, \quad (2.84)$$

yielding the following balance between mean wall shear stress and pressure gradient:

$$\frac{\tau_w}{\delta} = -\frac{\partial p_w}{\partial x}, \quad (2.85)$$

Based on the definition of the mean wall shear stress (2.84), characteristic velocity and length scales for the near wall flow can be defined. These are the friction velocity

$$u_{\tau_w} := \sqrt{\frac{\tau_w}{\rho}} \quad (2.86)$$

and the viscous length scale

$$\delta_\nu := \nu \sqrt{\frac{\rho}{\tau_w}} = \frac{\nu}{u_{\tau_w}}. \quad (2.87)$$

It is an important observation that the viscous length scale depends on the kinematic viscosity while, according to equations (2.85) and (2.86), the friction velocity is independent of the kinematic viscosity. The friction velocity gives rise to the definition of a friction REYNOLDS number

$$\text{Re}_\tau := \frac{u_{\tau_w} \cdot \delta}{\nu} \quad (2.88)$$

The distance from the wall normalised by the viscous length scale, i.e. the distance to the wall measured in wall units, is defined by

$$y^+ := \frac{y}{\delta_\nu} = \frac{u_{\tau_w} \cdot y}{\nu}. \quad (2.89)$$

This can be interpreted as a local REYNOLDS number relating the relative importance of turbulent and viscous stresses.

Wall regions and the law of the wall

Different regions in the flow can be defined based on the definition of y^+ . The region associated with $y^+ < 50$ is called viscous wall layer. It is chosen such that the viscous forces have a significant contribution to the effective shear stress in this region. In the outer layer corresponding to $y^+ > 50$, the contribution of viscous stresses can be neglected in comparison to the REYNOLDS shear stress.

Furthermore, for sufficiently high REYNOLDS numbers, an inner layer is postulated according to PRANDTL [175] as the region in which the mean velocity profile is determined by viscous scales δ_ν independent of δ . For a summary of the definitions of the inner layer, the viscous wall region and the outer layer the reader is referred to Figure 2.9. Subsequently, an equation for the gradient of the mean streamwise velocity, $\frac{\partial \langle u \rangle}{\partial y}$, will be derived by means of a dimensional

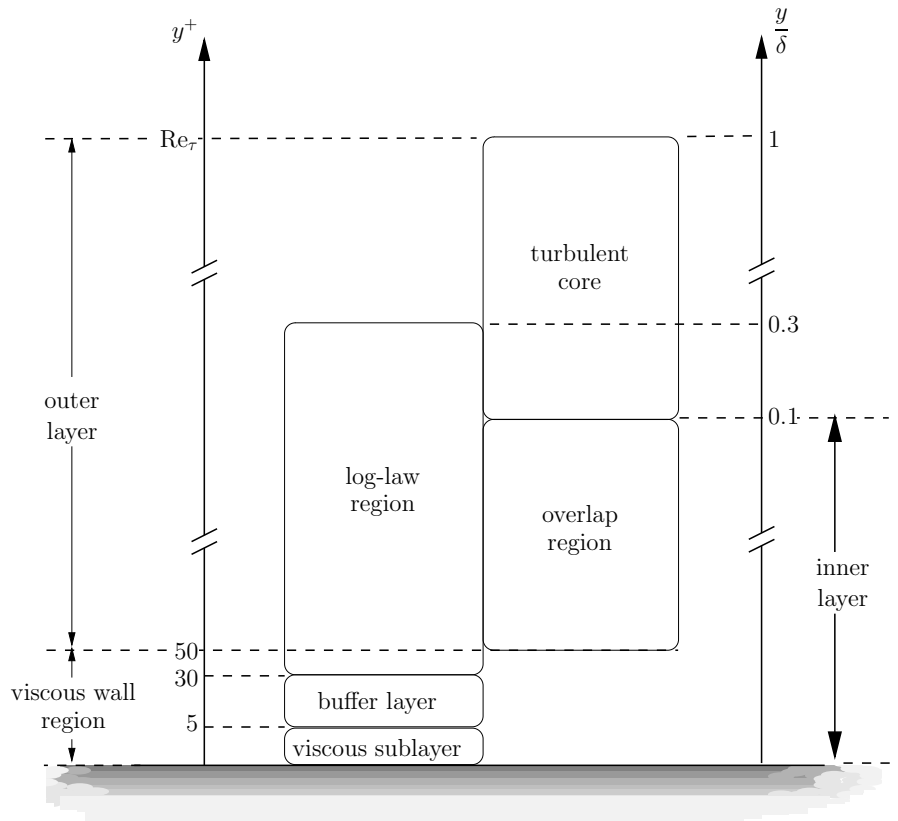


Figure 2.9: Wall regions and properties in turbulent channel flow at sufficiently high REYNOLDS number, adapted from POPE [174].

analysis. In general, the velocity profile in a fully developed channel flow will be defined by the four parameters ν , δ , ρ and $\frac{\partial p_w}{\partial x}$. Thus, the gradient of the mean streamwise velocity at position y will depend only on y , ν , δ , ρ and $\frac{\partial p_w}{\partial x}$. These five quantities introduce three different units, meaning that two independent dimensionless variables, $\frac{y}{\delta}$ and $\frac{y}{\delta_\nu}$, can be deduced from them. Using these dimensionless parameters, the gradient of the mean streamwise velocity can be written using a universal non-dimensional function \mathcal{F} :

$$\frac{\partial \langle u \rangle}{\partial y} = \frac{u_{\tau_w}}{y} \cdot \mathcal{F} \left(\frac{y}{\delta}, \frac{y}{\delta_\nu} \right) \quad (2.90)$$

The function \mathcal{F} was chosen such that for the inner layer, the PRANDTL hypothesis can be readily applied to (2.90), yielding

$$\frac{\partial \langle u \rangle}{\partial y} = \frac{u_{\tau_w}}{y} \cdot \mathcal{F}^{\text{inner}} \left(\frac{y}{\delta_\nu} \right) \quad (2.91)$$

with a universal non-dimensional function $\mathcal{F}^{\text{inner}}$ depending only on the distance to the wall in wall units $y^+ = \frac{y}{\delta_\nu}$. Using the normalised mean streamwise velocity

$$u^+ := \frac{\langle u \rangle}{u_{\tau_w}}, \quad (2.92)$$

equation (2.91) can be integrated yielding the law of the wall:

$$u^+ = u^+(y^+) = \int_0^{y^+} \frac{1}{\tilde{y}^+} \cdot \mathcal{F}^{\text{inner}}(\tilde{y}^+) d\tilde{y}^+ \quad (2.93)$$

This is a fundamental, characteristic formula not only for turbulent channel flow but also for other turbulent flows near walls like pipe flow and boundary layers.

Viscous sublayer

In the proximity of the wall, the law of the wall can be expanded in a TAYLOR series around $y^+ = 0$:

$$u^+(\Delta y^+) = u^+(0) + \frac{\partial u^+}{\partial y^+}(0) \cdot \Delta y^+ + O(\Delta y^{+2}) \quad (2.94)$$

According to the no-slip condition, $u^+(0) = 0$ holds. Furthermore, the first derivative of the normalised mean velocity can be computed based on the mean wall shear stress, i.e. using equation (2.84):

$$\frac{\partial u^+}{\partial y^+}(0) = \frac{\delta_\nu}{u_{\tau_w}} \cdot \left(\frac{\partial \langle u \rangle}{\partial y} \right)_{y=0} = \frac{\delta_\nu}{u_{\tau_w}} \cdot \frac{\tau_w}{\rho\nu} = \frac{\nu}{u_{\tau_w}^2} \cdot \frac{\tau_w}{\rho\nu} = 1 \quad (2.95)$$

This results in the following formula for the law of the wall close to the wall:

$$u^+(\Delta y^+) = \Delta y^+ + O(\Delta y^{+2}) \quad (2.96)$$

Equation (2.96) is a decent approximation for $\Delta y^+ < 5$. This region is called viscous sublayer. A TAYLOR series expansion is also possible for velocity fluctuations. Due to the no-slip condition, it starts at most with the first order term:

$$\underline{u}(\Delta y) = \frac{\partial \underline{u}}{\partial y}(0) \cdot \Delta y + \frac{\partial^2 \underline{u}}{\partial y^2}(0) \cdot \frac{\Delta y^2}{2} + O(\Delta y^3) \quad (2.97)$$

$$\underline{v}(\Delta y) = \frac{\partial \underline{v}}{\partial y}(0) \cdot \Delta y + \frac{\partial^2 \underline{v}}{\partial y^2}(0) \cdot \frac{\Delta y^2}{2} + O(\Delta y^3) \quad (2.98)$$

$$\underline{w}(\Delta y) = \frac{\partial \underline{w}}{\partial y}(0) \cdot \Delta y + \frac{\partial^2 \underline{w}}{\partial y^2}(0) \cdot \frac{\Delta y^2}{2} + O(\Delta y^3) \quad (2.99)$$

Furthermore, the continuity equation gives

$$\frac{\partial \underline{u}}{\partial x}(0) + \frac{\partial \underline{v}}{\partial y}(0) + \frac{\partial \underline{w}}{\partial z}(0) = \frac{\partial \underline{v}}{\partial y}(0) = 0 \quad (2.100)$$

implying the following scalings for the REYNOLDS stresses close to the wall:

$$\begin{aligned} \langle \underline{u}\underline{u} \rangle &\sim \Delta y^2 & \langle \underline{v}\underline{v} \rangle &\sim \Delta y^4 \\ \langle \underline{w}\underline{w} \rangle &\sim \Delta y^2 & \langle \underline{u}\underline{v} \rangle &\sim \Delta y^3 \end{aligned} \quad (2.101)$$

Log-law theory

At very high REYNOLDS numbers, the viscosity can be assumed to have little effect on the mean flow close to $\frac{y}{\delta} = 0.1$ in the outer part of the inner layer. In this region, the universal function in equation (2.91) can be assumed to be independent of the viscosity and hence to be independent of $\frac{y}{\delta_\nu}$ yielding

$$\frac{\partial u^+}{\partial y^+} = \frac{1}{\kappa_{\log\text{-law}} y^+} \quad (2.102)$$

with the VON KÁRMÁN constant $\kappa_{\log\text{-law}}$. Integration of (2.102) results in the log-law

$$u^+(y^+) = \frac{1}{\kappa_{\log\text{-law}}} \ln(y^+) + B_{\log\text{-law}}. \quad (2.103)$$

Suitable choices for the parameters are $\kappa_{\log\text{-law}} = 0.41$ and $B_{\log\text{-law}} = 5.2$, see for instance the book by POPE [174].

Although the assumption which was used to derive the log-law is quite restrictive, it provides a reasonable representation of the mean flow even in parts of the outer layer, see the size of the log-law region displayed in Figure 2.9. For an extension of this theory to incorporate finite REYNOLDS numbers effects and for a more detailed investigation of the range above the buffer layer see WOSNIK et al. [223]. Furthermore, in BUSCHMANN and GAD-EL-HAK [44], a review on contemporary advances in analytical and asymptotic approaches to determine the mean-velocity profile can be found.

SPALDING'S law

An important empirical formula is SPALDING'S law [193], combining the formulas for viscous sublayer and log-law region:

$$y^+ = u^+ + e^{-\kappa_{\log\text{-law}} B_{\log\text{-law}}} \cdot \left(e^{\kappa_{\log\text{-law}} u^+} - 1.0 - \kappa_{\log\text{-law}} u^+ - \frac{(\kappa_{\log\text{-law}} u^+)^2}{2} - \frac{(\kappa_{\log\text{-law}} u^+)^3}{6} \right) \quad (2.104)$$

SPALDING'S law is visualised in Figure 2.10. For a given y^+ , u^+ is defined implicitly by a nonlinear equation. Thus, u^+ has to be determined iteratively.

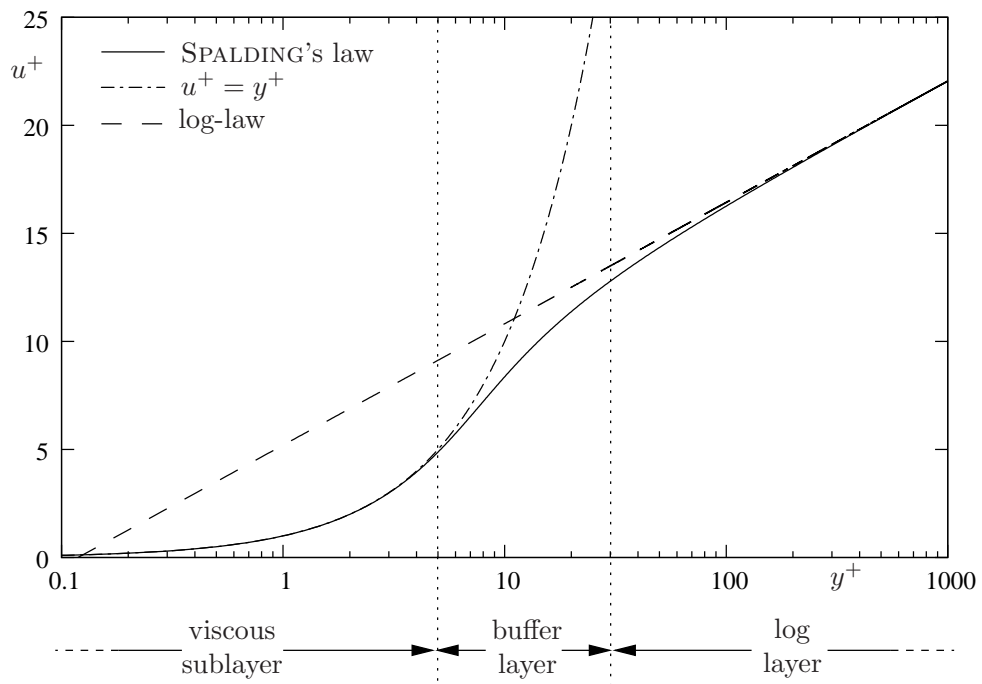


Figure 2.10: log-lin plot of SPALDING's law, providing a smooth transition between the linear viscous sublayer and the log-law region.

3 Finite elements for incompressible flows — base algorithm

The instationary, incompressible NAVIER-STOKES equations contain a spatial and a temporal component. A numerical approximation of the whole equation requires a treatment of both of these parts. For this purpose, basically two options are available. The first option, which was selected in this thesis, is to perform a discretisation of both components in a sequential manner. The approach to perform time discretisation prior to space discretisation, which is usually called ROTHE's method [183], prescribes the way this chapter is structured. Section 3.1 on implicit time integration with special respect to the generalised-alpha time integration precedes sections 3.2 to 3.7, which provide information on the spatial discretisation approach and related solution procedures. Nevertheless the approach often termed 'method of lines', which is equivalent to perform spatial discretisation before temporal discretisation, is very useful as well. For example, it allows the interpretation of the semi-discrete system as a differential algebraic problem. For the sake of completeness, another option shall be mentioned here as well. It is to perform space and time discretisation in a single step using a space-time finite element procedure. This approach allows an alternative treatment of deforming fluid domains without requiring an ALE formulation. See for example JAMET and BONNEROT [129, 130], TEZDUYAR et al. [206, 205] and BEHR [24].

The spatial discretisation approach chosen for this thesis is the finite element method. Common literature on this approach is for example the book by HUGHES [116], the book series by ZIENKIEWICZ and TAYLOR [225, 226, 227], the book by BRENNER and SCOTT [41] and the book by BRAESS [40]. Books on finite elements with a focus on fluid mechanics are for instance DONEA and HUERTA [64] and the book series by GRESHO and SANI [102, 103]. The approach used in this thesis is not the only way to perform a spatial discretisation. Finite volume methods, which are based on an integral form of the conservation equations, are a widespread alternative in computational fluid dynamics. Furthermore, finite difference methods are frequently used, but are less well-suited for complicated geometries since they are preferably used in conjunction with structured grids. The book by FERZIGER and PERIC [76] provides a brief introduction to these methods, as well as the book by WESSELING [219] to finite volume schemes. Discontinuous GALERKIN methods can be interpreted as a generalisation of finite volume methods incorporating ideas of numerical fluxes into the framework of finite elements. The interested reader is referred to the overview article by COCKBURN, KARNIADAKIS and SHU [51]. Compared to continuous GALERKIN methods, as are used in traditional finite element approaches, discontinuous GALERKIN methods are more flexible since they allow jumps along element edges, but this naturally comes along with an increased number of degrees of freedom, see for instance the article by ENGEL et al. [69]. In contrast to all methods described above, mesh-free methods do not require the generation of elements in the computational domain, see for example NAYROLES, TOUZOT and VILLON [164] and BELYTSCHKO, LU and GU [26]. For turbulent flow compu-

tations, this method seems to be inadequate for efficiency reasons. In contrast to the aforementioned approaches, spectral methods as described in CANUTO, HUSSAINI, QUARTERONI and ZANG [46] are well known to be a very efficient choice and are widespread in the turbulence community, especially for computations on simple periodic domains as they are required for turbulent channel flow or homogeneous isotropic turbulence. Spectral methods can not only be realised as GALERKIN methods, but also as collocation methods, see e.g. PEYRET [172]. The idea of collocation is to enforce the partial differential equation at discrete ‘collocation’ points. These methods are impressively simple and efficient which makes them a valid alternative to finite element analysis.

3.1 Implicit time integration

The incompressible NAVIER-STOKES equations include a constraint equation, the incompressibility condition. The momentum equation contains a time derivative of velocity, but pressure is defined instantaneously at each time by the current velocity field via the so-called pressure POISSON equation. This pressure equation can be obtained by a time differentiation of the incompressibility condition in combination with the momentum equation. Based on finite elements, a semi-discretisation of the incompressible NAVIER-STOKES equations in space results in a differential algebraic equation. Problems of this type are well known to be very challenging for time integration methods, and thus requiring implicit time integration procedures with adequate stability properties, see for instance RANNACHER [178]. The preferred method in the present work is the generalised-alpha time integration presented in CHUNG and HULBERT [49], JANSEN, WHITING and HULBERT [132]. It provides an accurate method which allows control of numerical damping by a single parameter ρ_∞ . The analysis of several time integration methods by DETTMER and PERIC [61] as well as many successful applications of this method indicate that it is a very good choice for fluid problems in general. Furthermore, due to numerical damping control, the impact of time integration on turbulence modelling is kept to a minimum, making it especially well-suited for the investigation of residual-based variational modelling of turbulence.

A general initial value problem of order one is defined by an ordinary differential equation

$$\frac{\partial y}{\partial t}(t) = f(y(t), t) \quad (3.1)$$

in combination with initial values for the solution $y(t_0)$. This generic initial value problem will be used to introduce the generalised-alpha time integration in subsection 3.1.1. Special parameter settings and the resulting schemes will be discussed, providing a relationship of the generalised-alpha method to other well-known time integration schemes. This subsection also briefly reviews important stability properties of the method. Afterwards, in subsection 3.1.2, a time-discretised version of the NAVIER-STOKES equations will be presented.

For general literature on ordinary differential equations, the reader is referred to the book series by HAIRER et al. [106, 107]. In the context of stiff systems, as are encountered in this thesis, the second volume by HAIRER and WANNER proved to be especially valuable. Further literature which can be consulted for general statements on existence and uniqueness of solutions, stability and consistency are for example DEUFLHARD and BORNEMANN [62], SCHWARZ [188], BORNEMANN [38] and STUART and HUMPHRIES [197].

3.1.1 Generalised-alpha time integration

For the generalised-alpha time integration as it is described in JANSEN, WHITING and HULBERT [132], the intermediate time levels

$$t^{n+\alpha_F} = t^n + \alpha_F \cdot (t^{n+1} - t^n) = t^n + \alpha_F \cdot \Delta t \quad (3.2)$$

and

$$t^{n+\alpha_M} = t^n + \alpha_M \cdot (t^{n+1} - t^n) = t^n + \alpha_M \cdot \Delta t \quad (3.3)$$

are introduced based on two parameters α_F, α_M . For the time discretised version of differential equation (3.1),

$$\dot{y}^{n+\alpha_M} = f(y^{n+\alpha_F}, t^{n+\alpha_F}) \quad (3.4)$$

$$\dot{y}^{n+\alpha_M} = \dot{y}^n + \alpha_M \cdot (\dot{y}^{n+1} - \dot{y}^n) \quad (3.5)$$

$$y^{n+\alpha_F} = y^n + \alpha_F \cdot (y^{n+1} - y^n) \quad (3.6)$$

$$y^{n+1} = y^n + \Delta t \cdot (\dot{y}^n + \gamma \cdot (\dot{y}^{n+1} - \dot{y}^n)), \quad (3.7)$$

the evaluation of the acceleration term \dot{y} is shifted to $t^{n+\alpha_M}$ and the evaluation of the right hand side is shifted to $t^{n+\alpha_F}$, see equation (3.4). In equations (3.5), (3.6), the intermediate quantities $\dot{y}^{n+\alpha_M}$ and $y^{n+\alpha_F}$ are defined as linear combinations of the respective values at time steps n and $n + 1$. The acceleration \dot{y} is not taken as an independent variable but is related to the solution y according to equation (3.7). For many parameter settings, the generalised-alpha method (3.4)–(3.6) requires initial values not only for the solution y^0 but also for the acceleration \dot{y}^0 .

Special cases

Depending on the choice of the parameters, the four equations (3.4)–(3.6) are equivalent to some well-known implicit single or double step methods. Choices for single-step methods are:

- One-stage θ methods for $\alpha_M = \gamma$

This choice allows to eliminate all dependencies on acceleration in equations (3.4) to (3.5) for a single time step, yielding

$$\frac{y^{n+1} - y^n}{\Delta t} = f(y^n + \alpha_F \cdot (y^{n+1} - y^n), t^{n+\alpha_F}). \quad (3.8)$$

This is equivalent to a one-stage RUNGE-KUTTA method

$$\frac{\eta_1}{y^{n+1}} = \frac{y^n + \Delta t \cdot \alpha_F \cdot f(\eta_1, t^{n+\alpha_F})}{y^n + \Delta t \cdot f(\eta_1, t^{n+\alpha_F})} \quad (3.9)$$

with the BUTCHER tableau

$$\begin{array}{c|c} \alpha_F & \alpha_F \\ \hline & 1 \end{array}. \quad (3.10)$$

One-stage θ methods include the second order midpoint rule for $\alpha_M = \gamma = \alpha_F = \frac{1}{2}$

$$\frac{y^{n+1} - y^n}{\Delta t} = f\left(\frac{y^{n+1} + y^n}{2}, t^{n+\frac{1}{2}}\right) \quad (3.11)$$

and the first order implicit EULER method for $\alpha_F = 1$

$$\frac{y^{n+1} - y^n}{\Delta t} = f(y^{n+1}, t^{n+1}). \quad (3.12)$$

- The one-step-theta family for $\alpha_M = \alpha_F = 1$

Evaluation of (3.4) for two succeeding time steps and combination with equation (3.7) yields the following linear one step method

$$y^{n+1} = y^n + \Delta t \cdot \left((1 - \gamma) \cdot f(y^n, t^n) + \gamma \cdot f(y^{n+1}, t^{n+1}) \right), \quad (3.13)$$

equivalent to a two-stage RUNGE-KUTTA method

$$\begin{aligned} \eta_1 &= y^n \\ \eta_2 &= y^n + \Delta t \cdot (1 - \gamma) \cdot f(\eta_1, t^n) + \Delta t \cdot \gamma \cdot f(\eta_2, t^{n+1}) \\ y^{n+1} &= \frac{y^n + \Delta t \cdot (1 - \gamma) \cdot f(\eta_1, t^n) + \Delta t \cdot \gamma \cdot f(\eta_2, t^{n+1})}{1} \end{aligned} \quad (3.14)$$

with the BUTCHER tableau

$$\begin{array}{c|cc} 0 & & \\ 1 & 1 - \gamma & \gamma \\ \hline & 1 - \gamma & \gamma \end{array}. \quad (3.15)$$

This is the well-known one-step-theta family, including for $\gamma = \frac{1}{2}$ the second order trapezoidal (CRANK-NICHOLSON) rule as well as the implicit EULER rule described above. For linear problems, the one-step-theta family is equivalent to the one-stage θ methods above.

For more general parameter choices, the generalised-alpha method can be considered as a two-step method. Evaluation of (3.4)–(3.6) for two consecutive time steps $n - 1$ and n allows to eliminate all dependencies on the acceleration. The resulting scheme,

$$\begin{aligned} \alpha_M \cdot y^{n+1} + (1 - 2\alpha_M) \cdot y^n - (1 - \alpha_M) \cdot y^{n-1} &= \\ &= (1 - \gamma) \cdot \Delta t \cdot f\left((1 - \alpha_F) \cdot y^{n-1} + \alpha_F \cdot y^n, t^{n-1+\alpha_F}\right) + \\ &+ \gamma \cdot \Delta t \cdot f\left((1 - \alpha_F) \cdot y^n + \alpha_F \cdot y^{n+1}, t^{n+\alpha_F}\right), \end{aligned} \quad (3.16)$$

clearly reveals the method's character of a two-step method. Since f is evaluated at an intermediate time-level $t^{n+\alpha_F}$, a linear multi-step method can only be recovered for linear problems or the choice $\alpha_F = 1$. The multi-step character also explains that in general it is not sufficient to prescribe only the initial velocity but that a second quantity corresponding to the 'old' time step is also required. Choices for two-step methods are for example:

- The BDF2 time integration for $\gamma = \alpha_F = 1$ and $\alpha_M = \frac{3}{2}$

This parameter choice leads to the second order linear multi-step method of CURTISS and HIRSCHFELDER [60], see also GEAR [88]:

$$y^{n+1} - \frac{4}{3} \cdot y^n + \frac{1}{3} \cdot y^{n-1} = \frac{2}{3} \Delta t \cdot f(y^{n+1}, t^{n+1}) \quad (3.17)$$

Due to its excellent stability properties, this method is widely used for the solution of stiff problems, see for instance FÖRSTER [78] for an application in the context of finite element flow computations on deforming meshes.

- The ρ_∞ family of JANSEN, WHITING and HULBERT [132]

For $0 \leq \rho_\infty \leq 1$, a family of second order time integration methods is defined by the parameters

$$\alpha_M = \frac{1}{2} \left(\frac{3 - \rho_\infty}{1 + \rho_\infty} \right), \quad \alpha_F = \frac{1}{1 + \rho_\infty} \quad (3.18)$$

and the second order condition which can be derived from equation (3.16) by TAYLOR expansion of the discrete evolution of y^{n-1} :

$$\alpha_M + \frac{1}{2} = \alpha_F + \gamma \quad (3.19)$$

This second order condition is equivalent to

$$\gamma = \frac{1}{1 + \rho_\infty}. \quad (3.20)$$

The only parameter of this family, ρ_∞ , is called spectral radius of an infinite time step, see the original paper or the discussion on linear stability below for further explanation. The parameter ρ_∞ defines a smooth transition from maximum damping for the BDF2 method at $\rho_\infty = 0$ to minimum damping for the midpoint rule at $\rho_\infty = 1$, see Figure 3.1 for the resulting parameters. The choice $\rho_\infty = \frac{1}{2}$, for which JANSEN, WHITING and HULBERT [132] report a good numerical performance with an acceptable amount of damping, is the base for the numerical results that will be presented later in this thesis.

Some results of linear stability analysis for the generalised-alpha method

The linear test equation

$$\dot{y}(t) = \lambda \cdot y(t), \quad \text{Re}(\lambda) < 0 \quad (3.21)$$

can be used to investigate basic stability properties of time integration methods. The exact solution $y(t) = y(t_0) \cdot e^{\lambda t}$ of equation (3.21) decays in time if and only if the real part of the complex parameter λ is less than zero, i.e. $\lambda \in \mathbb{C}^-$. According to GRESHO and SANI [102], the real part of λ can be interpreted in analogy to a diffusive term in a convection diffusion problem, while the imaginary part is related to the convective part.

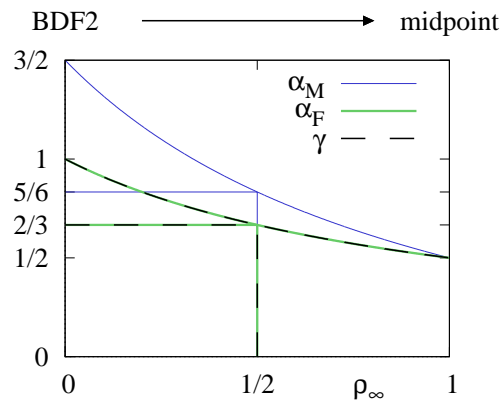


Figure 3.1: Second order parameter choices for generalised-alpha methods plotted over the spectral radius ρ_∞ of an infinite time step. The graphs for α_F and γ are identical. Values are provided for $\rho_\infty = \frac{1}{2}$, the parameter choice used in this thesis.

Application of the generalised-alpha method to the test equation (3.21) yields the linear difference equation

$$\begin{aligned} & y^{n+1} \cdot [\alpha_M - \gamma\alpha_F \cdot \lambda\Delta t] + \\ & + y^n \cdot [(1 - 2\alpha_M) - (\alpha_F + \gamma - 2\alpha_F \cdot \gamma) \cdot \lambda\Delta t] + \\ & + y^{n-1} \cdot [-(1 - \alpha_M) - (1 - \gamma) \cdot (1 - \alpha_F) \cdot \lambda\Delta t] = 0. \end{aligned} \quad (3.22)$$

According to DEUFLHARD and BORNEMANN [62], this linear difference equation is stable if and only if the absolute values of all solutions ζ of the equation

$$\begin{aligned} \wp^{\lambda\Delta t}(\zeta) := & [\alpha_M - \gamma\alpha_F \cdot \lambda\Delta t] \cdot \zeta^2 + \\ & + [(1 - 2\alpha_M) - (\alpha_F + \gamma - 2\alpha_F \cdot \gamma) \cdot \lambda\Delta t] \cdot \zeta + \\ & + [-(1 - \alpha_M) - (1 - \gamma) \cdot (1 - \alpha_F) \cdot \lambda\Delta t] = 0 \end{aligned} \quad (3.23)$$

are less than or equal one and solutions of absolute value one are unique. This condition is called root condition and $\wp^{\lambda\Delta t}(\zeta)$ is called the associated characteristic polynomial of the linear difference equation (3.22). For an interpretation of the roots of equation (3.23), equation (3.22) can be restated in a matrix recursion form

$$\begin{pmatrix} y^{n+1} \\ y^n \end{pmatrix} = \mathbf{A} \cdot \begin{pmatrix} y^n \\ y^{n-1} \end{pmatrix} \quad (3.24)$$

using the amplification matrix

$$\mathbf{A} = \begin{pmatrix} \frac{[-(1-2\alpha_M) + (\alpha_F + \gamma - 2\alpha_F \cdot \gamma) \cdot \lambda\Delta t]}{\alpha_M - \gamma\alpha_F \cdot \lambda\Delta t} & \frac{[(1-\alpha_M) + (1-\gamma) \cdot (1-\alpha_F) \cdot \lambda\Delta t]}{\alpha_M - \gamma\alpha_F \cdot \lambda\Delta t} \\ 1 & 0 \end{pmatrix}. \quad (3.25)$$

A straightforward computation of the eigenvalues of \mathbf{A} shows that they are identical to the roots of equation (3.23). This interpretation allows the conclusion that the difference equation (3.22) is asymptotically stable, i.e. it holds that

$$\lim_{n \rightarrow \infty} y^n = 0, \quad (3.26)$$

if and only if the recursion (3.24) is contractive, i.e. all roots of equation (3.23) are strictly smaller than one.

The region of stability of the linear difference equation (3.22) and hence the region of stability of the generalised-alpha method applied to the test problem is defined as the set of all complex $\lambda\Delta t$ for which the root condition is satisfied. The boundary of the stability region is the root locus curve. It can be obtained from equation (3.23) by setting $\zeta := e^{i\varphi}$ for $\varphi \in [0; 2\pi[$ and solving the resulting equation

$$(\lambda\Delta t)^{\text{rootloc}} = \frac{\alpha_M \cdot e^{2i\varphi} + (1 - 2\alpha_M) \cdot e^{i\varphi} - (1 - \alpha_M)}{\gamma\alpha_F \cdot e^{2i\varphi} + (\alpha_F + \gamma - 2\alpha_F \cdot \gamma) \cdot e^{i\varphi} + (1 - \gamma) \cdot (1 - \alpha_F)} \quad (3.27)$$

for $\lambda\Delta t$. Figure 3.2 contains several examples of root locus curves for the generalised-alpha method for special parameter choices.

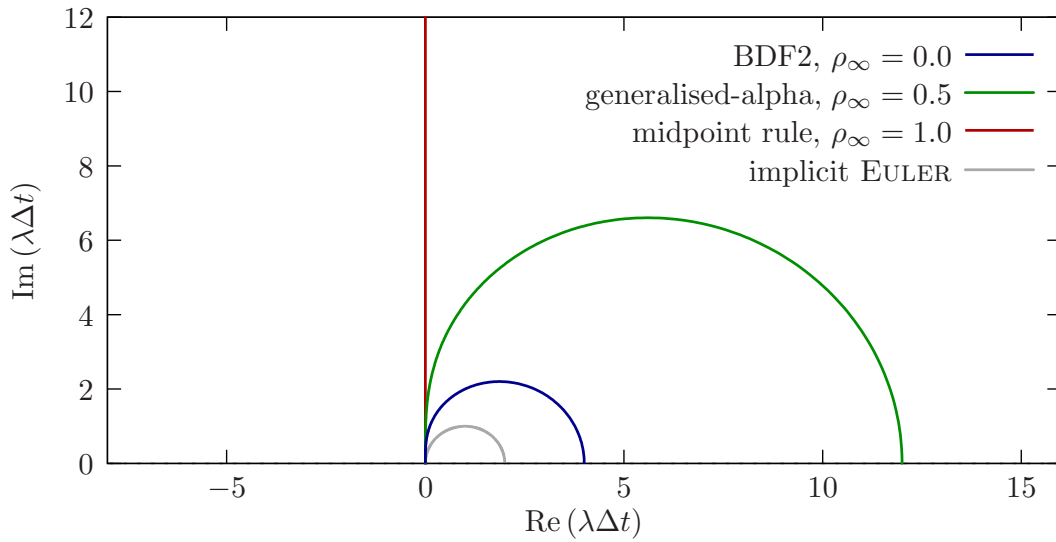


Figure 3.2: Root locus curves for several parameter choices of the generalised-alpha method. Due to symmetry, only the positive part of the imaginary axis is displayed. The stability regions of the methods are outside the closed curves for implicit EULER, $\rho_\infty = 0.5$ and $\rho_\infty = 0.0$ respectively on the left of the imaginary axis for the midpoint rule $\rho_\infty = 1.0$.

For extremely stiff problems, as they are encountered in the context of incompressible fluid flows, it is required that the method applied is stable for all $\lambda\Delta t$ with a negative real part. Such methods, whose stability region comprises \mathbb{C}^- , are called *A*-stable. The paper by JANSEN, WHITING and HULBERT [132] contains investigations of the roots of equation (3.23) for infinitely large and infinitely small time steps. From these investigations and the second order condition (3.19), they derive the following necessary stability condition

$$\alpha_M \geq \alpha_F \geq \frac{1}{2} \quad (3.28)$$

and show that in the limit of infinitely large time steps, the roots (ζ_1, ζ_2) of equation (3.23) are given as

$$\lim_{\Delta t \rightarrow \infty} (\zeta_1, \zeta_2) = \left(\frac{-1 + 2(\alpha_M - \alpha_F)}{1 + 2(\alpha_M - \alpha_F)}, 1 - \frac{1}{\alpha_F} \right). \quad (3.29)$$

The ρ_∞ family is defined such that

$$\lim_{\Delta t \rightarrow \infty} |\zeta_1| = \lim_{\Delta t \rightarrow \infty} |\zeta_2| = \rho_\infty, \quad (3.30)$$

explaining the name ‘spectral radius of an infinite time step’ for ρ_∞ . For this family, the root locus curve can be obtained in the form

$$\begin{aligned} (\lambda \Delta t)_{\rho_\infty}^{\text{rootloc}} = & \frac{(1 - \rho_\infty)^3 \cdot (\rho_\infty + 1) \cdot (\cos(\varphi) - 1)^2}{(2\rho_\infty \cdot \cos(\varphi) + \rho_\infty^2 + 1)^2} + \\ & + i \cdot \frac{(\rho_\infty + 1)^2 \cdot \sin(\varphi) \cdot (2\rho_\infty^2 - 2\rho_\infty + 2 - (\rho_\infty^2 - 4\rho_\infty + 1) \cos(\varphi))}{(2\rho_\infty \cdot \cos(\varphi) + \rho_\infty^2 + 1)^2} \end{aligned} \quad (3.31)$$

for $\rho_\infty < 1$. The case $\rho_\infty = 1$ has to be treated separately. For this parameter choice, the real part in equation (3.31) converges to zero independent of φ while the imaginary part exhibits a singularity at $\varphi = \pi$. The stability properties for this choice are exactly the well-known properties of the midpoint rule, see Figure 3.2. For $\rho_\infty \in [0; 1[$, the real part of the root locus curve (3.31) is positive and zero only for $\varphi = 0$, yielding a closed curve on the right side of the imaginary axis. By differentiation, it becomes clear that the real part is monotonic increasing for $\varphi \in]0; \pi[$ and monotonic decreasing for $\varphi \in]\pi; 2\pi[$. Furthermore, the imaginary part is positive for $\varphi \in]0; \pi[$ and negative in $\varphi \in]\pi; 2\pi[$, resulting in a ‘circle-like’ shape of the root locus curve. Thus the stability region outside the root locus curve contains \mathbb{C}^- and all members of the ρ_∞ family inherit the stability from the continuous problem for all time step sizes Δt , i.e. they are in fact *A*-stable.

According to its definition, the parameter ρ_∞ controls the behaviour of the method for infinite time steps. At $\rho_\infty = 0$, the numerical method will return the correct solution 0 for the linear test problem (3.21) in only one infinite time step $\Delta t \rightarrow \infty$. This is a well-known property of the BDF2 method. In contrast to that, for $\rho_\infty = 1$, the method exhibits the problems of the midpoint rule, for which in the limit $\Delta t \rightarrow \infty$ the sign of the solution switches in every time step corresponding to an eigenvalue -1 .

3.1.2 Application to the incompressible NAVIER-STOKES equations

In this subsection, the generalised-alpha time integration will be applied to the NAVIER-STOKES equations. The most general formulation, the discretisation on deforming domains, is presented first. The versions for convective and conservative EULERIAN descriptions are depicted afterwards.

ALE version

The generalised-alpha time integration applied to the ALE version of the NAVIER-STOKES equations (2.47) results in the time discrete momentum equation

$$\begin{aligned} \dot{\mathbf{u}}^{n+\alpha_M} + ((\mathbf{u}^{n+\alpha_F} - \mathbf{u}_G^{n+\alpha_F}) \cdot \nabla) \mathbf{u}^{n+\alpha_F} + \\ + \frac{1}{\rho} \nabla p^{n+1} - 2\nu \nabla \cdot \boldsymbol{\varepsilon}(\mathbf{u}^{n+\alpha_F}) - \mathbf{b}^{n+\alpha_F} = \mathbf{0}, \end{aligned} \quad (3.32)$$

the incompressibility constraint

$$\nabla \cdot \mathbf{u}^{n+1} = 0 \quad (3.33)$$

and the following linear relations corresponding to equations (3.5)–(3.7):

$$\mathbf{u}^{n+\alpha_F} = \alpha_F \cdot (\mathbf{u} \circ \Phi)^{n+1} \circ \Phi^{-1} + (1 - \alpha_F) \cdot (\mathbf{u} \circ \Phi)^n \circ \Phi^{-1} \quad (3.34)$$

$$\dot{\mathbf{u}}^{n+\alpha_M} = \alpha_M \cdot \left(\frac{\partial(\mathbf{u} \circ \Phi)}{\partial t} \right)^{n+1} \circ \Phi^{-1} + (1 - \alpha_M) \cdot \left(\frac{\partial(\mathbf{u} \circ \Phi)}{\partial t} \right)^n \circ \Phi^{-1} \quad (3.35)$$

$$\begin{aligned} \mathbf{u}^{n+1} = (\mathbf{u} \circ \Phi)^n \circ \Phi^{-1} + (1 - \gamma) \Delta t \cdot \\ \cdot \left(\frac{\partial(\mathbf{u} \circ \Phi)}{\partial t} \right)^n \circ \Phi^{-1} + \gamma \Delta t \cdot \left(\frac{\partial(\mathbf{u} \circ \Phi)}{\partial t} \right)^{n+1} \circ \Phi^{-1} \end{aligned} \quad (3.36)$$

These equations are stated with respect to the control volume $\Omega(t^{n+1})$ at the new time level, i.e. Φ^{-1} in equations (3.34)–(3.36) belongs to the same new time level. This implies that

$$(\mathbf{u} \circ \Phi)^{n+1} \circ \Phi^{-1} = \mathbf{u}^{n+1}, \quad (3.37)$$

but in general

$$(\mathbf{u} \circ \Phi)^n \circ \Phi^{-1} \neq \mathbf{u}^n. \quad (3.38)$$

In equations (3.34)–(3.36) quantities are averaged in the reference domain. This reflects the fact that for the Arbitrary-LAGRANGEan-EULERian approach, the time derivative is computed with respect to the reference configuration.

The fully implicit treatment of the pressure in equation (3.32) for incompressible flows is done according to WHITING [220]. It takes into account the fact that the pressure is actually not integrated in time but instantaneously enforces the incompressibility constraint in each new time step. In agreement with this idea, the incompressibility constraint is also requested at the new time step in equation (3.33). This extension of the method proposed in WHITING [220] is intended to provide more robustness in the context of turbulent channel flow simulations, which are started from a randomly perturbed initial profile which possibly violates the incompressibility.

Up to now, the body force and the grid velocity in equation (3.32) have been considered as known quantities, which can be evaluated at the intermediate time level $t^{n+\alpha_F}$. Unfortunately, in practice, an explicitly defined grid velocity is not available. Instead, a mesh motion algorithm will provide only mesh displacements at discrete time levels as defined in (2.11),

$$(\mathbf{d}_G \circ \Phi)(\boldsymbol{\xi}, t) = \Phi(\boldsymbol{\xi}, t) - \boldsymbol{\xi}. \quad (3.39)$$

The actual mesh velocity has to be obtained from these values by a finite difference approximation. As pointed out by FÖRSTER et al. [79], the order of accuracy of this approximation has to match the temporal accuracy of the fluid time integration to maintain the overall order of accuracy. For the generalised-alpha time integration used in this thesis, a second order finite difference approximation equivalent to the one proposed in the above-mentioned reference is applied to determine the new grid velocities at time t^{n+1} :

$$\mathbf{u}_G^{n+1} = \frac{3(\mathbf{d}_G \circ \Phi)^{n+1} \circ \Phi^{-1} - 4(\mathbf{d}_G \circ \Phi)^n \circ \Phi^{-1} + (\mathbf{d}_G \circ \Phi)^{n-1} \circ \Phi^{-1}}{2\Delta t} \quad (3.40)$$

The intermediate grid velocity used in equation (3.32) is then computed in the usual way

$$\mathbf{u}_G^{n+\alpha_F} = \alpha_F \cdot \mathbf{u}_G^{n+1} + (1 - \alpha_F) \cdot (\mathbf{u}_G \circ \Phi)^n \circ \Phi^{-1}, \quad (3.41)$$

a procedure which can as well be applied to the body force term if it is available only at discrete time levels.

Convective and conservative EULERian version

For a vanishing mesh displacement $\mathbf{d}_G \equiv \mathbf{0}$, equations (3.32)–(3.36) immediately yield the time-discretised, convective form of the NAVIER-STOKES equations in EULERian description. The momentum equation is

$$\begin{aligned} \dot{\mathbf{u}}^{n+\alpha_M} + (\mathbf{u}^{n+\alpha_F} \cdot \nabla) \mathbf{u}^{n+\alpha_F} + \\ + \frac{1}{\rho} \nabla p^{n+1} - 2\nu \nabla \cdot \varepsilon(\mathbf{u}^{n+\alpha_F}) - \mathbf{b}^{n+\alpha_F} = \mathbf{0}, \end{aligned} \quad (3.42)$$

the continuity equation is identical to the ALE case (3.33). Furthermore, the intermediate quantities are defined by the following linear equations:

$$\mathbf{u}^{n+\alpha_F} = \alpha_F \cdot \mathbf{u}^{n+1} + (1 - \alpha_F) \cdot \mathbf{u}^n \quad (3.43)$$

$$\dot{\mathbf{u}}^{n+\alpha_M} = \alpha_M \cdot \dot{\mathbf{u}}^{n+1} + (1 - \alpha_M) \cdot \dot{\mathbf{u}}^n \quad (3.44)$$

$$\mathbf{u}^{n+1} = \mathbf{u}^n + (1 - \gamma) \Delta t \cdot \dot{\mathbf{u}}^n + \gamma \Delta t \cdot \dot{\mathbf{u}}^{n+1} \quad (3.45)$$

For the conservative form, equation (3.42) is simply replaced by

$$\begin{aligned} \dot{\mathbf{u}}^{n+\alpha_M} + \nabla \cdot (\mathbf{u}^{n+\alpha_F} \otimes \mathbf{u}^{n+\alpha_F}) + \\ + \frac{1}{\rho} \nabla p^{n+1} - 2\nu \nabla \cdot \varepsilon(\mathbf{u}^{n+\alpha_F}) - \mathbf{b}^{n+\alpha_F} = \mathbf{0}. \end{aligned} \quad (3.46)$$

3.2 Weak form of the semi-discrete problem

To obtain a weak, variational form of the time-discretised NAVIER-STOKES system, the boundary value problem is multiplied by appropriate test, i.e. weighting, functions. The arising weighted residual is integrated over the current computational domain, yielding a weighted residual form of the problem. A successive partial integration results in a weak form of the problem

which is the base for spatial discretisation as it will be described later. The solution of the weak equation are velocity and pressure functions for which the weak variational equation holds true for all admissible weighting functions.

Before explicit equations for the weak forms of the convective ALE and conservative EULERIAN form will be given in subsections 3.2.1 and 3.2.2, suitable spaces for weighting and solution, i.e. admissible trial functions will be defined. The reader who is not familiar with the general function spaces, their inner products and related notations used in the following definitions, is referred to appendix A.4 for a short introduction. For the velocities, the trial space \mathcal{S}_u is defined by

$$\mathcal{S}_u := \left\{ \mathbf{u} \in [\mathbf{H}^1(\Omega(t^{n+1}))]^3 \mid \mathbf{u}|_{\Gamma_D(t^{n+1})} = \mathbf{u}_D \right\}. \quad (3.47)$$

The prescribed DIRICHLET velocity in this definition cannot be chosen arbitrarily, but has to be the restriction of a function in the trace space onto the DIRICHLET part of the boundary:

$$\mathbf{u}_D(\mathbf{x}, t^{n+1}) = \mathbf{g}|_{\Gamma_D(t^{n+1})}(\mathbf{x}) \text{ for a } \mathbf{g} \in \Gamma^{-\frac{1}{2}}(t^{n+1}) \quad (3.48)$$

The velocity weighting function space \mathcal{T}_u corresponding to \mathcal{S}_u is defined as

$$\mathcal{T}_u := \left\{ \mathbf{v} \in [\mathbf{H}^1(\Omega(t^{n+1}))]^3 \mid \mathbf{v}|_{\Gamma_D(t^{n+1})} = \mathbf{0} \right\}. \quad (3.49)$$

If DIRICHLET and domain boundary are equivalent, the velocity weighting function space \mathcal{T}_u is also termed $[\mathbf{H}_0^1(\Omega(t^{n+1}))]^3$. According to equations (3.47) and (3.49), the DIRICHLET boundary conditions for velocities are directly incorporated in the formulation via the definition of trial and weighting function spaces. The definitions of weighting and trial function spaces for pressure are depending on DIRICHLET boundary conditions applied to velocities. For a not purely DIRICHLET bounded domain, i.e. $\partial\Omega(t^{n+1}) \neq \Gamma_D(t^{n+1})$, the following choices for pressure solution function space

$$\mathcal{S}_p := \mathbf{L}^2(\Omega(t^{n+1})) \quad (3.50)$$

and pressure weighting function space

$$\mathcal{T}_p := \mathbf{L}^2(\Omega(t^{n+1})) \quad (3.51)$$

are appropriate. In the special case $\partial\Omega(t^{n+1}) = \Gamma_D(t^{n+1})$, i.e. for solely DIRICHLET bounded domains, the pressure solution is defined only up to a constant, see subsection 2.1.5. One option to ensure an unique solution in this case is to set the pressure level in one point $\mathbf{x}_0 \in \Omega(t^{n+1})$ to a prescribed value p_0 using a DIRICHLET boundary condition on the pressure. This procedure requires a modification of pressure weighting and trial function spaces similar to equations (3.47) and (3.49), viz.

$$\mathcal{S}_p^{\text{mod,Dirichlet}} := \{ p \in \mathbf{L}^2(\Omega(t^{n+1})) \mid p(\mathbf{x}_0) = p_0 \} \quad (3.52)$$

$$\mathcal{T}_p^{\text{mod,Dirichlet}} := \{ q \in \mathbf{L}^2(\Omega(t^{n+1})) \mid q(\mathbf{x}_0) = 0 \}. \quad (3.53)$$

The second, preferred option to obtain a unique solution is to keep the pressure weighting function space \mathcal{T}_p and to look for a pressure solution only in the quotient space of equivalence classes

$$\mathcal{S}_p^{\text{restricted}} := \mathbf{L}^2(\Omega(t^{n+1})) / \mathbb{R}. \quad (3.54)$$

The elements of this space $\mathcal{S}_p^{\text{restricted}}$ are groups of functions which only differ by a constant. The modified solution process for this approach will be discussed in detail in appendix E. Having introduced appropriate weighting and trial spaces, weak forms will now be given for the different formulations. For ease of notation, only the case of a not purely DIRICHLET bounded domain will be depicted in the following.

3.2.1 ALE and convective EULERian formulation

First, the weak form of the ALE version of the NAVIER-STOKES equations will be presented. It is: Find $(\mathbf{u}^{n+1}, p^{n+1}) \in \mathcal{S}_u \times \mathcal{S}_p$ such that for all $(\mathbf{v}, q) \in \mathcal{T}_u \times \mathcal{T}_p$ the variational equation

$$\begin{aligned} & (\dot{\mathbf{u}}^{n+\alpha_M}; \mathbf{v})_{\Omega(t^{n+1})} + \left([((\mathbf{u}^{n+\alpha_F} - \mathbf{u}_G^{n+\alpha_F}) \cdot \nabla) \mathbf{u}^{n+\alpha_F}]; \mathbf{v} \right)_{\Omega(t^{n+1})} - \\ & - \frac{1}{\rho} (p^{n+1}, \nabla \cdot \mathbf{v})_{\Omega(t^{n+1})} + \nu (\boldsymbol{\varepsilon}(\mathbf{u}^{n+\alpha_F}) : \boldsymbol{\varepsilon}(\mathbf{v}))_{\Omega(t^{n+1})} - \\ & - (\mathbf{b}^{n+\alpha_F}; \mathbf{v})_{\Omega(t^{n+1})} + (\nabla \cdot \mathbf{u}^{n+1}, q)_{\Omega(t^{n+1})} = \frac{1}{\rho} (\mathbf{t}^{n+\alpha_F}; \mathbf{v})_{\Gamma_N(t^{n+1})} \end{aligned} \quad (3.55)$$

holds with prescribed boundary traction

$$\mathbf{t}^{n+\alpha_F} := -p^{n+1} \cdot \mathbf{n} + 2\mu \cdot \boldsymbol{\varepsilon}(\mathbf{u}^{n+\alpha_F}) \cdot \mathbf{n}. \quad (3.56)$$

The NEUMANN boundary condition term on the right hand side of equation (3.55) arises from partial integration of the viscous and the pressure term and thus is often referred to as the natural boundary condition. The intermediate quantities $\dot{\mathbf{u}}^{n+\alpha_M}$ and $\mathbf{u}^{n+\alpha_F}$ in equation (3.55) can be expanded in terms of the unknowns \mathbf{u}^{n+1} according to equations (3.34)–(3.36). Naturally, the convective EULERian version can be recovered from equation (3.55) for a vanishing mesh displacement (2.11).

3.2.2 Conservative EULERian version

For the weak form of the conservative EULERian equation, the nonlinear convective term can be partially integrated as well. Thus the weak problem is to find velocity and pressure solutions $(\mathbf{u}^{n+1}, p^{n+1}) \in \mathcal{S}_u \times \mathcal{S}_p$ such that for all $(\mathbf{v}, q) \in \mathcal{T}_u \times \mathcal{T}_p$ the variational equation

$$\begin{aligned} & (\dot{\mathbf{u}}^{n+\alpha_M}; \mathbf{v})_{\Omega(t^{n+1})} - (\mathbf{u}^{n+\alpha_F}; [(\mathbf{u}^{n+\alpha_F} \cdot \nabla) \mathbf{v}])_{\Omega(t^{n+1})} - \\ & - \frac{1}{\rho} (p^{n+1}, \nabla \cdot \mathbf{v})_{\Omega(t^{n+1})} + \nu (\boldsymbol{\varepsilon}(\mathbf{u}^{n+\alpha_F}) : \boldsymbol{\varepsilon}(\mathbf{v}))_{\Omega(t^{n+1})} - \\ & - (\mathbf{b}^{n+\alpha_F}; \mathbf{v})_{\Omega(t^{n+1})} + (\nabla \cdot \mathbf{u}^{n+1}, q)_{\Omega(t^{n+1})} = \\ & = \frac{1}{\rho} (\mathbf{t}^{n+\alpha_F}; \mathbf{v})_{\Gamma_N(t^{n+1})} - ((\mathbf{u}^{n+\alpha_F} \cdot \mathbf{n}), (\mathbf{u}^{n+\alpha_F} \cdot \mathbf{v}))_{\Gamma_N(t^{n+1})} \end{aligned} \quad (3.57)$$

holds.

The boundary term $-((\mathbf{u}^{n+\alpha_F} \cdot \mathbf{n}), (\mathbf{u}^{n+\alpha_F} \cdot \mathbf{v}))_{\Gamma_N(t^{n+1})}$ is generated by partial integration of the convective term and has to be taken into account if a conservative form is used in combination with a NEUMANN boundary. Again, the intermediate quantities $\dot{\mathbf{u}}^{n+\alpha_M}$, $\mathbf{u}^{n+\alpha_F}$ are related to the unknown velocity \mathbf{u}^{n+1} as prescribed by the time integration in equations (3.43)–(3.45).

3.2.3 Abstract notation

Both formulations (3.55) and (3.57) can be written in the generic form

$$B(\mathbf{u}^{n+1}, \mathbf{v}) - G(p^{n+1}, \mathbf{v}) + D(\mathbf{u}^{n+1}, q) - F(\mathbf{v}) = 0. \quad (3.58)$$

The linear contributions of pressure

$$G(p^{n+1}, \mathbf{v}) = \frac{1}{\rho} (p^{n+1}, \nabla \cdot \mathbf{v})_{\Omega(t^{n+1})} \quad (3.59)$$

and continuity

$$D(\mathbf{u}^{n+1}, q) = (\nabla \cdot \mathbf{u}^{n+1}, q)_{\Omega(t^{n+1})} \quad (3.60)$$

are explicitly separated from the rest of the equation. $B(\mathbf{u}^{n+1}, \mathbf{v})$ is defined such that each of its contributions depends at least linearly on the unknown velocity. Since it contains contributions from the convective term, it is obviously nonlinear in the new velocities. The linear form $F(\mathbf{v})$ contains surface traction and body force effects as well as contributions from previous time steps.

3.3 Geometry approximation

The weak form (3.58) is based on integrals over the current domain which have to be evaluated numerically. For this purpose, a discretised representation of the domain is required. The approximation of the solution will take place on the discrete representation. Consequently, a good approximation of the geometry is a prerequisite for a proper approximation of the solution.

This section has two main purposes. Firstly, a brief introduction into non-uniform rational B-splines (NURBS) as a tool for geometric design will be given in subsection 3.3.1. Secondly, two methods to acquire an analysis-suitable finite element model from a geometry will be described in subsection 3.3.2. The first approach described in that subsection is the standard finite element method using a LAGRANGEan element domain representation. The second approach presented is the isogeometric finite element method proposed by HUGHES et al. [117]. In this approach, the description of the geometry in the computation is based on a NURBS representation, allowing among other things an exact, smooth representation of many realistic designs. The isogeometric finite element method is not the only technique capable of an exact representation of computer aided design (CAD) geometries in a finite element framework. Another option that should be mentioned here is the NURBS enhanced finite element method by SEVILLA et al. [189], which uses enhanced elements only next to curved boundaries.

For further motivation, a list of classes of problems for which the quality of the solution is particularly influenced by the approximation of the domain boundaries will be given in the following. The first class are problems in fluid mechanics involving curved boundaries. For these applications, the necessity of an appropriate boundary representation has been pointed out for instance in ESKILSSON and SHERWIN [70], KRIVODONOVA and BERGER [147] and BASSI and REBAY [9]. Additionally, when considering turbulent flows and fluid-structure interaction, it becomes obvious that a proper representation of the boundary should be provided for these problems as well. The second class are problems involving sliding contact surfaces. For these problems, an improved performance can be obtained utilising smooth discretisations of contact

surfaces using HERMITE or BÉZIER splines. See for instance the book by WRIGGERS [224]. Another class are sliding mesh applications for the simulation of fluid flow around rotating bodies as they are presented in BAZILEVS and HUGHES [20]. In this type of application, the exact circular shape of the domain boundary provided by a NURBS approximation is exploited.

3.3.1 Introduction to NURBS

In classical engineering applications, geometries are often generated by computer aided design using NURBS representations. This subsection summarises properties of NURBS, which are required for a basic understanding and that will be used later on for the isogeometric finite element implementation. Fundamentals on NURBS are well documented in literature, for instance in the textbooks by PIEGL and TILLER [173], ROGERS [182] or FARIN [74].

B-spline polynomials

In the following, the construction of l B-spline polynomials of order p corresponding to a knot vector

$$\mathbf{u} = (u_1, u_2, \dots, u_{l+p+1}) \quad (3.61)$$

will be explained. In equation (3.61) $u_i \in \mathbb{R}$ is the i^{th} knot value and $u_i \leq u_{i+1}$. The interval $[u_i; u_{i+1}]$ will be referred to as the i^{th} knot span of the knot vector. The knot vector is called uniform if all knot values are equally spaced, otherwise it is called non-uniform. Multiples of knot values are possible. Knot vectors are termed open if the first and last knot is repeated $p + 1$ times. Furthermore, they are termed periodic if

$$u_{i+1} - u_i = u_{l+i+1} - u_{l+i} \text{ for } i = 1, \dots, p. \quad (3.62)$$

B-spline polynomials of degree p are defined by recursion over the degree. The recursion is initialised by piecewise constant functions for the degree 0.

$$B_i^0(u) := \begin{cases} 1 & \text{if } u_i \leq u < u_{i+1} \\ 0 & \text{otherwise} \end{cases} \quad (3.63)$$

The desired B-spline polynomials are then obtained using the COX-DE BOOR-MANSFIELD recursion formula

$$B_i^d(u) := \frac{u - u_i}{u_{i+d} - u_i} \cdot B_i^{d-1}(u) + \frac{u_{i+d+1} - u}{u_{i+d+1} - u_{i+1}} \cdot B_{i+1}^{d-1}(u), \quad d = 1, \dots, p. \quad (3.64)$$

The recursion can be represented by a truncated triangle table, see Figure 3.3 for an example with quadratic B-splines defined on the open knot vector

$$\mathbf{u} = (0.0, 0.0, 0.0, 0.3, 0.6, 0.9, 1.4, 1.7, 2.0, 2.0, 2.0). \quad (3.65)$$

The B-splines corresponding to the triangle table are visualised in Figure 3.4.

This figure also exemplifies several important properties of B-splines. The basis functions are nonnegative and they constitute a partition of unity, i.e.

$$\sum_{i=1}^l B_i^p \equiv 1. \quad (3.66)$$

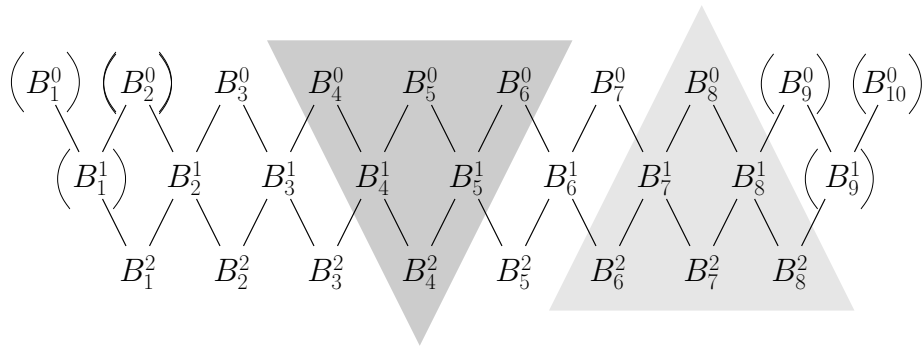


Figure 3.3: Truncated triangle table for the computation of the B-spline basis functions shown in Figure 3.4. The light grey triangle marks all nonvanishing basis functions on knot span eight. The darker grey triangle illustrates that the support of the fourth basis function comprises knot spans four to six.

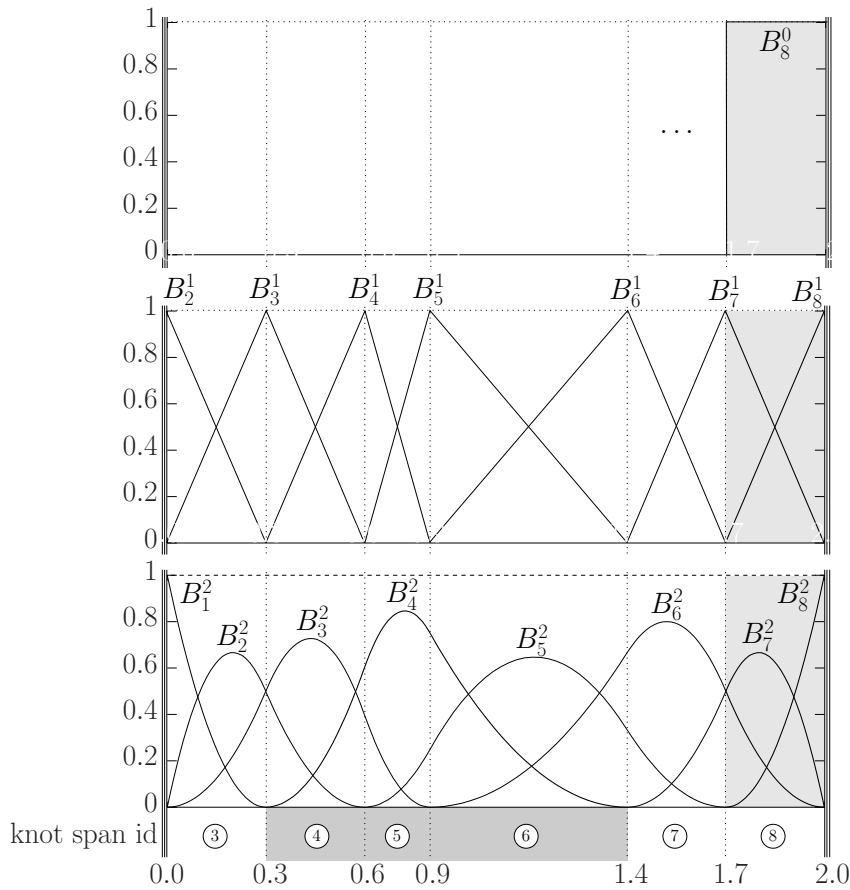


Figure 3.4: B-spline basis functions corresponding to the truncated triangle table in Figure 3.3. The light grey colour highlights the nonzero basis functions on knot span eight, the darker grey colour indicates the support of basis function number four.

Furthermore, each basis function B_i^p has compact support $[u_i, u_{i+p+1}]$. For open knot vectors, the first basis function equals one at $u_1 = \dots = u_{p+1}$ and the last basis function equals one at $u_{l+1} = \dots = u_{l+p+1}$. In the interior of $[u_1, u_{l+p+1}]$, a basis function B_i^p equals one only at a p times repeated knot. For repeated knots, some basis functions required in recursion formula (3.64) may not be well defined since their support vanishes. In the example of Figure 3.3, this is the case for all basis functions in brackets. In this case, the respective basis functions will not be computed. For the computation of basis functions which require the value of an undefined basis function, the summand in equation (3.64) corresponding to the undefined function is set to zero.

B-splines exhibit certain smoothness properties. In the interior of a knot span, continuous derivatives of arbitrary order exist. At the position of knots of multiplicity m , B-spline basis functions with adjacent support are $(p - m)$ times continuously differentiable. The first derivatives of B-spline polynomials of order p can be computed as a linear combination of B-spline polynomials of order $(p - 1)$:

$$\frac{d}{du} B_i^p(u) = \frac{p}{u_{i+p} - u_i} \cdot B_i^{p-1}(u) - \frac{p}{u_{i+p+1} - u_{i+1}} \cdot B_{i+1}^{p-1}(u) \quad (3.67)$$

Furthermore, higher order derivatives are computable as linear combinations of lower order derivatives of basis polynomials of lower degree:

$$\frac{d^k}{du^k} B_i^d(u) = \frac{d}{u_{i+d} - u_i} \cdot \frac{d^{k-1}}{du^{k-1}} B_i^{d-1}(u) - \frac{d}{u_{i+d+1} - u_{i+1}} \cdot \frac{d^{k-1}}{du^{k-1}} B_{i+1}^{d-1}(u) \quad (3.68)$$

Of special interest for the application of B-splines in finite elements is an algorithm which computes all values and derivatives of nonzero B-spline polynomials at a given point, corresponding to the light grey triangle in the truncated triangle table in Figure 3.3. Among a collection of other efficient algorithms, such an algorithm which is also avoiding divisions by zero can be found in PIEGL and TILLER [173].

B-spline curves, surfaces, volumes

B-spline polynomials can be used to construct B-spline curves as linear combinations of l control points $\mathbf{X}_i^B \in \mathbb{R}^n$:

$$\mathbf{C}^{\text{B-spline}}(u) := \sum_{i=1}^l B_i^p(u) \cdot \mathbf{X}_i^B \quad (3.69)$$

Linear interpolation of these control points defines the control polygon of the curve. In contrast to the control polygon, B-spline curves do not necessarily interpolate the control points.

A generalisation to B-spline surfaces and volumes is straightforward. B-spline surfaces are defined on the CARTESIAN product space of two knot vectors

$$\mathbf{u} = (u_1, u_2, \dots, u_{l_u+p_u+1}), \quad \mathbf{v} = (v_1, v_2, \dots, v_{l_v+p_v+1}) \quad (3.70)$$

using a control net of $l_u \cdot l_v$ control points $\mathbf{X}_{i,j}^B \in \mathbb{R}^n$:

$$\mathbf{S}^{\text{B-spline}}(u, v) := \sum_{i=1}^{l_u} \sum_{j=1}^{l_v} B_i^{p_u}(u) \cdot B_j^{p_v}(v) \cdot \mathbf{X}_{i,j}^B \quad (3.71)$$

As indicated in equation (3.71), the combined basis functions $B_i^{p_u} \cdot B_j^{p_v}$ can be constructed from one-dimensional basis functions of different degree. Nevertheless, for ease of notation, it will be assumed that all basis functions involved are of the same degree, i.e. $p_u = p_v = p$. Finally, B-spline volumes are defined on the CARTESIAN product of three knot vectors

$$\mathbf{u} = (u_1, \dots, u_{l_u+p+1}), \quad \mathbf{v} = (v_1, \dots, v_{l_v+p+1}), \quad \mathbf{w} = (w_1, \dots, w_{l_w+p+1}) \quad (3.72)$$

and a control net of $l_u \cdot l_v \cdot l_w$ control points $\mathbf{X}_{i,j,k}^B \in \mathbb{R}^n$:

$$\mathbf{V}^{\text{B-spline}}(u, v, w) := \sum_{i=1}^{l_u} \sum_{j=1}^{l_v} \sum_{k=1}^{l_w} B_i^p(u) \cdot B_j^p(v) \cdot B_k^p(w) \cdot \mathbf{X}_{i,j,k}^B \quad (3.73)$$

For implementation purposes, it should be kept in mind that the computation of a sum as in equation (3.73) on knot span $(i+p, j+p, k+p)$ actually involves only $(p+1)^3$ nonzero summands. These nonzero summands are the ones with numbers

$$(i + \mathcal{I} - 1, j + \mathcal{J} - 1, k + \mathcal{K} - 1) \\ \mathcal{I} = 1, \dots, p+1, \quad \mathcal{J} = 1, \dots, p+1, \quad \mathcal{K} = 1, \dots, p+1. \quad (3.74)$$

For B-spline curves, surfaces and volumes it is possible to perform knot insertion and degree elevation without a modification of their geometrical and parametrical representation. The reader is referred to appendix B.1 or the book by PIEGL and TILLER [173] for more information.

NURBS curves, surfaces, volumes and basis functions

Many geometric entities cannot be represented exactly using piecewise polynomial interpolation. Nevertheless, conic sections such as circles or ellipses can be recovered by projective transformation of B-spline curves. In order to obtain a projected B-spline curve in n -dimensional space, a generating B-spline curve has to be provided in $(n+1)$ -dimensional space.

Let $\mathbf{C}^{\text{B-spline}}$ be a generic B-spline curve in $n+1$ -dimensional space described by

$$\mathbf{C}^{\text{B-spline}}(u) = \sum_{i=1}^l \left(B_i^p(u) \cdot \begin{bmatrix} (\mathbf{X}_i^B)_1 \\ \vdots \\ (\mathbf{X}_i^B)_n \\ \hline \omega_i \end{bmatrix} \right). \quad (3.75)$$

The notation ω_i for the last component of \mathbf{X}_i^B already emphasises that this entry will be associated with the weight of the corresponding control point of the generated NURBS curve. The projected curve is obtained by scaling with the inverse of the last component:

$$\mathbf{C}^{\text{projected B-spline}}(u) = \sum_{i=1}^l \frac{B_i^p(u)}{\sum_{j=1}^l B_j^p(u) \cdot \omega_j} \cdot \begin{bmatrix} (\mathbf{X}_i^B)_1 \\ \vdots \\ (\mathbf{X}_i^B)_n \\ \hline 1 \end{bmatrix} \quad (3.76)$$

The first n components of the projected curve constitute the NURBS curve:

$$\mathbf{C}^{\text{NURBS}}(u) = \sum_{i=1}^l N_i^p(u) \cdot \mathbf{X}_i \quad (3.77)$$

with rational NURBS basis functions

$$N_i^p(u) = \frac{\omega_i \cdot B_i^p(u)}{\sum_{j=1}^l \omega_j \cdot B_j^p(u)} \quad (3.78)$$

and NURBS control points

$$\mathbf{X}_i := \frac{\mathbf{X}_i^{\text{B}}}{\omega_i}. \quad (3.79)$$

For a geometric interpretation of this definition as a cone section and the example of a B-spline curve generating a circle segment, the reader is referred to appendix B.2.

A generalisation to surfaces and volumes based on tensor products of B-spline basis functions is straightforward. For example NURBS volumes can be defined using the B-spline basis polynomials from equation (3.73) by

$$\mathbf{V}^{\text{NURBS}}(u, v, w) = \sum_{i=1}^{l_u} \sum_{j=1}^{l_v} \sum_{k=1}^{l_w} N_{i,j,k}^p(u, v, w) \cdot \mathbf{X}_{i,j,k}. \quad (3.80)$$

The rational NURBS basis functions in this equation are defined as follows:

$$N_{i,j,k}^p(u, v, w) := \frac{\omega_{i,j,k} \cdot B_{i,j,k}^p(u, v, w)}{\sum_{r=1}^{l_u} \sum_{s=1}^{l_v} \sum_{t=1}^{l_w} \omega_{r,s,t} \cdot B_{r,s,t}^p(u, v, w)} \quad (3.81)$$

NURBS basis functions inherit many important properties from B-spline polynomials. They, too, constitute a partition of unity, they have the same compact support, they are guaranteed to equal one in places where the corresponding B-spline polynomials equal one. Furthermore, they inherit the smoothness properties of B-splines. Derivatives of NURBS basis functions can be derived from B-splines derivatives by application of the chain rule. For instance for a NURBS volume, the resulting formula for the first derivatives in direction α , where α can be u , v or w , reads

$$\frac{\partial N_{i,j,k}^p}{\partial \alpha} = \frac{\omega_{i,j,k}}{\sum_{r,s,t} \omega_{r,s,t} \cdot B_{r,s,t}^p} \left[\frac{\partial B_{i,j,k}^p}{\partial \alpha} - \frac{B_{i,j,k}^p \cdot \left(\sum_{r,s,t} \omega_{r,s,t} \cdot \frac{\partial B_{r,s,t}^p}{\partial \alpha} \right)}{\sum_{r,s,t} \omega_{r,s,t} \cdot B_{r,s,t}^p} \right]. \quad (3.82)$$

The formula for the second derivatives in directions (β, α) , with β as well equal to u , v or w , can be computed as

$$\frac{\partial^2 N_{i,j,k}^p}{\partial \beta \partial \alpha} = \frac{\omega_{i,j,k}}{\sum_{r,s,t} \omega_{r,s,t} \cdot B_{r,s,t}^p} \cdot \left[\frac{\partial^2 B_{i,j,k}^p}{\partial \beta \partial \alpha} - \square_1 - \square_2 - \square_3 + \square_4 \right] \quad (3.83)$$

with

$$\square_1 = \frac{\frac{\partial B_{i,j,k}^p}{\partial \alpha} \cdot \left(\sum_{r,s,t} \omega_{r,s,t} \cdot \frac{\partial B_{r,s,t}^p}{\partial \beta} \right)}{\left(\sum_{r,s,t} \omega_{r,s,t} \cdot B_{r,s,t}^p \right)}, \quad (3.84)$$

$$\square_2 = \frac{\frac{\partial B_{i,j,k}^p}{\partial \beta} \cdot \left(\sum_{r,s,t} \omega_{r,s,t} \cdot \frac{\partial B_{r,s,t}^p}{\partial \alpha} \right)}{\left(\sum_{r,s,t} \omega_{r,s,t} \cdot B_{r,s,t}^p \right)}, \quad (3.85)$$

$$\square_3 = \frac{B_{i,j,k}^p \cdot \left(\sum_{r,s,t} \omega_{r,s,t} \cdot \frac{\partial^2 B_{r,s,t}^p}{\partial \beta \partial \alpha} \right)}{\left(\sum_{r,s,t} \omega_{r,s,t} \cdot B_{r,s,t}^p \right)}, \quad (3.86)$$

$$\square_4 = \frac{2 \cdot B_I^p \cdot \left(\sum_{r,s,t} \omega_{r,s,t} \cdot \frac{\partial B_{r,s,t}^p}{\partial \alpha} \right) \cdot \left(\sum_{r,s,t} \omega_{r,s,t} \cdot \frac{\partial B_{r,s,t}^p}{\partial \beta} \right)}{\left(\sum_{r,s,t} \omega_{r,s,t} \cdot B_{r,s,t}^p \right)^2}. \quad (3.87)$$

The partial derivatives of B-spline basis functions in equations (3.82)-(3.87) are computed using the product rule and the derivatives of B-spline polynomials from equations (3.67) and (3.68). For a triple index i, j, k , these derivatives are

$$\begin{aligned} \frac{\partial B_{i,j,k}^p}{\partial u}(u, v, w) &= \frac{\partial B_i^p}{\partial u}(u) \cdot B_j^p(v) \cdot B_k^p(w), \\ \frac{\partial^2 B_{i,j,k}^p}{\partial u^2}(u, v, w) &= \frac{\partial^2 B_i^p}{\partial u^2}(u) \cdot B_j^p(v) \cdot B_k^p(w), \\ \frac{\partial^2 B_{i,j,k}^p}{\partial u \partial v}(u, v, w) &= \frac{\partial B_i^p}{\partial u}(u) \cdot \frac{\partial B_j^p}{\partial v}(v) \cdot B_k^p(w), \dots \end{aligned} \quad (3.88)$$

Patches

For more complex geometries, a description using a single NURBS curve, surface or volume is not possible. This shortcoming can be overcome in many practical cases by a subdivision of the geometry into a set of patches. These patches are designed such that they can be described by a single NURBS entity. Each patch is associated with one CARTESIAN product of knot vectors. Thus, using the mapping defined by the NURBS entity, each patch is topologically equivalent to a CARTESIAN product of knot vectors. In most applications, the knot vectors are chosen to be open. In this case the surfaces and lines on the patch boundary will represent NURBS entities themselves. As can be seen from the example in Figure 3.5, the patches may share control points.

3.3.2 Finite element geometry representation

For finite element approaches, the computational domain in three-dimensional space is partitioned into a set of nonoverlapping subdomains Ω_e , the so-called computational element domains:

$$\Omega(t^{n+1}) = \bigcup_{\text{elements } e} \Omega_e \quad (3.89)$$

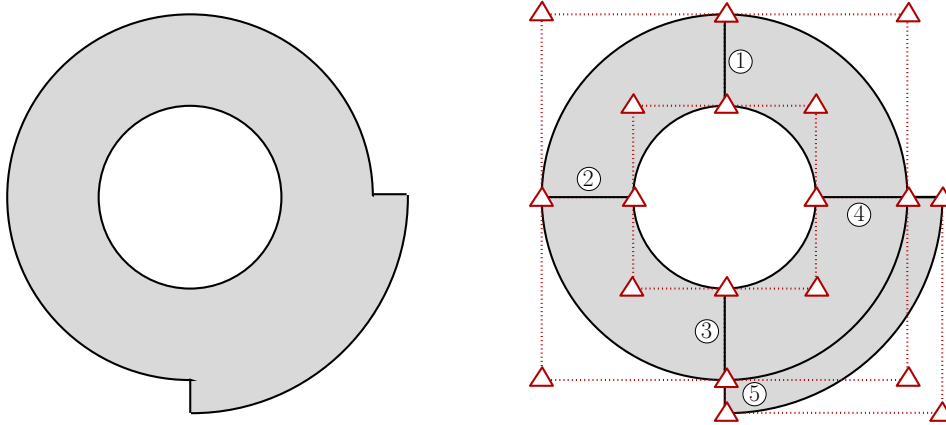


Figure 3.5: The design geometry on the left can be represented by 5 NURBS patches as shown on the right. Patches 1 to 4 can equivalently be represented in one patch using a knot vector which allows interpolation in the patch interior, i.e. which has multiple knots.

They are chosen such that they can be mapped to a simple standard element geometry, for instance the normalised cube $[-1; 1]^3$, via a mapping

$$\chi_e : [-1; 1]^3 \rightarrow \Omega_e, \quad (\xi_1, \xi_2, \xi_3) \mapsto \chi_e(\xi_1, \xi_2, \xi_3). \quad (3.90)$$

All numerical integration in equation (3.58) will be performed by quadrature on the reference element, for example by GAUSS-quadrature. One of the key features of the finite element concept is that the complete spatial representation is defined using a finite number n_{np} of point coordinates $\mathbf{x}_i^{h,n+1}$ and corresponding basis functions $N_\iota(\mathbf{x})$. The basis functions are chosen as continuous functions with local support restricted to a small number of neighbouring elements. Only a small amount n_{np}^e of basis functions are nonzero on an arbitrary element e . The nonzero basis functions on element e are defined such that they can be evaluated on the reference element using element shape functions $S_I^e(\xi_1, \xi_2, \xi_3)$:

$$N_{\text{ien}(e,I)}(\chi_e(\xi_1, \xi_2, \xi_3)) = S_I^e(\xi_1, \xi_2, \xi_3), \quad I = 1, \dots, n_{\text{np}}^e \quad (3.91)$$

Here, $\text{ien}(e, I)$ is the mapping from the element local number of the basis function to the associated global index ι of the basis function. Using these basis functions, the mapping to the computational element domain (3.90) can be written as

$$\begin{aligned} \chi_e(\xi_1, \xi_2, \xi_3) &= \sum_{I=1}^{n_{\text{np}}^e} N_{\text{ien}(e,I)}(\chi_e(\xi_1, \xi_2, \xi_3)) \cdot \mathbf{x}_{\text{ien}(e,I)}^{h,n+1} = \\ &= \sum_{I=1}^{n_{\text{np}}^e} S_I^e(\xi_1, \xi_2, \xi_3) \cdot \mathbf{x}_{\text{ien}(e,I)}^{h,n+1}. \end{aligned} \quad (3.92)$$

In moving mesh applications, the current coordinate has to be continuously updated by the mesh displacement $\underline{\mathbf{d}}_G^{h,n+1}$, viz.

$$\underline{\mathbf{x}}^{h,n+1} = \underline{\mathbf{x}}_0^h + \underline{\mathbf{d}}_G^{h,n+1}. \quad (3.93)$$

The underbar indicates that the vectors in equation (3.93) contain all coordinate vectors from all points. The restriction of the geometry representation to a finite dimensional basis representation naturally limits the amount of geometries which can be represented exactly. In the rest of this subsection, several possible choices for shape functions will be presented. These are based on LAGRANGEan, serendipity or isogeometric formulations. This selection of shape functions is not complete. There are other concepts like hierarchical basis functions, see for instance ZIENKIEWICZ and TAYLOR [225] or WHITING and JANSEN [221], but these approaches will not be considered in this thesis.

LAGRANGEan and serendipity approaches

For LAGRANGEan approaches, the element shape functions are chosen to be LAGRANGEan basis polynomials. They equal one in exactly one node position and are zero in all other node positions on the element. Therefore, the arising continuous global basis functions define an interpolatory set of nodal basis functions. Figure 3.6 exemplifies the relation between the point coordinates in the global system and the corresponding node positions on the reference element. In LAGRANGEan approaches, the point coordinates correspond to real physical positions inside the computational domain and are identified with the nodes of the discretisation. Serendipity elements are similar to higher order LAGRANGEan elements without inner nodes. For information on these standard element types, the reader is referred to the textbook by ZIENKIEWICZ

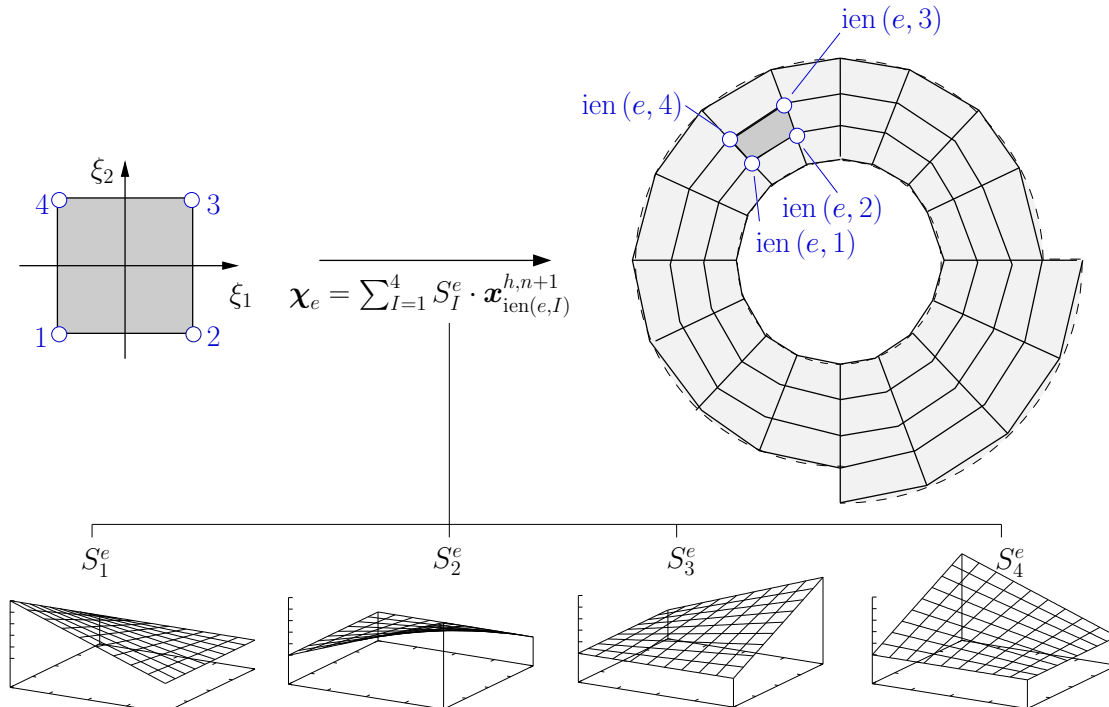


Figure 3.6: Two-dimensional example for a LAGRANGEan geometry representation using bilinear shape functions on a four-noded element.

and TAYLOR [225], which provides explicit formulas for the shape functions $S_I^e(\xi_1, \xi_2, \xi_3)$ of various types of hexahedral and tetrahedral elements.

LAGRANGEan geometry representation will always lead to polynomially bounded domains, i.e. the representation of cylindrical shapes will not be exact. The quality of the approximation can be improved by h -refinement, i.e. by using a larger number of smaller elements to represent the geometry, or by p -refinement, i.e. by the use of higher order shape functions which allow a curved boundary approximation. Nevertheless, curved boundaries will not be smoothly represented and maintain a ‘facet’ structure with kinks between elements.

Isogeometric geometry representation

Isogeometric analysis uses the same set of functions for design and analysis, i.e. NURBS as a basis for finite element analysis. Elements for the isogeometric approach are identified with element knot spans, see the sketch in Figure 3.7. Let e be the element associated with element knot span $[u_{p+i}; u_{p+i+1}] \times [v_{p+j}; v_{p+j+1}] \times [w_{p+k}; w_{p+k+1}]$ of patch n_{patch} . If the element knot span has a nonzero volume, i.e. no repeated knots, then it is connected to the reference element by an affine transformation

$$\begin{pmatrix} u(\xi_1) \\ v(\xi_2) \\ w(\xi_3) \end{pmatrix} = \begin{pmatrix} u_{p+i} \\ v_{p+j} \\ w_{p+k} \end{pmatrix} + \begin{pmatrix} \xi_1 \cdot (u_{p+i+1} - u_{p+i}) \\ \xi_2 \cdot (v_{p+j+1} - v_{p+j}) \\ \xi_3 \cdot (w_{p+k+1} - w_{p+k}) \end{pmatrix}. \quad (3.94)$$

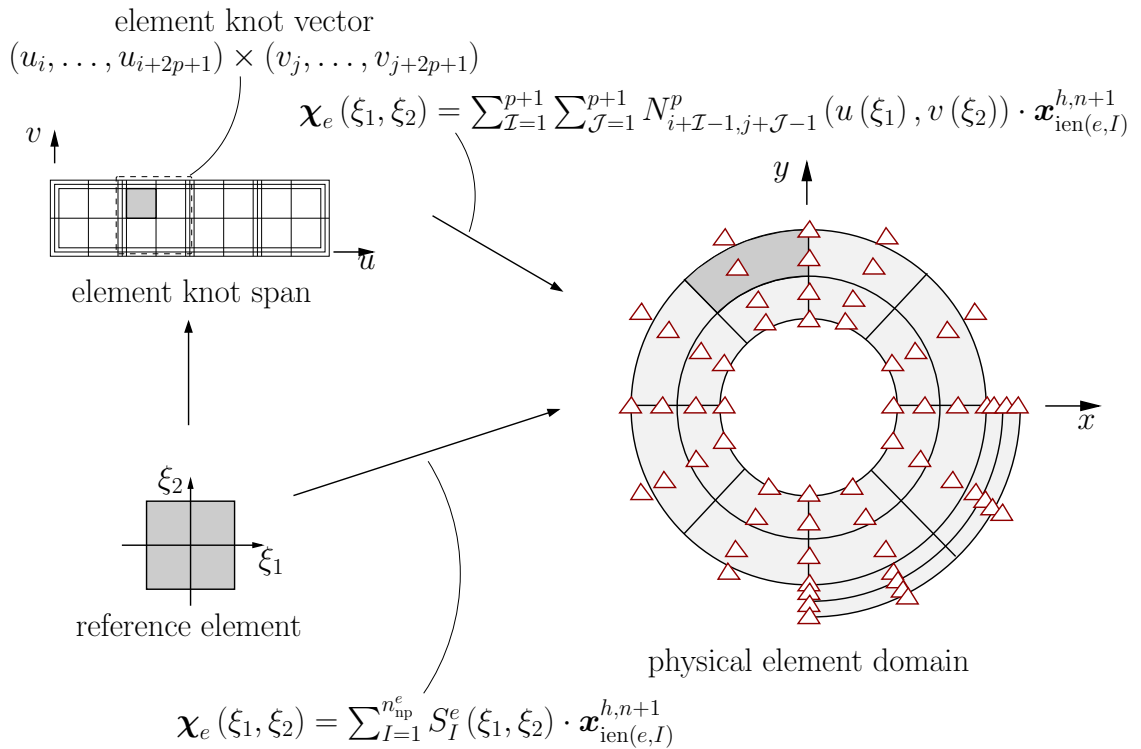


Figure 3.7: Two-dimensional example for an isogeometric geometry representation using quadratic NURBS shape functions.

Based on this mapping, isogeometric shape functions can be defined as the pull-back of NURBS basis functions to the reference element. The $n_{\text{np}}^e = (p+1)^3$ element shape functions with element-local indices

$$\begin{aligned} I &:= \mathcal{I} + (p+1) \cdot (\mathcal{J} - 1) \cdot (1 + (p+1) \cdot (\mathcal{K} - 1)), \\ \mathcal{I} &= 1, \dots, p+1, \quad \mathcal{J} = 1, \dots, p+1, \quad \mathcal{K} = 1, \dots, p+1 \end{aligned} \quad (3.95)$$

are thus defined by

$$S_I^e(\xi_1, \xi_2, \xi_3) := N_{i+\mathcal{I}-1, j+\mathcal{J}-1, k+\mathcal{K}-1}^p(u(\xi_1), v(\xi_2), w(\xi_3)). \quad (3.96)$$

The recursive evaluation of the element shape functions requires all knot values collected in the element knot vector

$$(u_i, \dots, u_{i+2p+1}) \times (v_j, \dots, v_{j+2p+1}) \times (w_k, \dots, w_{k+2p+1}). \quad (3.97)$$

The number of possible element knot vectors and thus elements in a patch is $(l_u - p) \cdot (l_v - p) \cdot (l_w - p)$. In case of repeated knots, some of these elements will actually be of size zero. Nevertheless, they are likely to be kept in a practical implementation, since they allow a convenient CARTESIAN numbering of the elements:

$$\begin{aligned} e &\longleftrightarrow (i, j, k, n_{\text{patch}}) \\ e &= \text{offset}(n_{\text{patch}}) + i + (l_u - p) \cdot (j - 1) \cdot (1 + (l_v - p) \cdot (k - 1)) \end{aligned} \quad (3.98)$$

e is the unique element index, i, j, k the corresponding patch-local CARTESIAN index in patch n_{patch} . The value $\text{offset}(n_{\text{patch}})$ corresponds to the number of elements contained in patches with an index smaller than n_{patch} . For integration, elements with size zero will simply be skipped.

For isogeometric elements, the point coordinates correspond to the control points of the geometrical design. In general, they can be located outside the physical domain and they do not have a corresponding location on the reference element like nodes in the LAGRANGEAN approach. Furthermore, control points store an additional weight value in comparison to nodes. Derivatives of the shape functions with respect to the reference element can be computed from the derivatives on the element knot span (3.82), (3.83) and the JACOBIAN of transformation (3.94). In contrast to the LAGRANGEAN approach, the shape functions in the isogeometric approach are not only specific to the element type but rather specific to individual elements, i.e. they are defined by the element's knot vector and weights of its control points.

The representation of the geometry using a NURBS basis is exact for NURBS-based CAD geometries. Nevertheless, a refinement of the approximation may be required since the same functions that represent the geometry will be used to represent the solution later on. NURBS provide refinement strategies that allow h -refinement by knot insertion as well as p -refinement by order elevation without changing the represented domain. A local refinement seems also possible using multiple patches, see KAGAN, FISCHER and BAR-YOSEPH [138] for a discussion in the context of B-spline-based finite elements.

3.4 Spatial approximation of the solution

Having an appropriate geometry representation at hand, a spatially discretised version of the weak form (3.58) can be deduced by a finite element approximation. In this section, the isoparametric concept for LAGRANGEAN and isogeometric finite elements will be presented. The

GALERKIN approximation including its shortcomings for equal order interpolation and convection dominated problems will be introduced. A discussion of several well-known stabilisation techniques to overcome these problems will follow in the next section.

3.4.1 Restriction to finite dimensional subspaces

The approximation of the solution of the weak problem in every time step is primarily achieved by a restriction of weighting and trial function spaces to finite dimensional subspaces. The resulting variational problem,

$$\begin{aligned} R_{\mathbf{u}}(\mathbf{u}^{h,n+1}, p^{h,n+1}, \mathbf{v}^h) &= 0 \\ R_p(\mathbf{u}^{h,n+1}, p^{h,n+1}, q^h) &= 0, \end{aligned} \quad (3.99)$$

is then solved on these subspaces in form of a nonlinear equation. The finite dimensional subspaces are labelled by an index h :

$$\begin{aligned} \mathcal{S}_{\mathbf{u}}^h \times \mathcal{S}_p^h &\subset \mathcal{S}_{\mathbf{u}} \times \mathcal{S}_p \\ \mathcal{T}_{\mathbf{u}}^h \times \mathcal{T}_p^h &\subset \mathcal{T}_{\mathbf{u}} \times \mathcal{T}_p \end{aligned} \quad (3.100)$$

Accordingly, the members of these spaces are characterised by the same label.

For the moment, a simple GALERKIN approach

$$\begin{aligned} R_{\mathbf{u}}(\mathbf{u}^{h,n+1}, p^{h,n+1}, \mathbf{v}^h) &= B(\mathbf{u}^{h,n+1}, \mathbf{v}^h) - G(p^{h,n+1}, \mathbf{v}^h) - F(\mathbf{v}^h) \\ R_p(\mathbf{u}^{h,n+1}, p^{h,n+1}, q^h) &= D(\mathbf{u}^{h,n+1}, q^h) \end{aligned} \quad (3.101)$$

is assumed. Later on, $R_{\mathbf{u}}(\mathbf{u}^{h,n+1}, p^{h,n+1}, \mathbf{v}^h)$ and $R_p(\mathbf{u}^{h,n+1}, p^{h,n+1}, q^h)$ will be extended in the discussion of stabilised methods and residual-based variational multiscale approaches. In order to avoid an unnecessary repetition of the general solution procedure for these more general cases, the dependency of $R_p(\mathbf{u}^{h,n+1}, p^{h,n+1}, q^h)$ on $p^{h,n+1}$ is already included at this point. For the rest of this section, the geometry is considered to be represented exactly and all integrals are assumed to be evaluated exactly. As we have seen in section 3.3, this is in general not the case for finite elements. Nevertheless, this simplification does not affect the following basic explanations, so it is kept here for ease of notation.

3.4.2 Isoparametric concept, basis representations and degrees of freedom

The choice of finite dimensional subspaces in equation (3.100) will be done according to the isoparametric concept. This means that finite dimensional trial function spaces will be chosen such that their members can be expressed using the same basis functions $N_\ell(\mathbf{x})$ that have been used to represent the geometry in equation (3.92).

The basis representation for a member of the velocity trial function space reads

$$\mathbf{u}^{h,n+1}(\mathbf{x}) = \sum_{\iota=1}^{n_{\text{np}}} \left(\sum_{j=1}^3 \mathbf{e}_j \cdot N_\iota(\mathbf{x}) \cdot u_{\iota,j}^{h,n+1} \right). \quad (3.102)$$

e_j is the unit vector in direction j , a three-dimensional physical space is assumed. Using an unique index for the velocity degree of freedom,

$$\delta := 3 \cdot (\iota - 1) + j, \quad (3.103)$$

a basis function for the representation of the velocity solution can be defined. It will be denoted by

$$\mathbf{N}_{\delta}^{\mathcal{S}_u^h}(\mathbf{x}) := e_j \cdot N_{\iota}(\mathbf{x}) \quad (3.104)$$

and $u_{\delta}^{h,n+1} := u_{\iota,j}^{h,n+1}$ is the corresponding value of the velocity degree of freedom. Without loss of generality, it can be assumed that all basis functions are numbered such that basis functions which are zero on DIRICHLET boundaries have numbers $1, \dots, n_u^{\text{dof}}$. The number of non-DIRICHLET velocity degrees of freedom, n_u^{dof} , corresponds to the dimension of the finite dimensional subspace of velocity trial functions \mathcal{S}_u^h . Accordingly, basis functions which are nonzero on DIRICHLET boundaries have numbers $n_u^{\text{dof}} + 1, \dots, \bar{n}_u^{\text{dof}} = 3 \cdot n_{\text{np}}$. The corresponding functions are used to incorporate the DIRICHLET condition in the basis representation, viz.

$$\mathbf{u}^{h,n+1}(\mathbf{x}) = \sum_{\delta=1}^{n_u^{\text{dof}}} \mathbf{N}_{\delta}^{\mathcal{S}_u^h}(\mathbf{x}) \cdot u_{\delta}^{h,n+1} + \underbrace{\sum_{\delta=n_u^{\text{dof}}+1}^{\bar{n}_u^{\text{dof}}} \mathbf{N}_{\delta}^{\mathcal{S}_u^h}(\mathbf{x}) \cdot u_{D,\delta}^{h,n+1}}_{\mathbf{u}_D^{h,n+1}(\mathbf{x})}. \quad (3.105)$$

The function $\mathbf{u}_D^{h,n+1}$ is called a lifting. In contrast to the boundary condition $\mathbf{u}_D(\mathbf{x}, t^{n+1})$, which is defined only on the domain boundary, it is defined on the whole domain. Equation (3.105) implicitly contains the assumption that the prescribed DIRICHLET boundary condition is compatible with the finite dimensional trial function space, i.e.

$$\mathbf{u}_D(\mathbf{x}, t^{n+1}) = \mathbf{u}_D^{h,n+1} \Big|_{\Gamma_D(t^{n+1})}(\mathbf{x}) \quad \text{for a } \mathbf{u}_D^{h,n+1} \in \mathcal{S}_u^h. \quad (3.106)$$

This assumption will be revisited in subsection 3.7.1. The lifting can always be used to define an auxiliary solution variable

$$\mathbf{u}_{\text{zero Dirichlet}}^{h,n+1} := \mathbf{u}^{h,n+1} - \mathbf{u}_D^{h,n+1}. \quad (3.107)$$

Using this auxiliary variable, the problem can be restated as an equivalent problem with homogeneous DIRICHLET boundary conditions.

The basis representation of a solution function for pressure reads

$$p^{h,n+1}(\mathbf{x}) = \sum_{\kappa=1}^{n_p^{\text{dof}}} N_{\kappa}^{\mathcal{S}_p^h}(\mathbf{x}) \cdot p_{\kappa}^{h,n+1}. \quad (3.108)$$

Here, n_p^{dof} corresponds to the number of pressure degrees of freedom $p_{\kappa}^{h,n+1}$. If an isoparametric equal order approach is applied, the pressure basis functions can be expressed using the same geometry basis functions that already have been used for the basis representation of velocity:

$$N_{\iota}^{\mathcal{S}_p^h}(\mathbf{x}) = N_{\iota}(\mathbf{x}) \quad (3.109)$$

In this case, the number of pressure degrees of freedom equals n_{np} .

A basis representation for velocity and pressure weighting functions is defined accordingly:

$$\mathbf{v}^h(\mathbf{x}) = \sum_{\delta=1}^{n_{\mathbf{u}}^{\text{dof}}} \mathbf{N}_{\delta}^{\mathcal{T}_{\mathbf{u}}^h}(\mathbf{x}) \cdot v_{\delta}^h \quad (3.110)$$

and

$$q^h(\mathbf{x}) = \sum_{\kappa=1}^{n_p^{\text{dof}}} N_{\kappa}^{\mathcal{T}_p^h}(\mathbf{x}) \cdot q_{\kappa}^h. \quad (3.111)$$

The span of functions $\mathbf{N}_{\delta}^{\mathcal{T}_{\mathbf{u}}^h}(\mathbf{x})$ with $\delta = 1, \dots, n_{\mathbf{u}}^{\text{dof}}$ is equal to the weighting function space $\mathcal{T}_{\mathbf{u}}^h$. Nevertheless, it is convenient to define the additional weighting functions

$$\mathbf{N}_{\delta}^{\mathcal{T}_{\mathbf{u}}^h} \text{ with } \delta = n_{\mathbf{u}}^{\text{dof}} + 1, \dots, \bar{n}_{\mathbf{u}}^{\text{dof}}. \quad (3.112)$$

They will be used to introduce DIRICHLET conditions in the resulting system of equations later on. For the moment, it will be assumed that weighting and trial functions are identical, i.e. that

$$\mathbf{N}_{\delta}^{\mathcal{S}_{\mathbf{u}}^h} = \mathbf{N}_{\delta}^{\mathcal{T}_{\mathbf{u}}^h} \text{ with } \delta = 1, \dots, \bar{n}_{\mathbf{u}}^{\text{dof}} \quad (3.113)$$

and

$$N_{\kappa}^{\mathcal{S}_p^h} = N_{\kappa}^{\mathcal{T}_p^h} \text{ with } \kappa = 1, \dots, n_p^{\text{dof}}. \quad (3.114)$$

Such approaches, in which trial and weighting function spaces are chosen analogously, are termed BUBNOV-GALERKIN methods. They are widespread in finite element analysis, and they have proven to be very successful in applications based on elliptic problems. For zero DIRICHLET boundary conditions, trial and weighting function spaces are identical for BUBNOV-GALERKIN methods. Approaches which allow the usage of different basis functions for trial and weighting function spaces are usually termed PETROV-GALERKIN methods. They naturally arise when methods of BUBNOV-GALERKIN type are enhanced by residual-based stabilisation techniques. A discussion of such methods which are especially valuable for convection dominated problems will follow later in section 3.5.

To sum up, the basis functions for the whole product spaces $\mathcal{S}_{\mathbf{u}}^h \times \mathcal{S}_p^h$ and $\mathcal{T}_{\mathbf{u}}^h \times \mathcal{T}_p^h$ are defined by the individual basis functions as it is usually done for CARTESIAN product spaces. For example, a basis for the weighting function space is obtained from the $n_{\mathbf{u}}^{\text{dof}} + n_p^{\text{dof}}$ basis functions

$$\left(\begin{array}{c} \mathbf{N}_{\ell}^{\mathcal{T}_{\mathbf{u}}^h} \cdot \mathbf{e}_1 \\ 0 \\ 0 \\ 0 \end{array} \right), \left(\begin{array}{c} 0 \\ \mathbf{N}_{\ell}^{\mathcal{T}_{\mathbf{u}}^h} \cdot \mathbf{e}_2 \\ 0 \\ 0 \end{array} \right), \left(\begin{array}{c} 0 \\ 0 \\ \mathbf{N}_{\ell}^{\mathcal{T}_{\mathbf{u}}^h} \cdot \mathbf{e}_3 \\ 0 \end{array} \right), \left(\begin{array}{c} 0 \\ 0 \\ 0 \\ N_{\kappa}^{\mathcal{T}_p^h} \end{array} \right). \quad (3.115)$$

The total number of non-DIRICHLET degrees of freedom is defined as

$$n^{\text{dof}} = n_{\mathbf{u}}^{\text{dof}} + n_p^{\text{dof}}. \quad (3.116)$$

Furthermore, the total number of degrees of freedom including the prescribed DIRICHLET boundary values is

$$\bar{n}^{\text{dof}} = \bar{n}_{\mathbf{u}}^{\text{dof}} + n_p^{\text{dof}}. \quad (3.117)$$

The components of the basis representations are associated with the degrees of freedom of the discretised problem. The vectors containing these degrees of freedom will be denoted by an underbar, for instance $\underline{\mathbf{u}}^h$ for the vector of velocity degrees of freedom.

3.4.3 Time derivatives of discretised degrees of freedom

Similar to the data from the current time step introduced above, all data from previous time steps, that is required for the time integration process, is also available only in spatially discretised form. For the computation of intermediate velocities and accelerations, discrete data from the last and the current time step has to be combined. This is straightforward for EULERian approaches. Since the domain does not change in time, the same set of basis functions can be used for all time steps. Thus, the equations (3.43)–(3.45) are equivalent to simple linear combinations of the components of the basis representations.

At first view, the setting in the ALE case seems to be more complicated. Since the domain is continuously deforming, basis functions in spatial configuration are changing in every time step. Fortunately, as indicated in equations (3.34)–(3.36), the intermediate velocities and accelerations have to be computed with respect to the reference domain. The basis functions defined in spatial configuration can be seen as a push-forward of basis functions on the reference domain, a fact that has already been described for example in the thesis by BAZILEVS [11]. The basis functions stated on the reference domain can be chosen independent of the time step. Thus all linear combinations corresponding to equations (3.34)–(3.36) can be equally realised by linear combinations of the components of the basis representations with respect to the reference domain.

Let $\underline{\mathbf{u}}^{h,n+1}$ and $\underline{\mathbf{a}}^{h,n+1}$ be the degrees-of-freedom vectors of the basis representations of the velocity and acceleration with respect to the reference domain. Furthermore, let $\underline{\mathbf{u}}^{h,n}$ and $\underline{\mathbf{a}}^{h,n}$ be the respective representations of the previous time step. The above-mentioned facts mean that the equations corresponding to (3.34)–(3.36) and (3.43)–(3.45) can equally be expressed as

$$\underline{\mathbf{u}}^{h,n+\alpha_F} = \alpha_F \cdot \underline{\mathbf{u}}^{h,n+1} + (1 - \alpha_F) \cdot \underline{\mathbf{u}}^{h,n} \quad (3.118)$$

$$\underline{\mathbf{a}}^{h,n+\alpha_M} = \alpha_M \cdot \underline{\mathbf{a}}^{h,n+1} + (1 - \alpha_M) \cdot \underline{\mathbf{a}}^{h,n} \quad (3.119)$$

$$\underline{\mathbf{u}}^{h,n+1} = \underline{\mathbf{u}}^{h,n} + (1 - \gamma) \Delta t \cdot \underline{\mathbf{a}}^{h,n} + \gamma \Delta t \cdot \underline{\mathbf{a}}^{h,n+1}. \quad (3.120)$$

3.4.4 Resulting nonlinear system and solution process

On the finite dimensional subspaces, the variational form of the boundary value problem is reduced to a nonlinear system of \bar{n}^{dof} equations and unknowns:

$$\underline{R}_{\mathbf{u},\delta}(\mathbf{u}^{h,n+1}, p^{h,n+1}) = R_{\mathbf{u}}(\mathbf{u}^{h,n+1}, p^{h,n+1}, \mathbf{N}_{\delta}^{\mathcal{T}_{\mathbf{u}}^h}) = 0 \quad (3.121)$$

$$\underline{R}_{p,\kappa}(\mathbf{u}^{h,n+1}, p^{h,n+1}) = R_p(\mathbf{u}^{h,n+1}, p^{h,n+1}, \mathbf{N}_{\kappa}^{\mathcal{T}_p^h}) = 0 \quad (3.122)$$

| predictor | $\underline{\mathbf{u}}_0^{h,n+1} = \dots$ | $\underline{p}_0^{h,n+1} = \dots$ |
|-----------------------|---|-----------------------------------|
| constant | $\underline{\mathbf{u}}^{h,n}$ | $\underline{p}^{h,n}$ |
| zero acceleration | $\underline{\mathbf{u}}^{h,n} + (1 - \gamma) \Delta t \cdot \underline{\mathbf{a}}^{h,n}$ | $\underline{p}^{h,n}$ |
| constant acceleration | $\underline{\mathbf{u}}^{h,n} + \Delta t \cdot \underline{\mathbf{a}}^{h,n}$ | $\underline{p}^{h,n}$ |
| constant increment | $2 \cdot \underline{\mathbf{u}}^{h,n} - \underline{\mathbf{u}}^{h,n-1}$ | $\underline{p}^{h,n}$ |

Table 3.1: Predictors for velocities and pressure according to JANSEN, WHITING and HULBERT [132].

The equations for $\delta = 1, \dots, n_{\mathbf{u}}^{\text{dof}}$ and $\kappa = 1, \dots, n_p^{\text{dof}}$ arise directly from the weak form (3.58). The additional equations for $\delta = n_{\mathbf{u}}^{\text{dof}} + 1, \dots, \bar{n}_{\mathbf{u}}^{\text{dof}}$ are introduced to enforce the DIRICHLET boundary condition, i.e. they enforce

$$u_{\delta}^{h,n+1} = u_{D,\delta}^{h,n+1} \quad \text{for all } \delta = n_{\mathbf{u}}^{\text{dof}} + 1, \dots, \bar{n}_{\mathbf{u}}^{\text{dof}}. \quad (3.123)$$

Assuming a suitable choice of function spaces which provides solvability for the system, it can be linearised and treated iteratively by a predictor corrector iteration. For this iteration, it is common to replace the basis representation of the new velocity $\underline{\mathbf{u}}^{h,n+1}$ by a basis representation of the acceleration at the new time step $\underline{\mathbf{a}}^{h,n+1}$ according to the linear relationship (3.120). Thus the actual unknowns in this procedure are $(\underline{\mathbf{a}}^{h,n+1}, \underline{p}^{h,n+1})^T$. The solution process consists of the following stages:

- Predictor stage

For degrees of freedom which are not constrained by a DIRICHLET condition, Table 3.1 provides several options for predictors to start the nonlinear iteration. For DIRICHLET constrained degrees of freedom, the predictor is simply the prescribed boundary value. The actual predictor for the acceleration is obtained from the velocity predictor using the linear relationship (3.120), i.e.

$$\underline{\mathbf{a}}_0^{h,n+1} = \frac{\underline{\mathbf{u}}_0^{h,n+1} - \underline{\mathbf{u}}^{h,n}}{\gamma \Delta t} + \frac{\gamma - 1}{\gamma} \cdot \underline{\mathbf{a}}^{h,n}. \quad (3.124)$$

- Averaging stage

Averaged quantities are computed according to equations (3.118) and (3.119)

$$\underline{\mathbf{u}}_i^{h,n+\alpha_F} = \alpha_F \cdot \underline{\mathbf{u}}_i^{h,n+1} + (1 - \alpha_F) \cdot \underline{\mathbf{u}}^{h,n} \quad (3.125)$$

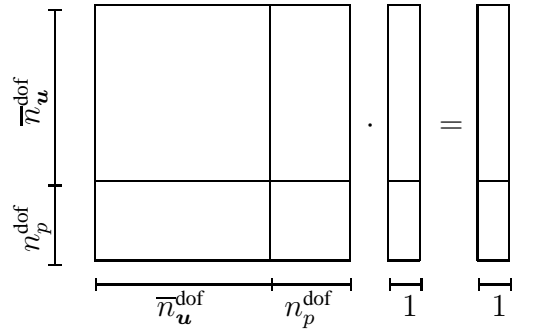
$$\underline{\mathbf{a}}_i^{h,n+\alpha_M} = \alpha_M \cdot \underline{\mathbf{a}}_i^{h,n+1} + (1 - \alpha_M) \cdot \underline{\mathbf{a}}^{h,n} \quad (3.126)$$

- System set-up and solution stage

Given a prediction for pressure $\underline{p}_i^{h,n+1}$, velocity $\underline{\mathbf{u}}_i^{h,n+1}$ and corresponding averaged quantities $\underline{\mathbf{u}}_i^{h,n+\alpha_F}$, $\underline{\mathbf{a}}_i^{h,n+\alpha_M}$ from nonlinear iteration step i , a linear system can be set up:

$$\begin{pmatrix} \left(\frac{\partial R_{\mathbf{u}}}{\partial \underline{\mathbf{a}}^{h,n+1}} \right)_i & \left(\frac{\partial R_{\mathbf{u}}}{\partial \underline{p}^{h,n+1}} \right)_i \\ \left(\frac{\partial R_p}{\partial \underline{\mathbf{a}}^{h,n+1}} \right)_i & \left(\frac{\partial R_p}{\partial \underline{p}^{h,n+1}} \right)_i \end{pmatrix} \cdot \begin{pmatrix} \Delta \underline{\mathbf{a}}_i^{h,n+1} \\ \Delta \underline{p}_i^{h,n+1} \end{pmatrix} = \begin{pmatrix} R_{\mathbf{u}_i} \\ R_{p_i} \end{pmatrix} \quad (3.127)$$

The sizes of the involved matrices and vectors are visualised in the following picture:



The lines corresponding to indices $\delta = n_{\mathbf{u}}^{\text{dof}} + 1, \dots, \bar{n}_{\mathbf{u}}^{\text{dof}}$, i.e. the DIRICHLET boundary conditions from equation (3.123), are blanked with zeros and get a one on the diagonal. The corresponding entry on the right hand side of the system is zero. Other boundary conditions influence this system as described in sections 3.7 and 4.5.

Assuming unique solvability, updates $(\Delta \underline{\mathbf{a}}_i^{h,n+1}, \Delta \underline{p}_i^{h,n+1})^T$ for the estimated solution values are computed from this linear system. The right hand side of equation (3.127) is the residual of the last iteration step. The lower right matrix block on the left hand side is nonzero only for methods enhanced by stabilisation terms, see the discussion in section 3.5 and the significantly simplified matrix system for the BUBNOV-GALERKIN approach in equation (3.134).

- Nonlinear update stage

Solution variables are updated using the increments:

$$\underline{\mathbf{a}}_{i+1}^{h,n+1} = \underline{\mathbf{a}}_i^{h,n+1} + \Delta \underline{\mathbf{a}}_i^{h,n+1} \quad (3.128)$$

$$\underline{p}_{i+1}^{h,n+1} = \underline{p}_i^{h,n+1} + \Delta \underline{p}_i^{h,n+1} \quad (3.129)$$

For the velocities, a synchronised update formula is given by

$$\underline{\mathbf{u}}_{i+1}^{h,n+1} = \underline{\mathbf{u}}^{h,n} + (1 - \gamma) \Delta t \cdot \underline{\mathbf{a}}^{h,n} + \gamma \Delta t \cdot \underline{\mathbf{a}}_{i+1}^{h,n+1}. \quad (3.130)$$

This non-incremental update formula ensures that numerical errors of accelerations and velocities can not develop independently, and thus it makes sure that equation (3.120) is satisfied exactly.

- Time update stage

After convergence of the nonlinear iteration, accelerations, velocities and pressure are updated:

$$\underline{\mathbf{a}}^{h,n} \leftarrow \underline{\mathbf{a}}_{i+1}^{h,n+1} \quad (3.131)$$

$$\underline{\mathbf{u}}^{h,n} \leftarrow \underline{\mathbf{u}}_{i+1}^{h,n+1} \quad (3.132)$$

$$\underline{p}^{h,n} \leftarrow \underline{p}_{i+1}^{h,n+1} \quad (3.133)$$

These stages are combined to an algorithm as described in Figure 3.8.

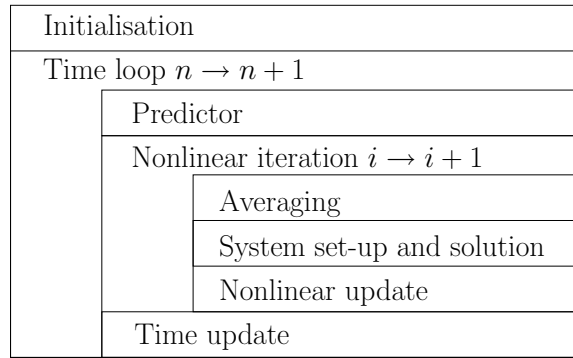


Figure 3.8: Overall algorithm for a generalised-alpha time integration.

Matrix equation for a BUBNOV-GALERKIN approximation, the LBB condition

For a BUBNOV-GALERKIN approach, the linear system (3.127) has the form

$$\begin{pmatrix} \mathbf{B}_i & -\frac{1}{\rho}\mathbf{G} \\ \alpha_F\gamma\Delta t \cdot \mathbf{G}^T & \mathbf{0} \end{pmatrix} \cdot \begin{pmatrix} \Delta \underline{\mathbf{a}}_i^{h,n+1} \\ \Delta \underline{p}_i^{h,n+1} \end{pmatrix} = \begin{pmatrix} \underline{\mathbf{R}}_{u,i} \\ \underline{\mathbf{R}}_{p,i} \end{pmatrix}. \quad (3.134)$$

The only matrix block which has to be updated during the nonlinear iteration is

$$\mathbf{B}_i = \left(\frac{\partial \underline{B}}{\partial \underline{\mathbf{a}}^{h,n+1}} \right)_i, \quad (3.135)$$

and due to the symmetry of the inner product, the off-diagonal blocks can both be represented using

$$\mathbf{G} = \left(\frac{\partial \underline{G}}{\partial \underline{p}^{h,n+1}} \right), \quad (\mathbf{G})_{\delta,\kappa} = \left(N_{\kappa}^{T_p^h}, \nabla \cdot \left(N_{\delta}^{T_u^h} \right) \right)_{\Omega(t^{n+1})} \quad (3.136)$$

with $\delta = 1, \dots, n_{\mathbf{u}}^{\text{dof}}$, $\kappa = 1, \dots, n_p^{\text{dof}}$. One of the shortcomings of the BUBNOV-GALERKIN approach is that a suitable choice of function spaces for velocity and pressure is necessary for the

matrix system (3.134) to have full rank. The requirement for such a suitable choice is the LADY-SHENSKAYA-BABUŠKA-BREZZI (LBB) condition which demands that for a positive $c \in \mathbb{R}$ the inf-sup condition

$$\inf_{0 \neq q^h \in \mathcal{T}_p^h} \sup_{0 \neq \mathbf{v}^h \in \mathcal{T}_u^h} \frac{(\nabla \cdot \mathbf{v}^h, q^h)_{\Omega(t^{n+1})}}{\|\mathbf{v}^h\|_{\mathbf{H}^1} \cdot \|q^h\|_{L^2}} \geq c > 0 \quad (3.137)$$

holds. This LBB condition provides full row rank for \mathbf{G}^T . If the LBB condition holds and it is assumed that \mathbf{B}_i is invertible, an algebraic counterpart to the pressure POISSON equation can be formed:

$$(\mathbf{G}^T \cdot \mathbf{B}_i^{-1} \cdot \mathbf{G}) \cdot \Delta \underline{p}_i^{h,n+1} = \rho \left(\frac{1}{\alpha_F \gamma \Delta t} \cdot \underline{R}_{p,i} - \mathbf{G}^T \cdot \mathbf{B}_i^{-1} \cdot \underline{R}_{u,i} \right) \quad (3.138)$$

If the LBB condition is violated, as it is the case for equal order interpolation which will be used in this thesis, $\mathbf{G}^T \cdot \mathbf{B}_i^{-1} \cdot \mathbf{G}$ will be rank deficient and thus spurious pressure modes will occur. For the STOKES problem, the full row rank of \mathbf{G}^T is a necessary and sufficient condition for the unique solvability of the equation system corresponding to (3.134), since \mathbf{B}_i is symmetric and positive definite. A proof for this unique solvability can be found for example in NOCEDAL and WRIGHT [166]. A reference to an optimisation textbook might seem surprising in this place, but equation (3.134) is very similar to a KARUSH-KUHN-TUCKER matrix which appears in optimisation of constrained quadratic problems. For further information on the treatment of saddle point problems see for instance BENZI, GOLUB and LIESEN [29] and for a further discussion of the LBB conditions and examples for inf-sup stable pairs of function spaces see BREZZI and FORTIN [42].

Convection induced instabilities

To discuss another shortcoming of the BUBNOV-GALERKIN approach, the differences between problems based on a symmetric, positive definite bilinear form and problems of advection-diffusion type will be studied more closely. The first class, which contains for instance linear elasticity applications and POISSON problems, is perfectly suited for the BUBNOV-GALERKIN approach. For these problems, this approach provides the best approximation on the finite dimensional subspace of trial functions with respect to the energy norm $\|\cdot\|_E$ introduced by the underlying bilinear form. For a proof, the reader is referred to the books by HUGHES [116] and KNABNER, ANGERMANN [141]. This statement also implies that the difference between exact weak solution and BUBNOV-GALERKIN approximation, i.e. the numerically unresolved part of the solution, is orthogonal to the finite dimensional subspace of trial functions with respect to the induced scalar product. This point is of special interest when the method is examined from a multiscale point of view.

Unfortunately, such a statement is not available for problems of advection-diffusion type. In this case, the underlying bilinear form is not symmetric and thus these problems do not provide an intrinsic energy norm. The statement of the best approximation has to be weakened, yielding the quasi-optimality of the BUBNOV-GALERKIN solution for advection-diffusion problems as described in ELMAN, SILVESTER and WATHEN [68]. The computed solution recovers the best approximation bound only up to a constant factor $1 + \text{Pe}$, which is linearly related to the PécLET

number

$$\text{Pe} = \frac{\mathcal{U}\mathcal{L}}{\varepsilon}. \quad (3.139)$$

In this definition, \mathcal{U} provides an upper bound for the norm of convective velocity, \mathcal{L} is a measure of the size of the domain and ε corresponds to the diffusion constant. Thus, the BUBNOV-GALERKIN solution is a bad choice for convection dominated problems where sharp boundary layers are present. Although convergence can be obtained under mesh refinement, the quality of the solution can still be poor for a finite resolution. From the multiscale perspective, it can be stated that for convection dominated problems the numerical error associated with the unresolved part of the solution is no longer orthogonal to the trial space. Thus, the approach of seeking better approximations in the solution space using stabilised methods, or more general methods which try to account for the effect of the unresolved onto the resolved scales, is well justified.

3.4.5 LAGRANGEan and isogeometric finite elements

According to the isoparametric concept, the basis functions used for the spatial representation of the solution have already been introduced in subsection 3.3.2. As previously pointed out in that subsection, basis functions for LAGRANGEan and isogeometric approaches have local support and only a few basis functions are nonzero on a specific element. As a consequence, the integrals involved in the set-up of the linear system (3.127) can be done element-based using only basis functions and values associated with the specific element. As it is usually done for finite elements, all integrals are evaluated on the reference element using numerical quadrature. For both approaches, the required JACOBIAN of the element mapping χ_e is defined by the isoparametric approach, i.e. via derivatives of shape functions and coordinates of nodes respectively control points of the element. The contributions of all elements are assembled into the global system, resulting in a sparse matrix system representation.

Isoparametric LAGRANGEan finite elements can be considered to be a well established approach in the numerical solution of partial differential equations. Applications are diverse and range from structural analysis to fluid-structure interaction and other multiphysics problems. Stability and convergence properties of the method are well investigated, especially for elliptic boundary value problems. For instance, the textbooks by BRENNER and SCOTT [41], STRANG and FIX [196] and KNABNER and ANGERMANN [141] can be consulted for some error analysis for isoparametric LAGRANGEan finite element approaches, including the effects of interpolated boundary data, non-exact geometry representation and the impact of numerical quadrature.

Isogeometric finite elements are a more recent development, initiated by COTTRELL et al. in [117]. The best overview of this topic is given in the recent book by COTTRELL et al. [57]. The isogeometric analysis allows a convenient combination of geometrical design and mechanical analysis, a long-term objective in the development of finite element methods. See for instance the earlier work by KAGAN et al. [137], in which B-spline functions as a basis for finite element analysis and design are investigated. Meanwhile, isogeometric finite elements have been applied to many problems, for instance to structural vibrations in COTTRELL et al. [58]. In this paper, a superior representation of frequency spectra is reported for the isogeometric method in comparison to classical higher order finite elements. Isogeometric finite elements have also been successfully applied to structural shape optimisation by WALL et al. [216]. For these problems, the isogeometric approach establishes a link between geometry description and numerical

model. The possible smoothness of isogeometric shape functions makes them a valuable tool for KIRCHHOFF-LOVE shell formulations, see KIENDL et al. [140]. Although not requiring the C^1 -continuity, good results were also reported for REISSNER-MINDLIN shells in BENSON et al. [27]. Furthermore, successful applications to fluid-structure interaction have been reported in BAZILEVS et al. [16, 17]. Multiscale formulations in fluid mechanics employing isogeometric finite elements have also been investigated, see for instance AKKERMAN et al. [3] and BAZILEVS et al. [15]. Section 4.4 contains more information on the application of isogeometric finite elements in the residual-based variational multiscale modelling of turbulence. An extension of isogeometric analysis to T-splines, allowing a local refinement, was given in DÖRFEL et al. [67] and BAZILEVS et al. [14]. For elliptic boundary value problems, error estimation and stability analysis have been performed in BAZILEVS et al. [13]. One of the main results is that discretisations based on NURBS elements of order p have the same order of convergence with respect to h -refinement as classical LAGRANGEan finite element approaches of polynomial order p . This means that under certain regularity assumptions, the solution of the isogeometric problem converges to the exact solution as $C \cdot h^p$ in the $\|\cdot\|_{H^1}$ norm and as $C \cdot h^{p+1}$ in the $\|\cdot\|_{L^2}$ norm. For this statement, a sufficiently smooth solution was assumed. The generic constant C depends on the distortion of the mesh, but not on the measure of the element size h . The impact of quadrature in isogeometric analysis has also been studied. In HUGHES et al. [124], efficient quadrature rules for isogeometric analysis have been proposed which try to account for the additional smoothness of NURBS basis functions across element boundaries. Nevertheless, the implementation in this thesis is based on a classical 27 point GAUSS rule for each quadratic NURBS volume element.

The algorithm which is used to set up the system matrix in the implementation used in this thesis is displayed in Figure 3.9. It is optimised so that the differences between an isogeometric multi-patch code and a classical finite element program are minimised. For isogeometric finite element analysis, this algorithm could be further simplified by replacing the element loop by a double loop over patches and corresponding elements as it is described in COTTRELL et al. [57]. For such an implementation, the determination of the patch and the element knot vector becomes straightforward. For parallel implementations, it turned out to be convenient and affordable to keep the knot vectors redundant on all processors. This ensures that each element has access to its element knot vector which is required for the evaluation of shape functions and derivatives. The weights involved in the shape function evaluation can be stored in the same way as the point coordinates. In that case, the standard ghosting strategies adopted from LAGRANGEan finite elements ensure that each element has access not only to all its degrees of freedom and point coordinates, but also to the required weights for the shape function evaluation.

Comparing isogeometric and LAGRANGEan finite elements, some further similarities and differences can be identified. For the interpolation of discontinuous data, higher order LAGRANGEan polynomials are well known to exhibit an oscillatory behaviour. In contrast, NURBS possess variation diminishing properties, making them a perfect tool for the representation of sharp boundary layers as they appear for example in high REYNOLDS number flows. The number of degrees of freedom associated with a NURBS element of degree p is equivalent to the number of degrees of freedom of a LAGRANGEan element of order p . Nevertheless, the support of a NURBS basis function is larger than the support of a LAGRANGEan basis function of the same order. Figure 3.10 displays these properties for a one-dimensional example with quadratic NURBS and quadratic LAGRANGEan basis functions. For the one-dimensional example, a

| | |
|---|--|
| Loop elements e | |
| Determine $(i, j, k, n_{\text{patch}})$ from e | |
| Acquire element knot vector \mathbf{u}_e in patch n_{patch} | |
| Determine n_{np}^e weights ω_I required for shape function evaluation | |
| Acquire geometry information \mathbf{x}_I and solution data $\mathbf{p}_I^{h,n+1}, \mathbf{u}_I^{h,n+1}, \mathbf{u}_I^{h,n+\alpha_F}, \mathbf{a}_I^{h,n+\alpha_M}$ for all n_{np}^e nonzero basis functions of local index I | |
| Loop GAUSS points ξ_{Gp} | |
| Evaluate shape functions and derivatives in ξ_{Gp} | |
| (Requires \mathbf{u}_e and ω_I) | |
| Interpolate required solution data to GAUSS point | |
| Compute and add contributions of GAUSS point to element matrix and residual vector | |
| Assemble contributions of element into global matrix and residual | |

Figure 3.9: Set-up for linear system (3.127). The highlighted grey parts are special for isogeometric implementations, the white parts are shared by isogeometric and LAGRANGEan finite element implementations.

quadratic NURBS basis function can be nonzero on three elements, while a LAGRANGEan basis function of the same order has a support of one element for center nodes and two elements for corner nodes. This, in terms of elements, larger support of the basis function has no severe impact on the sparsity pattern of the matrix. In the one-dimensional example, a NURBS basis function

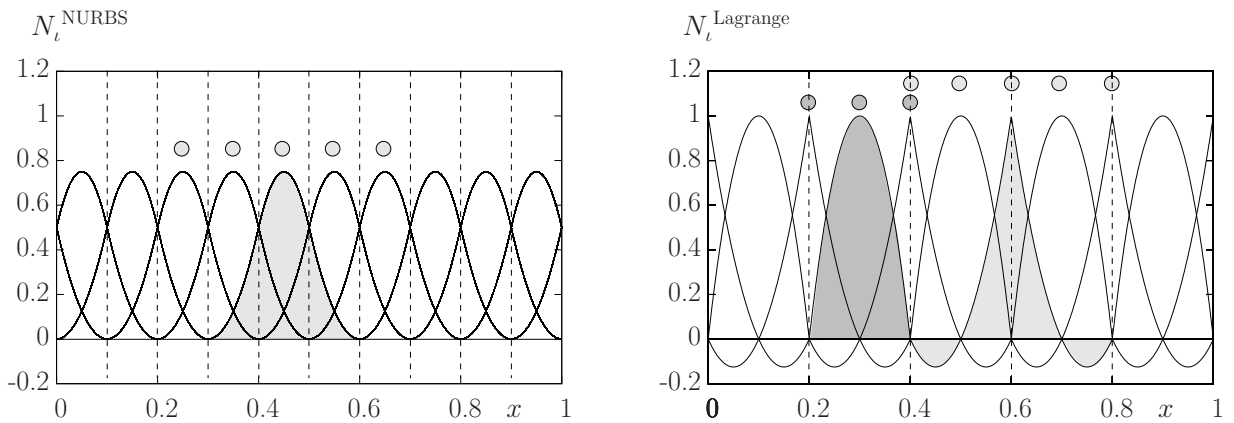


Figure 3.10: Comparison of quadratic NURBS and LAGRANGEan basis functions. The element boundaries are indicated by dashed vertical lines. Both approaches have three nonzero basis functions per element. The grey dots on top of the shape functions mark the basis functions which are connected to the shape function of corresponding colour.

interacts with five basis functions. For the same example, LAGRANGEan basis functions are also connected to five shape functions in the case of corner nodes. Only the LAGRANGEan basis functions in the interior of the element are connected to only three shape functions. Another more general example for the impact of the formulation on the sparsity pattern will be given later in section 5.3. Further important differences between higher order LAGRANGEan and isogeometric approximations can also be seen in Figure 3.10. For the same number of basis functions, the isogeometric approach generates a larger number of elements. This fact has to be considered when the amount of work required for the integration of the elements is estimated. On the other hand, for the same number of elements, the isogeometric approach will lead to a much smaller matrix system. In this sense, it can be considered as a very efficient choice. By definition, NURBS basis functions are always positive in contrast to LAGRANGEan basis functions which can also be negative. According to their definition, NURBS basis functions do in general not have a pointwise interpolation property. This will affect the imposition of DIRICHLET boundary conditions as well as post-processing, a matter that will be revisited in subsection 3.7.1 .

3.5 Residual-based stabilisation techniques

As pointed out before, the BUBNOV-GALERKIN formulation has severe drawbacks for incompressible and convection dominated flows. Residual-based stabilised methods provide a remedy for these shortcomings. In this section, three classical residual-based stabilisation techniques will be reviewed, the pressure-stabilising PETROV-GALERKIN (PSPG) method allowing equal order interpolation, the streamline upwind PETROV-GALERKIN (SUPG) for convection dominated problems and the least-squares incompressibility stabilisation (LSIC or grad-div) enhancing local mass conservation for flows with a high REYNOLDS number.

Other residual-based approaches like GALERKIN-least-squares (GLS) and the unusual stabilised finite element method (USFEM), see FRANCA and FREY [82], are not considered in this section but they will be briefly revisited in section 4.4. For a review on residual-based stabilisation techniques and some other recent stabilisation approaches, the reader is referred to BRAACK et al. [39].

As described in HUGHES [115] as well as in the review article by HUGHES et al. [126], residual-based stabilised methods can be derived from a multiscale perspective. The multiscale point of view allows several enhancements of the stabilised formulation. Nevertheless, the discussion in this section will be restricted to stabilised formulations in the traditional sense. Extension to time-dependent subgrid-scale stabilisation and residual-based variational multiscale modelling of turbulence will be discussed later in subsection 4.4.

3.5.1 PSPG, SUPG and LSIC stabilisation

The stabilised counterpart of equation (3.99) reads as follows:

$$B(\mathbf{u}^{h,n+1}, \mathbf{v}^h) - G(p^{h,n+1}, \mathbf{v}^h) + D(\mathbf{u}^{h,n+1}, q^h) + \sum_e (\tau_{Mp} \cdot \mathbf{r}_M^h(\mathbf{u}^{h,n+1}, p^{h,n+1}); \nabla q^h)_{\Omega_e} +$$

$$\begin{aligned}
 & + \sum_e (\tau_M \cdot \mathbf{r}_M^h(\mathbf{u}^{h,n+1}, p^{h,n+1}); (\mathbf{c}^{h,n+\alpha_F} \cdot \nabla) \mathbf{v}^h)_{\Omega_e} + \\
 & + \sum_e (\tau_C \cdot \mathbf{r}_C^h(\mathbf{u}^{h,n+1}), \nabla \cdot \mathbf{v}^h)_{\Omega_e} - F(\mathbf{v}^h) = 0
 \end{aligned} \tag{3.140}$$

Here, \mathbf{r}_M^h represents the residual obtained by insertion of the numerical approximation into the strong form of the advective momentum equation. For convective and conservative EULERian formulations, this means that

$$\begin{aligned}
 \mathbf{r}_M^h(\mathbf{u}^{h,n+1}, p^{h,n+1}) = & \dot{\mathbf{u}}^{h,n+\alpha_M} + (\mathbf{u}^{h,n+\alpha_F} \cdot \nabla) \mathbf{u}^{h,n+\alpha_F} + \frac{1}{\rho} \nabla p^{h,n+1} - \\
 & - 2\nu \nabla \cdot \boldsymbol{\varepsilon}(\mathbf{u}^{h,n+\alpha_F}) - \mathbf{b}^{h,n+\alpha_F},
 \end{aligned} \tag{3.141}$$

and for ALE formulations this implies that

$$\begin{aligned}
 \mathbf{r}_M^h(\mathbf{u}^{h,n+1}, p^{h,n+1}) = & \dot{\mathbf{u}}^{h,n+\alpha_M} + (\mathbf{c}^{h,n+\alpha_F} \cdot \nabla) \mathbf{u}^{h,n+\alpha_F} + \frac{1}{\rho} \nabla p^{h,n+1} - \\
 & - 2\nu \nabla \cdot \boldsymbol{\varepsilon}(\mathbf{u}^{h,n+\alpha_F}) - \mathbf{b}^{h,n+\alpha_F}.
 \end{aligned} \tag{3.142}$$

The residual of the continuity equation,

$$\mathbf{r}_C^h(\mathbf{u}^{h,n+1}) = \nabla \cdot \mathbf{u}^{h,n+1}, \tag{3.143}$$

is obtained by insertion of the discretised velocity into the strong form of the incompressibility constraint (3.33). τ_{Mp} , τ_M , τ_C are element-specific algebraic stabilisation parameters, their definitions will be provided below. By definition, all additional stabilisation terms vanish for the exact solution. Thus consistency is ensured for the residual-based approach. The residual of the momentum equation \mathbf{r}_M^h , which is required for this technique of stabilisation, contains second derivatives of shape functions. Especially for lower order finite elements, these second derivatives are not reasonably represented. A reconstruction of these second derivatives, as proposed in JANSEN et al. [131], is possible but not considered in the implementation in this thesis.

The PSPG stabilisation terms in the second line of equation (3.140) are motivated by considerations for the STOKES problem, see HUGHES et al. [120]. They allow the LBB condition to be circumvented and thus enable equal order interpolation. Looking at rates of convergence for stable and stabilised GALERKIN formulations, as it has been done for instance in GERDES and SCHÖTZAU [90], it becomes apparent that equal order interpolation is indeed a desirable property since it provides an optimal rate of convergence.

The SUPG stabilisation terms in the third line of equation (3.140) are based on considerations for the advection-diffusion equation which date back to a work by BROOKS and HUGHES [43]. Concerning the rate of convergence for advection-diffusion problems, SUPG stabilised methods are reported to have common features with H_0^1 -optimal methods in HUGHES and SANGALLI [125]. The combination of both approaches in application to the NAVIER-STOKES equations was termed SUPG/PSPG by TEZDUYAR et al. [207]. For problems on moving meshes, the advective velocity $\mathbf{c}^{h,n+\alpha_F}$ in the SUPG weighting function $(\mathbf{c}^{h,n+\alpha_F} \cdot \nabla) \mathbf{v}^h$ is the ALE convective velocity, see equations (2.16) and (2.17) for a definition of the ALE convective velocity and equation (3.41) for the discrete representation of the required intermediate grid velocity. An

analysis of a stabilised finite element approximation for an ALE formulation of the transient convection-diffusion equation can be found in BADIA and CODINA [6]. Furthermore, investigations of the performance of stabilised methods for the NAVIER-STOKES equations on distorted meshes can be obtained from FÖRSTER et al. [81]. For EULERian formulations, the ALE convective velocity in the weighting function in line three of equation (3.140) is actually equivalent to the fluid velocity, and thus the weighting function reduces to $(\mathbf{u}^{h,n+\alpha_F} \cdot \nabla) \mathbf{v}^h$.

The LSIC stabilisation in line four of equation (3.140) is a stabilisation procedure of least-squares type. This term is adopted from the stabilised formulation proposed by HANSBO and SZEPESY [109]. It provides an enhancement for discrete mass conservation, as it is exemplified in LINKE [156]. However, this improved discrete mass conservation comes along with numerical dissipation. Among other things, this artificial dissipation will be investigated in section 5.6 in the context of turbulent flow simulations. As similarly pointed out in OLSHANSKII et al. [168], LSIC stabilisation will always be a trade-off between mass conservation and stability on the one hand and energy conservation on the other hand.

3.5.2 Stabilisation parameters

The computation of stabilisation parameters is required during the evaluation of element integrals in equation (3.140). Since all integration is performed numerically, values for the stabilisation parameters are needed in the integration points of the elements. Stabilisation parameters are not defined as global constants, but depend on element and solution. In the following, three element and solution-specific contributions to the parameters will be listed. Afterwards examples for stabilisation parameter definitions will be provided. All definitions will be given for the EULERian case. A generalisation to the ALE case will be briefly addressed at the end of this subsection.

Element length definitions

All stabilisation parameter definitions depend on a measure of element size h_e . For problems in two or three spatial dimensions, the definition of this element ‘length’ is not unique. In the following, several possible choices for h_e will be provided.

- Variant based on a volume-equivalent diameter

$$h_e = \frac{2 \cdot \left(\frac{3}{4\pi} \int_{\Omega_e} d\mathbf{x} \right)^{\frac{1}{3}}}{\sqrt{3}} \quad (3.144)$$

In this definition, the element length h_e is chosen as two times the radius of a sphere with the same volume as the element divided by $\sqrt{3}$. The choice is purely geometrical, i.e. solution independent.

- Choice as stream length

$$h_e = \frac{2}{\left| \sum_{I=1}^{n_{\text{np}}^e} \frac{\mathbf{u}^h}{\|\mathbf{u}^h\|} \cdot \nabla N_I \right|} \quad (3.145)$$

This definition estimates the element length in direction of the fluid velocity. Usually, it is used in the context of convection stabilisation, while for pressure and continuity stabilisation the geometrical approach above is preferred, see also WALL [215] and references therein.

- Gradient-based definition

$$h_e = \frac{2}{\left| \sum_{I=1}^{n_{\text{fp}}} \frac{d_{\nabla}}{\|d_{\nabla}\|} \cdot \nabla N_I \right|} \quad (3.146)$$

This choice is very similar to the definition based on the stream length above. The only difference is that the direction in which the size of the element is estimated is replaced by

$$(d_{\nabla})_i = \sqrt{\sum_{j=1}^3 \frac{\partial \mathbf{u}_j^h}{\partial \mathbf{x}_i} \cdot \frac{\partial \mathbf{u}_j^h}{\partial \mathbf{x}_i}}. \quad (3.147)$$

This quantity is assumed to be large in the direction of large solution gradients. In a boundary layer mesh of a turbulent flow, this definition will select the minimum edge length close to the wall, a property that has proven beneficial in the turbulent channel flow simulations that will be shown in section 5.5. This observation is also in agreement with observations by MITTAL [161], who reports that for large aspect ratio elements, a definition based on minimum edge length results in better solutions for the transient laminar test problem investigated in that reference.

- Choice based on the metric tensor

In some definitions of the stabilisation parameter, a measure for element length is included implicitly using the second rank covariant metric tensor

$$\begin{aligned} \mathbf{G}_{ij}(\mathbf{x}) &= \sum_{k=1}^3 \frac{\partial (\chi_e^{-1})_k}{\partial \mathbf{x}_i}(\mathbf{x}) \cdot \frac{\partial (\chi_e^{-1})_k}{\partial \mathbf{x}_j}(\mathbf{x}) = \\ &= \sum_{k=1}^3 \left(\frac{\partial \chi_e}{\partial \xi}(\chi_e^{-1}(\mathbf{x})) \right)_{ki}^{-1} \cdot \left(\frac{\partial \chi_e}{\partial \xi}(\chi_e^{-1}(\mathbf{x})) \right)_{kj}^{-1}. \end{aligned} \quad (3.148)$$

The derivatives of mapping χ_e from the reference element to Ω_e are computable using equation (3.92). From this covariant metric tensor, a purely geometric element length can be obtained as

$$(\mathbf{G} : \mathbf{G})^{-\frac{1}{4}} = \left(\sum_{i=1}^3 \sum_{j=1}^3 \mathbf{G}_{ij} \cdot \mathbf{G}_{ij} \right)^{-\frac{1}{4}} \quad (3.149)$$

as well as an analogon to the stream length

$$\frac{1}{\|\mathbf{u}^h\|} \cdot \sqrt{\mathbf{u}^h \cdot (\mathbf{G} \mathbf{u}^h)} = \frac{1}{\|\mathbf{u}^h\|} \cdot \sqrt{\sum_{i=1}^3 \sum_{j=1}^3 \mathbf{u}_i^h \mathbf{G}_{ij} \mathbf{u}_j^h}. \quad (3.150)$$

Stabilisation parameter definitions based on \mathbf{G} can be found for instance in TAYLOR et al. [198] and BAZILEVS et al. [15]. The latter reference also introduces the quantity

$$\begin{aligned} \mathbf{g}_i(\mathbf{x}) &= \sum_{k=1}^3 \frac{\partial (\chi_e^{-1})_k}{\partial \mathbf{x}_i}(\mathbf{x}) \\ &= \sum_{k=1}^3 \left(\frac{\partial \chi_e}{\partial \boldsymbol{\xi}}(\chi_e^{-1}(\mathbf{x})) \right)_{ki}^{-1}, \end{aligned} \quad (3.151)$$

and uses its norm for a definition of element length in τ_C .

Especially for distorted elements, the different choices can result in significantly different values of h_e . This influence is investigated in detail in subsection 5.5 for the example of a boundary layer mesh with high aspect ratios in a turbulent channel flow simulation. Unfortunately, it is not possible to determine an optimal choice among the options above. For instance the choice which leads to the best results in subsection 5.5 lacks the required robustness in the simulations of section 6.2.1.

Shape function dependence

In addition to the dependence on h_e , there is also a dependence on the type of the element shape functions through a constant m_e . Following FRANCA and VALENTIN [83], this parameter can be determined by

$$m_e = \min \left\{ \frac{1}{3}, C_{\text{inv}} \right\} \quad (3.152)$$

with a constant C_{inv} from the inverse estimate

$$C_{\text{inv}} \cdot \sum_e h_e^2 \cdot (\Delta v, \Delta v)_{\Omega_e} \leq (\nabla v; \nabla v)_{\Omega(t^{n+1})}, \quad (3.153)$$

which must hold for all functions v in the space generated by the basis functions N_i .

The reason why this inverse estimate enters the parameter definition is related to the proof of error bounds for the convection-diffusion problem. In order to ensure the required coercivity of the stabilised bilinear form on the finite dimensional space of weighting functions with respect to the so-called streamline diffusion norm, the stabilisation parameter has to be bounded by $\frac{C_{\text{inv}} h_e^2}{4\nu}$. Such a proof can be found for instance in the book by KNABNER and ANGERMANN [141].

As it is usually done, the implementation used to generate the numerical results in chapters 5 and 6 is based on a constant choice of m_e as listed in Table 3.2. The values are chosen such that they are in good agreement with example values for simple elements, which can be found in HARARI and HUGHES [110].

Nonlinearity introduced by velocity dependence

Finally, the stabilisation parameter also depends on current velocity. In an implementation, this can be either the velocity at the integration point at time $t^{n+\alpha_F}$ or the corresponding velocity at time t^{n+1} . For classically stabilised methods, the impact of this additional nonlinearity is small

| element type | n_{np}^e | m_e |
|--------------------------|------------|----------------|
| trilinear LAGRANGEan | 8 | $\frac{1}{3}$ |
| trilinear NURBS | 8 | $\frac{1}{3}$ |
| triquadratic serendipity | 20 | $\frac{1}{12}$ |
| triquadratic LAGRANGEan | 27 | $\frac{1}{12}$ |
| triquadratic NURBS | 27 | $\frac{1}{12}$ |

Table 3.2: Number of shape functions per element n_{np}^e and values for m_e for different types of elements.

and it is not necessary to account for the velocity dependence of the stabilisation parameter in the linearisation process. As we will see later in subsection 4.4.3, the situation might change for a time-dependent subgrid approximation.

Scaling laws for stabilisation parameters

The stabilisation parameters τ_M and τ_{Mp} define intrinsic time-scales while parameter τ_C has the unit of an artificial viscosity. The various choices for τ_M , τ_{Mp} can be grouped into definitions that do include a time-step-dependent, reactive contribution and definitions that do not. The latter will be marked by an index $\cdot^{VX\ominus\Delta t}$, time-step-dependent versions by an index $\cdot^{VX\oplus\Delta t}$. All parameters associated with the residual of the momentum equation obey certain scaling rules as they are depicted in Table 3.3. The scaling law $O(h_e)$ for τ_C in the convective limit is also charac-

| | $\tau_M^{VX\ominus\Delta t}$ | $\tau_M^{VX\oplus\Delta t}$ |
|-----------------------|------------------------------|-----------------------------|
| convective limit | $O(h_e)$ | $O(h_e)$ |
| viscous limit | $O(h_e^2)$ | $O(h_e^2)$ |
| small-time-step limit | no Δt -dependence | $O(\Delta t)$ |

Table 3.3: Scaling of stabilisation parameters $\tau_M^{VX\ominus\Delta t}$ and $\tau_M^{VX\oplus\Delta t}$. The same scaling with potentially modified element length definition applies to $\tau_{Mp}^{VX\ominus\Delta t}$ and $\tau_{Mp}^{VX\oplus\Delta t}$. The small-time-step limit is meant for unchanged element sizes.

teristic for all versions of τ_C . Nevertheless, the different choices exhibit significant differences in the viscous and small-time-step limit. For the six choices of stabilisation parameters given below, these scalings are summarised in Table 3.4. All following parameter definitions for τ_C are provided for equal order elements. For inf-sup stable elements, different choices are suggested in OLSHANSKII et al. [168].

| | viscous limit | small-time-step limit |
|------------------------------|---------------|---|
| $\tau_C^{V1\oplus\Delta t}$ | $O(1)$ | $O\left(\frac{1}{\Delta t}\right) \rightarrow \infty$ |
| $\tau_C^{V1\ominus\Delta t}$ | $O(1)$ | constant |
| $\tau_C^{V2\oplus\Delta t}$ | $O(h_e^2)$ | constant |
| $\tau_C^{V2\ominus\Delta t}$ | $O(h_e^2)$ | constant |
| $\tau_C^{V3\oplus\Delta t}$ | $O(1)$ | $O\left(\frac{1}{\Delta t}\right) \rightarrow \infty$ |
| $\tau_C^{V3\ominus\Delta t}$ | $O(1)$ | constant |

 Table 3.4: Scaling of stabilisation parameters τ_C for various parameter definitions.

Stabilisation parameter choices

- Choice of stabilisation parameter: $(V1 \oplus \Delta t)$

The most straightforward formula for τ_M is adopted from a definition of a stabilisation parameter for advection-diffusion-reaction problems as it can be found in CODINA [52]:

$$\tau_M^{V1\oplus\Delta t} = \tau_{Mp}^{V1\oplus\Delta t} = \frac{1.0}{\frac{1}{\gamma \cdot \Delta t} + \frac{2}{m_e} \cdot \frac{\|\mathbf{u}^{h,n+\alpha_F}\|}{h_e} + \frac{4}{m_e} \cdot \frac{\nu}{h_e^2}} \quad (3.154)$$

The version given here includes a transient, reactive contribution dependent on the time step size. It is motivated from the temporally semi-discretised system, in which an approximation of the acceleration yields a reaction-type term. Contributions related to the convective and viscous limit case can easily be identified as the second and third summand in the denominator of this definition. The stabilisation parameter can be derived for instance by asymptotic scaling arguments or FOURIER analysis as in CODINA [53]. This reference also provides a definition for τ_C ,

$$\tau_C^{V1\oplus\Delta t} = \frac{m_e}{4.0} \cdot \frac{h_e^2}{\tau_M^{V1\oplus\Delta t}}. \quad (3.155)$$

- Choice of stabilisation parameter: $(V1 \ominus \Delta t)$

This parameter definition is equivalent to $(V1 \oplus \Delta t)$ without a reaction-type contribution from time integration:

$$\tau_M^{V1\ominus\Delta t} = \tau_{Mp}^{V1\ominus\Delta t} = \frac{1.0}{\frac{2}{m_e} \cdot \frac{\|\mathbf{u}^{h,n+\alpha_F}\|}{h_e} + \frac{4}{m_e} \cdot \frac{\nu}{h_e^2}} \quad (3.156)$$

The definition of τ_C is done accordingly:

$$\tau_C^{V1\ominus\Delta t} = \frac{m_e}{4.0} \cdot \frac{h_e^2}{\tau_M^{V1\ominus\Delta t}} \quad (3.157)$$

Parameter definitions of this kind are perfectly suited for stationary problems as well as for stabilisation using the time-dependent subgrid-scale approach by CODINA et al. [55]. Preferably, it is used with element length definition (3.144).

- Choice of stabilisation parameter: $(V2 \oplus \Delta t)$

This choice is a mixture of a parameter designed for advection-diffusion-reaction problems by FRANCA and VALENTIN [83] and a parameter developed for the STOKES problem by BARRENECHEA and VALENTIN [8].

$$\tau_M^{V2 \oplus \Delta t} = \frac{1.0}{\max\left(\frac{4}{m_e} \cdot \frac{\nu}{h_e^2}, \frac{1}{\gamma \cdot \Delta t}\right) + \max\left(2 \cdot \frac{\|\mathbf{u}^{h,n+\alpha_F}\|}{h_e}, \frac{4}{m_e} \cdot \frac{\nu}{h_e^2}\right)}. \quad (3.158)$$

This parameter contains all important scaling laws. It switches between the different regimes using the max-operator. For $\tau_M^{V2 \oplus \Delta t}$, a choice of h_e as stream length is common. The second parameter, $\tau_{Mp}^{V2 \oplus \Delta t}$ is defined by the same equation, but usually based on a purely geometric definition of element length (3.144). In the implementation used in this thesis, this parameter definition is combined with the expression

$$\tau_C^{V2 \oplus \Delta t} = \frac{\|\mathbf{u}^{h,n+1}\| h_e}{2} \cdot \min\left(\frac{\|\mathbf{u}^{h,n+1}\| \cdot h_e}{\nu} \cdot \frac{m_e}{2}, 1\right), \quad (3.159)$$

for the missing least-squares continuity stabilisation. Again, as it is done in WALL [215], the element length definition (3.144) is used for this parameter.

- Choice of stabilisation parameter: $(V2 \ominus \Delta t)$

The definition corresponding to $(V2 \oplus \Delta t)$ without a reactive contribution reads

$$\tau_M^{V2 \ominus \Delta t} = \tau_{Mp}^{V2 \ominus \Delta t} = \frac{1.0}{\frac{4}{m_e} \cdot \frac{\nu}{h_e^2} + \max\left(2 \cdot \frac{\|\mathbf{u}^{h,n+\alpha_F}\|}{h_e}, \frac{4}{m_e} \cdot \frac{\nu}{h_e^2}\right)}. \quad (3.160)$$

Since this parameter definition is usually used in the context of time-dependent subgrid-scale approximations, it does not distinguish between $\tau_M^{V2 \ominus \Delta t}$ and $\tau_{Mp}^{V2 \ominus \Delta t}$. Consequently, both choices are defined using the same purely geometric element length definition. The third parameter $\tau_C^{V2 \ominus \Delta t}$ that is usually combined with $\tau_M^{V2 \ominus \Delta t}$ is identical to the one from equation (3.159).

- Choice of stabilisation parameter: $(V3 \oplus \Delta t)$

A parameter choice based on an implicit element length definition using the covariant metric tensor (3.148) is given in BAZILEVS et al. [15]:

$$\begin{aligned} \tau_M^{V3 \oplus \Delta t} &= \tau_{Mp}^{V3 \oplus \Delta t} = \\ &= \left(\sqrt{\frac{4}{\Delta t^2} + \mathbf{u}^{h,n+\alpha_F} \cdot (\mathbf{G} \mathbf{u}^{h,n+\alpha_F}) + \frac{12}{m_e} \nu^2 (\mathbf{G} : \mathbf{G})} \right)^{-1} \end{aligned} \quad (3.161)$$

Although it contains a square root, it still shows the correct asymptotic behaviour. This parameter includes a term of reactive type. The parameter choice is completed by the definition

$$\tau_C^{V3\oplus\Delta t} = \left(\tau_M^{V3\oplus\Delta t} (\mathbf{g} \cdot \mathbf{g}) \right)^{-1}. \quad (3.162)$$

Here, vector \mathbf{g} from equation (3.151) is used.

- Choice of stabilisation parameter: $(V3 \ominus \Delta t)$

Finally, the counterparts to parameters $V3 \oplus \Delta t$ without the reactive contribution are

$$\begin{aligned} \tau_M^{V3\ominus\Delta t} &= \tau_{Mp}^{V3\ominus\Delta t} = \\ &= \left(\sqrt{\mathbf{u}^{h,n+\alpha_F} \cdot (\mathbf{G}\mathbf{u}^{h,n+\alpha_F}) + \frac{12}{m_e} \nu^2 (\mathbf{G} : \mathbf{G})} \right)^{-1} \end{aligned} \quad (3.163)$$

and least-squares continuity stabilisation parameter

$$\tau_C^{V3\ominus\Delta t} = \left(\tau_M^{V3\ominus\Delta t} (\mathbf{g} \cdot \mathbf{g}) \right)^{-1}. \quad (3.164)$$

This list of possible choices for the stabilisation parameter is not meant to be complete, it is just a selection of parameters which were actually used for calculations in this thesis. Other options to determine stabilisation parameters would be, for instance, estimation by an extension of the variational GERMANO identity, as it is proposed in OBERAI and WANDERER [167], or element-vector-based definitions of stabilisation parameters as introduced by TEZDUYAR and OSAWA [208].

For problems on deforming domains, the velocity in definitions (3.154)–(3.164) is replaced by the ALE convective velocity \mathbf{c}^h at the corresponding time level. The same statement applies to the computation of solution-based element length definitions (3.145), (3.146) and (3.150). Another possible modification, designed to improve the stability of the method on contracting elements, was proposed by FÖRSTER [78]. It is based on the inclusion of a generalised reaction coefficient into the stabilisation parameter for the ALE problem. Assuming $\nabla \cdot \mathbf{u}^{h,n+\alpha_F} \approx \mathbf{0}$, this generalised stabilisation parameter τ_M^{ALE} reads

$$\tau_M^{\text{ALE}} = \min \left(\tau_M^{\text{VX}\oplus\Delta t}, \sigma \right) \quad (3.165)$$

with

$$\sigma = \begin{cases} \gamma \Delta t \cdot \left(1 + \frac{\gamma \Delta t}{2} \min \left(\nabla \cdot \mathbf{u}_G^{h,n+\alpha_F} \right) \right) & \text{for } \left(\nabla \cdot \mathbf{u}_G^{h,n+\alpha_F} \right) < 0 \\ \gamma \Delta t & \text{for } \left(\nabla \cdot \mathbf{u}_G^{h,n+\alpha_F} \right) \geq 0 \end{cases}. \quad (3.166)$$

Small-time-step deficiencies

Shortcomings of residual-based stabilisation approaches at small time step sizes have been investigated in several publications, see BOCHEV et al. [33], FÖRSTER [78] and HSU et al. [114] amongst others. The major facts will be reviewed in the next paragraphs since they are of great importance for the interpretation of results in chapter 5.

All definitions $\tau_M^{\text{VX}\oplus\Delta t}$ that include a reactive, time-step-dependent contribution have obvious shortcomings for the small-time-step limit. The stabilisation parameter $\tau_M^{\text{VX}\oplus\Delta t}$ vanishes in that limit, causing a quasi unstabilised behaviour. In addition, most of the definitions of $\tau_C^{\text{VX}\oplus\Delta t}$ tend to infinity, see Table 3.4, and stationary solutions of the NAVIER-STOKES equations exhibit a significant unphysical dependence on the time step size. The shortcomings of parameter definitions $\tau_M^{\text{VX}\ominus\Delta t}$ without a Δt contribution are not as obvious but nevertheless even more severe. They do not occur in the context of pure advection-diffusion problems, see for instance BOCHEV et al. [34] and HSU et al. [114]. However, they can appear for a STOKES problem in the small-time-step limit. For this problem, the stabilisation parameter has to scale as $O(\Delta t)$ in order to ensure velocity-pressure stability. This condition was derived in another publication by BOCHEV et al. [32] and is clearly violated by the parameter choices $\tau_M^{\text{VX}\ominus\Delta t}$. The severity of this deficiency can be seen in the example of turbulent channel flow computations based on a fixed spatial resolution as it is commonly used for this kind of application. For decreasing time step sizes, the solutions in HSU et al. [114] are reported to diverge rapidly for parameter choices $\tau_M^{\text{VX}\ominus\Delta t}$. On the contrary, solutions for a parameter choice $\tau_M^{\text{VX}\oplus\Delta t}$ are reported to perform better, i.e. more robust, in that publication. This observation was also confirmed by computations performed within the context of chapter 5, see also GAMNITZER et al. [85].

In classical stabilised methods, the above mentioned inconsistencies can only be avoided if spatial and temporal discretisations are refined accordingly, i.e. an inequality $\frac{\Delta t}{h_e^2} > \alpha$ holds for a fixed, sufficiently large $\alpha > 0$. For many practical problems, a sufficient spatial refinement is not affordable. For this reason, the equally not optimal but more robust choice $\tau_M^{\text{VX}\oplus\Delta t}$ is preferred in this thesis. An exception to this statement is the application of definitions $\tau_M^{\text{VX}\ominus\Delta t}$ in the context of time-dependent subgrid approximations, as it will be discussed in section 4.4.

3.6 Imposition of initial conditions

According to the discussion in subsection 3.4.3, all data from previous time steps including the initial flow field has to be available in spatially discretised form. Thus the imposed initial condition has to be compatible with the finite dimensional trial subspace, i.e. only initial fields of the form $\mathbf{u}_0 = \mathbf{u}_0^h$ are admissible. In general, this assumption will not be satisfied exactly and thus a slightly modified initial condition will be used for the numerical solution. For a given initial field \mathbf{u}_0 , a good approximation can be computed using the least-squares problem

$$\min_{\underline{\mathbf{u}}_0^h} \left\| \sum_{\delta=1}^{\overline{n}_u^{\text{dof}}} \left(\mathbf{N}_\delta^{S_u^h}(\mathbf{x}) \cdot u_{0,\delta}^h \right) - \mathbf{u}_0(\mathbf{x}) \right\|_{L^2}^2. \quad (3.167)$$

This minimisation problem is equivalent to a linear problem

$$\sum_{\delta=1}^{\overline{n}_u^{\text{dof}}} \left(\mathbf{N}_\kappa^{S_u^h}; \mathbf{N}_\delta^{S_u^h} \right)_{\Omega(t^{n+1})} \cdot u_{0,\delta}^h = \left(\mathbf{N}_\kappa^{S_u^h}; \mathbf{u}_0 \right)_{\Omega(t^{n+1})} \quad (3.168)$$

for $\kappa = 1 \dots \overline{n}_u^{\text{dof}}$. The system matrix in this problem is of sparse ‘mass’-matrix type, and thus the linear system could be solved efficiently using an iterative solver. Problem (3.168) is of

comparable size to the linearised problem (3.127), but it has to be solved only once. Thus this way to impose initial conditions can be considered affordable in terms of computing time.

For LAGRANGEan finite elements, an alternative approach is to impose the initial condition pointwise at the nodes. A similar procedure in the context of isogeometric analysis would be to evaluate the initial condition at the control points and to subsequently assign the resulting values to the corresponding degrees of freedom. Since the NURBS basis functions do usually not interpolate all control points, this procedure will lead to a slightly smeared representation of the initial condition. For many cases the result might be accurate enough, but initial fields obtained by (3.167) will provide a better approximation, at least in an integral sense.

From the physical point of view, proper initial fields can be for instance a zero-flow field or solutions from a stationary STOKES problem on the same domain.

3.7 Basic boundary conditions

As already mentioned in the statement of the initial and boundary value problem in subsection 2.1.5, the way to impose boundary values is closely related to the numerical method which is actually used. In this section, several basic variants to impose boundary conditions for flows will be discussed.

3.7.1 DIRICHLET boundary conditions

As it was already discussed in subsection 3.4.2, DIRICHLET velocities are assumed to have a basis representation (3.105). Based on this basis representation, the solution process including the choice of the predictor and necessary matrix modifications were described in section 3.4.4. The remaining problem is to specify values for the components $u_{D,\delta}^{h,n+1}$ of the basis representation. A natural choice for LAGRANGEan finite elements is to require the lifting $\mathbf{u}_D^{h,n+1}$ to interpolate the prescribed boundary condition at the DIRICHLET boundary nodes of the discretisation. Due to the interpolation properties of LAGRANGEan basis functions, this is equivalent to the condition

$$u_{D,\delta}^{h,n+1} = \left(\mathbf{u}_D \left(\mathbf{x}_\iota^{h,n+1}, t^{n+1} \right) \right)_j \quad (3.169)$$

for the DIRICHLET degree of freedom δ associated with node number ι and direction j from equation (3.103).

For higher order isogeometric elements, such a formulation is often not feasible since the basis functions do not interpolate in general. In NURBS discretisations, control points associated with a DIRICHLET boundary can be located outside of $\Gamma_D(t^{n+1})$. Furthermore, a boundary value in one point is always defined by several basis functions and their corresponding components. Thus an alternative strategy to prescribe DIRICHLET boundary values is required. Following the idea from subsection 3.6, DIRICHLET boundary degrees of freedom can be determined according to the following least-squares optimisation problem:

$$\min_{\mathbf{u}_D^{h,n+1}} \left\| \sum_{\delta=n_u^{\text{dof}}+1}^{\bar{n}_u^{\text{dof}}} \left(\mathbf{N}_\delta^{S_u^h}(\mathbf{x}) \cdot u_{D,\delta}^{h,n+1} \right) - \mathbf{u}_D(\mathbf{x}, t^{n+1}) \right\|_{L^2(\Gamma_D(t^{n+1}))}^2 \quad (3.170)$$

For this approach, a coupled system for all unknown DIRICHLET degrees of freedom has to be solved to provide an appropriate approximation to the original boundary condition. The approximation can not be expected to be pointwise exact, but it will be optimal in an integral sense. Since only DIRICHLET degrees of freedom are involved in the ‘mass’-matrix problem corresponding to the minimisation problem (3.170), it can be assumed to be small in comparison to the linear system associated with the linearised problem (3.127).

Nevertheless, there are some special cases in which equation (3.169) can be applied even in isogeometric analysis. One of these special cases is the very common choice of no-slip DIRICHLET conditions. Due to the zero boundary condition it will work even for complex, curved boundaries. Furthermore, in geometries with rotational or translational symmetries, suitable boundary conditions with corresponding symmetries can also be defined in a pointwise sense using a similar formula to (3.169). For curved boundaries, the prescribed boundary velocity in (3.169) has to be replaced by another appropriate spatial function that is defined also at the control points. See the example in section 6.1, where boundary conditions along a circular cylindrical surface are prescribed.

The non-interpolatory character of isogeometric elements introduces further problems in the context of slip boundary conditions. For these boundary conditions, only the velocity in wall-normal direction has to be constrained. In LAGRANGEan finite elements, the imposition of slip boundary conditions is straightforward. In this case, normal and tangential degrees of freedom can be easily decoupled using local coordinate systems in the nodes. Such a simple, node-based procedure is not possible for isogeometric representations of curved boundaries. For this kind of boundary condition, a weak imposition of the wall-normal DIRICHLET condition, as it will be discussed in section 4.5, appears to be a more promising approach.

When prescribing DIRICHLET boundary conditions on the inflow, it is advisable to avoid impulsive starts by using a kind of ramp function to slowly increase the inflow in the domain. Otherwise, convergence problems in the nonlinear iteration are likely to occur.

3.7.2 NEUMANN (traction) boundary conditions

Classical NEUMANN boundary conditions are often termed natural boundary conditions. They allow to specify a traction according to equation (2.56) on a part $\Gamma_N(t^{n+1})$ of the boundary which is not constrained by DIRICHLET conditions:

$$R_{\mathbf{u}}(\mathbf{u}^{h,n+1}, p^{h,n+1}, \mathbf{v}^h) = \dots - \frac{1}{\rho} (\mathbf{t}; \mathbf{v}^h)_{\Gamma_N(t^{n+1})} = 0 \quad (3.171)$$

These (normalised) traction boundary conditions do not depend on the current iteration value of the solution, i.e. they have to be evaluated only once per time step. A common choice in fluid problems are so-called do-nothing zero traction boundary conditions. Furthermore, traction boundary conditions can be used to approximately define the distribution of pressure on $\Gamma_N(t^{n+1})$. Obviously, the quality of this ‘pressure’ boundary condition will depend on the magnitude of viscous stresses on the surface.

3.7.3 A consistency term for conservative formulations

The type of boundary condition described in this subsection is special for the weak form associated with the conservative EULERian equation (2.52). The partial integration of the convective term in that equation gives rise to a consistency term that has to be included in the residual of the weak form of the momentum equation:

$$\begin{aligned} R_{\mathbf{u}}(\mathbf{u}^{h,n+1}, p^{h,n+1}, \mathbf{v}^h) &= \\ &= \dots + (\mathbf{u}^{h,n+\alpha_F} \cdot \mathbf{n}, \mathbf{u}^{h,n+\alpha_F} \cdot \mathbf{v}^h)_{\Gamma(t^{n+1}) \setminus \Gamma_D(t^{n+1})} = 0 \end{aligned} \quad (3.172)$$

It is required on $\Gamma(t^{n+1}) \setminus \Gamma_D(t^{n+1})$, i.e. the whole part of the boundary that is not associated with a strong DIRICHLET condition. Thus this consistency term is required for instance on a NEUMANN boundary as well as on a weak DIRICHLET boundary which will be discussed later in section 4.5.

3.7.4 Stabilised outflow boundary conditions

One of the weaknesses of the EULERian description of flows is that appropriate outflow conditions have to be provided. Usually, these outflow boundary conditions will be of traction type. Unfortunately, the required tractions are not known ab initio. Hence, the boundary condition on the outflow, frequently a do-nothing condition, will not reflect the true distribution of pressure and viscous stresses along the outflow. This lack of consistency is well known to cause stability problems, especially for flows at high REYNOLDS numbers with vortex separation that induces a recirculation across the outflow boundary. To enhance stability of the fluid formulation, BAZILEVS et al. [18] propose a modification of the weak form. Assuming a fixed outflow, this formulation reads

$$\begin{aligned} R_{\mathbf{u}}(\mathbf{u}^{h,n+1}, p^{h,n+1}, \mathbf{v}^h) &= \dots + \\ &+ (\{\mathbf{u}^{h,n+\alpha_F} \cdot \mathbf{n}\}_-, \mathbf{u}^{h,n+\alpha_F} \cdot \mathbf{v}^h)_{\Gamma_{\text{outflow}}} = 0. \end{aligned} \quad (3.173)$$

The function

$$\{\cdot\}_- : \mathbb{R} \rightarrow \mathbb{R}, \quad x \mapsto \begin{cases} x & \text{for } x < 0 \\ 0 & \text{for } x \geq 0 \end{cases} \quad (3.174)$$

is zero on the part of the expected outflow that is in effect an outflow and non-zero in places of a recirculation across the outflow boundary. This modified boundary condition can not be expected to be more or less physical than a do-nothing condition for the outflow. Nevertheless, it often allows to perform computations on comparably small domains without running into severe stability problems. Otherwise, the only way to counteract these stability problems is to extrude the computational domain further downstream and to hope that due to the extended length, the vortices are sufficiently damped so that the do-nothing condition becomes an acceptable outflow condition again.

3.7.5 Periodic boundary conditions

Homogeneous flows will be approximated on periodic domains. In this subsection, the numerical implementation of the required periodic boundary conditions will be discussed. For simplicity,

the periodic domain is assumed to be a box of size $[0; \ell_x] \times [0; \ell_y] \times [0; \ell_z]$, and the procedure for the imposition of a periodic boundary condition in x -direction, i.e.

$$\begin{pmatrix} \mathbf{u}(0, y, z) \\ p(0, y, z) \end{pmatrix} = \begin{pmatrix} \mathbf{u}(\ell_x, y, z) \\ p(\ell_x, y, z) \end{pmatrix} \text{ for all } 0 \leq y \leq \ell_y \text{ and } 0 \leq z \leq \ell_z \quad (3.175)$$

will be described.

First, it will be assumed that the boundary of the periodic domain is interpolated by the finite element basis functions. This is the case, for instance, for LAGRANGEan finite elements. In this example, the periodic boundary conditions can simply be established on runtime by assigning the same degrees of freedom to two points on opposite boundary surfaces which coincide along a periodic direction, viz.

$$\text{if } \mathbf{x}_l^h + \ell_x \cdot \mathbf{e}_x = \mathbf{x}_\kappa^h \text{ then } \begin{pmatrix} \mathbf{u}_l^h \\ p_l^h \end{pmatrix} \equiv \begin{pmatrix} \mathbf{u}_\kappa^h \\ p_\kappa^h \end{pmatrix}. \quad (3.176)$$

By the connection of these degrees of freedom, the total number of degrees of freedom will be reduced in comparison to the unconstrained problem. Thus, renumbering will usually be required in order to maintain a consecutive numbering of the degrees of freedom. For parallel implementations, it will be important to keep coupled points on a common processor to be able to assign unique degrees of freedom to both of them. Consequently, a redistribution of points among processors is usually necessary before the degrees of freedom can be assigned. This redistribution affects the initial load balancing, a shortcoming that can be improved by an additional call to a graph-partitioning software, like PARMETIS by KARYPIS et al. [139], based on a weighted graph that associates connections between coupled points with a higher weight.

A generalisation of this approach to obtain periodic boundary conditions in several directions is straightforward. The major difference to the coupling in one direction is that points associated with periodic boundary conditions in several directions will have an increased number of coupled counterparts. For instance, a point associated with two periodic directions will be connected to three partner points.

In case of isogeometric analysis, a more elaborate coupling can be required if higher order basis functions based on periodic knot vectors (3.62) are employed. In this case, several layers of control points have to be coupled in the way described above, see the illustration in Figure 3.11.

The imposition of periodic boundary conditions as described above is reconcilable with the specification of a pressure drop

$$\Delta p = p(0, y, z) - p(\ell_x, y, z) \quad (3.177)$$

along the periodic domain. To do this, an auxiliary pressure $p^*(x, y, z)$ is introduced according to

$$p^*(x, y, z) = p(x, y, z) + \Delta p \cdot \frac{x}{\ell_x}. \quad (3.178)$$

Using this auxiliary pressure, the pressure gradient in the NAVIER-STOKES equations can be restated in the form

$$\nabla p(x, y, z) = \nabla \left(p(x, y, z) + \frac{\Delta p \cdot x}{\ell_x} \right) - \rho \begin{pmatrix} \frac{\Delta p}{\ell_x \cdot \rho} \\ 0 \\ 0 \end{pmatrix} = \nabla p^*(x, y, z) - \rho \cdot \mathbf{b}^*. \quad (3.179)$$

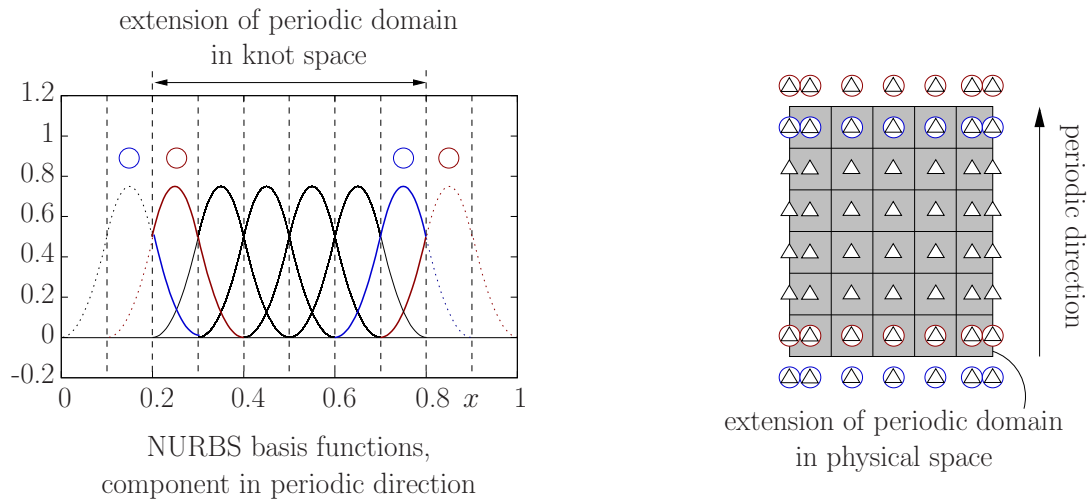


Figure 3.11: In order to establish periodic boundary conditions for second order NURBS basis functions, the degrees of freedom associated with the red and blue basis functions/circles have to be coupled. The figure on the right shows the respective coupled control points in physical space.

Thus the solution of the NAVIER-STOKES equations for velocity and pressure p based on a given pressure drop (3.177) and periodic boundary conditions for the velocity is equivalent to the solution of the NAVIER-STOKES equations for velocity and auxiliary pressure p^* using the additional body force per unit-mass term \mathbf{b}^* . This solution is now based on the simple periodic pressure condition

$$\begin{pmatrix} \mathbf{u}(0, y, z) \\ p^*(0, y, z) \end{pmatrix} = \begin{pmatrix} \mathbf{u}(\ell_x, y, z) \\ p^*(\ell_x, y, z) \end{pmatrix} \text{ for all } 0 \leq y \leq \ell_y \text{ and } 0 \leq z \leq \ell_z. \quad (3.180)$$

The initial pressure p can then be recovered by a single post-processing step according to equation (3.178).

To sum up, degrees of freedom associated with a periodic boundary are not considered as real boundary degrees of freedom anymore. They can be rather thought of as normal interior degrees of freedom. Thus problems involving periodic boundary conditions can result in systems that do not have a physical outflow, i.e. systems that are purely DIRICHLET constrained. Solution procedures for this case will be discussed in appendix E.

4 Turbulence modelling with a focus on residual-based large-eddy simulation

Assuming a sufficient resolution of the computational domain, the algorithm presented in chapter 3 can be used to compute a solution of the NAVIER-STOKES equations. Such an approach is referred to as direct numerical simulation (DNS). Unfortunately, as already anticipated in the discussion of the multiscale-character of turbulence in subsection 2.2.3, the required resolution is not affordable in many large REYNOLDS number applications. Section 4.1 is designated to highlight the potential and limitations of this approach.

The lack of resolution for high REYNOLDS number flows poses several problems which can be of physical or numerical nature. Concerning flow physics, an under-resolution of the flow implies that the energy cascade introduced in subsection 2.2.3 is truncated at a certain stage. Energy cannot be passed on to smaller eddies at this level, so an inconsistency in the energy budget occurs. Furthermore, the unrepresented turbulent stresses associated with the unresolved turbulent fluctuations cause erroneous predictions of the flow. This inadequate physical representation has to be accounted for by a suitable turbulence model in order to get the best prediction possible out of a given finite resolution. Section 4.2 describes two basic strategies to restate the equations in order to obtain a more meaningful physical solution. The REYNOLDS-averaged NAVIER-STOKES (RANS) approach will be touched upon only very briefly in subsection 4.2.1 in order to be able to point out the differences to the large-eddy simulation (LES) approach which will be discussed in subsection 4.2.2. This LES approach is the approach focused on in the current chapter and the rest of this thesis. In addition to the physical part, as we have seen in chapter 3, the finite resolution can also cause numerical problems, for instance by convection-induced instabilities. They have to be accounted for by suitable stabilisation procedures such as the ones from section 3.5.

The numerical formulation and the physical representation cannot be considered as separate problems. The numerical algorithm including discretisation scheme, stabilisation procedures and mesh definitions interacts with physical entities like contained energy and represented stresses. A special emphasis will be put on this relationship in the discussion of residual-based variational multiscale methods in section 4.4, which evolves from a review of the origins of variational multiscale modelling in section 4.3. The last section 4.5 of this chapter finally addresses a way to incorporate physically motivated wall laws in the framework of residual-based variational multiscale modelling of turbulence. Such laws for fully developed flow close to boundaries were described in subsection 2.2.5 and will be incorporated in a variationally consistent way using weak DIRICHLET conditions. The implementations presented in the current chapter form the basis for the investigations in the following chapters.

4.1 Limitations of direct numerical simulation

A direct numerical simulation of a turbulent flow requires a spatial and temporal resolution that is sufficiently high so that the impact of the unresolved scales on the resolved scales can be neglected. The number n_{np} of grid points required in this case can be estimated based on scale ratios for eddy sizes as are given in Table 2.2:

$$n_{\text{np}} \sim \left(\frac{\mathcal{L}}{\eta}\right)^3 \sim \text{Re}^{\frac{9}{4}} \quad (4.1)$$

In order to get a rough estimate for the number of time steps $n_{\Delta t}$ required for a sufficient temporal resolution, it is convenient to assume a time step proportional to the characteristic length scale, as it would be required for explicit time integration according to the COURANT-FRIEDRICHS-LEWY (CFL) condition [59]. Combining spatial and temporal resolution requirements, an overall estimate for the computational costs

$$n_{\text{np}} \cdot n_{\Delta t} \sim \left(\frac{\mathcal{L}}{\eta}\right)^3 \cdot \left(\frac{\mathcal{L}}{\eta}\right) \sim \text{Re}^3 \quad (4.2)$$

arises. Keeping in mind REYNOLDS numbers from the examples in Table 2.3, it is clearly evident that a direct numerical simulation of many real-life problems is pointless.

Nevertheless, as pointed out in the review article on direct numerical simulation of turbulent flows by MOIN and MAHESH [162], DNS has become an important research tool for the development of turbulence models. For moderate REYNOLDS numbers, DNS databases comprising values for mean flow quantities, fluctuations and other statistical data of interest are available for many canonical flows. Examples are the database for turbulent channel flow by MOSER et al. [163], the DNS data for TAYLOR-COUETTE flow by DONG [66] and the comprehensive AGARD collection [2], which includes results for channel flow, pipe flow, boundary layer flow and many more. The DNS reference solutions can be used both for a priori and a posteriori testing of a turbulence model's performance. In a priori tests, the approximation of the unresolved stresses is assessed directly. In an a posteriori approach, only the quality of resulting statistical quantities like mean values and fluctuations is considered. For a posteriori testing, results from DNS are an indispensable supplement to results obtained from experiments. It is possible that models perform poorly in a priori tests, but nevertheless yield quite acceptable results in a posteriori tests.

Most commonly, DNS results are obtained by using finite difference or spectral schemes. Nevertheless, stabilised methods as described in chapter 3 have also proven to be feasible for DNS computations. An example for a DNS performed using a stabilised method can be found in TROFIMOVA et al. [209].

4.2 Approaches for modelling turbulence

Depending on the complexity of the turbulent flow and the availability of sufficient computing resources, different approaches to turbulence modelling can be applied. The first variant that will be discussed in subsection 4.2.1 is based on the REYNOLDS-averaged NAVIER-STOKES

equations (2.63) and is therefore termed RANS approach. In this RANS technique, the quantities which are solved for are not the original unknowns but rather their averaged values. The average can be thought of as an ensemble, time or space average in a periodic direction. The second approach, large-eddy simulation, will be reviewed in subsection 4.2.2. For large-eddy simulation, the averaging of the RANS method is replaced by a filtering procedure. In contrast to the REYNOLDS averaging, filtering allows to separate scales of different sizes. This enables a restricted modelling in the LES approach. The model is only applied to the smaller scales while in the RANS method a model has to account for all scales contained in a flow.

Concerning resolution properties, there are clear differences between the approaches. Table 4.1 provides sketches for the different ways of looking at the flow. The direct numerical simulation

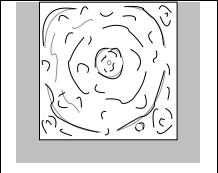
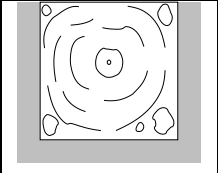
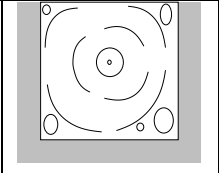
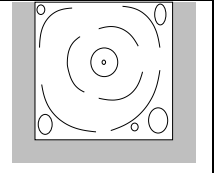



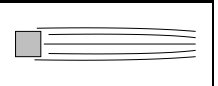
| DNS resolved | LES filtered | RANS | |
|--|--|---|--|
| | | URANS | time-avg. |
|  |  |  |  |
|  |  |  |  |

Table 4.1: Sketches for computed flow patterns in a driven cavity flow (top) and a flow around a square cylinder (bottom). DNS resolves all required scales. LES approaches correctly represent most of the energy-containing large scales, small-scale motions are filtered out and their impact on the large scales is accounted for by a model. RANS approaches include the highest degree of modelling. They provide results only for averaged quantities.

will resolve the motions of all necessary scales. For the RANS approach on the other hand, results are only obtained for averaged quantities. Thus, reasonable results can only be expected if the averaging procedure chosen to state the REYNOLDS-averaged NAVIER-STOKES equations matches the physical properties of the flow. For instance for flows that are not statistically stationary, like the turbulent flow around a square cylinder, the application of a RANS approach based on time-averaging will lead to poor results as they are sketched in Table 4.1. For a detailed investigation of this issue, the reader is referred to the paper by IACCARINO [128], in which results from unsteady RANS (URANS) calculations and RANS calculations based on time-averaging are compared. Large-eddy simulation is situated in between DNS and RANS. This statement applies to both resolution properties and computational costs. Large-scale motions are resolved using the LES technique and thus complex flow features can be represented accurately.

According to an estimation by RODI [180], RANS methods will be needed and used for many years to come in engineering calculations. However, inaccuracies must be accepted for complex flows involving separations and if it is affordable from the computational cost point of view, LES

provides a more general and better suited approach that has a great potential for representing this type of flows.

4.2.1 RANS closures

Approaches based on the REYNOLDS-averaged NAVIER-STOKES equations have to provide a closure for the unknown REYNOLDS-stress tensor (2.64). In this subsection, some basic strategies will be listed that can be used to construct a model for the REYNOLDS-stress tensor respectively its deviatoric part. For a deeper insight into RANS approaches, the reader is referred both to the well-known reference by WILCOX [222] and the overview article by ALFONSI [4].

RANS approaches are usually categorised in two classes, turbulent viscosity and REYNOLDS-stress models. Models based on the turbulent viscosity hypothesis assume

$$\boldsymbol{\tau}_{\text{rey}}^{\text{dev}} / \rho = \langle \underline{\mathbf{u}} \otimes \underline{\mathbf{u}} \rangle - \frac{1}{3} \sum_{i=1}^3 \langle \underline{\mathbf{u}}_i \underline{\mathbf{u}}_i \rangle = -2\nu_{\text{tur}} \cdot \boldsymbol{\varepsilon}(\langle \underline{\mathbf{u}} \rangle). \quad (4.3)$$

The turbulent viscosity can be interpreted as a product of a ‘mixing length’ scale ℓ_{mix} and a velocity scale u_{tur} .

$$\nu_{\text{tur}} = \ell_{\text{mix}} \cdot u_{\text{tur}} \quad (4.4)$$

Algebraic mixing length models for simple shear flow in x -direction with $\langle \underline{\mathbf{u}} \rangle = \langle u_x \rangle(y) \cdot \mathbf{e}_x$ assume

$$u_{\text{tur}} = \ell_{\text{mix}} \left\| \frac{\partial \langle u_x \rangle}{\partial y} \right\|. \quad (4.5)$$

This corresponds to PRANDTL’s mixing length hypothesis

$$\nu_{\text{tur}} = \ell_{\text{mix}}^2 \cdot \left\| \frac{\partial \langle u_x \rangle}{\partial y} \right\|. \quad (4.6)$$

Such a local model can be implemented rather easily. Nevertheless, it has severe drawbacks. For instance, it requires a problem dependent mixing length definition and no history effects are included in this model. A slight improvement to algebraic models are one-equation models. They include a transport equation for the turbulent kinetic energy k , which provides some non-local and history effects and yields a velocity scale. An empirical mixing length scale is still required for one-equation models. A slightly different one-equation approach, popular in aerodynamics applications, is the SPALART-ALLMARAS model which is based on a single transport equation for turbulent viscosity. Finally, two-equation models like the k - ϵ model solve two transport equations for turbulent kinetic energy k and dissipation rate ϵ . This approach is complete in the sense that the two quantities provide both a length and a velocity scale. Other variants like k - ω models are also possible. Like all approaches based on a turbulent viscosity hypothesis, two-equation models have deficiencies for complex flows causing REYNOLDS-stress anisotropies.

For such problems, REYNOLDS-stress models can provide better solutions. They involve transport equations for all REYNOLDS-stress components as well as a transport equation for the dissipation-rate. Among the RANS models, they are the most expensive models but are said to show the best performance for complex flows. Still, REYNOLDS-stress models cannot be considered universal.

4.2.2 Large-eddy simulation

Large-eddy simulation is a promising alternative to direct numerical simulation. In LES, the larger scales of turbulent flows are resolved. Only the impact of the smaller, unresolved scales is accounted for by a model. According to KOLMOGOROV's hypotheses, which were discussed in subsection 2.2.3, these smaller scales exhibit a more universal character in all fully-developed turbulent flows. This simplifies the modelling process and allows for models which are applicable to a broader range of flows. For the modelling of subgrid scales, various techniques have been established. The most exhaustive overview on such methods can be found in the book by SAGAUT [186]. The computational cost of LES is still high but it is substantially lower than for DNS.

As indicated before, the LES problem is stated only for the unknown large scales. Thus, in order to formulate an LES equation, a separation of scales has to be introduced. In traditional LES approaches, as described, e.g., in SAGAUT [186], this is done by explicit or implicit filtering, respectively. An example for an explicit filter \overline{G} is the box or top-hat filter

$$\overline{G}(\mathbf{x} - \hat{\mathbf{x}}) = \prod_{i=1}^3 \overline{G}_i(\mathbf{x}_i - \hat{\mathbf{x}}_i) \quad (4.7)$$

with

$$\overline{G}_i(\mathbf{x}_i - \hat{\mathbf{x}}_i) = \begin{cases} \frac{1}{\overline{\Delta}_i} & \text{if } |\mathbf{x}_i - \hat{\mathbf{x}}_i| \leq \frac{\overline{\Delta}_i}{2} \\ 0 & \text{otherwise} \end{cases} . \quad (4.8)$$

The resolution properties of a filter are defined by the filter width $\overline{\Delta}$. For instance for the box filter introduced above, $\overline{\Delta}$ is determined by the components of $\overline{\Delta}$. Other filters such as the sharp spectral cutoff filter, GAUSSIAN filters etc. can also be used. See the books by POPE [174] and SAGAUT [186] for a discussion. The application of the linear filter operator generated by the filter kernel \overline{G} defines a filtered velocity field

$$\overline{\mathbf{u}}(\mathbf{x}, t) = \iiint \overline{G}(\mathbf{x} - \hat{\mathbf{x}}) \cdot \mathbf{u}(\hat{\mathbf{x}}, t) d\hat{\mathbf{x}} . \quad (4.9)$$

The filtered field $\overline{\mathbf{u}}(\mathbf{x}, t)$ represents the large-scale content of the velocity field. For an illustration, Figure 4.1 provides an example for box-filtered vectors based on cross-stream and wall-normal velocity from the turbulent channel flow example introduced in Figure 2.4. The norm of the vectors is visualised for a cross section orthogonal to the mean stream-wise flow direction which is assumed to be aligned with the x -axis. The projections are computed according to the operator $\mathcal{P}_{yz}(\square) = \square - (\square \cdot \mathbf{e}_x) \mathbf{e}_x$. Filters do not necessarily have to be defined using an explicit filter kernel function \overline{G} . They can also result implicitly as a 'grid filter' from the finite mesh representation, from the employed numerical scheme or from an intrinsic cutoff length associated with a subgrid model. From the point of view of the variational multiscale approach for modelling turbulence, the filtering operation above corresponds to a GALERKIN projection into an a priori defined subspace of resolved scales. This procedure will be discussed in more detail in section 4.3. For the following explanations, the implicit grid filter associated with a stabilised finite element approach is used in the same way as a traditional implicit filter, i.e.

$$\overline{\mathbf{u}} = \mathbf{u}^h \quad (4.10)$$

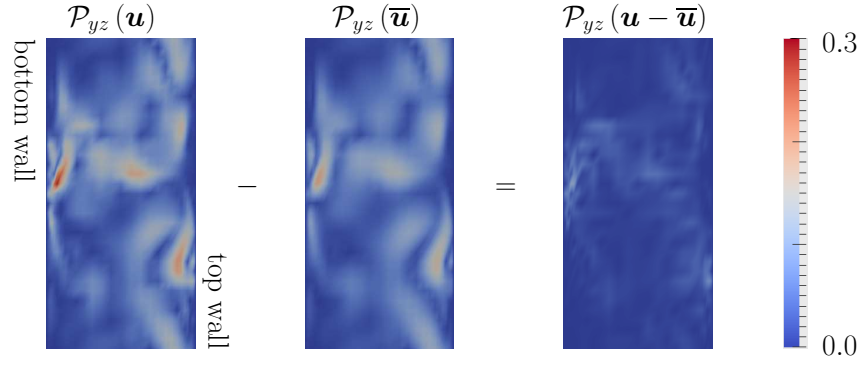


Figure 4.1: Visualisation of in-plane projected velocities in turbulent channel flow. From left to right: Projected velocity, projected filtered velocity and projection of their difference corresponding to the sub-filter scale.

The filter width for a GALERKIN projection is taken as the element size

$$\bar{\Delta} = h_e . \quad (4.11)$$

A definition for h_e can be obtained from equation (3.144).

The filter introduced above will now be applied to the NAVIER-STOKES equations in order to obtain an equation for the filtered solution field. The subsequent explanations are based on the conservative EULERian form of the NAVIER-STOKES equations (2.52). In analogy to the application of a REYNOLDS averaging as in equation (2.59),

$$\begin{aligned} \frac{\partial \bar{\mathbf{u}}}{\partial t} + \nabla \cdot \left(\overline{\mathbf{u} \otimes \mathbf{u}} + \frac{\bar{p}}{\rho} \cdot \mathbf{1} - 2\nu \varepsilon(\bar{\mathbf{u}}) \right) &= \bar{\mathbf{b}} \\ \nabla \cdot \bar{\mathbf{u}} &= 0 \end{aligned} \quad (4.12)$$

is obtained. Due to linearity properties of ε , the filtered strain rate tensor was obtained as

$$\overline{\varepsilon(\mathbf{u})} = \varepsilon(\bar{\mathbf{u}}) . \quad (4.13)$$

Furthermore, it was assumed that differentiation and filtering commute. Similar to the procedure applied for the RANS equations, a resolved stress tensor $\rho \cdot \bar{\mathbf{u}} \otimes \bar{\mathbf{u}}$ can be separated from the filtered nonlinear term in equation (4.12)

$$\rho \cdot \overline{\mathbf{u} \otimes \mathbf{u}} = \rho \cdot \bar{\mathbf{u}} \otimes \bar{\mathbf{u}} + \rho \cdot (\overline{\mathbf{u} \otimes \mathbf{u}} - \bar{\mathbf{u}} \otimes \bar{\mathbf{u}}) . \quad (4.14)$$

The remaining residual (subgrid) stress tensor,

$$\tau_{\bar{\Delta}}^{\text{res}} = \rho \cdot (\overline{\mathbf{u} \otimes \mathbf{u}} - \bar{\mathbf{u}} \otimes \bar{\mathbf{u}}) , \quad (4.15)$$

is obtained in analogy to the REYNOLDS stress tensor (2.64). Based on this residual stress tensor, the filtered version of the NAVIER-STOKES equations is given by

$$\begin{aligned} \frac{\partial \bar{\mathbf{u}}}{\partial t} + \nabla \cdot \left(\bar{\mathbf{u}} \otimes \bar{\mathbf{u}} + \frac{\bar{p}}{\rho} \cdot \mathbf{1} - 2\nu \varepsilon(\bar{\mathbf{u}}) + \frac{1}{\rho} \cdot \tau_{\bar{\Delta}}^{\text{res}} \right) &= \bar{\mathbf{b}} \\ \nabla \cdot \bar{\mathbf{u}} &= 0 . \end{aligned} \quad (4.16)$$

This is the base equation for large-eddy simulation, in which the residual stress tensor has to be substituted by a turbulence model.

Several approaches do not model the residual stress tensor itself but only its deviatoric part

$$\boldsymbol{\tau}_{\Delta}^{\text{res,dev}} = \boldsymbol{\tau}_{\Delta}^{\text{res}} - \frac{1}{3} \left(\sum_{i=1}^3 \tau_{\Delta,ii}^{\text{res}} \right) \mathbf{1}. \quad (4.17)$$

The trace of the residual stress tensor used in this definition, $\sum_{i=1}^3 \tau_{\Delta,ii}^{\text{res}}$, denotes two times the residual kinetic energy per unit volume. In order to be able to restate equation (4.16) using the deviatoric part of the residual stress tensor, a modified pressure

$$\bar{p}^{\text{dev}} = \bar{p} + \frac{1}{3} \cdot \left(\sum_{i=1}^3 \tau_{\Delta,ii}^{\text{res}} \right) \quad (4.18)$$

is introduced. Using this pressure, an equivalent version of the filtered NAVIER-STOKES equations can be stated:

$$\begin{aligned} \frac{\partial \bar{\mathbf{u}}}{\partial t} + \nabla \cdot \left(\bar{\mathbf{u}} \otimes \bar{\mathbf{u}} + \frac{1}{\rho} \cdot \boldsymbol{\tau}_{\Delta}^{\text{res,dev}} + \frac{\bar{p}^{\text{dev}}}{\rho} \cdot \mathbf{1} - 2\nu \boldsymbol{\varepsilon}(\bar{\mathbf{u}}) \right) &= \bar{\mathbf{b}} \\ \nabla \cdot \bar{\mathbf{u}} &= 0 \end{aligned} \quad (4.19)$$

The structure of equations (4.16) respectively (4.19) is very similar to the structure of the REYNOLDS-averaged equations (2.63). Nevertheless, the LES equations are obtained by filtering, not by averaging. Thus, the closure problem exists only for the residual stress tensor representing the small scales, not for the REYNOLDS-stress (2.64) containing information on all scales.

With regard to the energy spectrum, the filtering applied to the velocity field changes the spectral amplitude of the kinetic energy as sketched in Figure 4.2. For LES, the filtered velocity field should resolve all large, energy containing scales. Thus, the energy spectrum will be truncated near a cutoff wave number in the inertial range. The shape of the truncated energy spectrum shows that energy has to be dissipated from the resolved scales near the cutoff wave number. In comparison to the initial spectrum, the inertial range will be shortened and the dissipation range in the energy spectrum is shifted to the cutoff wave number of the filter. The view on this truncated energy spectrum explains that an important requirement for a turbulence model is that it must be able to extract a sufficient amount of energy from the large scales close to the cutoff wave number in order to obtain an energy spectrum from the solution of the filtered equation (4.16) or (4.19) respectively which is similar to the filtered exact energy spectrum from Figure 4.2.

LES modelling approaches can be categorised into two groups, functional and structural approaches. Functional modelling, which will be pursued in this thesis, tries to provide a correct representation of the impact of the unresolved scales on the resolved scales. Special emphasis is put here on a correct reproduction of dissipation properties as they were discussed above. Classical examples of a functional modelling approach are eddy-viscosity type models. A review of these models, including the discussion of SMAGORINSKY-type models which allow to inhibit the eddy viscosity in transitional regions, can be found in LESIEUR and MÉTAIS [154]. For the

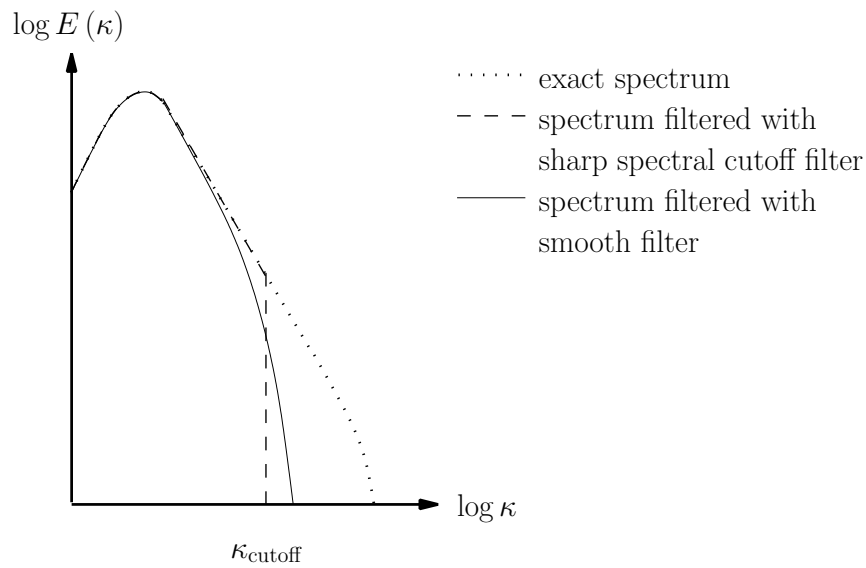


Figure 4.2: Impact of filtering on the energy spectrum, adopted from SAGAUT [186].

convenience of the reader who is not familiar with such methods, the most important properties of SMAGORINSKY-type models are summarised in appendix C.1. In this appendix, a detailed presentation of a finite element implementation of such a model, as it will be used in chapter 5 as a state-of-the-art physically motivated LES model for comparison, will be given. Eddy-viscosity models can also be used in the framework of variational multiscale models. Section 4.3 will provide some more information about this topic. The functional modelling is not necessarily applied explicitly. In implicit diffusion LES (ILES), the modelling is based on the assumption that the impact of the subgrid scales on the resolved scales is strictly dissipative and that this dissipation can be provided as numerical dissipation by the discretisation scheme. A well-known example for an ILES method is the MILES approach proposed by BORIS et al. [37] based on monotone computational fluid dynamics algorithms. Another option for an ILES approach is based on adaptive flux reconstruction as proposed by ADAMS, HICKEL et al. [1, 112]. In this approach, the weighted essentially non-oscillatory (WENO) approach, see SHU [190], of adaptive deconvolution is extended in such a way that by adjusting discretisation parameters implicit models for LES are obtained. The residual-based variational multiscale modelling of turbulence that will be presented in section 4.4 and investigated in the numerical examples later on also belongs to the class of functional approaches.

For completeness, two examples of structural modelling techniques, which are based on an approximation of the residual stresses directly, shall be mentioned here as well. They are the approximate deconvolution model by STOLZ and ADAMS [195] and the BARDINA scale similarity model [7]. More details on similarity subgrid models can be found in the review article by MENEVEAU and KATZ [160]. Mixed models combining the advantages of structural and functional modelling approaches are possible.

4.3 The original formulation of variational multiscale methods in turbulence modelling

A conceptual step in an LES approach is separation of scales. In traditional approaches, as they were discussed in subsection 4.2.2, separation of scales is based on a filtering operation which is often not projective. In contrast, scale separation in variational multiscale methods (VMM) is a priori based on variational projection. The origins of variational multiscale methods date back to early works by HUGHES [115] and HUGHES et al. [119], where it was established as a general framework for multiscale modelling in computational mechanics. Applications to large eddy simulation of the incompressible NAVIER-STOKES equations were first reported in HUGHES et al. [121]. Early examples for successful applications in LES followed, for instance the LES of homogeneous isotropic turbulence in HUGHES et al. [122] and the LES of turbulent channel flow in HUGHES et al. [123]. For these applications, a two-scale decomposition was achieved by a sharp cutoff in spectral space. A SMAGORINSKY model was applied only to the smaller scales in order to maintain consistency on the coarse scales. This idea was picked up and developed further in the context of three-level approaches by COLLIS et al. [56], see subsection 4.3.2 for more information. An application to compressible turbulent flows can be found in KOOBUS and FARHAT [146]. More recently, an alternative concept of residual-based variational multiscale modelling of turbulence was introduced in CALO [45]. For an overview article, the reader is referred to GRAVEMEIER [96] for the fluid context and furthermore to GRAVEMEIER et al. [99] for multiscale methods in general. A side-by-side presentation of VMM-based LES and traditional LES can be found in JOHN [133]. Furthermore, a review of recent developments in variational multiscale methods for turbulent flows is available in GAMNITZER et al. [86].

In general, variational multiscale modelling can provide both numerical stability and an inclusion of physical effects from unresolvable scales in turbulent flows. This section will give an overview of available variational multiscale approaches. The necessary scale separations are introduced as well as basic equations and solution concepts. Later on, in section 4.4, the focus will be turned to residual-based modelling of turbulence, providing details on the implementation of the approach and then used in subsequent computations.

4.3.1 Two-scale separation with explicit solution or approximation of the unresolved-scale equation

In a variational approach, the restriction of trial and weighting function spaces to finite dimensional subspaces, as it was described in section 3.4, corresponds to an a priori definition of a space that contains all resolved scales. A resolved-scale representation (\mathbf{u}^h, p^h) for an arbitrary pair (\mathbf{u}, p) of velocity and pressure trial functions can be obtained by selecting a continuous linear projector from $\mathcal{S}_{\mathbf{u}} \times \mathcal{S}_p$ on $\mathcal{S}_{\mathbf{u}}^h \times \mathcal{S}_p^h$. This projector is a surjective function

$$\mathbb{P} : \mathcal{S}_{\mathbf{u}} \times \mathcal{S}_p \rightarrow \mathcal{S}_{\mathbf{u}}^h \times \mathcal{S}_p^h \quad (4.20)$$

$$(\mathbf{u}, p) \mapsto \mathbb{P}(\mathbf{u}, p) \quad (4.21)$$

with $\mathbb{P} \circ \mathbb{P} = \mathbb{P}$. \mathbb{P} can be thought of as an L^2 - or H^1 -projector, see the remark in BAZILEVS et al. [15]. For each fixed choice of the projector, the resolved-scale representation

$$(\mathbf{u}^h, p^h) = \mathbb{P}(\mathbf{u}, p) \quad (4.22)$$

is unique. The projector furthermore introduces a space of unresolved-scale velocity and pressure trial functions by

$$(\mathbb{I} - \mathbb{P}) : \mathcal{S}_u \times \mathcal{S}_p \rightarrow \widetilde{\mathcal{S}}_u \times \widetilde{\mathcal{S}}_p \quad (4.23)$$

$$(\mathbf{u}, p) \mapsto (\mathbf{u}, p) - \mathbb{P}(\mathbf{u}, p). \quad (4.24)$$

For each fixed choice of the projector, the unresolved scales $(\widetilde{\mathbf{u}}, \widetilde{p})$ separated from (\mathbf{u}, p) are defined uniquely by

$$(\widetilde{\mathbf{u}}, \widetilde{p}) = (\mathbf{u}, p) - \mathbb{P}(\mathbf{u}, p). \quad (4.25)$$

Unlike the space of resolved scales, the space of unresolved scales is not uniquely defined but rather depends on the choice of \mathbb{P} . Furthermore, although the space of resolved scales is independent of the projector, the resolved-scale representation (\mathbf{u}^h, p^h) of (\mathbf{u}, p) will vary for different projectors.

An analogous scale separation based on the projection \mathbb{P} can be performed for the space of weighting functions, giving rise to a direct sum decomposition of all pressure and velocity weighting and trial function spaces as is summarised in the following equation:

$$\mathcal{S}_u = \mathcal{S}_u^h \oplus \widetilde{\mathcal{S}}_u, \quad \mathcal{S}_p = \mathcal{S}_p^h \oplus \widetilde{\mathcal{S}}_p, \quad (4.26)$$

$$\mathcal{T}_u = \mathcal{T}_u^h \oplus \widetilde{\mathcal{T}}_u, \quad \mathcal{T}_p = \mathcal{T}_p^h \oplus \widetilde{\mathcal{T}}_p. \quad (4.27)$$

The subspaces of unresolved scales are infinite dimensional. Due to the direct sum decomposition, each trial and weighting function has a unique decomposition into a resolved-scale and an unresolved-scale part, viz.

$$\mathbf{u} = \mathbf{u}^h + \widetilde{\mathbf{u}}, \quad p = p^h + \widetilde{p}, \quad (4.28)$$

$$\mathbf{v} = \mathbf{v}^h + \widetilde{\mathbf{v}}, \quad q = q^h + \widetilde{q}. \quad (4.29)$$

Using the scale decomposition of the solution functions (4.28), the weak form of the NAVIER-STOKES equations (3.58) can be restated as a combined system for the resolved and unresolved scales. For this purpose, the definitions

$$B_1(\mathbf{u}^{h,n+1}, \widetilde{\mathbf{u}}^{n+1}, \mathbf{v}) = \left. \frac{\partial}{\partial \epsilon} B(\mathbf{u}^{h,n+1} + \epsilon \cdot \widetilde{\mathbf{u}}^{n+1}, \mathbf{v}) \right|_{\epsilon=0} \quad (4.30)$$

and

$$B_2(\widetilde{\mathbf{u}}^{n+1}, \mathbf{v}) = \left. \frac{1}{2} \frac{\partial^2}{\partial \epsilon^2} B(\mathbf{u}^{h,n+1} + \epsilon \cdot \widetilde{\mathbf{u}}^{n+1}, \mathbf{v}) \right|_{\epsilon=0} \quad (4.31)$$

are introduced in order to be able to separate the influence of the unresolved scales from the nonlinear operator $B(\mathbf{u}^{h,n+1} + \tilde{\mathbf{u}}^{n+1}, \mathbf{v})$. Since B is only quadratic in the unresolved velocities, the NAVIER-STOKES equations (3.58) can be identically expressed as

$$\begin{aligned} B(\mathbf{u}^{h,n+1}, \mathbf{v}) + B_1(\mathbf{u}^{h,n+1}, \tilde{\mathbf{u}}^{n+1}, \mathbf{v}) + B_2(\tilde{\mathbf{u}}^{n+1}, \mathbf{v}) - \\ - G(p^{h,n+1}, \mathbf{v}) - G(\tilde{p}^{n+1}, \mathbf{v}) + \\ + D(\mathbf{u}^{h,n+1}, q) + D(\tilde{\mathbf{u}}^{n+1}, q) - F(\mathbf{v}) = 0. \end{aligned} \quad (4.32)$$

It should be pointed out that although equation (4.32) is stated only in the unknown velocities and pressures of the new time step it is still based on a time discretisation according to the generalised-alpha approach. Thus, discrete representations of the time derivatives of resolved and unresolved-scale velocity are still contained in equation (4.32). Since both resolved and unresolved-scale time derivatives emerge from the same term, it seems reasonable to treat them analogously when tracking the unresolved scales in time later on in section 4.4.

Incorporating an additional split of the weighting functions according to equation (4.29) induces two equations, a resolved-scale and an unresolved-scale equation. The momentum part of this resolved-scale equation reads

$$\begin{aligned} B(\mathbf{u}^{h,n+1}, \mathbf{v}^h) - G(p^{h,n+1}, \mathbf{v}^h) - F(\mathbf{v}^h) = \\ = - [B_1(\mathbf{u}^{h,n+1}, \tilde{\mathbf{u}}^{n+1}, \mathbf{v}^h) + B_2(\tilde{\mathbf{u}}^{n+1}, \mathbf{v}^h) - G(\tilde{p}^{n+1}, \mathbf{v}^h)] \end{aligned} \quad (4.33)$$

and the continuity equation for the resolved scales is given by

$$D(\mathbf{u}^{h,n+1}, q^h) = -D(\tilde{\mathbf{u}}^{n+1}, q^h). \quad (4.34)$$

The left hand side of equations (4.33) and (4.34) corresponds to the GALERKIN residual of equation (3.101). The right hand side of these equations represents the impact of unresolved velocity $\tilde{\mathbf{u}}^{n+1}$ and pressure \tilde{p}^{n+1} on the resolved scales. The unresolved pressure in this equation is usually replaced by a heuristic scaling in the style of a LSIC stabilisation. This will be discussed further in subsection 4.4.1. The remaining unknown unresolved velocity scales are defined by the second part of the equation system, the unresolved-scale equation. Its momentum part is given by

$$\begin{aligned} B(\mathbf{u}^{h,n+1}, \tilde{\mathbf{v}}) + B_1(\mathbf{u}^{h,n+1}, \tilde{\mathbf{u}}^{n+1}, \tilde{\mathbf{v}}) + B_2(\tilde{\mathbf{u}}^{n+1}, \tilde{\mathbf{v}}) - \\ - G(p^{h,n+1}, \tilde{\mathbf{v}}) - G(\tilde{p}^{n+1}, \tilde{\mathbf{v}}) - \\ - F(\tilde{\mathbf{v}}) = 0. \end{aligned} \quad (4.35)$$

It is usually assumed that the contribution of the unresolved pressure in this equation can be neglected, see for instance GRAVEMEIER [94] and CALO [45]. By this simplifying assumption, the unresolved-scale momentum equation can be rearranged yielding

$$\begin{aligned} B_1(\mathbf{u}^{h,n+1}, \tilde{\mathbf{u}}^{n+1}, \tilde{\mathbf{v}}) + B_2(\tilde{\mathbf{u}}^{n+1}, \tilde{\mathbf{v}}) = \\ = - [B(\mathbf{u}^{h,n+1}, \tilde{\mathbf{v}}) - G(p^{h,n+1}, \tilde{\mathbf{v}}) - F(\tilde{\mathbf{v}})]. \end{aligned} \quad (4.36)$$

The ‘source term’ on the right hand side of this equation corresponds to the projection of the residual of the resolved scales on the space of unresolved scales. Thus, the unresolved velocity scales can be considered to be driven by the residual of the resolved scales.

Another assumption that is usually made in the context of variational multiscale modelling of turbulence is that unresolved velocity scales vanish on element boundaries, i.e. that

$$\tilde{\mathbf{u}}^{n+1}|_{\partial\Omega_e} \equiv \mathbf{0} \text{ for all elements } e. \quad (4.37)$$

This localisation property is common in stabilised finite element methods and closely related to the idea of residual-free bubbles, see for instance GRAVEMEIER [94]. From the physical point of view, this assumption reflects the idea that smaller scales in a turbulent flow have a localised sphere of influence. In the following, two strategies will be described to solve the nonlinearly coupled set of resolved and unresolved-scale equations.

Numerical residual-free bubble approximation of unresolved scales

One approach is to approximate the unresolved-scale velocities by residual-free bubble functions. The solution process for this approach involves the solution of subproblems representing the unresolved-scale problem. This can be done for instance numerically on an element local subgrid in the sense of a two-level finite element method. The resulting combined bubble approximation for the solution of the unresolved-scale problem on all elements is then inserted into the resolved-scale equation, yielding a closed system for the resolved scales. Cases where an additional model term is included in the unresolved-scale problem, as it is done for instance in the original approach by HUGHES et al. [121], implicitly introduce a third level of scales. At this point, the transition to three-scale approaches is smooth. The interested reader is referred to the overview article by GRAVEMEIER [96] and references therein for more information.

Approximate analytical solution of the unresolved-scale problem

Another approach termed residual-based modelling of turbulence was introduced in the thesis by CALO [45]. It is based on the idea to systematically approximate the solution of the unresolved-scale equation in terms of resolved scales. Unlike for the numerically approximated residual-free bubble approach described above, no explicit subproblem solutions for unresolved scales are involved here. The approximation is rather done by local algebraic scalings. The most common approach is to account for the impact of unresolved scales by a local scaling of the resolved-scale residual as it is known from stabilised finite elements. The specific implementation depends on whether the equations are stated in conservative EULERian, convective EULERian or ALE form. Furthermore, it depends on whether time derivatives of unresolved scales are taken into account in the sense of a time-dependent subgrid-scale approximation as introduced in CODINA et al. [55] or not. Section 4.4 will provide a detailed discussion of the different variants.

Residual-based modelling of turbulence using a conventional closure was applied to fully developed turbulent channel flow and isotropic turbulence by BAZILEVS et al. [15], showing an excellent performance in the context of isogeometric finite element analysis. An LES of transitional flow based on a time-dependent subgrid-scale approximation can be found in PRINCIPE et al. [176]. Furthermore, GAMNITZER et al. [85] performed an LES investigation of fully developed turbulent channel flow using a time-dependent subgrid-scale approximation. The corresponding results will be summarised in chapter 5 and supplemented by investigations of the dissipative properties of the approaches implemented. A combination of time-dependent

subgrid-scale approximation and isogeometric analysis is also contained in this thesis, see the respective results in chapters 5 and 6.

4.3.2 Three-scale approaches keeping consistency on the large resolved scales

Three-scale methods were introduced by COLLIS in [56]. They are based on an additional separation of resolved velocity scales into large resolved scales and small resolved scales, denoted by a superscript H or δh respectively. The three-scale separation introduces an extended direct sum decomposition

$$\mathcal{S}_u = \underbrace{\mathcal{S}_u^H \oplus \mathcal{S}_u^{\delta h}}_{\mathcal{S}_u^h} \oplus \widetilde{\mathcal{S}}_u \quad \mathcal{T}_u = \underbrace{\mathcal{T}_u^H \oplus \mathcal{T}_u^{\delta h}}_{\mathcal{T}_u^h} \oplus \widetilde{\mathcal{T}}_u \quad (4.38)$$

of the velocity weighting and trial function spaces. Accordingly, trial and weighting functions have a unique decomposition

$$\mathbf{u} = \underbrace{\mathbf{u}^H + \mathbf{u}^{\delta h}}_{\mathbf{u}^h} + \widetilde{\mathbf{u}} \quad \mathbf{v} = \underbrace{\mathbf{v}^H + \mathbf{v}^{\delta h}}_{\mathbf{v}^h} + \widetilde{\mathbf{v}}. \quad (4.39)$$

In general, three-scale methods allow modelling to be confined to the smaller of the resolved scales, and hence to preserve consistency with respect to the larger resolved scales identified with the index H .

Approaches to separate resolved scales

The required scale separation for resolved scales can be based for instance on hierarchical approaches and bubbles as they were already mentioned in HUGHES et al. [121]. Another successfully applied approach to separate the scales is a p -type explicit L^2 -projection-based scale separation as it was proposed by JOHN and KAYA [134], see JOHN and KINDL [135] for further results based on this approach. Furthermore, a partition of scales can also be obtained using multiple grids. In this approach, the scale separation is introduced by a scale separating operator

$$\mathfrak{S}_h^H = \mathfrak{P}_H^h \circ \mathfrak{R}_h^H \quad (4.40)$$

$$\mathbf{u}^H = \mathfrak{S}_h^H (\mathbf{u}^h) \quad (4.41)$$

$$\mathbf{u}^{\delta h} = (\mathbb{I} - \mathfrak{S}_h^H) (\mathbf{u}^h) \quad (4.42)$$

consisting of a sequential application of restriction and prolongation operators, see GRAVEMEIER [95]. In a finite element context, the prolongation could be done for instance by linear interpolation and the restriction by injection. Purely algebraic multigrid operators for scale separation have also recently been explored in the algebraic variational multiscale-multigrid method proposed by GRAVEMEIER et al. [97]. The scale separation in that approach is done on a purely algebraic level using matrix representations of restrictor and prolongator which were generated using plain aggregation algebraic multigrid (PA-AMG).

A monolithic system of equations for the three-level approach

The additional separation of scales decomposes the resolved scale equation into two sub-equations, a large resolved-scale momentum equation

$$\begin{aligned} B(\mathbf{u}^{h,n+1}, \mathbf{v}^H) - G(p^{h,n+1}, \mathbf{v}^H) - F(\mathbf{v}^H) = \\ = - [B_1(\mathbf{u}^{h,n+1}, \tilde{\mathbf{u}}^{n+1}, \mathbf{v}^H) + B_2(\tilde{\mathbf{u}}^{n+1}, \mathbf{v}^H) - G(\tilde{p}^{n+1}, \mathbf{v}^H)] \end{aligned} \quad (4.43)$$

and a small resolved-scale momentum equation

$$\begin{aligned} B(\mathbf{u}^{h,n+1}, \mathbf{v}^{\delta h}) - G(p^{h,n+1}, \mathbf{v}^{\delta h}) - F(\mathbf{v}^{\delta h}) = \\ = - [B_1(\mathbf{u}^{h,n+1}, \tilde{\mathbf{u}}^{n+1}, \mathbf{v}^{\delta h}) + B_2(\tilde{\mathbf{u}}^{n+1}, \mathbf{v}^{\delta h}) - G(\tilde{p}^{n+1}, \mathbf{v}^{\delta h})] . \end{aligned} \quad (4.44)$$

This split allows modelling assumptions to be introduced separately on different scales. In the large resolved-scale equation (4.43), the impact of unresolved scales is neglected based on the assumption that their respective influence is relatively weak.

$$B(\mathbf{u}^{h,n+1}, \mathbf{v}^H) - G(p^{h,n+1}, \mathbf{v}^H) - F(\mathbf{v}^H) = 0 \quad (4.45)$$

In contrast, the impact of the unresolved scales on the small resolved scales in equation (4.44) is taken into account. For instance, it can be represented by a small-scale SMAGORINSKY-type model

$$\begin{aligned} B(\mathbf{u}^{h,n+1}, \mathbf{v}^{\delta h}) - G(p^{h,n+1}, \mathbf{v}^{\delta h}) + \\ + 2\nu_{\text{tur}}^{\delta h} (\boldsymbol{\varepsilon}(\mathbf{u}^{\delta h}), \boldsymbol{\varepsilon}(\mathbf{v}^{\delta h}))_{\Omega(t^{n+1})} - F(\mathbf{v}^{\delta h}) = 0 \end{aligned} \quad (4.46)$$

with a subgrid viscosity $\nu_{\text{tur}}^{\delta h}$ defined as

$$\nu_{\text{tur}}^{\delta h} = (C_{\text{Smag}} h_e)^2 \cdot \sqrt{\boldsymbol{\varepsilon}(\mathbf{u}^{\delta h}) : \boldsymbol{\varepsilon}(\mathbf{u}^{\delta h})} . \quad (4.47)$$

Such a small-scale constant-coefficient SMAGORINSKY model is known to perform well even in wall-bounded flows. Nevertheless, the model's constant can also be determined dynamically. See for instance GRAVEMEIER et al. [100, 101] for an implementation in the context of a three-level finite element method.

4.4 Residual-based modelling of turbulence

In this section, the approximate analytical solution of the unresolved-scale problem in the two-level approach introduced in subsection 4.3.1 will be described in detail. In a first subsection 4.4.1, three different subgrid velocity closures and a closure for the subgrid pressure will be provided. Then, the closed resolved-scale equations in convective ALE and conservative EULERian form will be given.

| unresolved-scale equation $\left[(\dots; \tilde{\mathbf{v}})_{\Omega(t^{n+1})} \right]$ | local algebraic scaling in integration point | |
|---|--|-----|
| $\tilde{\mathbf{u}}^{n+\alpha_M} +$ | $\sim \frac{1}{\Delta t} \cdot \tilde{\mathbf{u}}_{\text{IP}}^{n+\alpha_F}$, drop or keep | (I) |
| $+ (\mathbf{c}^{h,n+\alpha_F} \cdot \nabla) \tilde{\mathbf{u}}^{n+\alpha_F} +$ | $\sim \frac{\ [\mathbf{c}^{h,n+\alpha_F}]_{\text{IP}}\ }{h_e} \cdot \tilde{\mathbf{u}}_{\text{IP}}^{n+\alpha_F}$ | (C) |
| $+ (\tilde{\mathbf{u}}^{n+\alpha_F} \cdot \nabla) \tilde{\mathbf{u}}^{n+\alpha_F} +$ | drop | (D) |
| $+ (\tilde{\mathbf{u}}^{n+\alpha_F} \cdot \nabla) \mathbf{u}^{h,n+\alpha_F} -$ | drop | (D) |
| $- 2\nu \nabla \cdot \varepsilon (\tilde{\mathbf{u}}^{n+\alpha_F}) =$ | $\sim \frac{\nu}{h_e^2} \cdot \tilde{\mathbf{u}}_{\text{IP}}^{n+\alpha_F}$ | (V) |
| $= -\mathbf{r}_M^h (\mathbf{u}^{h,n+1}, p^{h,n+1})$ | $= -[\mathbf{r}_M^h (\mathbf{u}^{h,n+1}, p^{h,n+1})]_{\text{IP}}$ | |

Table 4.2: Unresolved-scale momentum equation and its approximate closure in terms of resolved-scale quantities by local algebraic scaling in integration points.

4.4.1 Subgrid closures

In order to motivate a representation for the subgrid velocity in terms of resolved-scale quantities, equation (4.36) is expanded in the left column of Table 4.2. For every term in this column, a corresponding scaling is provided in the second column. These scalings are used to approximate the partial differential unresolved-scale equation by a set of ordinary differential or algebraic equations in the integration points. The residual of the momentum equation \mathbf{r}_M^h that governs the right hand side of the unresolved-scale momentum equation is taken from equation (3.142). The approximation of the unresolved-scale velocity in the integration points is collected in a vector $\tilde{\mathbf{u}}^{n+\alpha_F}$. The notation $[\cdot]_{\text{IP}}$ indicates that a quantity is evaluated in the respective integration point. All algebraic scalings in the second column of Table 4.2 can be combined to one scaling parameter which can be identified with the inverse stabilisation parameter introduced in section 3.5. Table 4.2 and the scalings therein are based on a formulation of the NAVIER-STOKES equations in ALE form. The corresponding scalings for the EULERian form can simply be obtained by setting the grid velocity to zero. There are several comments to be made on the scalings introduced in Table 4.2:

(I) Time-derivative in the unresolved-scale momentum equation

One option for treating the time derivative in the unresolved-scale equation is to include a $\frac{1}{\Delta t}$ contribution in the scaling parameter definition. This case corresponds to the choice $\tau_M^{\text{VX} \oplus \Delta t}$ for the stabilisation parameter from section 3.5.

A purely algebraic closure can also be obtained by dropping the time derivative completely. This yields the approach termed quasi-static subgrid-scale approximation by

CODINA et al. [55]. This case corresponds to the choice $\tau_M^{\text{VX}\ominus\Delta t}$ for the stabilisation parameter.

Finally, it is possible to keep the time derivative in the approximated unresolved-scale equation as proposed in CODINA et al. [55]. This approach turns the unresolved-scale equation into a decoupled system of ordinary differential equations at the integration points. It is known as a time-dependent subgrid-scale approximation.

(C) Convective term in unresolved-scale momentum equation

In the convective limit, the algebraic scaling introduced by this term provides the well-known $(h_e / \|\mathbf{u}\|)$ -scaling for the stabilisation parameter.

(D) Nonlinear and reactive term

In conventional stabilised methods, these terms are usually dropped. In general, a different treatment as provided in CALO [45] is also possible. In this reference, the scaling is applied to unresolved-scale contributions in an asymptotic series approximation of the unresolved-scale momentum equation, yielding nonlinear approximations of subgrid velocities. Nevertheless, the implementation in this thesis is based on the more common approach to neglect these contributions.

(V) Viscous term

This term provides the well-known (h_e^2 / ν) -scaling of the stabilisation parameter in the viscous limit.

All following closure equations are evaluated at the integration points IP.

Conventional subgrid velocity closure

In the conventional closure, the subgrid velocity at every integration point is assumed to be proportional to the residual at that point:

$$\frac{1}{\tau_M^{\text{VX}\oplus\Delta t}} \cdot \tilde{\mathbf{u}}_{\text{IP}}^{n+\alpha_F} = - [\mathbf{r}_M^h(\mathbf{u}^{h,n+1}, p^{h,n+1})]_{\text{IP}} \quad (4.48)$$

Hence, equation (4.48) can be used to eliminate all contributions of unresolved-scale velocities in the resolved-scale equation.

Quasi-static subgrid velocity closure

The quasi-static approach can be seen as a special case of equation (4.48) using a stabilisation parameter independent of the time step size:

$$\frac{1}{\tau_M^{\text{VX}\ominus\Delta t}} \cdot \tilde{\mathbf{u}}_{\text{IP}}^{n+\alpha_F} = - [\mathbf{r}_M^h(\mathbf{u}^{h,n+1}, p^{h,n+1})]_{\text{IP}} \quad (4.49)$$

Time-dependent subgrid velocity closure

The time-dependent subgrid-scale approximation was introduced in CODINA et al. [55] from the viewpoint of a stabilised method. The closure equation for the unresolved-scale velocities in the integration points reads

$$\dot{\tilde{\mathbf{u}}}_{\text{IP}}^{n+\alpha_M} + \frac{1}{\tau_M^{\text{VX}\ominus\Delta t}} \cdot \tilde{\mathbf{u}}_{\text{IP}}^{n+\alpha_F} = - [\mathbf{r}_M^h(\mathbf{u}^{h,n+1}, p^{h,n+1})]_{\text{IP}} \quad (4.50)$$

with \mathbf{r}_M^h taken from equation (3.141) in the EULERian case. The extension of this equation for the ALE case reads

$$\dot{\tilde{\mathbf{u}}}_{\text{IP}}^{n+\alpha_M} + \frac{1}{\tau_M^{\text{VX}\ominus\Delta t}} \cdot \tilde{\mathbf{u}}_{\text{IP}}^{n+\alpha_F} = - [\mathbf{r}_M^h(\mathbf{u}^{h,n+1}, p^{h,n+1})]_{\text{IP}} \quad (4.51)$$

with \mathbf{r}_M^h taken from (3.142) and a modified version of the stabilisation parameter. In this thesis, these ordinary differential equations for the subgrid velocity in the integration points are treated with the same generalised-alpha time integration scheme as the resolved scales, i.e. in analogy to the results of subsection 3.4.3 the equations

$$\begin{aligned} \tilde{\mathbf{u}}^{n+\alpha_F} &= (1 - \alpha_F) \cdot \tilde{\mathbf{u}}^n + \alpha_F \cdot \tilde{\mathbf{u}}^{n+1} \\ \tilde{\mathbf{a}}^{n+\alpha_M} &= (1 - \alpha_M) \cdot \tilde{\mathbf{a}}^n + \alpha_M \cdot \tilde{\mathbf{a}}^{n+1} \\ \tilde{\mathbf{u}}^{n+1} &= \tilde{\mathbf{u}}^n + \Delta t \cdot (1 - \gamma) \cdot \tilde{\mathbf{a}}^n + \Delta t \cdot \gamma \cdot \tilde{\mathbf{a}}^{n+1} \end{aligned} \quad (4.52)$$

are obtained. This time discretisation yields the following expression for the unresolved-scale velocity at the new time level

$$\begin{aligned} \tilde{\mathbf{u}}_{\text{IP}}^{n+1} &= \frac{(\alpha_M - \gamma) \cdot \Delta t \cdot \tau_M^{\text{VX}\ominus\Delta t}}{\alpha_M \cdot \tau_M^{\text{VX}\ominus\Delta t} + \alpha_F \cdot \gamma \cdot \Delta t} \cdot \tilde{\mathbf{a}}_{\text{IP}}^n + \\ &+ \frac{\alpha_M \cdot \tau_M^{\text{VX}\ominus\Delta t} + (1 - \alpha_F) \cdot \gamma \cdot \Delta t}{\alpha_M \cdot \tau_M^{\text{VX}\ominus\Delta t} + \alpha_F \cdot \gamma \cdot \Delta t} \cdot \tilde{\mathbf{u}}_{\text{IP}}^n - \\ &- \frac{\gamma \cdot \Delta t \cdot \tau_M^{\text{VX}\ominus\Delta t}}{\alpha_M \cdot \tau_M^{\text{VX}\ominus\Delta t} + \alpha_F \cdot \gamma \cdot \Delta t} \cdot [\mathbf{r}_M^h(\mathbf{u}^{h,n+1}, p^{h,n+1})]_{\text{IP}}. \end{aligned} \quad (4.53)$$

It depends on the history of subgrid velocities $\tilde{\mathbf{u}}_{\text{IP}}^n$ and accelerations $\tilde{\mathbf{a}}_{\text{IP}}^n$. Thus, these additional variables have to be stored for every integration point. In all computations shown in this thesis, the subgrid quantities are initialised to zero in the beginning of a computation. The storage of data at integration points is quite expensive in terms of memory. For that reason, an alternative variant of the method, in which the data is transferred from the integration points to the nodes, was proposed by CODINA and PRINCIPE [54]. However, the additional memory requirements turned out not to be crucial for the type of flows under consideration in this thesis, so the implementation used here does not use this extension.

A closure for the unresolved pressure

The closure equation for the unresolved pressure is adopted from stabilised methods. According to the implicit treatment of the incompressibility constraint it is evaluated at the new time level:

$$\frac{1}{\tau_C} \cdot \tilde{p}_{\text{IP}}^{n+1} = -\rho \cdot ([\nabla \cdot \mathbf{u}^{h,n+1}]_{\text{IP}}) \quad (4.54)$$

4.4.2 The resolved-scale continuity equation

The local scaling is not suitable to represent spatial derivatives of unresolved-scale velocities in the resolved-scale equation. Hence, several terms on the right hand side of the resolved-scale equations (4.33) respectively (4.34) have to be integrated by parts on every element in order to shift the derivatives to the resolved-scale weighting functions. For the continuity equation (4.34) this results in

$$\begin{aligned}
 R_p(\mathbf{u}^{h,n+1}, p^{h,n+1}, q^h) &= \\
 &= (\nabla \cdot \mathbf{u}^{h,n+1}, q^h)_{\Omega(t^{n+1})} + \sum_e (\nabla \cdot \tilde{\mathbf{u}}^{n+1}, q^h)_{\Omega_e} = \\
 &= (\nabla \cdot \mathbf{u}^{h,n+1}, q^h)_{\Omega(t^{n+1})} - \sum_e (\tilde{\mathbf{u}}^{n+1}; \nabla q^h)_{\Omega_e} = 0
 \end{aligned} \tag{4.55}$$

Boundary terms in this partial integrations are neglected according to bubble property (4.37). For a conventional subgrid velocity closure (4.48), this equation obviously recovers the PSPG stabilisation term in equation (3.140). Hence equation (4.55) provides LBB stability as usual in stabilised methods.

4.4.3 Resolved-scale equation in advective ALE form

A similar partial integration on element domains using property (4.37) has to be applied to the resolved-scale momentum equation as well. For the convective part, this partial integration is simplified using the incompressibility constraint as follows:

$$\begin{aligned}
 &\left(\left(\left(\mathbf{u}^{h,n+\alpha_F} + \tilde{\mathbf{u}}^{n+\alpha_F} - \mathbf{u}_G^{h,n+\alpha_F} \right) \cdot \nabla \right) \tilde{\mathbf{u}}^{n+\alpha_F}; \mathbf{v}^h \right)_{\Omega_e} = \\
 &= \left(\nabla \cdot \left(\tilde{\mathbf{u}}^{n+\alpha_F} \otimes \left(\mathbf{u}^{h,n+\alpha_F} + \tilde{\mathbf{u}}^{n+\alpha_F} - \mathbf{u}_G^{h,n+\alpha_F} \right) \right); \mathbf{v}^h \right)_{\Omega_e} - \\
 &\quad - \left(\left(\nabla \cdot \left(\mathbf{u}^{h,n+\alpha_F} + \tilde{\mathbf{u}}^{n+\alpha_F} \right) \right) \tilde{\mathbf{u}}^{n+\alpha_F}; \mathbf{v}^h \right)_{\Omega_e} + \\
 &\quad + \left(\left(\nabla \cdot \mathbf{u}_G^{h,n+\alpha_F} \right) \tilde{\mathbf{u}}^{n+\alpha_F}; \mathbf{v}^h \right)_{\Omega_e} = \\
 &= - \left(\tilde{\mathbf{u}}^{n+\alpha_F}; \left(\left(\mathbf{u}^{h,n+\alpha_F} - \mathbf{u}_G^{h,n+\alpha_F} \right) \cdot \nabla \right) \mathbf{v}^h \right)_{\Omega_e} - \\
 &\quad - \left(\tilde{\mathbf{u}}^{n+\alpha_F}; \left(\tilde{\mathbf{u}}^{n+\alpha_F} \cdot \nabla \right) \mathbf{v}^h \right)_{\Omega_e} + \\
 &\quad + \left(\left(\nabla \cdot \mathbf{u}_G^{h,n+\alpha_F} \right) \tilde{\mathbf{u}}^{n+\alpha_F}; \mathbf{v}^h \right)_{\Omega_e}
 \end{aligned} \tag{4.56}$$

The resulting resolved-scale equation

$$R_{\mathbf{u}}(\mathbf{u}^{h,n+1}, p^{h,n+1}, \mathbf{v}^h) = R_{\mathbf{u}}^{\text{Gal}}(\mathbf{u}^{h,n+1}, p^{h,n+1}, \mathbf{v}^h) + \sum_e \square_e \tag{4.57}$$

splits into a GALERKIN part

$$\begin{aligned}
 R_{\mathbf{u}}^{\text{Gal}}(\mathbf{u}^{h,n+1}, p^{h,n+1}, \mathbf{v}^h) &= \\
 &= \left(\overset{\circ}{\mathbf{u}}^{h,n+\alpha_M}; \mathbf{v}^h \right)_{\Omega(t^{n+1})} - \frac{1}{\rho} \left(p^{h,n+1}, \nabla \cdot \mathbf{v}^h \right)_{\Omega(t^{n+1})} + \\
 &+ \left(\left(\left(\mathbf{u}^{h,n+\alpha_F} - \mathbf{u}_G^{h,n+\alpha_F} \right) \cdot \nabla \right) \mathbf{u}^{h,n+\alpha_F}; \mathbf{v}^h \right)_{\Omega(t^{n+1})} + \\
 &+ 2\nu \left(\boldsymbol{\varepsilon}(\mathbf{u}^{h,n+\alpha_F}) : \boldsymbol{\varepsilon}(\mathbf{v}^h) \right)_{\Omega(t^{n+1})} - \left(\mathbf{b}^{n+\alpha_F}; \mathbf{v}^h \right)_{\Omega(t^{n+1})}
 \end{aligned} \tag{4.58}$$

and element-specific subgrid contributions

$$\begin{aligned}
 \square_e &= \left(\overset{\circ}{\mathbf{u}}^{n+\alpha_M}; \mathbf{v}^h \right)_{\Omega_e} + \left(\left(\nabla \cdot \mathbf{u}_G^{h,n+\alpha_F} \right) \tilde{\mathbf{u}}^{n+\alpha_F}; \mathbf{v}^h \right)_{\Omega_e} + \\
 &+ \left(\left(\tilde{\mathbf{u}}^{n+\alpha_F} \cdot \nabla \right) \mathbf{u}^{h,n+\alpha_F}; \mathbf{v}^h \right)_{\Omega_e} - \\
 &- \left(\tilde{\mathbf{u}}^{n+\alpha_F}; \left(\left(\mathbf{u}^{h,n+\alpha_F} - \mathbf{u}_G^{h,n+\alpha_F} \right) \cdot \nabla \right) \mathbf{v}^h \right)_{\Omega_e} - \\
 &- \left(\tilde{\mathbf{u}}^{n+\alpha_F}; \left(\tilde{\mathbf{u}}^{n+\alpha_F} \cdot \nabla \right) \mathbf{v}^h \right)_{\Omega_e} - \\
 &- \frac{1}{\rho} \left(\tilde{p}^{n+1}, \nabla \cdot \mathbf{v}^h \right)_{\Omega_e} - 2\nu \left(\tilde{\mathbf{u}}^{n+\alpha_F}; \nabla \cdot \boldsymbol{\varepsilon}(\mathbf{v}^h) \right)_{\Omega_e}.
 \end{aligned} \tag{4.59}$$

An interpretation of these subgrid contributions is done in the following list in combination with some remarks on their treatment:

- Time derivative of subgrid velocity in resolved-scale equation

$$\left(\overset{\circ}{\mathbf{u}}^{n+\alpha_M}; \mathbf{v}^h \right)_{\Omega_e} \tag{4.60}$$

This term is dropped in combination with a conventional or quasi-static closure. For the time-dependent subgrid closure, this term is cancelled out only if orthogonal subscales are used, as they were introduced by CODINA [53]. The approach chosen in this thesis is not to use orthogonal subscales and thus this term does not vanish. Consequences of this fact for the nonlinear character of the resolved-scale equation will be briefly described in subsection 4.4.4.

- Divergence of grid velocity term

$$+ \left(\left(\nabla \cdot \mathbf{u}_G^{h,n+\alpha_F} \right) \tilde{\mathbf{u}}^{n+\alpha_F}; \mathbf{v}^h \right)_{\Omega_e} \tag{4.61}$$

For a conventional subgrid closure, this term is very similar to a reactive stabilisation contribution. Assuming for simplicity a spatially constant divergence of the grid velocity, a constant stabilisation parameter and a solely DIRICHLET bounded domain, the sum over all terms (4.61) can be restated in the form of a scaled GALERKIN residual

$$-\tau_M^{\text{VX}\oplus\Delta t} \cdot \left(\nabla \cdot \mathbf{u}_G^{h,n+\alpha_F} \right) \cdot R_{\mathbf{u}}^{\text{Gal}}(\mathbf{u}^{h,n+1}, p^{h,n+1}, \mathbf{v}^h). \tag{4.62}$$

Thus, according to these assumptions, the impact of this term can be represented using a rescaled ‘effective’ stabilisation parameter

$$\tau_M^{\text{VX}\oplus\Delta t} \longrightarrow \tau_M^{\text{ALE,VX}\oplus\Delta t} = \frac{\tau_M^{\text{VX}\oplus\Delta t}}{1 - \tau_M^{\text{VX}\oplus\Delta t} \cdot \left(\nabla \cdot \mathbf{u}_G^{h,n+\alpha_F} \right)}. \quad (4.63)$$

Assuming $\tau_M^{\text{VX}\oplus\Delta t} \cdot \left(\nabla \cdot \mathbf{u}_G^{h,n+\alpha_F} \right)$ to be sufficiently small, a TAYLOR series expansion yields

$$\begin{aligned} \frac{\tau_M^{\text{VX}\oplus\Delta t}}{1 - \tau_M^{\text{VX}\oplus\Delta t} \cdot \left(\nabla \cdot \mathbf{u}_G^{h,n+\alpha_F} \right)} &= \\ &= \tau_M^{\text{VX}\oplus\Delta t} \cdot \sum_{n=0}^{\infty} \left(\tau_M^{\text{VX}\oplus\Delta t} \cdot \left(\nabla \cdot \mathbf{u}_G^{h,n+\alpha_F} \right) \right)^n \doteq \\ &\doteq \tau_M^{\text{VX}\oplus\Delta t} \cdot \left(1 + \tau_M^{\text{VX}\oplus\Delta t} \cdot \left(\nabla \cdot \mathbf{u}_G^{h,n+\alpha_F} \right) \right). \end{aligned} \quad (4.64)$$

In the small-time-step limit where $\tau_M^{\text{VX}\oplus\Delta t} \sim \Delta t$, the asymptotic behaviour of the generalised stabilisation parameter definition (3.165) by FÖRSTER [78] is recovered. In practice, the divergence of the grid velocity times the stabilisation parameter will often be sufficiently smaller than one, allowing to drop this term for most of the applications.

- Cross-stress term

$$+ \left(\left(\tilde{\mathbf{u}}^{n+\alpha_F} \cdot \nabla \right) \mathbf{u}^{h,n+\alpha_F}; \mathbf{v}^h \right)_{\Omega_e} \quad (4.65)$$

This subgrid term is not available in conventional stabilised methods. It enables conservation properties for the advective form of the incompressible NAVIER-STOKES equations, see HUGHES and WELLS [127] or the related work for the scalar advection-diffusion equation by HUGHES et al. [118].

- SUPG term

$$- \left(\tilde{\mathbf{u}}^{n+\alpha_F}; \left(\left(\mathbf{u}^{h,n+\alpha_F} - \mathbf{u}_G^{h,n+\alpha_F} \right) \cdot \nabla \right) \mathbf{v}^h \right)_{\Omega_e} \quad (4.66)$$

For the conventional closure, this term corresponds to the SUPG stabilisation term. It ensures stability in the convection-dominated regime.

- REYNOLDS-stress term

$$- \left(\tilde{\mathbf{u}}^{n+\alpha_F}; \left(\tilde{\mathbf{u}}^{n+\alpha_F} \cdot \nabla \right) \mathbf{v}^h \right)_{\Omega_e} \quad (4.67)$$

Similar to the cross-stress term, the REYNOLDS-stress term arising from the nonlinear convective term is not available in conventional stabilised methods. Usually, this term is small since it is quadratic in the unresolved-scale quantity.

- Subgrid pressure term

$$- \frac{1}{\rho} \left(\tilde{p}^{n+1}, \nabla \cdot \mathbf{v}^h \right)_{\Omega_e} \quad (4.68)$$

Based on the subgrid model (4.54), this term is equivalent to the LSIC stabilisation term. It is strictly dissipative, provides additional stability for high REYNOLDS number flows and enhances local mass conservation, see section 3.5.

- Viscous stabilisation term $\varepsilon(\mathbf{v}^h)$

$$-2\nu (\tilde{\mathbf{u}}^{n+\alpha_F}; \nabla \cdot \varepsilon(\mathbf{v}^h))_{\Omega_e} \quad (4.69)$$

For a conventional subgrid closure, this viscous contribution corresponds to the second order derivative part of an USFEM stabilisation operator. In this thesis, it is neglected in the resolved-scale equation. This procedure is standard in residual-based modelling of turbulence, for instance BAZILEVS et al. [15] also omit this term in their implementation. For lower-order elements, the second order derivatives involved in this operator are not sufficiently represented. Aside from this, a recent work by FÖRSTER [78] indicates that this term can be problematic for applications on distorted meshes.

4.4.4 A comment on the nonlinear character of the time-dependent subgrid-scale approximation

The consideration of time derivatives of subgrid velocities (4.60) adds to the nonlinearity of the resolved-scale equation. To understand this, subgrid closure (4.51) is rewritten in the form

$$\underline{\mathbf{u}}_{\text{IP}}^{n+\alpha_M} = -\frac{1}{\tau_{\text{M}}^{\text{VX}\ominus\Delta t}} \cdot \tilde{\mathbf{u}}_{\text{IP}}^{n+\alpha_F} - [\mathbf{r}_M^h(\mathbf{u}^{h,n+1}, p^{h,n+1})]_{\text{IP}} \quad (4.70)$$

If this representation of the time derivative of the subgrid velocity is included in the resolved-scale equation evaluated by quadrature, the second summand, i.e. the negative residual of the strong advective form, will cancel out all of the GALERKIN terms which have not been integrated by parts. The cancelled terms are now contained implicitly in the representation of the subgrid velocity in the first term on the right hand side of equation (4.70). The terms which have been integrated by parts, i.e. the viscous and the pressure term will not introduce additional difficulties. Nevertheless, the first term is equivalent to a contribution

$$-\sum_e \left(\frac{1}{\tau_{\text{M}}^{\text{VX}\ominus\Delta t}} \cdot \tilde{\mathbf{u}}^{n+\alpha_F}; \mathbf{v}^h \right)_{\Omega_e} \quad (4.71)$$

to the nonlinear system. In this contribution, the inverse stabilisation parameter introduces a significant nonlinearity with respect to its dependence on the velocity. This can be illustrated using the stabilisation parameter (3.156). For this parameter, one obtains

$$\frac{1}{\tau_{\text{M}}^{\text{VI}\ominus\Delta t}} = \frac{2}{m_e} \cdot \frac{\|\mathbf{u}^{h,n+\alpha_F}\|}{h_e} + \frac{4}{m_e} \cdot \frac{\nu}{h_e^2}. \quad (4.72)$$

and thus (4.71) is equivalent to

$$-\sum_e \left(\frac{2}{m_e} \cdot \frac{\|\mathbf{u}^{h,n+\alpha_F}\|}{h_e} \cdot \tilde{\mathbf{u}}^{n+\alpha_F}; \mathbf{v}^h \right)_{\Omega_e} - \sum_e \left(\frac{4}{m_e} \cdot \frac{\nu}{h_e^2} \cdot \tilde{\mathbf{u}}^{n+\alpha_F}; \mathbf{v}^h \right)_{\Omega_e}. \quad (4.73)$$

Once more, the second term in this equation will not be problematic. Nevertheless, the first term contains the nonlinear contribution

$$\|\mathbf{u}^{h,n+\alpha_F}\| \cdot \tilde{\mathbf{u}}^{n+\alpha_F} \quad (4.74)$$

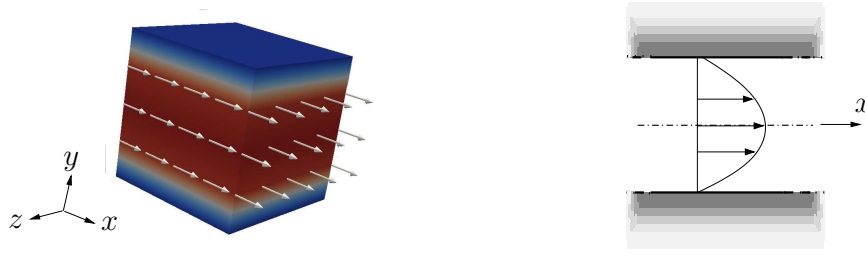


Figure 4.3: Laminar flow through a plane channel which will be used to investigate the influence of the time-dependent subgrid representation on the nonlinearity of the resolved-scale equation.

which can be expected to have a significant impact because of the h_e^{-1} -scaling. The possibility of a linearisation of the nonlinear term (4.74) is limited by the fact that the norm of the velocity $\|\mathbf{u}^{h,n+\alpha_F}\|$ is not differentiable for $\mathbf{u}^{h,n+\alpha_F} = \mathbf{0}$.

For a further illustration of this problem, the results for a very simple test case will be presented. A laminar flow through a 5^3 element channel with no-slip DIRICHLET boundary conditions on the top and bottom wall and periodic boundary conditions on all other sides is considered, see Figure 4.3. The flow is driven by a constant pressure gradient and started from a zero initial velocity field. Due to the symmetry of the problem, the expected solution is a parabolic velocity profile. All vectors are oriented in x direction, the nonlinear convective term in the GALERKIN part vanishes. Solved with a conventional subgrid closure, the iteration behaviour clearly indicates the vanishing nonlinearity in the GALERKIN part, i.e. for each time step the residual of the nonlinear iteration is smaller than 10^{-6} after the first nonlinear iteration step. This is visualised in Figure 4.4. For the time-dependent subgrid closure, the picture is different. In order to be able to trace back the introduced nonlinearity to the velocity dependence of the stabilisation parameter, the parameter $\tau_M^{V2\ominus\Delta t}$ from equation (3.160) was chosen. In the beginning, the velocity in this test problem is so small that the velocity dependence of the parameter is deactivated by the max operation involved in its definition. For the parameter choice under consideration, this was observed to happen for steps one to four. In all following steps, the velocity contribution was active. Looking at the numbers of iterations required to solve the nonlinear system in each time step, as they are displayed in Figure 4.4, a sudden increase can be observed as soon as the

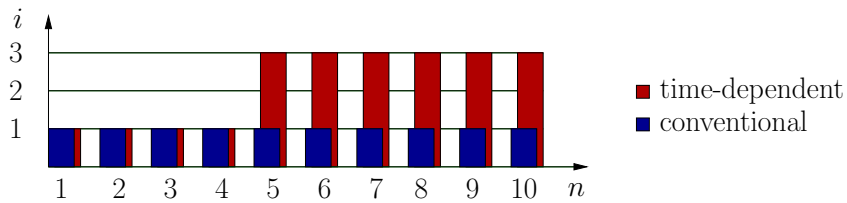


Figure 4.4: For a time-dependent subgrid approximation, the number of iterations i required to solve the nonlinear problem in each time step n increases as soon as the velocity dependence in the stabilisation parameter gets active.

velocity dependence gets active in the stabilisation parameter.

A consequence for practical computations is that computations using a time-dependent subgrid approximation require a slightly smaller time step to run stable than the corresponding problems based on a conventional subgrid approximation.

4.4.5 Conservative EULERian resolved-scale equation

For the conservative EULERian form, the counterpart to equation (4.57) can as well be separated in a GALERKIN part

$$\begin{aligned}
 R_{\mathbf{u}}^{\text{Gal}}(\mathbf{u}^{h,n+1}, p^{h,n+1}, \mathbf{v}^h) &= \\
 &= (\dot{\mathbf{u}}^{h,n+\alpha_M}; \mathbf{v}^h)_{\Omega(t^{n+1})} - \frac{1}{\rho} (p^{h,n+1}, \nabla \cdot \mathbf{v}^h)_{\Omega(t^{n+1})} - \\
 &- (\mathbf{u}^{h,n+\alpha_F}; (\mathbf{u}^{h,n+\alpha_F} \cdot \nabla) \mathbf{v}^h)_{\Omega(t^{n+1})} + \\
 &+ 2\nu (\boldsymbol{\varepsilon}(\mathbf{u}^{h,n+\alpha_F}); \boldsymbol{\varepsilon}(\mathbf{v}^h))_{\Omega(t^{n+1})} - (\mathbf{b}^{n+\alpha_F}; \mathbf{v}^h)_{\Omega(t^{n+1})}
 \end{aligned} \tag{4.75}$$

and element-specific subgrid contributions

$$\begin{aligned}
 \square_e &= (\tilde{\mathbf{u}}^{n+\alpha_M}; \mathbf{v}^h)_{\Omega_e} - (\mathbf{u}^{h,n+\alpha_F}; (\tilde{\mathbf{u}}^{n+\alpha_F} \cdot \nabla) \mathbf{v}^h)_{\Omega_e} - \\
 &- (\tilde{\mathbf{u}}^{n+\alpha_F}; (\mathbf{u}^{h,n+\alpha_F} \cdot \nabla) \mathbf{v}^h)_{\Omega_e} - (\tilde{\mathbf{u}}^{n+\alpha_F}; (\tilde{\mathbf{u}}^{n+\alpha_F} \cdot \nabla) \mathbf{v}^h)_{\Omega_e} - \\
 &- \frac{1}{\rho} (\tilde{p}^{n+1}, \nabla \cdot \mathbf{v}^h)_{\Omega_e}.
 \end{aligned} \tag{4.76}$$

Compared to the subgrid expressions of the convective form in equation (4.59), the cross-stress term

$$- (\mathbf{u}^{h,n+\alpha_F}; (\tilde{\mathbf{u}}^{n+\alpha_F} \cdot \nabla) \mathbf{v}^h)_{\Omega_e} \tag{4.77}$$

has changed. As in the convective case, the viscous term is neglected and thus not included in equation (4.76) anymore. Furthermore, the time derivative of the subgrid velocity is considered only for the time-dependent subgrid approximation.

4.4.6 Implementation

The solution process for the resolved-scale equation is based on the nonlinear predictor-corrector scheme which was introduced in subsection 3.4.4. The right hand side of equation system (3.127) now consists of the discretised residual of the resolved-scale equations for momentum (4.57) and continuity (4.55):

$$\left[\left(\underline{R}_{\mathbf{u}} \right)_{(i)} \right]_{3 \cdot (A-1) + k} = R_{\mathbf{u}} \left(\mathbf{u}_{(i)}^{h,n+1}, p_{(i)}^{h,n+1}, N_A \mathbf{e}_k \right) \tag{4.78}$$

$$\left[\left(\underline{R}_p \right)_{(i)} \right]_A = R_p \left(\mathbf{u}_{(i)}^{h,n+1}, p_{(i)}^{h,n+1}, N_A \right) \tag{4.79}$$

For the approximation of the corresponding tangent matrix, several strategies can be applied.

(N) NEWTON-like strategy

For this approach, the whole discretised residual is linearised except for the stabilisation parameters which are treated in a fixed-point manner. This is computationally the most expensive way to set up the linear system. Nevertheless, it provides the best approximation to the tangent and thus the highest rate of convergence for the nonlinear iteration. Although NEWTON's iteration is well-known to have only local convergence properties, convergence problems were not encountered for the chosen time steps in the problems considered in this thesis.

(F) Fixed-point-like strategy

In addition to the stabilisation parameter contributions, this approach omits all tangent contributions that are reactive type linearisations of convective expressions.

(M) Minimal linearisation strategy

The minimal approach is a fixed-point-like strategy for which additionally all linearisations of subgrid terms involving the viscosity are dropped. This is by far the cheapest way to set up a system matrix. If the user is interested only in a limited accuracy, the viscosity is very small and the problem is computed at a small time step, this strategy is very efficient.

Appendix D contains a detailed listing of all matrix contributions for the three schemes.

4.5 Weak DIRICHLET boundary conditions in residual-based variational multiscale modelling of turbulent flows

In turbulent flows, the resolution requirements close to walls are especially high. Thus, a common approach in LES is to use known empirical relations for the near-wall velocities in order to improve the quality of the solution for a given finite resolution. The framework of variational multiscale modelling of turbulence provides a straightforward possibility to include such wall laws in a variationally consistent way using weak DIRICHLET boundary conditions.

The type of method that will be used here to impose these weak DIRICHLET boundary conditions dates back to a work by NITSCHKE [165] in 1971. It can be understood as a special choice for a stabilised formulation of a LAGRANGE-multiplier approach as it was introduced by BABUŠKA [5]. A discussion of this close relation between the two approaches can be found in STENBERG [194]. As it is pointed out in HUERTA and FERNÁNDEZ-MÉNDEZ [75], this method of imposing essential boundary conditions can be understood as a consistent improvement of a penalty method. In contrast to a LAGRANGE-multiplier approach, no additional degrees of freedom for multipliers and corresponding weighting functions have to be introduced in this formulation.

The weak imposition of no-slip DIRICHLET boundary conditions in the tangential direction for wall-bounded fluid flows was encouraged by BAZILEVS and HUGHES in [19]. The formulation provided in that publication was modified to incorporate a wall model, i.e. SPALDING's law (2.104), for wall-bounded turbulent flows in BAZILEVS et al. [21]. In the simulation of flows about rotating components in BAZILEVS and HUGHES [20], the formulation was extended to include weak conditions also in boundary-normal direction. Additionally, HANSBO et al. [108] invoked a weak coupling based on NITSCHKE's method for fluid-structure interaction problems using a space-time finite element approach.

4.5.1 Required extensions to the weak form

Let τ_B be a suitable element-specific stability parameter that will be defined below and $\gamma_{\text{wdbc}} = 1$ the constant that defines the adjoint consistent approach. Furthermore, let $\Gamma_{D,\text{weak}}(t^{n+1})$ define the DIRICHLET boundary on which the conditions have to be imposed weakly. Then, the extended weak form of equation (3.99) with a weak imposition of DIRICHLET boundary conditions reads

$$\begin{aligned}
 R_{\mathbf{u}}(\mathbf{u}^{h,n+1}, p^{h,n+1}, \mathbf{v}^h) &= \dots + \\
 &+ \left(\frac{1}{\rho} p^{h,n+1}, \mathbf{v}^h \cdot \mathbf{n} \right)_{\Gamma_{D,\text{weak}}(t^{n+1})} - \\
 &- 2\nu \left(\boldsymbol{\varepsilon}(\mathbf{u}^{h,n+\alpha_F}) \cdot \mathbf{n}; \mathbf{v}^h \right)_{\Gamma_{D,\text{weak}}(t^{n+1})} - \\
 &- 2\nu \gamma_{\text{wdbc}} \left(\mathbf{u}^{h,n+\alpha_F} - \mathbf{u}_D^{h,n+\alpha_F}; \boldsymbol{\varepsilon}(\mathbf{v}^h) \cdot \mathbf{n} \right)_{\Gamma_{D,\text{weak}}(t^{n+1})} - \\
 &- \left(\mathbf{u}^{h,n+\alpha_F} - \mathbf{u}_D^{h,n+\alpha_F}; \{ \mathbf{c}^{h,n+\alpha_F} \cdot \mathbf{n} \}_- \mathbf{v}^h \right)_{\Gamma_{D,\text{weak}}(t^{n+1})} + \\
 &+ \left(\tau_B \left(\mathbf{u}^{h,n+\alpha_F} - \mathbf{u}_D^{h,n+\alpha_F} \right); \mathbf{v}^h \right)_{\Gamma_{D,\text{weak}}(t^{n+1})} = 0
 \end{aligned} \tag{4.80}$$

for the momentum part and

$$\begin{aligned}
 R_p(\mathbf{u}^{h,n+1}, p^{h,n+1}, q^h) &= \\
 &= \dots - \left(\left(\mathbf{u}^{h,n+1} - \mathbf{u}_D^{h,n+1} \right) \cdot \mathbf{n}, q^h \right)_{\Gamma_{D,\text{weak}}(t^{n+1})} = 0
 \end{aligned} \tag{4.81}$$

for the continuity part. All additional inner products in these equations are evaluated by integration over $\Gamma_{D,\text{weak}}(t^{n+1})$. The function $\{ \cdot \}_-$ defined in equation (3.174) is used to restrict the enforcement of DIRICHLET boundary conditions in the hyperbolic limit to the part of the boundary with an inflow. In contrast to BAZILEVS and HUGHES [20], this formulation uses the ALE convective velocity in the fifth line of (4.80). This is not a contradiction since the approach in that reference is designed for rigid body mesh rotations of circular domains, in which the mesh velocity is always tangential to the boundary by definition.

The summands in the second and third line of equation (4.80) arise from partial integration during construction of the weak form. They are required for consistency. The corresponding adjoint consistency terms are located in line two of equation (4.81) and line four of equation (4.80), respectively. These adjoint consistency terms can be motivated by the fact that the GAUSS divergence theorem is applicable only to the interior of the domain, since the difference between

weakly imposed boundary velocity and prescribed DIRICHLET velocity can be interpreted as a jump in the trial function which has to be accounted for by a special source term on the boundary for the integral balance equations. Finally, line six of equation (4.80) contains a penalty-like term that is required for the stability of the approximation. Possible choices for the penalty parameter τ_B will be provided in the following.

4.5.2 Definition of τ_B

The most straightforward definition for the penalty, i.e. stability, parameter τ_B is given in BAZILEVS and HUGHES [19]:

$$\tau_B = \frac{C_B \nu}{h_B} \quad (4.82)$$

The element length in the direction normal to the boundary is estimated using the boundary normal \mathbf{n} and the covariant metric tensor from equation (3.148) by

$$h_B = \frac{2}{\sqrt{\mathbf{n} \cdot (\mathbf{G}\mathbf{n})}} \quad (4.83)$$

C_B is a positive constant related to the local boundary inverse estimate. In the implementation of this thesis, the constant is taken to $C_B = 4.0$ as suggested in the example contained in BAZILEVS and HUGHES [19]. Nevertheless, this constant can also be estimated for instance as the maximum eigenvalue of a generalised eigenvalue problem as it was motivated by GRIEBEL and SCHWEITZER [104], see also HUERTA and FERNÁNDEZ-MÉNDEZ [75].

Wall-law-based extension

In the following, a brief review of the results of BAZILEVS et al. [21] concerning the incorporation of a wall law will be given. This formulation is designed for the EULERian description of a wall-bounded flow with no-slip DIRICHLET condition $\mathbf{u}_D \equiv \mathbf{0}$ on the wall. The no penetration condition $\mathbf{u} \cdot \mathbf{n}$ on the wall is included as a strong DIRICHLET condition, only the tangential components are enforced weakly. The strong enforcement of the boundary condition in normal direction implicates several redundant terms in the weak forms (4.80) and (4.81). The equations can be rewritten as

$$\begin{aligned} R_{\mathbf{u}}(\mathbf{u}^{h,n+1}, p^{h,n+1}, \mathbf{v}^h) = & \dots + \\ & - 2\nu (\boldsymbol{\varepsilon}(\mathbf{u}^{h,n+\alpha_F}) \cdot \mathbf{n}; \mathbf{v}^h)_{\Gamma_{D,\text{weak}}(t^{n+1})} - \\ & - 2\nu \gamma_{\text{wdbc}} (\mathbf{u}^{h,n+\alpha_F}; \boldsymbol{\varepsilon}(\mathbf{v}^h) \cdot \mathbf{n})_{\Gamma_{D,\text{weak}}(t^{n+1})} + \\ & - \left((\tau_B \cdot \|\mathbf{u}^{h,n+\alpha_F}\|) \cdot \left(-\frac{\mathbf{u}^{h,n+\alpha_F}}{\|\mathbf{u}^{h,n+\alpha_F}\|} \right); \mathbf{v}^h \right)_{\Gamma_{D,\text{weak}}(t^{n+1})} = 0 \\ R_p(\mathbf{u}^{h,n+1}, p^{h,n+1}, q^h) = & 0. \end{aligned} \quad (4.84)$$

For the incorporation of a wall law, the penalty term in equation (4.84) is identified with a wall shear stress that is normalised by the density. Instead of setting strong DIRICHLET conditions at the boundary, the weak formulation will set a boundary traction derived from a wall law via this term.

The induced boundary stress is obviously acting parallel to $\mathbf{u}^{h,n+\alpha_F}$ on the weak DIRICHLET boundary $\Gamma_{D,\text{weak}}(t^{n+1})$. Its magnitude is given as

$$\frac{\tau_w}{\rho} = u_{\tau_w}^2 = \tau_B \cdot \|\mathbf{u}^{h,n+\alpha_F}\|. \quad (4.85)$$

In this equation, the friction velocity (2.86) was used. For a given estimate of the mean velocity and a given estimate for the thickness of the unresolved boundary layer, this traction and thus the stabilisation parameter τ_B are defined implicitly using SPALDING's law (2.104).

The estimate y for the thickness of the unresolved boundary layer is chosen in the order of magnitude of the distance of the first node to the wall. BAZILEVS et al. [21] suggest

$$y = \frac{h_B}{C_B} \quad (4.86)$$

and thus using equations (4.85) and (2.89)

$$y^+ = \frac{h_B}{C_B} \cdot \frac{u_{\tau_w}}{\nu} = \frac{h_B}{C_B \nu} \cdot \sqrt{\tau_B \cdot \|\mathbf{u}^{h,n+\alpha_F}\|}. \quad (4.87)$$

Furthermore, in that reference, $\|\mathbf{u}^{h,n+\alpha_F}\|$ is taken as an estimate for the mean velocity yielding the approximation

$$u^+ \approx \frac{\|\mathbf{u}^{h,n+\alpha_F}\|}{u_{\tau_w}} = \sqrt{\frac{\|\mathbf{u}^{h,n+\alpha_F}\|}{\tau_B}}. \quad (4.88)$$

The combination of equations (4.87), (4.88) and SPALDING's law (2.104) finally results in a single nonlinear equation for the unknown stabilisation parameter τ_B . This scalar equation has to be solved by a NEWTON procedure in every integration point on the weak DIRICHLET boundary every time the linear system (3.127) is set up.

Decoupling of wall-normal and tangential penalty term

In a generalisation of equation (4.80), the penalty parameter τ_B can be extended to a matrix valued quantity

$$\tau_B \longrightarrow \boldsymbol{\tau}_B = \tau_{B,\text{tangential}} \cdot (\mathbf{1} - \mathbf{n} \otimes \mathbf{n}) + \tau_{B,\text{normal}} \cdot (\mathbf{n} \otimes \mathbf{n}). \quad (4.89)$$

This idea, which can also be found in BAZILEVS et al. [22], enables a separate treatment of tangential and normal components of the penalty term.

For instance, the matrix valued extension allows to use a wall-law-based definition of $\tau_{B,\text{tangential}}$ in tangential direction while in wall-normal direction, the part of the penalty term which cannot be associated with a wall shear stress can be treated in the usual way using an appropriate constant value $\tau_{B,\text{normal}}$.

4.5.3 Nonlinearity, implementation issues

Weak DIRICHLET conditions are set implicitly, i.e. the actual values on $\Gamma_{D,\text{weak}}(t^{n+1})$ are defined by the solution of the nonlinear system (4.80), (4.81). Thus, the extra terms in these equations will correspond to extra modifications of the system matrix and of the right hand side

of equation system (3.127). Since derivatives of weighting and trial functions are involved in these extra terms, the modifications are not restricted to the degrees of freedom associated with $\Gamma_{D,\text{weak}}(t^{n+1})$ but also affect adjacent degrees of freedom. Furthermore, the term in the fifth line of equation (4.80) introduces another nonlinearity into the weak form of the NAVIER-STOKES equations. Since this nonlinearity involves $\{x\}_-$, a non-differentiable function at $x = 0$, it is hard to deal with in the context of a NEWTON's iteration which is used to solve the nonlinear system set up by equations (3.121) and (3.122). For higher REYNOLDS number applications, it is often recommended to drop the matrix contribution associated with this non-smooth term, i.e. to perform a fixed-point type iteration with respect to this nonlinearity. Compared to a NEWTON-type linearised formulation based on strong DIRICHLET boundary conditions, the rate of convergence of the weak approach will be reduced. Nevertheless, the fixed-point type treatment of the non-smooth term is often required for the stability of the nonlinear procedure in the case of weak DIRICHLET boundary conditions. In the simplified setting of equation (4.84), this problem naturally disappears due to the strong imposition of the non-penetration condition which eliminates the additional nonlinearity.

5 Residual-based time-dependent subgrid-scale modelling of plane channel turbulence

In this chapter, turbulent flow through a plane channel is used to investigate basic properties of residual-based variational multiscale models for turbulence. The flow, which was already used as an illustrative example in Figure 2.4, is well suited for model evaluation for the following reasons: The two homogeneous directions allow a convenient computation of averaged quantities, the flow includes wall effects, DNS data is available for several REYNOLDS numbers, and the theory of these flows is well understood. See also subsection 2.2.5 and references therein.

The residual-based models used in this chapter will mostly be based on the convective form of the equations. Only the investigations of section 5.6 will be based on the conservative form. In general, the computations were done using the minimal linearisation approach, as it can be found in subsection 4.4.6. For the comparably small time step sizes used in the computations of this chapter, this turned out to be a good choice.

The chapter is structured as follows. At the beginning, the problem setup for all investigated test cases will be provided in section 5.1. Afterwards, the averaging strategies applied to compute mean quantities are described in section 5.2. The third section 5.3 is intended to provide some further information on the nature of isogeometric finite element implementations and on the performance of serendipity elements for turbulent channel flow computations. Section 5.4 summarises the improvements due to a consideration of the time-dependency of the subgrid scales and shows which properties remain unaffected. The performance of various element length definitions and choices of stabilisation parameters for stretched boundary layer meshes is examined in section 5.5. The chapter is concluded by a section on the analysis of modelled turbulent dissipation in section 5.6, paying special attention to the different subgrid approximations and to the influence of the element type.

5.1 Problem setup

The infinitely extended plane channel is represented by a characteristic box-shaped domain of size $l_x \times l_y \times l_z$. In the homogeneous, streamwise (x) and spanwise (z) direction, periodic boundary conditions are assumed. On the top and bottom wall, no-slip DIRICHLET boundary conditions hold. The flow is driven by a constant pressure gradient which is applied as it is described in subsection 3.7.5.

The domain sizes and material parameters used for the test cases are given in Table 5.1. All DNS data which will be used as a reference for the resolved-scale quantities is taken from MOSER et al. [163]. Note that in the $Re_\tau = 395$ case, the geometry deviates slightly from

| Re_τ | Re_c | l_x | $l_y = 2\delta$ | l_z | ν | ρ | $(\nabla p)_x$ |
|-----------|--------|--------|-----------------|------------------|-------------|--------|----------------|
| 180 | 3300 | 2π | 2 | $\frac{4}{3}\pi$ | 0.000357 | 1.0 | 0.00413 |
| 395 | 8000 | 2π | 2 | $\frac{2}{3}\pi$ | 0.0001472 | 1.0 | 0.00337204 |
| 590 | 12600 | 2π | 2 | π | 0.001694915 | 1.0 | 1.0 |

Table 5.1: Channel geometry, material parameters and forcing by pressure gradient in stream-wise direction $(\nabla p)_x$. Re_c is the REYNOLDS number defined using the channel half-height and the centre-line velocity, Re_τ is the REYNOLDS number based on the wall shear stress and the channel half-height.

the one in MOSER et al. [163]. The spanwise length for this case was chosen to be able to compare the results to other existing LES computations by BAZILEVS et al. [15].

All computations were carried out on structured meshes. A hyperbolic mesh stretching according to

$$h : [-1, 1] \rightarrow [-1, 1], \quad y \mapsto h(y) = \frac{\tanh(C_{\text{stretch}} \cdot y)}{\tanh(C_{\text{stretch}})} \quad (5.1)$$

was applied in order to get a sufficient refinement of the boundary-layer mesh close to the wall. Its characteristics are shown in Figure 5.1. For eight-noded trilinear (HEX8) elements, the

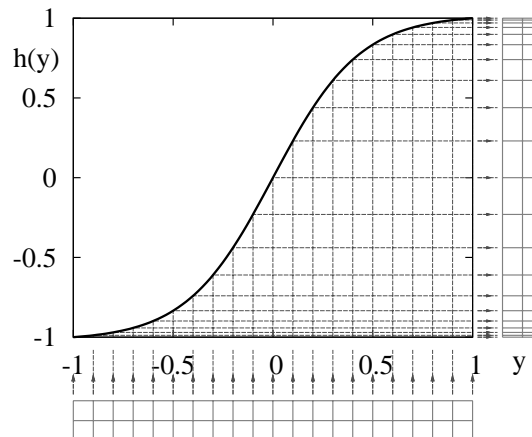


Figure 5.1: The unstretched mesh on the bottom is transformed into the stretched boundary layer mesh on the right by a hyperbolic mesh stretching function $h(y)$.

stretching was applied to the y -coordinate of all nodes. For twenty-noded serendipity (HEX20) elements, the stretching was only applied to nodes located at the corner of an element. Interior nodes were placed in the middle between the corner nodes, as usual. Application of a mesh-stretching in the context of second order NURBS (NURBS27) elements means that the stretching is applied to the knot vector associated with the wall-normal direction.

All investigated discretisations are listed in Table 5.2. The table contains detailed information on the mesh stretching which can have a certain influence on the results, see JOHN and ROLAND [136] for a comparison of cosine and hyperbolic mesh stretchings. In addition to the

| Re_τ | element type | n_{ele} | n_{np} | $C_{stretch}$ | y_{first}^+ |
|-----------|--------------|-----------|----------|---------------|---------------|
| 180 | HEX8 | 32^3 | 35937 | 2.1 | 1.6 |
| | HEX8 | 64^3 | 274625 | 1.7 | 1.3 |
| | HEX20 | 16^3 | 18785 | 2.4 | 1.2 |
| | HEX20 | 32^3 | 140481 | 1.9 | 1.1 |
| | NURBS27 | 25^3 | 19683 | 2.1 | 1.1 |
| 395 | HEX8 | 32^3 | 35937 | 2.75 | 1.4 |
| | NURBS27 | 32^3 | 39304 | 2.3 | 1.3 |
| 590 | HEX8 | 64^3 | 274625 | 2.5 | 1.3 |

Table 5.2: Investigated spatial discretisations. n_{ele} is the number of elements, n_{np} is the number of nodes respectively control points, $C_{stretch}$ the mesh stretching constant and y_{first}^+ the distance of the first node to the wall.

mesh stretching constant $C_{stretch}$, the quantity y_{first}^+ is listed for all meshes. For HEX8 elements it is equivalent to the height of an element next to the wall. For HEX20, it corresponds to the position of the first interior node, i.e. half of the first element's height. Finally, for NURBS27 elements, this quantity corresponds to the position of the first control point away from the wall. For LES, a value of y_{first}^+ sufficiently close to one is desirable, a requirement that all meshes employed fulfil.

All computations were started from a randomly perturbed initial laminar flow profile. For computations based on time-dependent subgrid scales, all subgrid quantities were initialised to zero in the beginning.

5.2 Averaging procedures

All results will be reported in the form of statistics which are obtained after a statistically steady state has been achieved. Exploiting the symmetries of the problem, statistical data for a sample value X is obtained by a sequential averaging process in space $\langle \cdot \rangle_{space}$ and time $\langle \cdot \rangle_{time}$, i.e.

$$\langle X \rangle_{space,time} = \left\langle \langle X \rangle_{space} \right\rangle_{time} . \quad (5.2)$$

5.2.1 Time averages

The time average is computed as the arithmetic mean over N consecutive time steps

$$\langle X \rangle_{space,time} = \frac{1}{N} \sum_{n=1}^N \langle X_n \rangle_{space} . \quad (5.3)$$

N is chosen such that the sampling period corresponds to a value between 15 and 45 flow-through times. Usually, flows with a low REYNOLDS number are associated with a longer

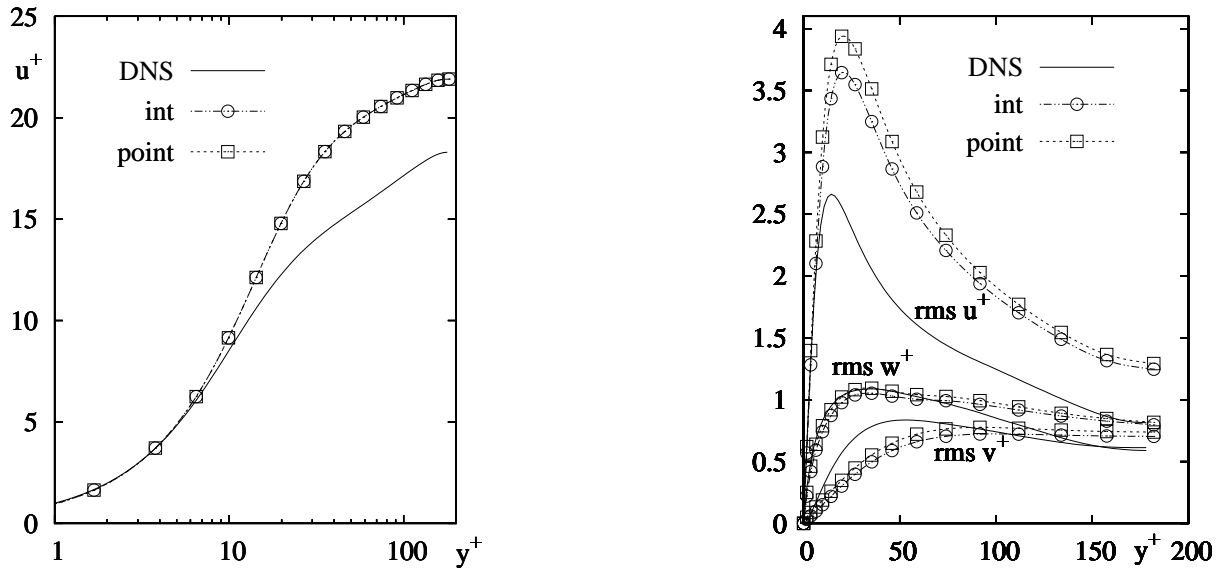


Figure 5.2: Mean streamwise velocity and root-mean-square values of velocity fluctuations in wall coordinates for integration-based (int) and pointwise (point) spatial averaging for 32^3 HEX8 elements, $Re_\tau = 180$.

sampling time in order to obtain meaningful statistics. For a choice of the time step size in the order of magnitude that was proposed by CHOI and MOIN [47] for numerical simulation of turbulent flow, $N = 5000$ was found to be a reasonable value.

5.2.2 Spatial averaging for resolved-scale quantities

Spatial averaging of resolved-scale quantities at any time level is done by integration over wall-parallel planes

$$\langle X_n \rangle_{\text{space}} = \frac{1}{\int 1 dx dz} \int X_n dx dz. \quad (5.4)$$

The integrals are evaluated numerically using GAUSS quadrature, a procedure that is equally applicable to HEX8, HEX20 and NURBS27 elements.

In contrast, the widely-used approach to compute spatial averages as the arithmetic mean of nodal values is not feasible for HEX20 and NURBS27 elements. For HEX20 elements, this statement is based on the observation that the finite element solution in a cutting-plane normal to the y -axis in the middle of an element depends not only on the values of the nodes in that plane but also on values of the remaining nodes. For NURBS27 approaches, the nodal values correspond to control point values which have to be transformed first into a physical meaningful quantity by interpolation using the shape functions.

Although being consistent for all element types considered, the integration-based averaging procedure will predict slightly smaller fluctuations than the ones computed by nodal averaging, even in the HEX8 case. The reason for this is that the second-order moments in the quadrature points are calculated using the interpolated velocity. Figure 5.2 exemplifies this fact by comparison of results for both pointwise (point) and integration-based (int) spatial averaging. The

results in Figure 5.2 belong to the identical turbulent channel flow computation at $Re_\tau = 180$ on a 32^3 HEX8 mesh. As expected, there is no difference for the mean velocity. Nevertheless, the quadrature/integration-based averaging exhibits slightly lower values for the root-mean-square value (rms) of the fluctuations. For a sufficiently high grid resolution, both procedures will converge to the same result. A priori, we cannot expect one of the averaging procedures to be more accurate than the other. However, the difference between the averaging procedures gives an indication about the size of a ‘significant’ difference between the results of two simulation approaches.

5.2.3 Spatial averaging for unresolved-scale related data

Spatial averages for subgrid related data like stabilisation parameters, residuals, subgrid-scale velocities and accelerations are computed by an average over GAUSS-point values in a complete wall-parallel layer of elements. The results are displayed along the wall-normal direction of the channel. For this purpose, the value of each element layer is associated with the y^+ -coordinate of the layer’s centre plane, see Figure 5.3 for an illustration.

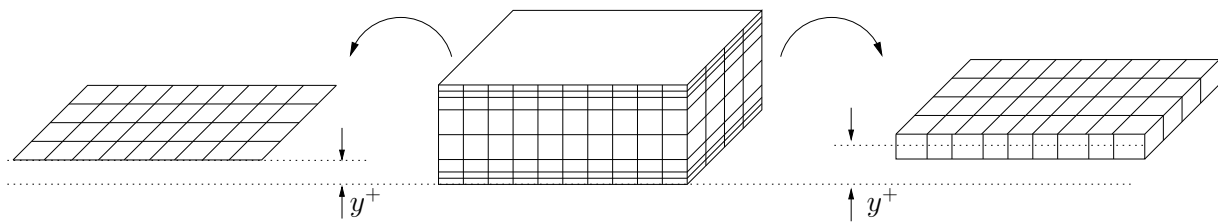


Figure 5.3: Spatial averaging of resolved-scale quantities is performed in wall-parallel planes along element boundaries (left). All obtained results are plotted against the distance of the plane to the wall in wall units. Averaging of quantities associated with the unresolved-scale approximation is done over volume slices (right). These results are plotted against the distance of the elements centre to the wall in wall units.

5.3 Size and sparsity of system matrices in residual-based variational multiscale modelling of turbulence

In this section, the sparsity structure arising from an isogeometric representation, as it was already dealt with in subsection 3.4.5, will be revisited. For this purpose, three spatial discretisations are compared. A mesh of 64^3 HEX8 elements, a mesh of 32^3 HEX20 elements and a mesh consisting of 32^3 NURBS27 elements.

5.3.1 Matrix structure

All three discretisations yield matrix representations for which the number of non-zeros is between $0.6 \cdot 10^8$ and $1.2 \cdot 10^8$, see Table 5.3. The structure of the sparse matrices involved in the

| element type | 64^3 HEX8 | 32^3 HEX20 | 32^3 NURBS27 |
|----------------------------------|--------------------|--------------------|--------------------|
| nnz | $1.138 \cdot 10^8$ | $1.235 \cdot 10^8$ | $0.672 \cdot 10^8$ |
| ndof | 1 064 960 | 536 576 | 139 264 |
| $\frac{\text{nnz}}{\text{ndof}}$ | 106.8 | 230.1 | 482.4 |

Table 5.3: Number of non-zeros on matrix (nnz) and ratio between nnz and number of unknowns (ndof). The quotient $\frac{\text{nnz}}{\text{ndof}}$ can be seen as a kind of measure for the degree of sparsity of the matrix. Note that in comparison to serendipity elements, triquadratic elements would have a larger number of degrees of freedom.

three discretisations is completely different. The 32^3 NURBS27 mesh yields a matrix in which the number of rows is much smaller than for the other two approaches. HEX8 elements have the lowest connectivity, yielding the least dense system matrix of all approaches considered. In comparison to the trilinear mesh or a corresponding triquadratic mesh, the use of serendipity elements in the 32^3 HEX20 case decreases the number of degrees of freedom by nearly fifty percent. The level of sparsity is situated in the middle of the values obtained for NURBS27 and HEX8 matrices. Based on the resulting number of non-zeros on the matrix, a matrix-vector multiplication in the 32^3 HEX20 case can be expected to be only about twice as expensive as in the 32^3 NURBS27 case. Since matrix-vector multiplications have a significant contribution to the amount of work required in an iterative solution procedure, see section E, it turns out that from the computational effort point of view 32^3 HEX20 discretisations are competitive with 32^3 NURBS27 discretisations.

In order to provide the reader with more information on the solution behaviour of the linear system in the three cases, this subsection will be concluded by some practical remarks on the iterative behaviour of the three approaches in the linear solution process. Although the number of non-zeros in the trilinear case is nearly as large as in the serendipity case, the iteration was found to converge at a faster rate in practice. The HEX20 as well as the NURBS27 case are much more demanding with respect to the choice of a good preconditioner. In these cases, the best choice among the methods mentioned in subsection E.1 were found to be multi-level preconditioners using symmetric GAUSS-SEIDEL smoothers with excessive relaxation on the finer levels. Finally, a comparison of NURBS27 and HEX20 problems showed that the HEX20 problem required more iterations to reach the required tolerance than its isogeometric counterpart. Thus, the NURBS27 version can be said to be more efficient than the HEX20 approach, but the difference is by far not as significant as it would be for triquadratic elements.

5.3.2 Resolved-scale results for the investigated discretisations

Having compared the system matrices and the required effort for a solution of the corresponding linear problem, this subsection provides a comparison of the mean velocity and the velocity fluctuations at $\text{Re}_\tau = 180$. The results for the 32^3 NURBS27 case are taken from the paper by AKKERMAN et al. [3], where a comparison to a 16^3 triquadratic finite element discretisation was performed. The results for the HEX20 and HEX8 case can be understood as an add-on to the work of GRAVEMEIER et al. [98] with a higher resolution and an updated sampling process according to section 5.2. The HEX8 and HEX20 computations were performed using a time step size of

$$\Delta t^+ = \Delta t \cdot \frac{u_{\tau_w}^2}{\nu} = 0.7 \quad (5.5)$$

which is in the range that was suggested by CHOI and MOIN [47]. They are based on a conventional subgrid closure using the stabilisation parameter definitions $\tau_M^{V3\oplus\Delta t}$ and $\tau_C^{V3\oplus\Delta t}$, see subsection 3.5.2 for a definition.

The results can be found in Figure 5.4. The numerical value for Re_τ obtained in the HEX20 case was 180.3 and 180.2 for the HEX8 setting. The results show that assuming a correct sampling and a sufficient resolution, serendipity elements are capable of reaching the accuracy of isogeometric approximations with a computational effort that is only slightly higher due to the increased solver time.

5.4 Benefits of a time-dependent subgrid representation

In this section, the main results of GAMNITZER et al. [85] will be summarised in order to point out advantages of a time-dependent subgrid representation. For this purpose, a comparison to the conventional approach with respect to resolved-scale quantities will be performed in subsection 5.4.1. Results will be presented for three REYNOLDS numbers, $\text{Re}_\tau = 180$ (32^3 HEX8, 16^3 HEX20), $\text{Re}_\tau = 395$ (32^3 HEX8) and $\text{Re}_\tau = 590$ (64^3 HEX8). For $\text{Re}_\tau = 395$, an investigation of the behaviour for a series of time step sizes will be performed. Although the impact of the time-dependent subgrid representation on resolved-scale quantities can be observed to be very small, subsection 5.4.2 shows that it allows a much more robust representation of unresolved-scale velocities with respect to a variation of the time step size.

All conventional residual-based variational multiscale computations in this section were performed using stabilisation parameters $\tau_M^{V2\oplus\Delta t}$ and $\tau_C^{V2\oplus\Delta t}$ according to equations (3.158) and (3.159). The time-dependent subgrid counterparts were computed using $\tau_M^{V2\ominus\Delta t}$ and $\tau_C^{V2\ominus\Delta t} = \tau_C^{V2\oplus\Delta t}$ according to equations (3.160) and (3.159). Throughout this section, results obtained with conventional residual-based models will be associated with a blue colour and the abbreviation ‘rV’, results obtained by a time-dependent subgrid modelling will be associated with a red colour and the abbreviation ‘td’.

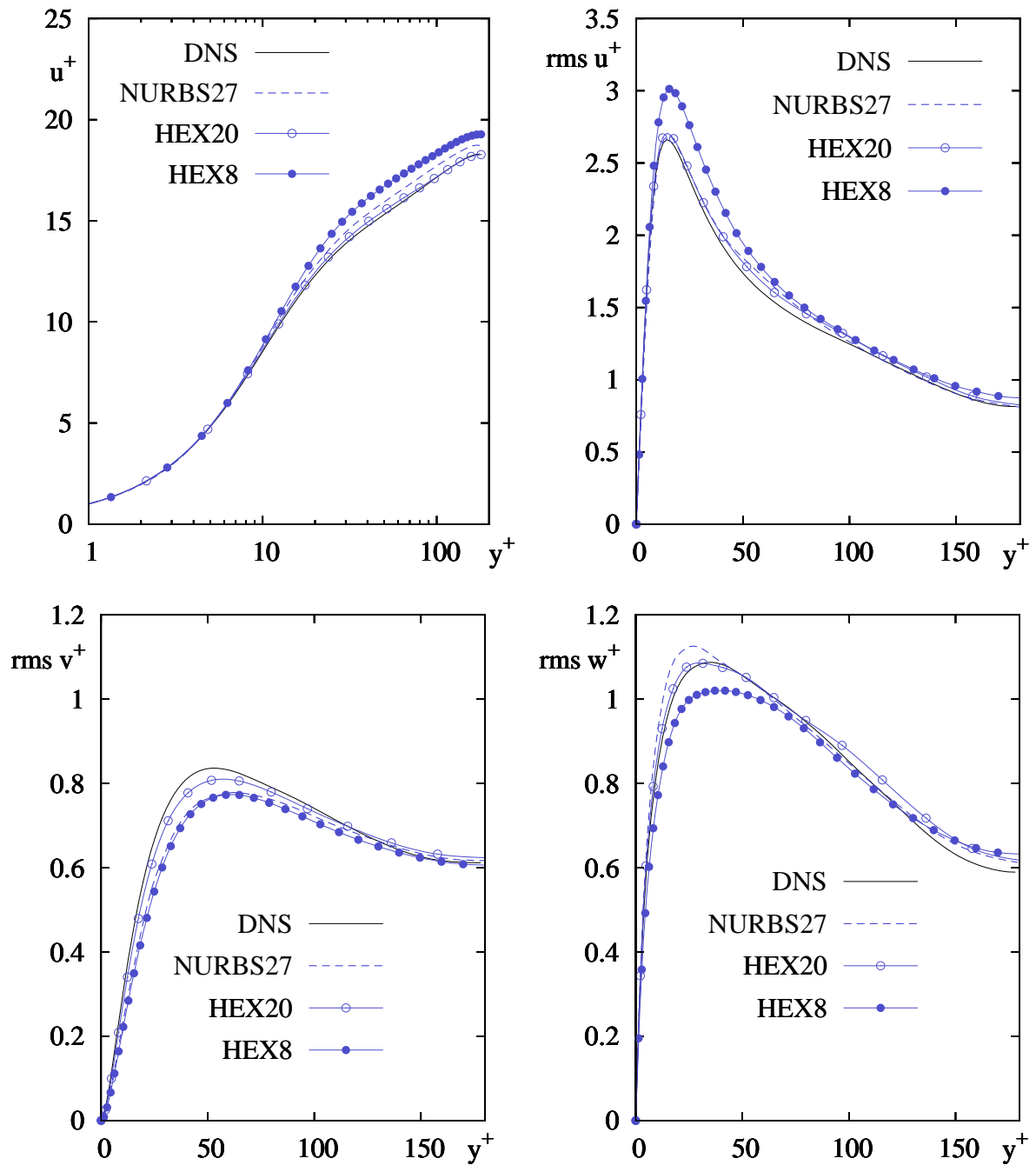


Figure 5.4: Results for mean streamwise velocity and velocity fluctuations in streamwise, wall-normal and cross-stream direction. The results for 64^3 HEX8 and 32^3 HEX20 elements are compared to the computation by AKKERMAN et al. [3] on 32^3 NURBS27 elements and the DNS data by MOSER et al. [163].

5.4.1 Mean resolved-scale quantities

In the first part of this subsection, solutions for problems at moderate time step sizes $0.7 \leq \Delta t^+ \leq 0.9$ will be considered. A variation of the time step size is done in the second part.

Results displayed will be mean velocity and velocity fluctuations. In addition, the obtained numerical values for Re_τ will be provided. A significantly incorrect value of this quantity usually indicates numerical problems with the solution such as mesh-dependent oscillations. These can be hard to detect in the mean velocity due to the spatial averaging process. As already anticipated above, all results in this subsection do not show significant differences for a time-dependent and a conventional subgrid approximation.

Results for moderate choices of the time step size

First, results for simulations at $Re_\tau = 180$ on 32^3 HEX8 and 16^3 HEX20 meshes are presented in Figure 5.5. They can be considered part of a refinement study in combination with the results from Figure 5.4. The computations are based on a time step size of $\Delta t^+ = 0.7$. Numerical values obtained for Re_τ are 180.5 (rV) and 179.1 (td) for the HEX8 discretisation and 179.6 (rV) and 180.1 (td) for the HEX20 mesh. For $Re_\tau = 590$, results for a computation on a 64^3 HEX8 mesh using a time step $\Delta t^+ = 0.9$ are shown in Figure 5.6. Numerical values for Re_τ corresponding to these results are 588.1 (td) and 590.8 (rV). The last REYNOLDS number case, $Re_\tau = 395$, is displayed in Figure 5.7. It provides an additional comparison of residual-based turbulence models to a dynamic SMAGORINSKY model as it is described in appendix C.1. The fluctuations in the dynamic SMAGORINSKY (ds) computation are significantly damped in comparison to the residual-based cases, yielding inferior results especially for the cross-stream component. Nevertheless, at the investigated time step size $\Delta t^+ = 0.7$, all three computations led to acceptable values of Re_τ , namely 394.9 (rV), 393.8 (td) and 394.1 (ds).

A variation of the time step size

To investigate the model performance for more extreme values of the time step size, two computations at $\Delta t^+ = 3.4$ and $\Delta t^+ = 0.05$ were performed. The higher value for Δt^+ was taken close to the maximal time step which still ensures convergence of the nonlinear solution procedure. The lower value $\Delta t^+ = 0.05$ was selected such that the number of time steps required to obtain a meaningful statistical result is still affordable. The results in Figure 5.8 show only small differences. Once more, a clear superiority of the time-dependent approach cannot be observed.

For the conventional model, the mean velocity for the smaller time step size was found to be slightly closer to the reference solution than for the larger time step size. This observation is in contrast to observations made by HSU et al. [114], who found that the quality of the solution deteriorates with decreasing time step size. This discrepancy can be attributed to the different choices of the stabilisation parameter. The parameter used here is not as accurate for moderate time step sizes but obviously provides more robustness with respect to small time steps. See also the discussion in section 5.5.

5.4.2 Averaged unresolved-scale quantities

In contrast to resolved scales, unresolved-scale quantities are affected significantly by a time-dependent subgrid modelling. This can be seen in Figure 5.9, where a distribution of the averaged subgrid velocity norm obtained for three time step sizes is presented. The results belong to the $Re_\tau = 395$ (32^3 HEX8) computations described above.

As a consequence of the $O(\Delta t)$ scaling of the stabilisation parameter in the conventional model, as it can be observed on the right side of Figure 5.9, the averaged subgrid velocity deteriorates with decreasing time step size. In contrast, the averaged subgrid velocity for the time-dependent model remains in the same order of magnitude for all time step sizes.

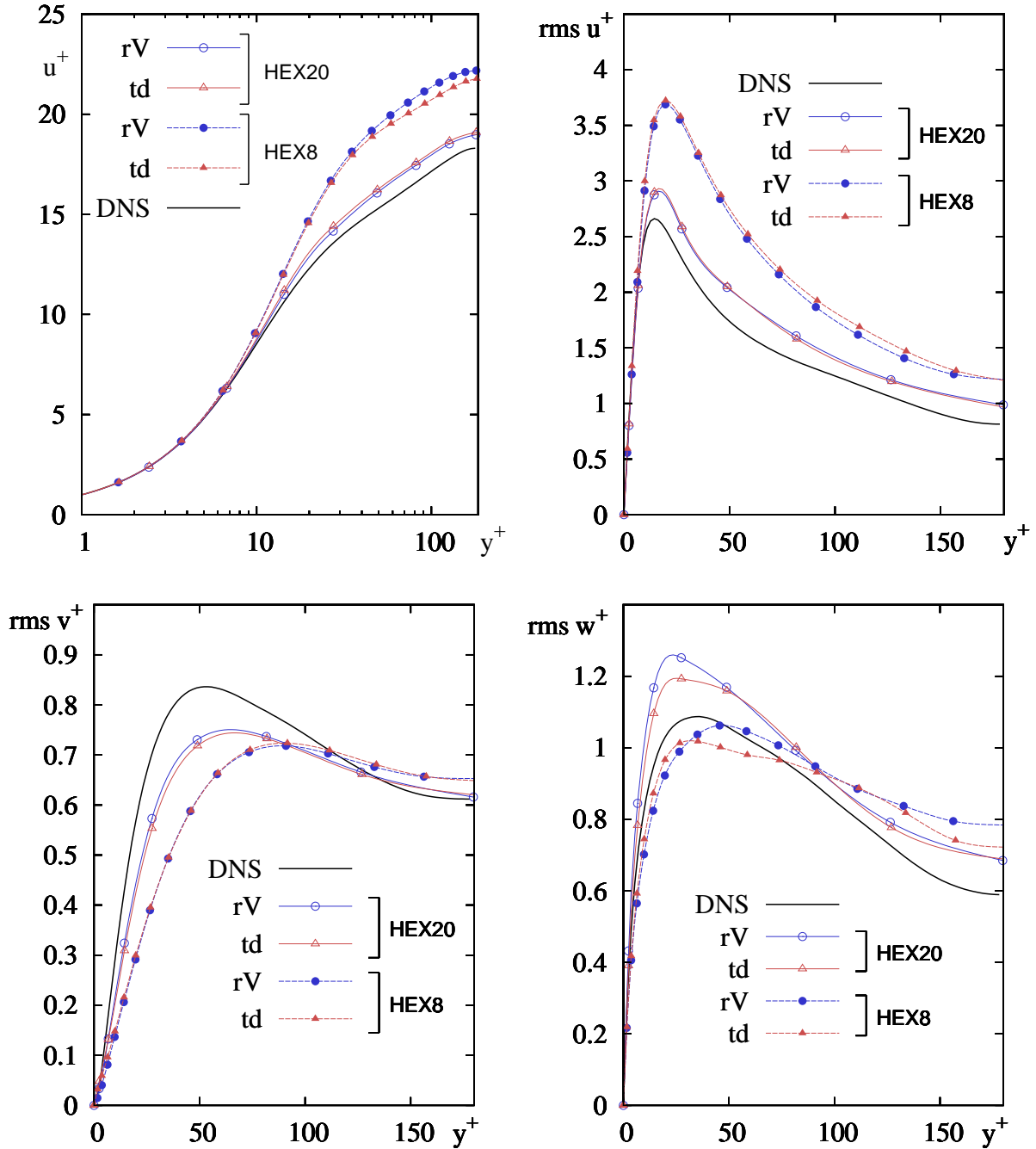


Figure 5.5: Mean streamwise velocity and velocity fluctuations in streamwise (u), wall-normal (v) and cross-stream (w) direction for 32^3 HEX8 and 16^3 HEX20 elements, $Re_\tau = 180$.

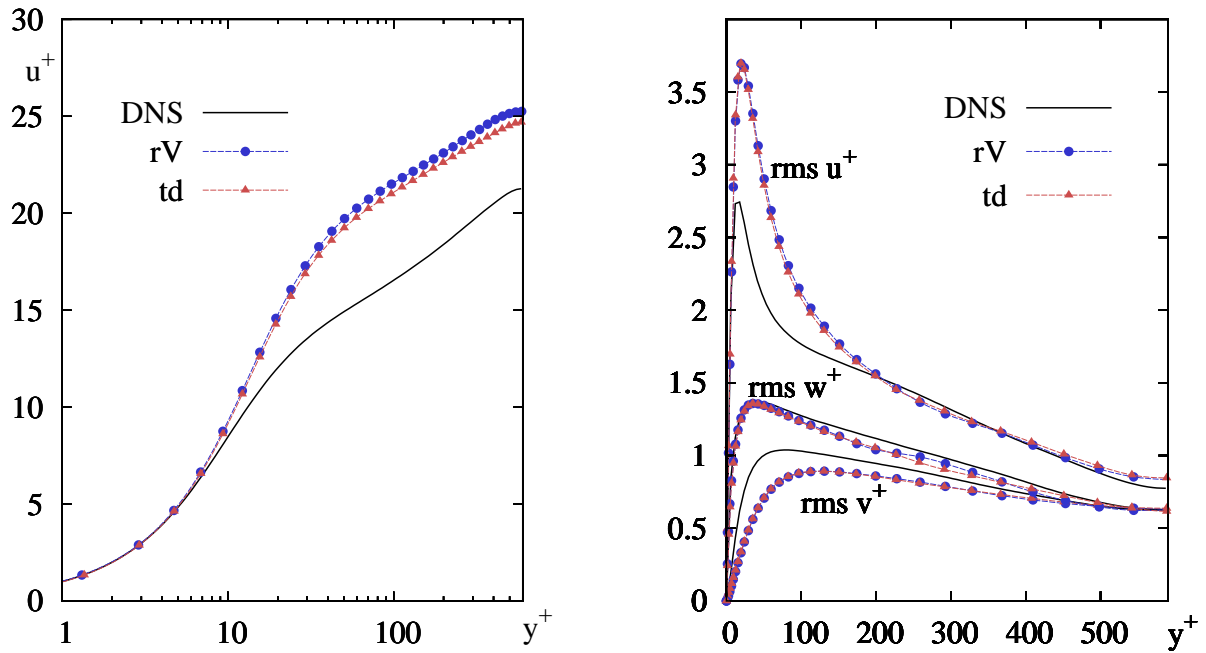


Figure 5.6: Mean streamwise velocity and velocity fluctuations in streamwise (u), wall-normal (v) and cross-stream (w) direction for computations on 64^3 HEX8 elements, $Re_\tau = 590$.

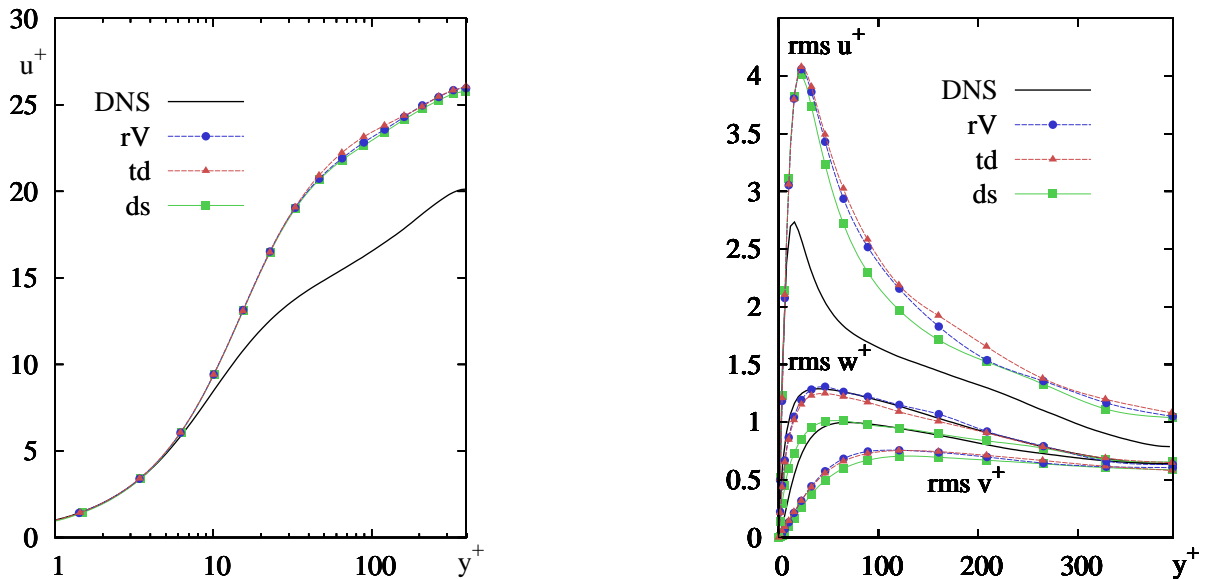


Figure 5.7: Mean streamwise velocity and velocity fluctuations in streamwise (u), wall-normal (v) and cross-stream (w) direction for a mesh of 32^3 HEX8 elements, $Re_\tau = 395$. The green solution (ds) corresponds to a dynamic SMAGORINSKY implementation.

A further insight into the time-dependent character of the subgrid velocities can be obtained from Figure 5.10. This picture shows that all three time step sizes investigated, even the largest

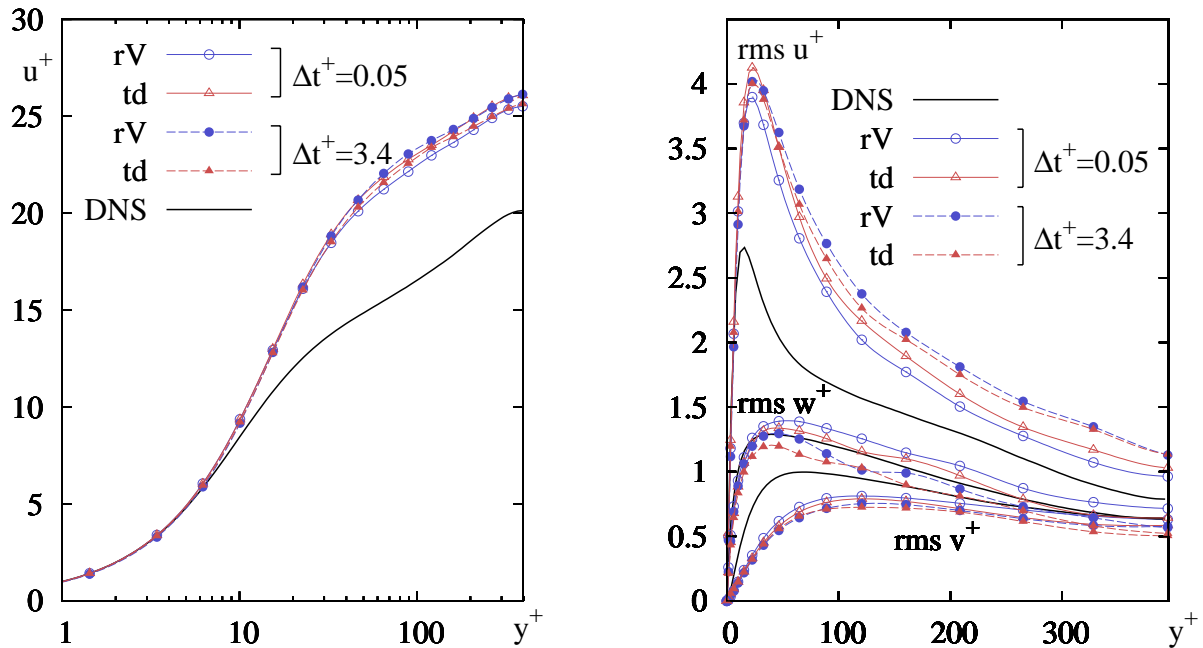


Figure 5.8: Mean streamwise velocity and velocity fluctuations in streamwise, wall-normal and cross-stream direction for computations on 32^3 HEX8 .

one, are small enough to resolve the dynamic character of the subgrid velocity. This observation is in agreement with the fact that the stabilisation parameter used for the time-dependent model, which can be thought of as a characteristic time-scale for the subgrid velocities, is in the order of the time step size applied, see Figure 5.9. Accordingly, the assumption of quasi-static subgrid scales, i.e. the usage of a stabilisation parameter not dependent on the time step size in combination with a conventional residual-based approach, is not justified for any of the three time step sizes. In fact, HSU et al. [114] report convergence problems for quasi-static approximations in turbulent channel flow at small time steps. A test performed with the present implementation confirmed this observation.

Keeping in mind the results for the unresolved-scale velocities in the conventional approach, it is surprising how unaffected the resolved scales are with respect to changes in the time step size. This phenomenon can be, at least partially, understood by a closer investigation of the dissipative behaviour of the modelled turbulent dissipation. A discussion will follow in subsection 5.6.1.

5.5 Influence of stabilisation parameter and element length definition

This section contains an investigation of the impact of the stabilisation parameter choice on the results in turbulent channel flow computations. Knowledge about these facts is important in order to understand the differences between the results shown in section 5.4 and results from other publications like BAZILEVS et al. [15] and HSU et al. [114].

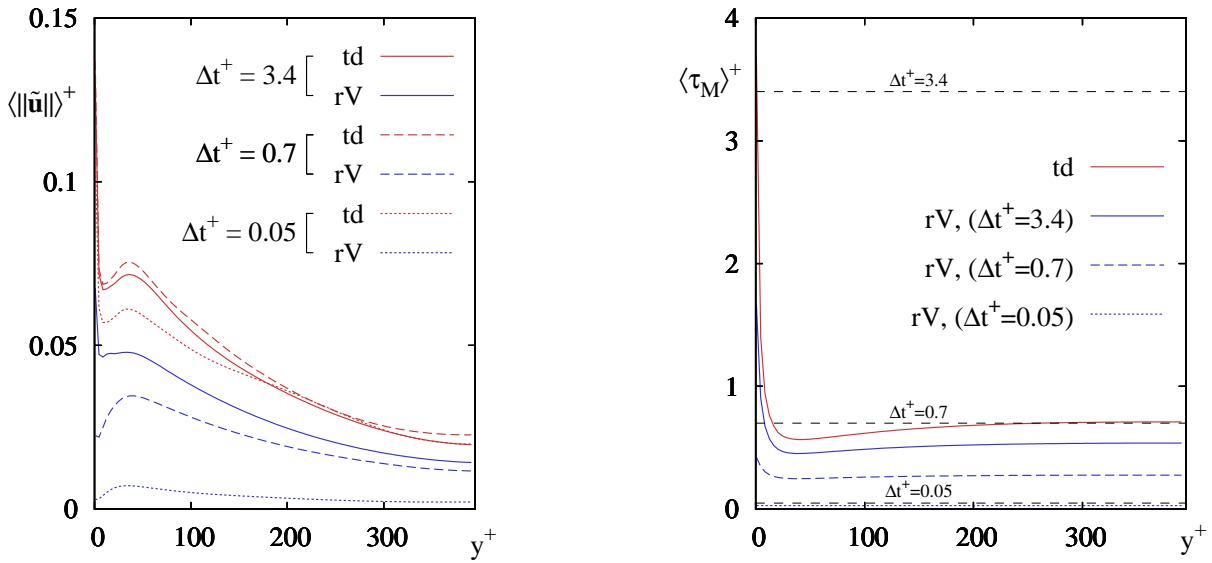


Figure 5.9: Distribution of the norm of the averaged subgrid velocity over one half of the channel in wall units (left). Graphs are shown for time-dependent and conventional residual-based subgrid scales. Distribution of the averaged stabilisation parameter (right). The parameter for time-dependent subgrid approximations is independent of Δt^+ , the conventional parameters vary with Δt^+ . In order to allow a comparison of time scales, the time step sizes are included as dashed lines.

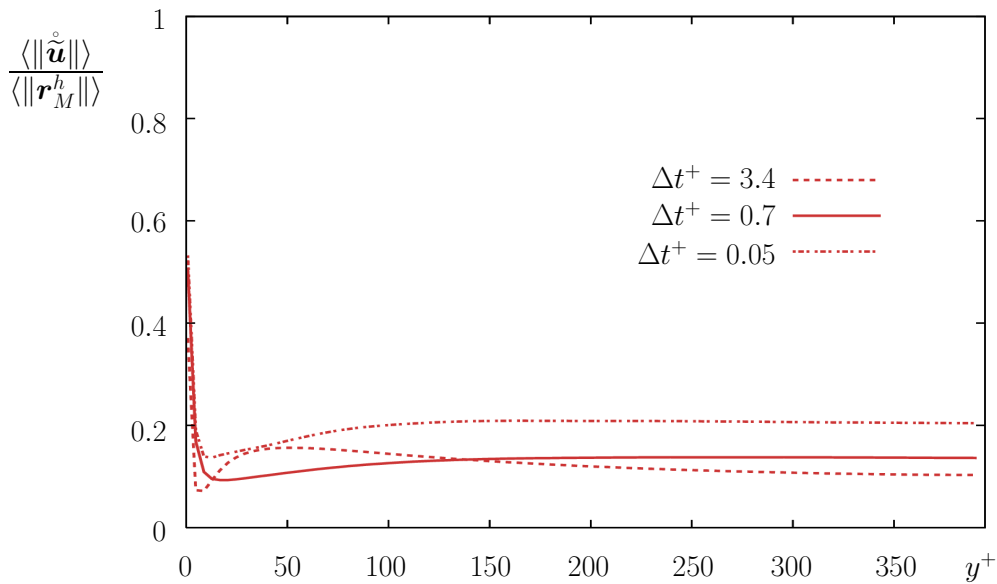


Figure 5.10: Ratio between the averaged norm of the time derivative of the subgrid velocity and the averaged norm of the residual.

All investigations in this section have been carried out on a 32^3 HEX8 mesh at $Re_\tau = 395$ and a time step size of $\Delta t^+ = 0.7$. In Figure 5.11, the distribution of different element length definitions along the height of the channel is displayed in wall units. Huge differences in the

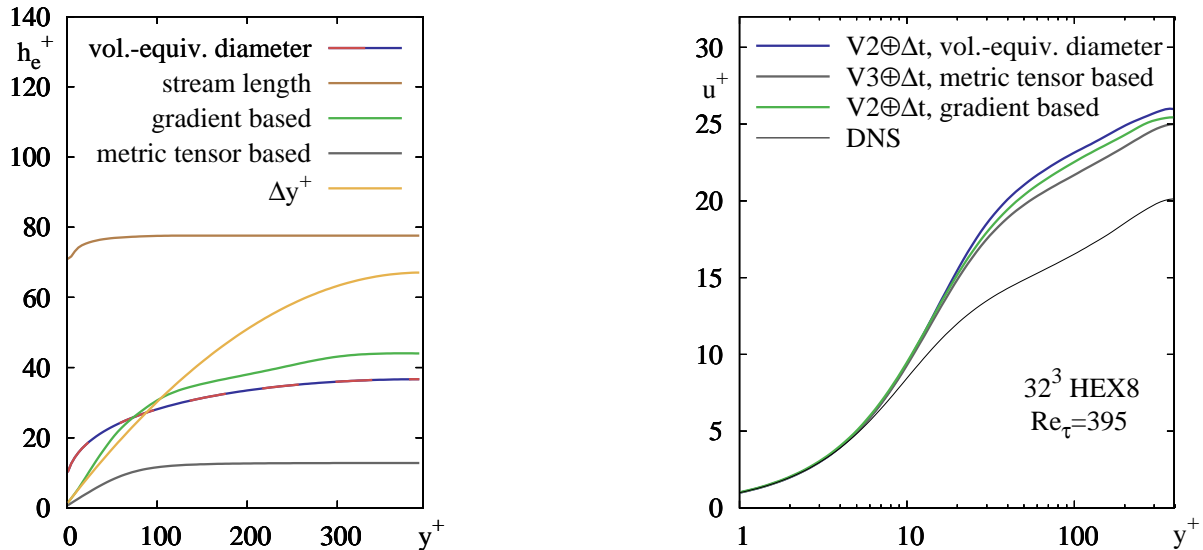


Figure 5.11: A comparison of various element length definitions. The yellow line corresponds to the distribution of the element height due to the mesh stretching (left). The second graph displays the averaged mean velocity for several choices of stabilisation parameter and element length (right).

impact of the boundary layer mesh stretching on the element length can be observed for the different definitions. The stream length according to equation (3.145) is nearly constant along the channel height. It corresponds to the element edge length in streamwise direction. Close to the channel wall, the definition based on the volume-equivalent diameter (3.144) is significantly larger than the definition using the gradient-based element length (3.146) and the definition based on the metric tensor (3.149).

The impact of this behaviour on the stabilisation parameter can be seen in Figure 5.12. While metric tensor-based and gradient-based stabilisation parameters decrease in the viscous sublayer close to the wall, the parameter based on the volume-equivalent diameter exhibits a completely different behaviour. In this region, where the viscous scaling $\sim \frac{h_e^2}{\nu}$ of the stabilisation parameter is dominant, the element length based on the volume-equivalent diameter causes an unnatural peak in the parameter distribution which can still be observed in the subgrid velocity distribution of Figure 5.9.

The different choices of the element length do not only have an impact on unresolved scales, but they also have a significant impact with respect to resolved-scale quantities. This is exemplified for the mean streamwise velocity on the right of Figure 5.11. The accuracy of the results shown in BAZILEVS et al. [15] can only be achieved using the stabilisation parameter definition $\tau_M^{V3\oplus\Delta t}$ given in equation (3.161). The gradient-based definition of $\tau_M^{V2\oplus\Delta t}$ according to equation (3.158) is already a little less accurate, and a definition based on volume-equivalent

diameter/stream length, as it was used in the last section, is even further off the reference solution. Unfortunately, the excellent performance of $\tau_M^{V3\oplus\Delta t}$ seems to be closely related to the choice of the time step size, see HSU et al. [114]. It is not possible to recover this accuracy with a time-dependent subgrid approximation using $\tau_M^{V3\ominus\Delta t}$. The results for the mean streamwise velocity obtained were found to be around 3% higher than the respective conventional result at the optimal time step size. Although for $\tau_M^{V2\oplus\Delta t}$ the choice of an element length based on volume-equivalent diameter/stream length was shown to be not as accurate, it seems to shift the small-time-step problem already observable for $\tau_M^{V3\oplus\Delta t}$ to even smaller values of Δt^+ . In addition, the ‘extra’ stabilisation close to the wall, as it is caused by the distribution of the element length based on volume-equivalent diameter/stream length, provided more robustness for complex flows like the flow around a square cylinder as it will be discussed in section 6.2.1.

5.6 Modelled turbulent dissipation

Further insight into the residual-based models can be obtained by examination of the modelled turbulent dissipation as it has been done by CALO [45] for simulations of bypass transition. For a further spectral analysis of the dissipation of the residual-based variational multiscale method the reader is referred to WANG and OBERAI [218]. The element-averaged modelled turbulent dissipation rate arising from the SUPG, cross and REYNOLDS term can be computed by

$$\begin{aligned} \varepsilon_{\text{SUPG}} &= -\frac{1}{\text{vol}(\Omega_e)} (\tilde{\mathbf{u}}; (\mathbf{u}^h \cdot \nabla) \mathbf{u}^h)_{\Omega_e} \\ \varepsilon_{\text{cross}} &= -\frac{1}{\text{vol}(\Omega_e)} (\mathbf{u}^h; (\tilde{\mathbf{u}} \cdot \nabla) \mathbf{u}^h)_{\Omega_e} \\ \varepsilon_{\text{Rey}} &= -\frac{1}{\text{vol}(\Omega_e)} (\tilde{\mathbf{u}}; (\tilde{\mathbf{u}} \cdot \nabla) \mathbf{u}^h)_{\Omega_e} \end{aligned} \quad (5.6)$$

These definitions assume that the equations were stated in conservative form. For the convective form, a different sign would be obtained for the cross stress term due to the partial integration.

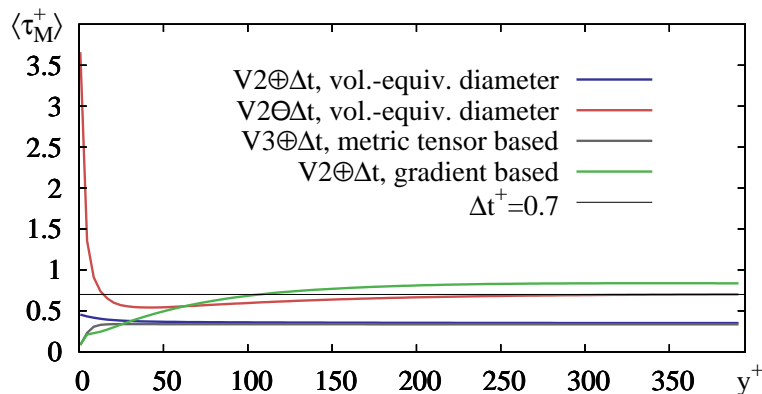


Figure 5.12: Distribution of the averaged stabilisation parameter for several choices of the element length.

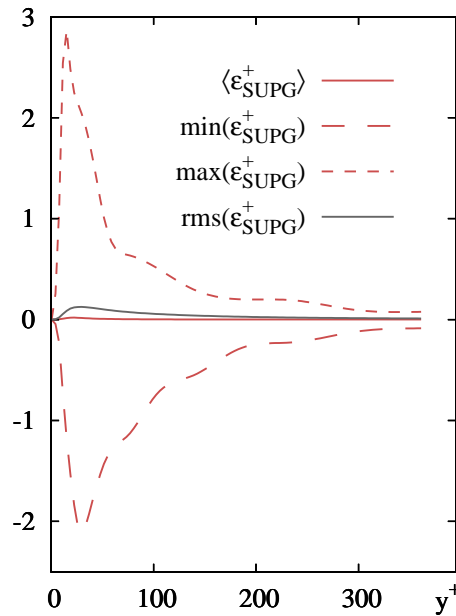


Figure 5.13: Mean, root mean square, minimum and maximum values for the SUPG dissipation rate with respect to the distance from the wall in wall units. See Figure 5.14 for a visualisation of $\langle \varepsilon_{\text{SUPG}} \rangle$ on a more suitable scale.

The terms are not strictly positive. This will be exemplified for $\varepsilon_{\text{SUPG}}$ normalised by wall units

$$\varepsilon_{\text{SUPG}}^+ = \frac{\nu}{u_{\tau_w}^4} \cdot \varepsilon_{\text{SUPG}}. \quad (5.7)$$

Mean values averaged over wall parallel layers of elements and corresponding minimum and maximum values in the respective layers are depicted in Figure 5.13. The results belong to a computation using a time-dependent subgrid approximation on 32^3 NURBS27 elements¹ at $\text{Re}_\tau = 395$, $\Delta t^+ = 0.6$. The stabilisation parameter definition used throughout this section is $\tau_M^{V3\oplus\Delta t}$ for the conventional and $\tau_M^{V3\ominus\Delta t}$ for the time-dependent subgrid case. It can be observed that $\varepsilon_{\text{SUPG}}^+$ takes on positive and negative values. Fluctuations occur, which are one order of magnitude larger than the averaged value. Nevertheless, the averaged dissipation rate caused by the SUPG term was observed to be always positive.

Further quantities can be introduced corresponding to the remaining subgrid terms:

$$\begin{aligned} \varepsilon_{\text{LSIC}} &= -\frac{1}{\text{vol}(\Omega_e)} \left(\tilde{p}, \nabla \cdot \mathbf{u}^h \right)_{\Omega_e} \\ \varepsilon_{\text{transient}} &= \frac{1}{\text{vol}(\Omega_e)} \left(\tilde{\mathbf{u}}; \mathbf{u}^h \right)_{\Omega_e} \\ \varepsilon_{\text{PSPG}} &= -\frac{1}{\text{vol}(\Omega_e)} \left(\tilde{\mathbf{u}}; \nabla p^h \right)_{\Omega_e} \end{aligned} \quad (5.8)$$

¹All computations on this 32^3 NURBS27 mesh have been done during my stay at ICES, UT Austin, where I was allowed to implement the time-dependent subgrid model in the residual-based VMM research code available at that institute. This support and the many helpful suggestions by V.M. CALO, Y. BAZILEVS and T.J.R. HUGHES are gratefully acknowledged.

$\varepsilon_{\text{LSIC}}$ corresponding to the least-squares continuity stabilisation is strictly dissipating, i.e. always positive. The term arising from the PSPG stabilisation, $\varepsilon_{\text{PSPG}}$, was observed to be small compared to the other terms, so it will not be investigated in more detail. The term $\varepsilon_{\text{transient}}$ is obviously only present for time-dependent subgrid-scale modelling that is not based on orthogonal subgrid scales. For implementations using a dynamic SMAGORINSKY model, an additional, strictly dissipative term occurs:

$$\varepsilon_{\text{ds}} = \frac{2\nu_{\text{ur}}}{\text{vol}(\Omega_e)} (\varepsilon(\mathbf{u}^h) : \varepsilon(\mathbf{u}^h))_{\Omega_e} \quad (5.9)$$

5.6.1 Investigations for a series of time step sizes

An investigation of dissipation rates for conventional and time-dependent subgrid models is very instructive with respect to the small-time-step behaviour of the methods. In the $\text{Re}_\tau = 395$, 32^3 NURBS27 element example, as it was already mentioned above, an energy budget for both approximations was determined for four different time step sizes. The resulting distributions for large time step sizes are shown in Figure 5.14. Figure 5.15 contains distributions for two smaller time step sizes. An immediate observation is that in all cases, the REYNOLDS stress term has no significant contribution to the total dissipation rate. The energy budget for the time-dependent subgrid approximation is virtually unaffected by the time step size. At the largest time step size, the red line corresponding to the total dissipation rate in the time-dependent subgrid approximation and the blue line corresponding to the total dissipation rate in the conventional residual-based approximation are very similar. For smaller time step sizes, the energy budget in the residual-based case changes dramatically. With decreasing time step size, the dissipation provided by SUPG and cross stress is more and more replaced by dissipation associated with the least-squares continuity stabilisation. The sum of all contributions in the conventional case, i.e. the blue line, can be observed to decrease only slightly due to this mechanism.

Results for mean velocities obtained with the conventional approach at small time step sizes can be found in HSU et al. [114]. The mean velocity corresponding to the smallest time step size investigated in Figure 5.15 is slightly off the reference solution but the difference is still small. Keeping in mind the deteriorating behaviour of the subgrid velocities for small time step sizes, as it was exemplified in Figure 5.9, the quality of the results is still surprisingly high. Using Figure 5.14 and Figure 5.15, this can at least be partially explained by the compensating dissipation mechanism introduced by the least-squares incompressibility stabilisation.

In accordance with the invariant energy budget for the time-dependent subgrid model, no change in the mean flow quantities was observed during the seventeen flow-through cycles investigated.

5.6.2 Influence of isogeometric representation on subgrid dissipation

This subsection contains a comparison of the modelled turbulent dissipation for different discretisations and subgrid models. All residual-based variational multiscale computations in this subsection correspond to $\text{Re}_\tau = 180$, the applied time step size was $\Delta t^+ = 0.7$. The results are summarised in Figure 5.16. For 32^3 HEX8 elements, the total modelled dissipation in the residual-based variational multiscale modelling using a time-dependent subgrid approximation

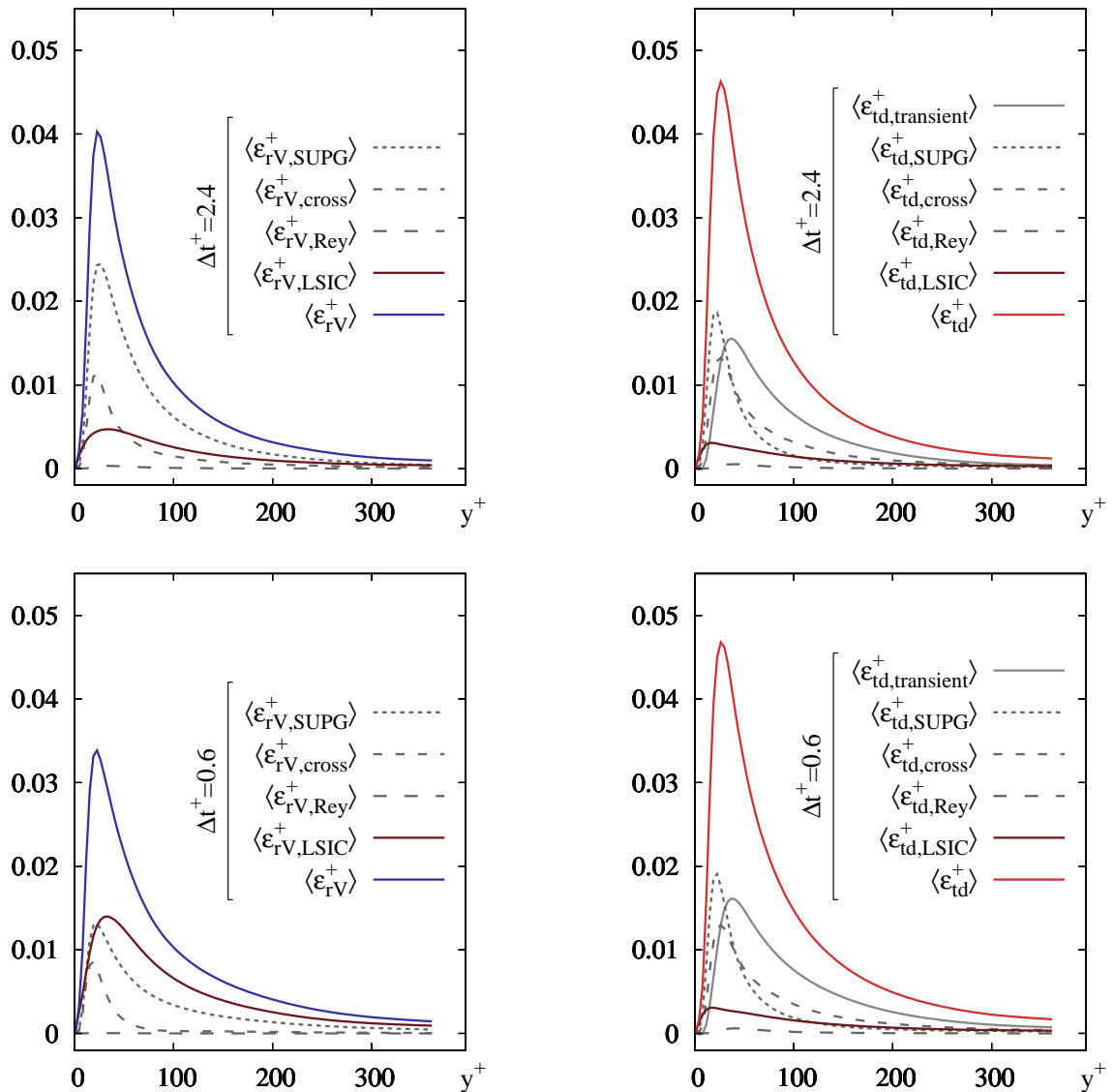


Figure 5.14: Energy budget, i.e. selected dissipation rates, for residual-based variational multiscale modelling at large time step sizes. conventional modelling on the left, time-dependent subgrid modelling on the right.

is only slightly different from the dissipation associated with a stabilised finite element method without cross and REYNOLDS stress terms. It is a little higher for simulations that apply a dynamic SMAGORINSKY model but does not show a distinct peak as it is present in filtered DNS solutions. The filtered DNS shown in Figure 5.16 is taken from a paper by HÄRTEL et al. [111]. It belongs to a computation at $Re_\tau = 211$ and the filtering corresponds to a resolution of 32×32 grid points. The purpose of this curve in Figure 5.16 is not to provide an exact reference solution but rather to give a rough idea of what a dissipation spectrum should look like. When the grid is refined to 64^3 trilinear elements, the amount of numerical dissipation associated with the

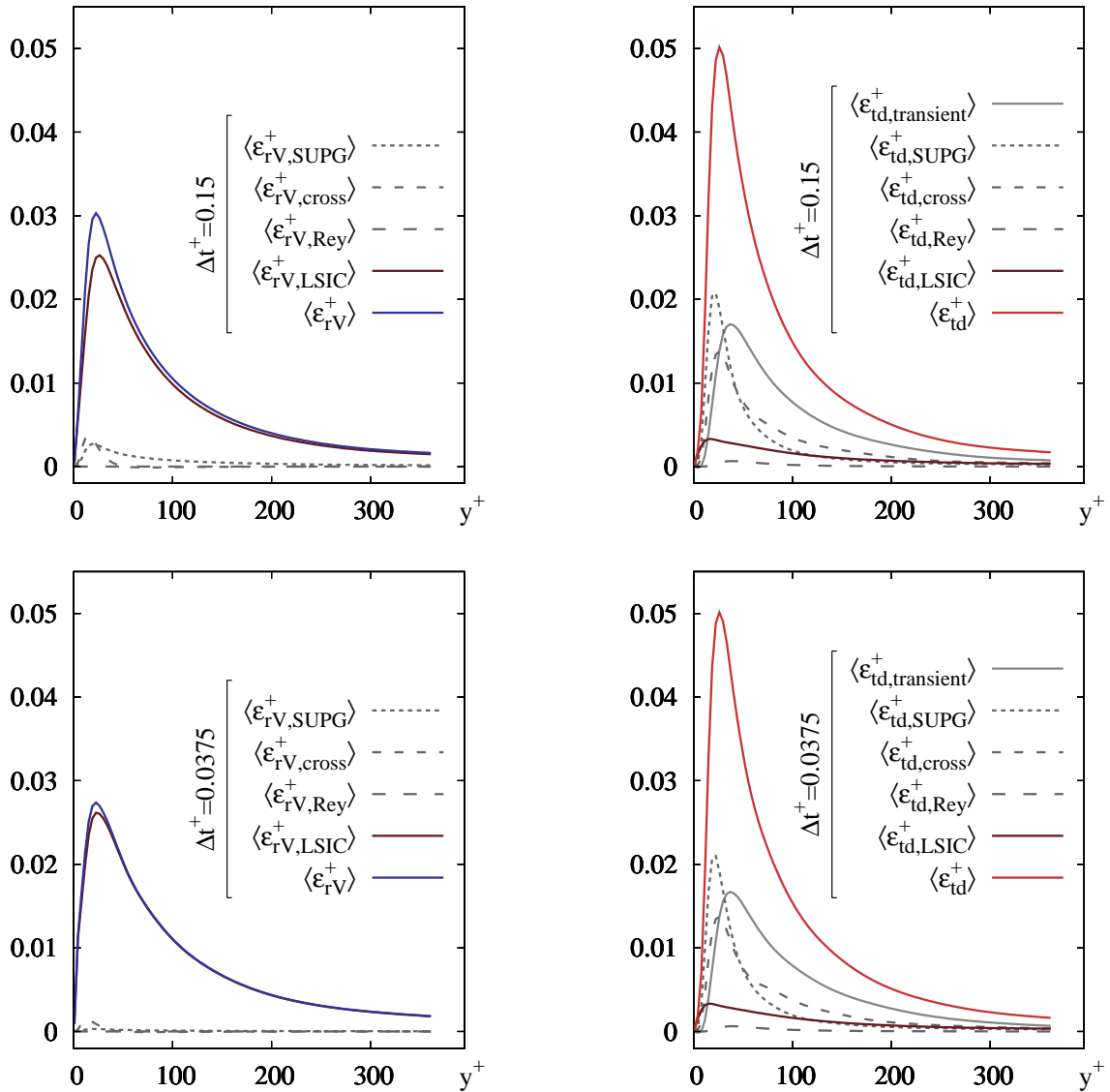


Figure 5.15: Energy budget for residual-based variational multiscale modelling at small time step sizes. Conventional modelling on the left, time-dependent subgrid modelling on the right.

modelled terms is decreasing. The picture is different if the 32^3 HEX8 solutions are compared to 25^3 NURBS27 solutions. From the accuracy point of view, the resolved-scale results associated with this discretisation are comparable to the 64^3 HEX8 discretisation, see Figure 5.17 and Figure 5.4. Nevertheless, the amount of modelled dissipation associated with the NURBS27 discretisation is much more pronounced. Thus it can be concluded that isogeometric finite elements do not only yield very accurate solutions for the resolved-scale quantities but also high quality representations of the behaviour of the unresolved scales. This makes them a valuable tool for turbulent flow computations.

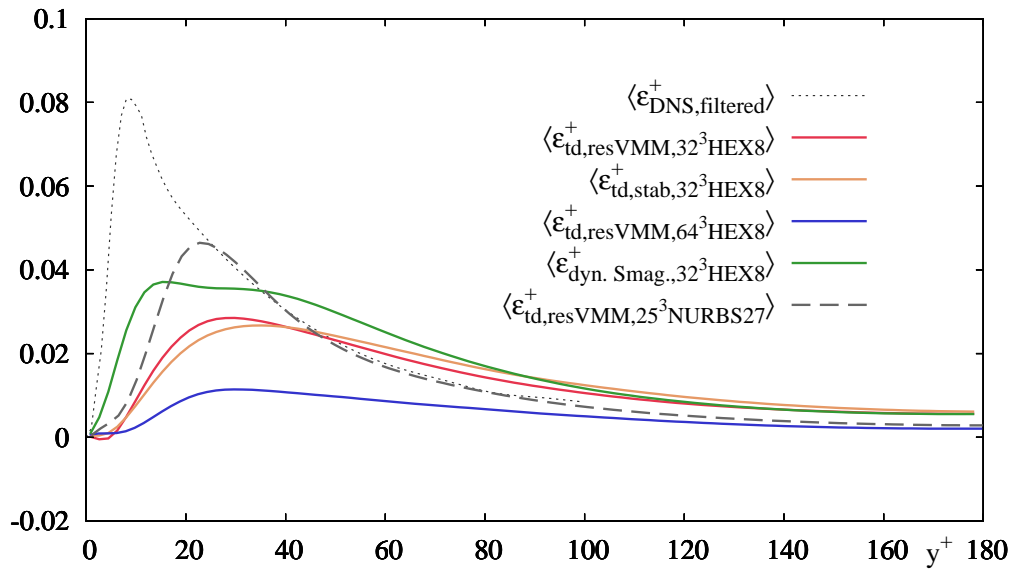


Figure 5.16: Total dissipation associated with model and stabilisation terms for residual-based time-dependent subgrid-scale modelling of turbulence, PSPG/SUPG/LSIC stabilised finite elements with and without an additional dynamic SMAGORINSKY model.

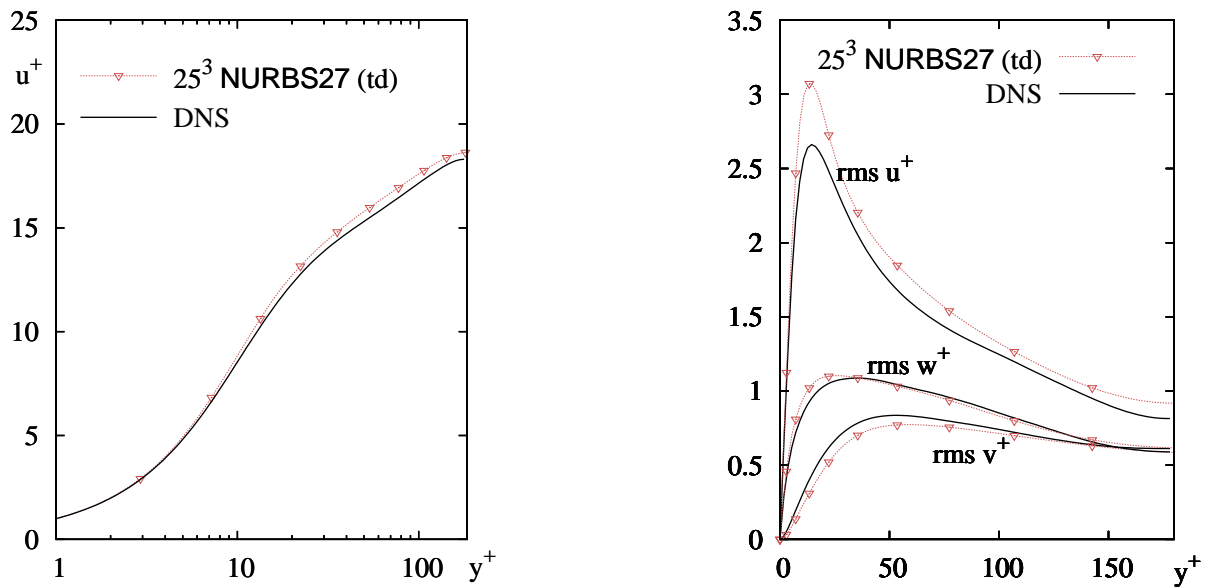


Figure 5.17: Results for mean streamwise velocity and velocity fluctuations in streamwise, wall-normal and cross-stream direction belonging to a 25^3 NURBS27 element discretisation, $Re_\tau = 180$.

6 Further examples of turbulent flow computations

Two further examples of residual-based variational multiscale modelling of turbulence using isogeometric finite elements will be studied in this chapter. The first one in section 6.1 is a turbulent TAYLOR-COUPETTE flow in a circular cylinder, highlighting the ability of the NURBS-based approach to exactly represent such geometries. The second example in section 6.2 is a physically more complex flow around a square cylinder. Among other things, it will be used to evaluate the performance of weak DIRICHLET boundary conditions with respect to their impact on lift and drag.

6.1 Exact representation of circular geometries — TAYLOR-COUPETTE flow

All computations in this section are based on the conservative form of the governing equations. A time-dependent subgrid-scale representation was applied using a parameter $\tau_M^{V3\ominus\Delta t}$ as it is defined in equation (3.163). For the relatively large time step sizes chosen, a NEWTON-type linearisation scheme with full linearisation of cross- and REYNOLDS stress terms proved to be a very efficient choice.

The computational setup is taken from a paper by DONG [66]. It consists of a fixed outer cylinder of radius R_a which contains an inner cylinder of radius R_i . The inner cylinder rotates about its axis z at a constant angular velocity ω , see Figure 6.1. The space between the inner and outer cylinder is filled with a fluid of kinematic viscosity ν and density $\rho = 1$. Based on the gap width $d = R_a - R_i$ and the magnitude $U_0 = \omega \cdot R_i$ of the velocity at the inner surface, the flow is characterised by a REYNOLDS number

$$\text{Re} = \frac{U_0 d}{\nu}. \quad (6.1)$$

Boundary conditions applied to the inner and outer cylindrical surfaces are of no-slip DIRICHLET type. In axis direction, periodic boundary conditions are assumed.

Spatial discretisation is performed using a mesh of quadratic NURBS27 elements. For this choice of elements, the smooth geometry of the boundaries is represented exactly. In order to obtain a better approximation of the boundary layers near the cylindrical surfaces, a hyperbolic mesh stretching is applied to the knot vector in radial direction. In all computations of the current section, the mesh stretching function is based on a constant $C_{\text{stretch}} = 2.3$.

Since the boundary conditions have the same rotational symmetries as the geometry, they can be prescribed analytically in this special case. The zero DIRICHLET boundary condition for

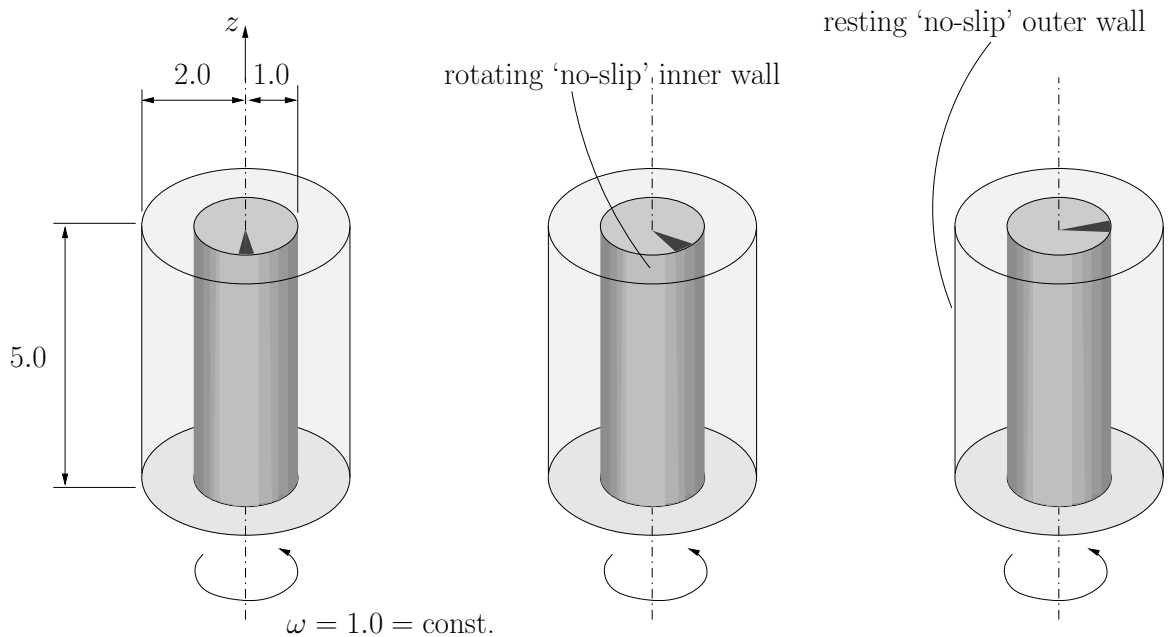


Figure 6.1: Setup for a TAYLOR-COUETTE flow around a rotating cylinder. The black triangle is used to visualise the rotation of the cylinder.

the outer boundary is imposed simply by setting every control point value associated with the outer surface to zero. In order to impose a constant tangential velocity on the inner surface, a DIRICHLET value for each control point ι associated with the inner surface is prescribed as

$$(\mathbf{u}_D)_\iota = \omega \cdot \begin{pmatrix} -\mathbf{x}_\iota^h \cdot \mathbf{e}_y \\ \mathbf{x}_\iota^h \cdot \mathbf{e}_x \\ 0 \end{pmatrix}. \quad (6.2)$$

Although the control point locations \mathbf{x}_ι^h are mostly not situated on the inner surface and hence $\|(\mathbf{u}_D)_\iota\| \neq \omega R_i$ in general, the desired constant tangential velocity is obtained on the cylinder surface due to the interpolation using NURBS basis functions. All computations are started from an initial flow field

$$\mathbf{u}_0(\mathbf{x}) = \begin{pmatrix} -\frac{\mathbf{x} \cdot \mathbf{e}_y}{\|\mathbf{x}\|} \cdot \left(\frac{1}{\|\mathbf{x}\|} - \frac{1}{2} \cdot (\|\mathbf{x}\| - 1) \right) \\ \frac{\mathbf{x} \cdot \mathbf{e}_x}{\|\mathbf{x}\|} \cdot \left(\frac{1}{\|\mathbf{x}\|} - \frac{1}{2} \cdot (\|\mathbf{x}\| - 1) \right) \\ 0 \end{pmatrix}, \quad (6.3)$$

which is set in a least-squares sense according to subsection 3.6. Unresolved-scale quantities are initialised to zero, as usual.

Due to the choice of boundary conditions, the TAYLOR-COUETTE problem investigated in this section does not have an outflow boundary. This means that the pressure level is defined only up to a constant and has to be set either by a DIRICHLET condition in one point or by a projection as it is described in appendix E.

6.1.1 Computations for selected REYNOLDS numbers

For $Re = 8000$, the flow is reported by DONG [66] to be fully turbulent. In an experimental setup, such a REYNOLDS number would be obtained for water, a gap width of 8.8cm and an angular velocity of ten rounds per minute. A computation was performed on a mesh of $60 \times 50 \times 50$ elements in Θ -, r - an z -direction, respectively. Together with the very recent results by BAZILEVS and AKKERMAN [12], this is one of the first LES computations reported for this test case. As usual, all quantities that will be shown in this subsection have been obtained after a statistically steady state has been reached. The computation is based on a time step size of $\Delta t^+ = 2.5$. The value of the friction velocity required for the conversion of the time step size into wall units was determined numerically to approximately 0.055. Based on this value, the element sizes of elements next to the surface of the inner cylinder were found to be approximately $\Delta r^+ = 1$ in radial direction and $\Delta \Theta^+ = \Delta z^+ = 44$ in azimuthal and periodic direction, respectively. A first visualisation of the flow can be found in Figure 6.2. It shows the distribution of the absolute value of the current velocity. For this picture, the solution on each NURBS27 element was interpolated to eight hexahedral visualisation sub-elements. This step is necessary to use a standard post-processing software in combination with isogeometric finite elements.

In addition to this qualitative result, profiles of the mean azimuthal velocity and corresponding fluctuations are compared to DNS results by DONG [66] in Figure 6.3. These averages were taken in space and time. The spatial averaging takes place in Θ - and z -direction. Time averaging was performed over a period of time corresponding to ten rotations of the inner cylinder. The solution obtained is in excellent agreement with the reference data, only the fluctuations close to the inner wall are predicted slightly higher.

The situation is different for $Re = 1000$, a REYNOLDS number for which DONG [66] predicts a laminar flow behaviour. The computation for this REYNOLDS number was done on the same

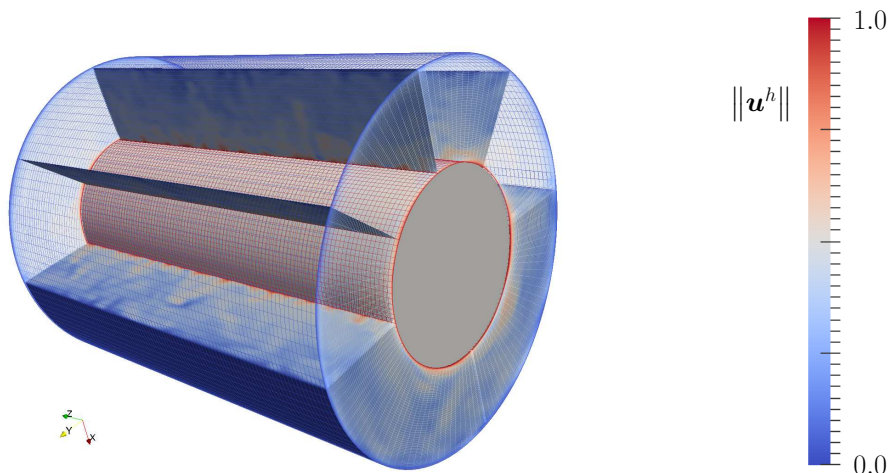


Figure 6.2: Absolute value of instantaneous velocity for a flow at $Re = 8000$. Several cuts are used to show the flow inside the fluid domain. The grid corresponds to a mesh of hexahedral cells which are used to visualise the NURBS solution.

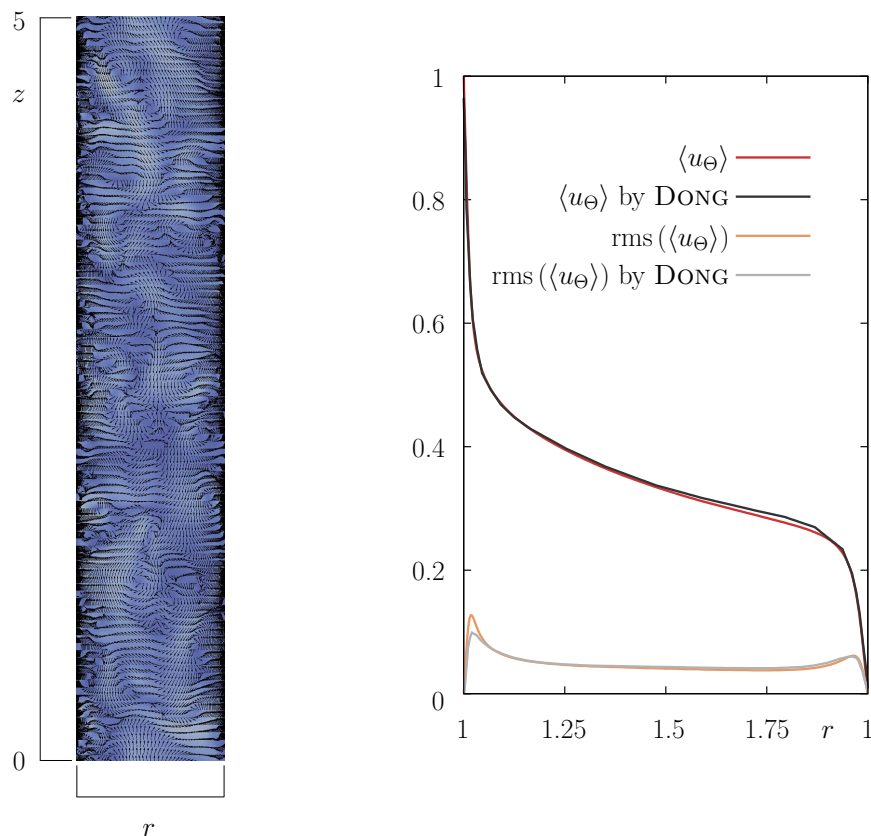


Figure 6.3: Mean azimuthal velocity and fluctuations at $\text{Re} = 8000$ (right). Corresponding zr -velocities in a radial-axial plane (left). The colour legend is the same as in Figure 6.2.

mesh as before. The whole setting except for the viscosity remains unmodified with respect to the first case. The obtained value for the friction velocity is now 0.089, the resulting time step in wall units is 0.8. Results obtained for the mean azimuthal velocity and corresponding fluctuations are shown in Figure 6.4. With respect to the DNS data, the solution obtained shows much larger differences than in the high REYNOLDS number case. As it can be seen on the left of Figure 6.4, these differences may be attributed in part to the fact that the residual-based variational multiscale computation does not predict vortices which have as well-defined boundaries as the ones shown in DONG [66]. Regular flow structures are well observable, but they are not as smooth as the ones in the publication mentioned above. A second problem can be related to the extension of the computational domain in z -direction. As can be seen on the left of Figure 6.4 and in the plot of the pressure isosurface in Figure 6.5, the flow at $\text{Re} = 1000$ contains some structures that can not be considered small with respect to the extension of the computational domain in axis direction. Thus, the length of the domain can be expected to have some influence on the results obtained. Note that for the higher REYNOLDS number case, flow structures observable in Figure 6.3 and Figure 6.5 are much smaller, indicating that size effects should be less problematic in that case.

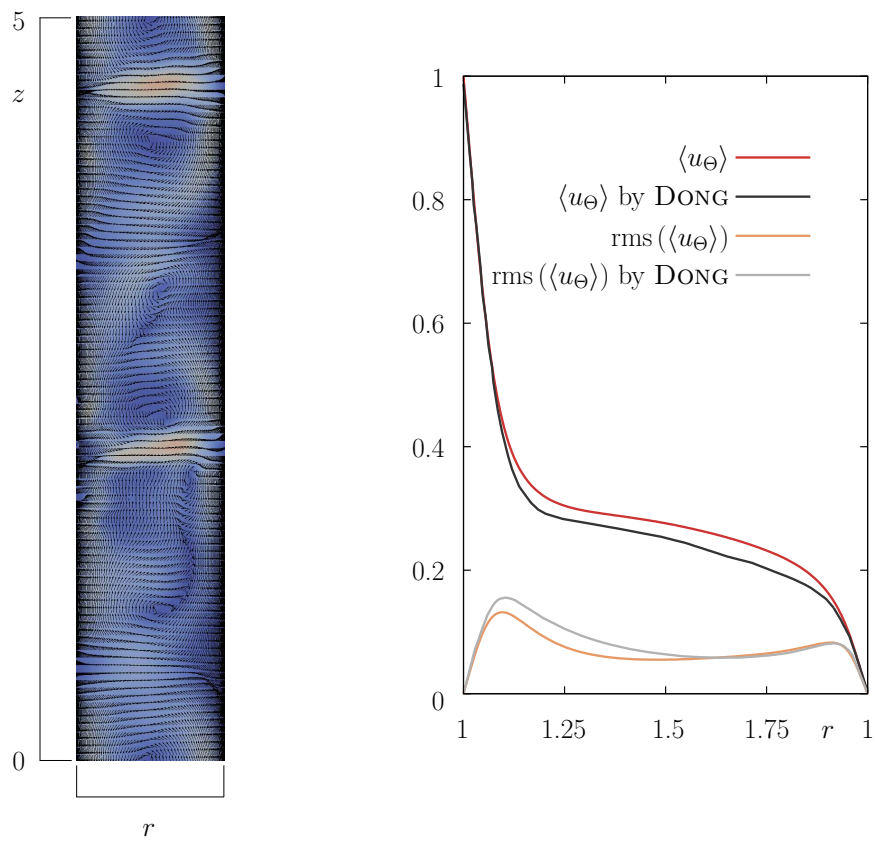


Figure 6.4: Mean azimuthal velocity and fluctuations at $\text{Re} = 1000$ (right). Corresponding zr -velocities in a radial-axial plane (left). The colour legend is the same as in Figure 6.2.

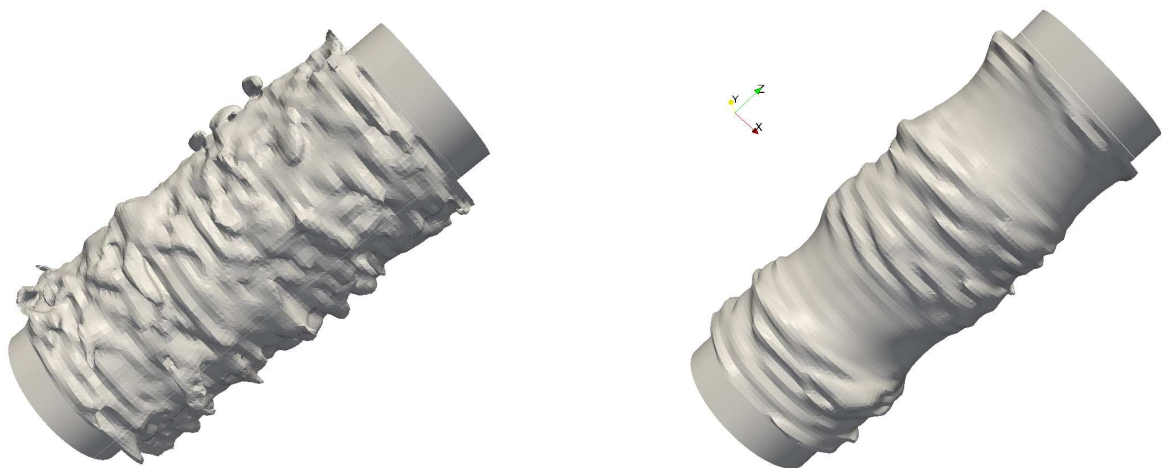


Figure 6.5: Pressure isosurfaces $p = -0.025$ for $\text{Re} = 8000$ (left) and $\text{Re} = 1000$ (right).

6.1.2 Advantages of a KRYLOV-projection-based solution method

In the current subsection, the advantages of the projection-based method to set the pressure level will be highlighted for a computation at $Re = 8000$ on a coarse test mesh of $16 \times 8 \times 12$ elements in azimuthal (Θ), radial (r) and periodic (z) direction, respectively.

For that purpose, the first three time steps of four computations are investigated. The computations differ in the choice of the preconditioner and the way of imposing the pressure level. The first preconditioner investigated is of algebraic multigrid type (ML), the second is a classical incomplete factorisation (ILU). For each choice of the preconditioner, the point-constrained DIRICHLET version was compared to a solution of an unconstrained system by projection. For all computations, a relative tolerance of 10^{-4} with respect to the initial residual was required in every linear solver call.

Figure 6.6 contains a comparison of the four variants with respect to the performance of the iterative GMRES solver used to solve the linear system (3.127) arising in each nonlinear iteration step. For all four variants, three or two nonlinear iteration steps respectively were required

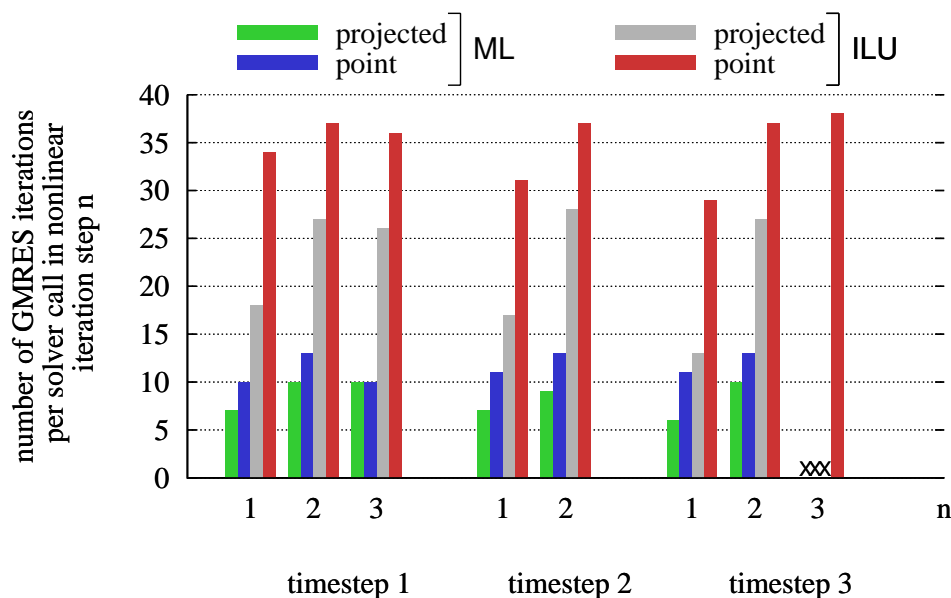


Figure 6.6: Performance of the linear solver for two choices of the preconditioner in the unconstrained (projected) and constrained setting, respectively.

to reach the convergence criterion of the nonlinear iteration in the first two time steps. In time step three, only the combination of point-constrained DIRICHLET formulation and ILU preconditioner required a third nonlinear iteration step to reach the convergence criterion. This behaviour can be attributed to an inferior conditioning of the arising system matrix, see the discussion in the next paragraph. For the ILU preconditioner, the average number of iterations required to solve the linear system is decreased by 36% for the choice of a projection-based definition of the pressure level. For the ML preconditioner, the improvement by 27% is slightly smaller but still significant.

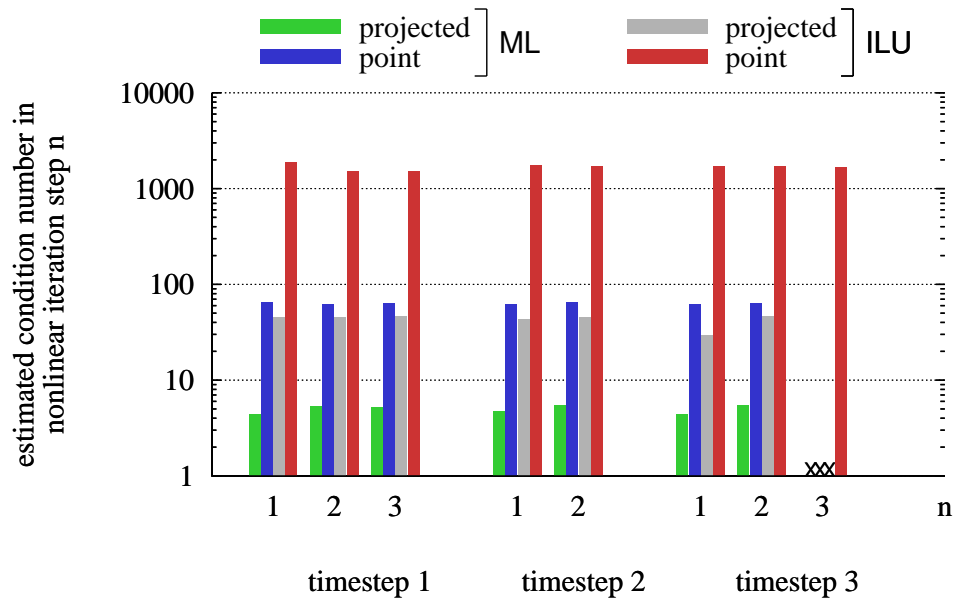


Figure 6.7: Estimated condition numbers for the preconditioned system matrix for ML and ILU preconditioners in the unconstrained (projected) and constrained setting, respectively.

An overview over estimated condition numbers of the preconditioned matrices in the four cases can be found in Figure 6.7. For both choices of the preconditioner, the estimated condition number was reduced by one order of magnitude in the case of the solution of the unconstrained system on a factor space.

6.2 Turbulent flow around a square-section cylinder

The flow around a square cylinder was selected as a further test case for the following reasons: It is characterised by relatively complex flow physics, for instance it contains separation. Additionally a sufficient amount of experimental data as well as many LES computations by other groups are available for comparison. Examples are RODI et al. [181], FARHAT and KOOBUS [146] and SOHANKAR et al. [192].

The test case will be used for a further careful evaluation of the performance of residual-based variational multiscale modelling using time-dependent as well as conventional subgrid closures. The stabilisation parameters used in the computations are $\tau_C^{V2\oplus\Delta t}$ from equation (3.159), and $\tau_M^{V2\oplus\Delta t}$ from equation (3.158) or $\tau_M^{V2\ominus\Delta t}$ from equation (3.160) respectively. All computations are based on the convective form of the resolved-scale equation (4.57). Three meshes have been investigated, as well as the impact of a weak imposition of no-slip boundary conditions on the cylinder's surface with special respect to the drag value.

6.2.1 Setup

The geometry of the flow is given in Figure 6.8. All computations have been done using a density $\rho = 1.0$, a kinematic viscosity $\nu = \frac{1}{22000}$ and an inlet velocity of norm $\|\mathbf{u}_{\text{inlet}}\| = 1$. Based on the edge length of the cylinder $\ell = 1$, the resulting REYNOLDS number is given as

$$\text{Re} = \frac{\ell \cdot \|\mathbf{u}_{\text{inlet}}\|}{\nu} = 22000. \quad (6.4)$$

In an experimental setup using water, this corresponds to a flow around a square cross-section cylinder of edge length 2.2 cm with an inlet velocity of $1 \frac{\text{m}}{\text{s}}$.

Spatial discretisation was performed using 33000, 90000 and 364500 quadratic NURBS elements. For this purpose, the computational domain was partitioned into five patches ①–⑤ which are also shown in Figure 6.8. The simple geometry of each patch was defined using linear NURBS functions. An order elevation and a successive knot insertion yielded the three meshes described in Table 6.1 and Table 6.2. In patches ①–④, a hyperbolic mesh stretching based on a constant $C_{\text{stretch}} = 2.5$ was applied to the knot vector associated with the surface-normal direction. According to the estimation of KOOBUS and FARHAT [146], who state that 0.05ℓ corresponds to approximately 10–80 wall units, the closest control point next to the cylinder's surface in the meshes from Table 6.1 is located in a distance of 6.5, 1.4 or 0.4 wall units.

In z -direction, periodic boundary conditions were applied according to subsection 3.7.5. The top and bottom surface of the computational domain were defined as slip surfaces, i.e. a DIRICHLET value is only set in the y -direction of the velocity in the associated control points. The inlet profile was set as a constant DIRICHLET condition as shown in Figure 6.8. For the finer meshes, a stabilised outflow boundary condition according to subsection 3.7.4 was required on the surface at $x = 24.0$. For the coarsest mesh, a do-nothing boundary condition was sufficient. Due

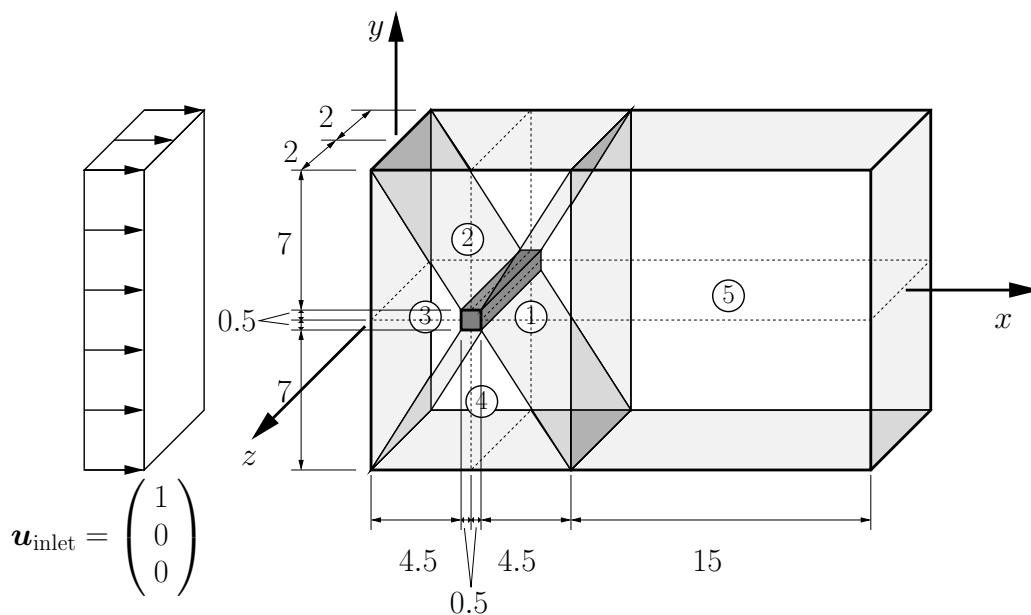


Figure 6.8: Flow geometry and patches ①–⑤ forming the discretisation.

| case | patches ①–④ | | |
|----------------|---------------------------------|------------------|---------------|
| | number of elements in direction | | |
| | surface-normal | surface-parallel | z -parallel |
| 33000 NURBS27 | 20 | 20 | 15 |
| 90000 NURBS27 | 30 | 30 | 20 |
| 364500 NURBS27 | 60 | 45 | 30 |

Table 6.1: Number of elements in patches ①–④.

to the small value of the viscosity, this do-nothing condition is very similar to a zero boundary condition for the pressure. Figure 6.9 shows the impact of the outflow boundary condition on the pressure. In the wake of the cylinder, the pressure isosurfaces are convected downstream in two separate lines. This structure disintegrates completely at the very end of the computational domain. In the case of a do-nothing boundary condition, the pressure can be observed to drop from the value in the domain to zero on the last element. The resulting enormous pressure gradient can be related to the stability problems that enforce the usage of a stabilised outflow condition at this point. Special attention has to be given to the boundary condition on the cylinder's surface. Results will be provided for a strong imposition of the boundary condition in terms of a zero DIRICHLET condition. For the cases 33000 NURBS27 and 90000 NURBS27, additional results will be shown corresponding to a weak imposition of the boundary condition according to section 4.5, see Figure 6.10 for an illustration. In these computations, a constant value for the parameter τ_B according to equation (4.82) was chosen. Time step sizes employed for the different subgrid approximations and boundary conditions are summarised in Table 6.3. In general, the time-dependent subgrid approximation required a smaller time step than the conventional subgrid approximation. This behaviour can be related to the additional nonlinearity introduced by the time-dependent subgrid approximation without orthogonal subgrid scales as it was discussed in subsection 4.4.4. The time step size had to be reduced further if weak DIRICHLET boundary conditions were applied. The linearisation strategy is usually NEWTON-type. Only for the weak boundary condition case, where the time step is small and the convective boundary term in the weak condition has to be treated fixed-point-like anyway, a reduced linearisation was found to be more efficient.

| case | patch ⑤ | | |
|----------------|---------------------------------|---------------|---------------|
| | number of elements in direction | | |
| | x -parallel | y -parallel | z -parallel |
| 33000 NURBS27 | 30 | 20 | 15 |
| 90000 NURBS27 | 30 | 30 | 20 |
| 364500 NURBS27 | 30 | 45 | 30 |

Table 6.2: Number of elements in patch ⑤.

Computations were started from a zero initial flow field. In an initial phase, they were run until the vortex street was fully developed. All results shown in the following sections were obtained over a sampling period corresponding to approximately ten vortex sheddings after that point.

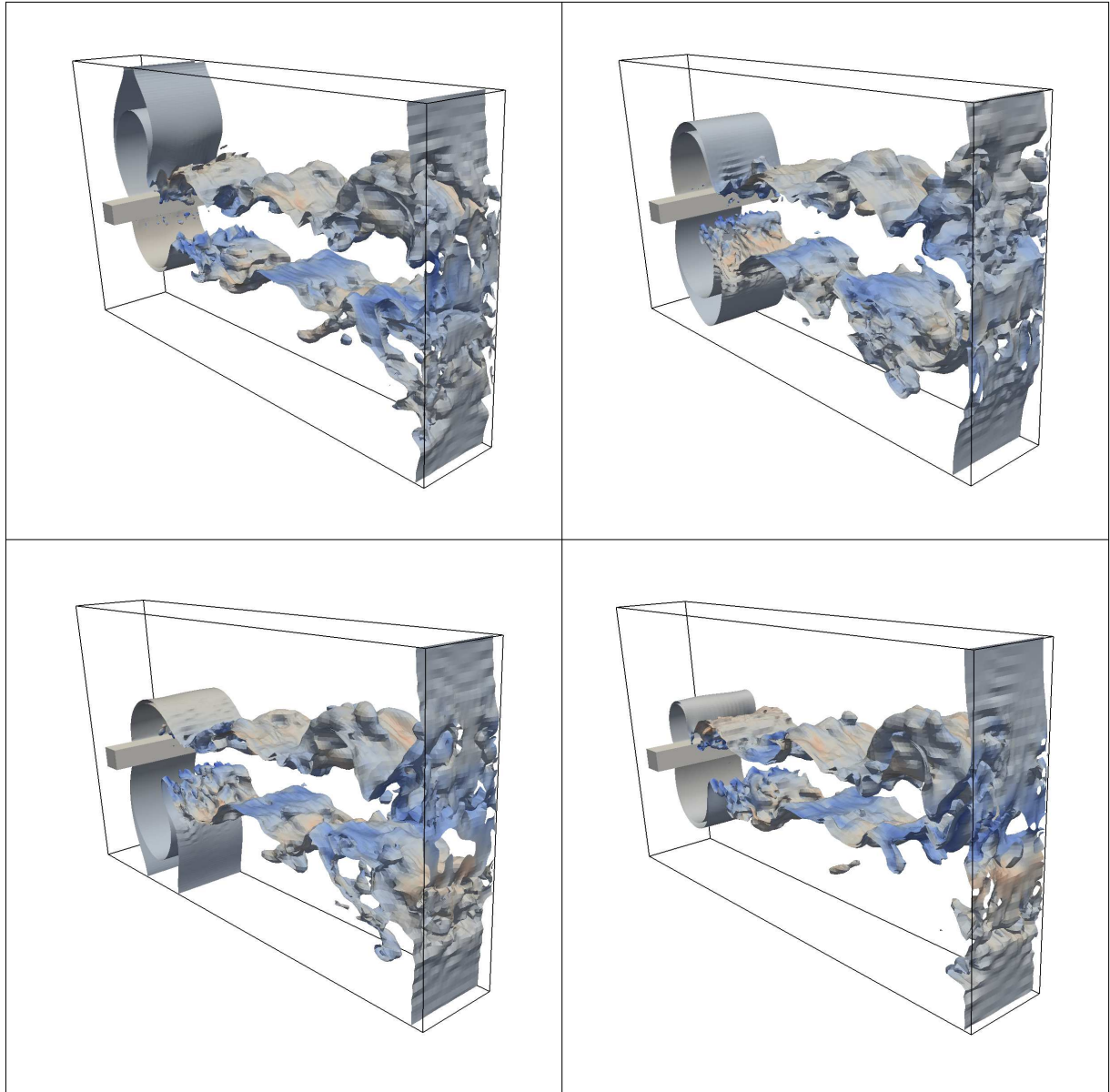


Figure 6.9: Pressure isosurfaces $p = 0.005$ and $p = -0.005$ for four time steps (coloured by the norm of the velocity). The pictures once more highlight the three-dimensionality of the turbulent flow in the cylinder wake. (364500 NURBS27 case)

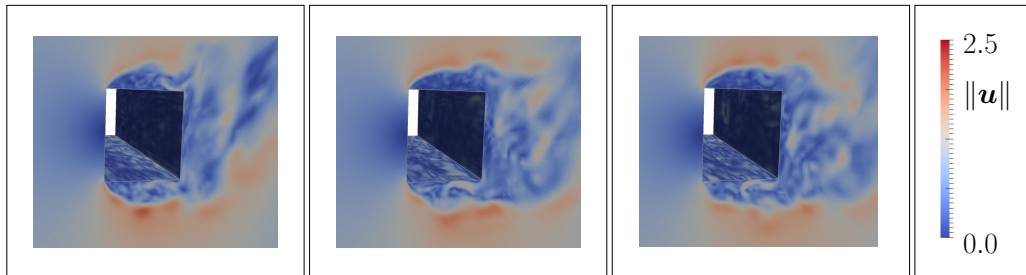


Figure 6.10: A look through the square cylinder's hole in the computational domain. The nonzero velocity distribution on the cylinder's surface, as it occurs for a weak imposition of the boundary conditions, is clearly observable (90000 NURBS27 case).

| subgrid approximation | boundary condition | time step size | linearisation strategy |
|-----------------------|--------------------|----------------|------------------------|
| rV | strong | 0.05 | (N) |
| td | strong | 0.025 | (N) |
| rV | weak | 0.0125 | (N)* |

Table 6.3: Time step sizes for different subgrid approximations and boundary conditions on the cylinder's surface. In the case of a strong DIRICHLET boundary condition, a NEWTON-type linearisation scheme was found to be appropriate. Only in the weak case, REYNOLDS and cross stress terms were not included in the linearisation (N)*.

6.2.2 Mean streamwise velocity distributions

The first results shown are mean streamwise velocity distributions computed in the planes indicated by the dashed lines in Figure 6.8. The averages are computed in time and space with the spatial averaging done along the z axis. The results will be visualised in graphs for the mean velocity distribution on the centre plane of the cylinder along the x -axis and a close-up of the averaged streamwise velocity near the body along the y -axis at $x = 5$.

In Figure 6.11, the results on the finest mesh are compared to data taken from the workshop paper by RODI et al. [181]. It shows that the residual-based modelling performed at least as well as the approaches applied in that reference. The length of the recirculation zone is predicted quite accurately, the near-wall behaviour is satisfactory. The only major point of criticism is a severe overprediction of the mean velocity further downstream of the cylinder, as it was also observed for other approaches, for instance in KOOBUS and FARHAT [146]. It cannot be obviated that this shortcoming is related to the finite size of the computational domain, i.e. to an insufficient extension of the domain in x - and y -direction.

Furthermore, Figure 6.12 and Figure 6.13 provide a comparison of different subgrid approximations and boundary conditions for the two coarser meshes. Similar to the observations in the channel flow setting, the mean streamwise velocity distribution in the centre plane is predicted

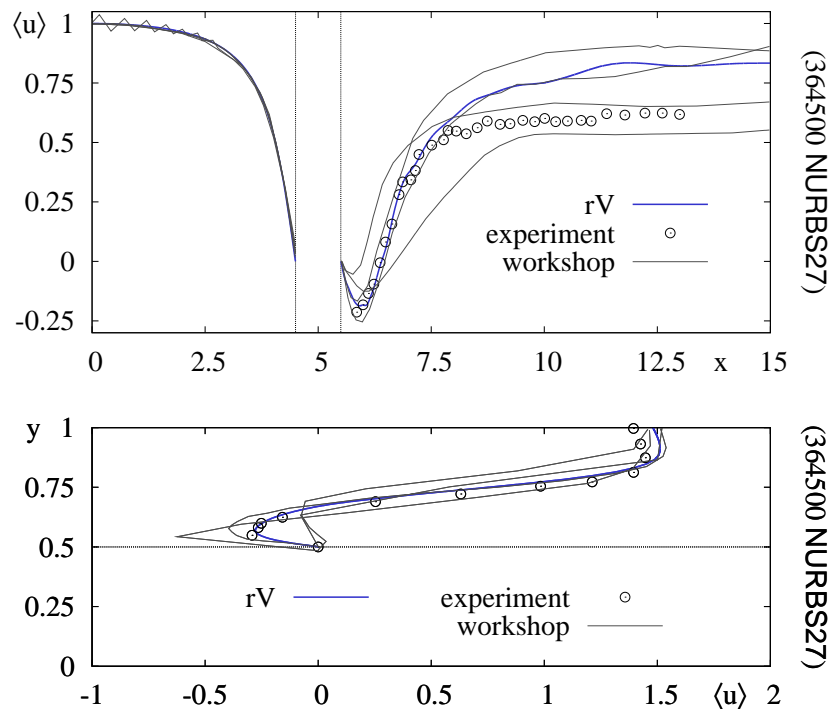


Figure 6.11: Mean streamwise velocity distributions for conventional residual-based modelling (rV). On top, distributions on the centre plane, on the bottom a close-up near the upper surface of the cylinder at $x = 5$. Experiment and workshop data in this and the following figures is taken from the paper by RODI et al. [181], see also the references therein.

very similar for both subgrid approximations. A weak imposition of the boundary condition clearly improves the results in the near-wake of the cylinder. The averaged streamwise velocity distribution near the upper surface of the cylinder is the only place where a small difference between the conventional and the time-dependent subgrid approximation can be observed. In both computations, the time-dependent version exhibited a lower level of reverse flow next to the surface.

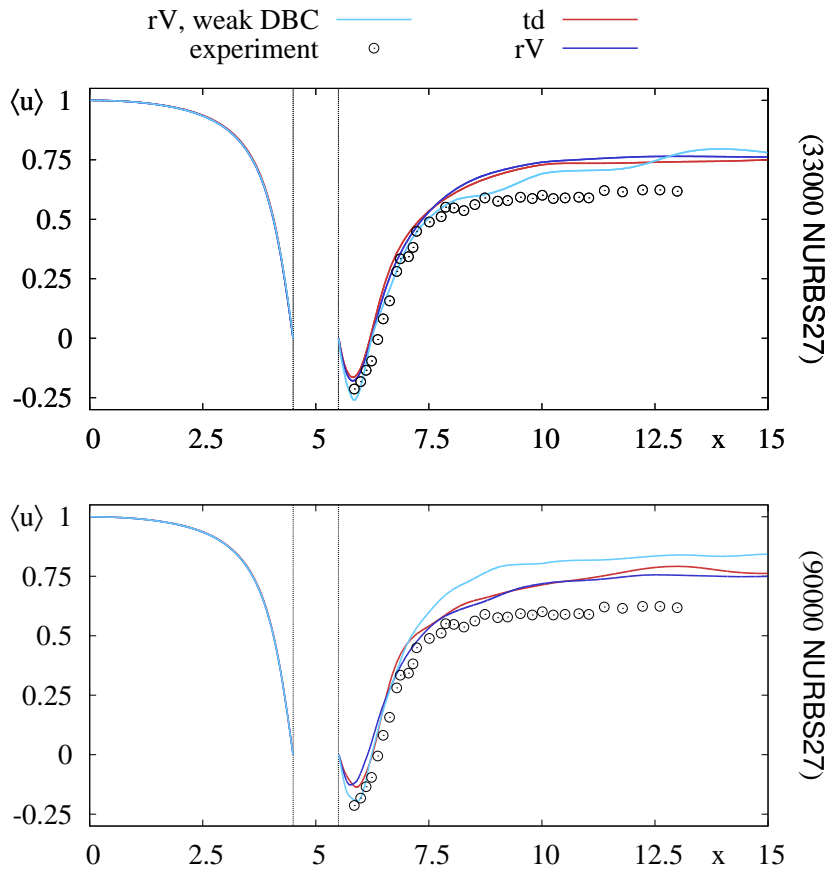


Figure 6.12: Mean streamwise velocity distributions on the centre plane for conventional (rV) and time-dependent subgrid-scale (td) modelling. The two computations based on strong boundary conditions are visualised together with a solution using weak DIRICHLET boundary conditions.

6.2.3 Mean pressure on the cylinder's surface

In this section, the distribution of the time and space averaged dimensionless pressure coefficient $\langle c_P \rangle$,

$$c_P = \frac{p - p_{\text{inlet}}}{\frac{\rho}{2} \|\mathbf{u}_{\text{inlet}}\|^2}, \quad (6.5)$$

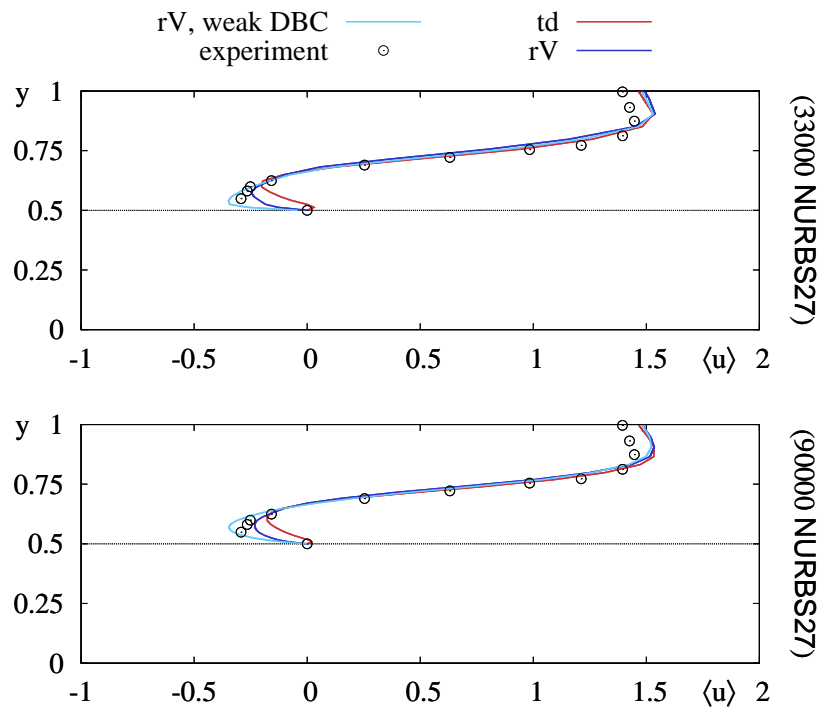


Figure 6.13: Mean streamwise velocity distributions near the upper surface of the cylinder at $x = 5$ for conventional (rV) and time-dependent subgrid-scale (td) modelling. The two computations based on strong boundary conditions are visualised together with a solution using weak DIRICHLET boundary conditions.

along the surface of the cylinder is investigated. Given the huge differences between different experiments and computations as they are shown in RODI et al. [181], the results obtained in Figure 6.14 are quite satisfactory. A study of the results for conventional and time-dependent subgrid modelling in Figure 6.15 shows no differences on the pressure, a picture we are already used to from the mean velocities. In comparison to computations based on a strong imposition of the no-slip condition, the computations enforcing a weak boundary condition exhibit a lower pressure drop along the cylinder.

6.2.4 Lift and drag

In fluid-structure interaction, forces acting on structures in flows are of special interest. For this reason, a closer investigation of the lift and drag coefficients obtained by a residual-based modelling of the flow under investigation can be very instructive. Using the force F_x on the cylinder in x -direction and the reference area A corresponding to the area of the cylinder's front face, the drag coefficient is defined as

$$c_D = \frac{F_x}{\frac{1}{2}\rho \|\mathbf{u}_{\text{inlet}}\|^2 A}. \quad (6.6)$$

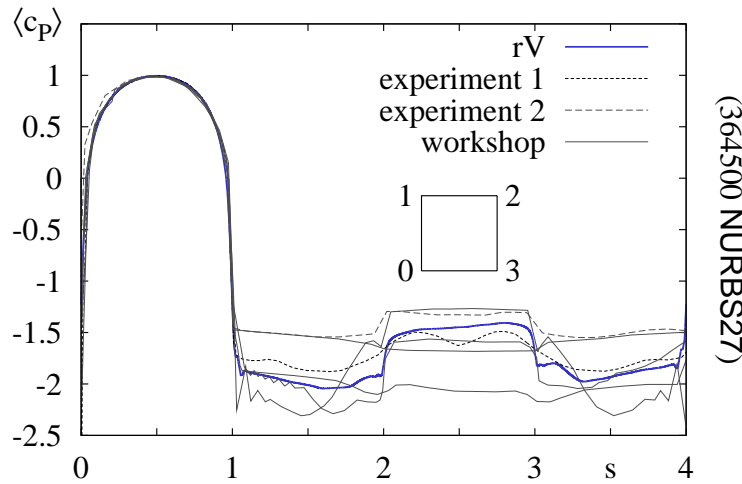


Figure 6.14: Distribution of mean pressure coefficient along the cylinder's surface. Results of conventional residual-based computations are compared to experiments by BEARMAN and OBASAJU [23] (experiment 1) and LEE [153] (experiment 2) as they are included in the collection of LES results by RODI et al. [181] (workshop).

Its distribution over time for the computation on the coarsest mesh is displayed in Figure 6.16. The results for the other meshes exhibit the same irregularly fluctuating behaviour. The amplitude of the fluctuation as well as the mean value is decreasing slightly with an increase in the number of elements. More information on the mean drag coefficient can be obtained from Figure 6.17. Time-dependent and conventional subgrid models yield nearly identical values for the drag coefficient. A significant improvement is obtained by using weak boundary conditions, an observation which is in agreement with the reduced pressure drop observed before. On the coarser meshes, the drag coefficient is overpredicted severely. Only the results on the finest mesh or on the medium mesh with weak boundary conditions are close to the region that is reported from experiments.

Finally, the distribution of the lift coefficient

$$c_L = \frac{F_y}{\frac{1}{2}\rho \|\mathbf{u}_{\text{inlet}}\|^2 A} \quad (6.7)$$

is shown in Figure 6.18. In equation (6.7), F_y denotes the vertical force on the cylinder. For a fixed mesh, time-dependent and conventional subgrid modelling did not show major differences with respect to the frequency of the vortex shedding. The result for the weak boundary condition deviates slightly, but no clear tendency towards a slower or faster vortex shedding is observable.

To sum up, the weak imposition of the boundary condition improved the quality of the results significantly. Nevertheless, this comes along with a decreased time step size and a worsened nonlinear iteration behaviour, i.e. in the setting described this improvement requires additional computational expenses.

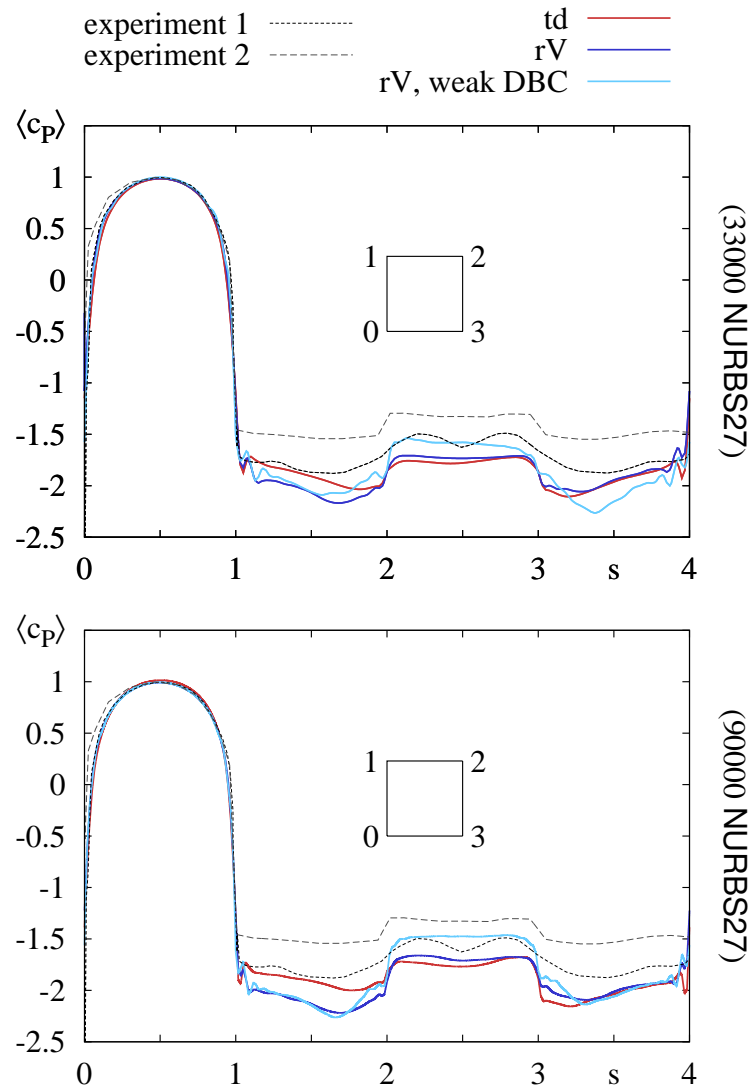


Figure 6.15: Distribution of mean pressure coefficient along cylinder surface, for conventional (rV) and time-dependent subgrid-scale (td) modelling. Once more, the two computations based on strong boundary conditions are visualised together with a solution using weak DIRICHLET boundary conditions.

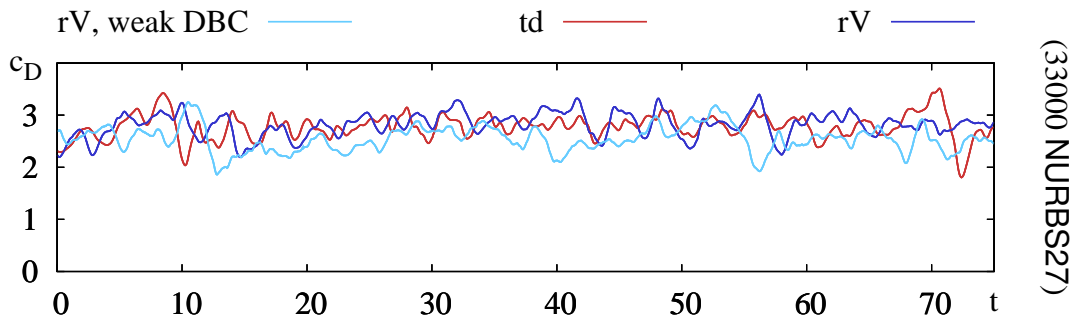


Figure 6.16: Fluctuations of the drag coefficient for the coarsest discretisation investigated.

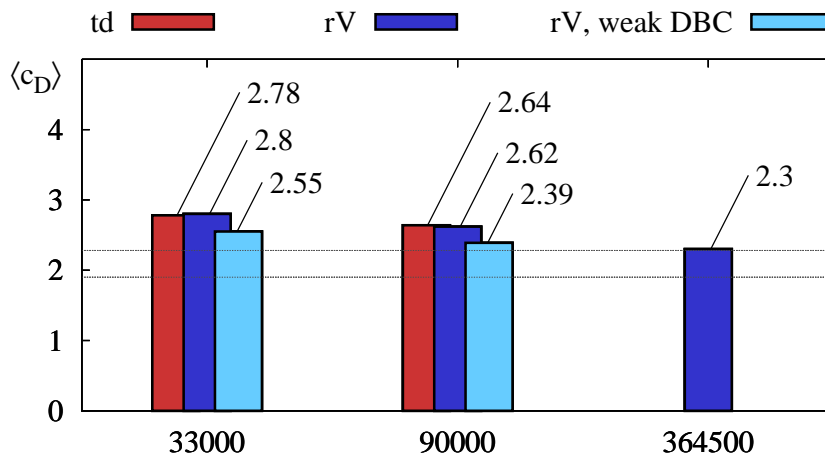


Figure 6.17: Time averaged values for the drag coefficient. The dotted lines indicate the range of experimental results referenced by RODI et al. [181] and KOOBUS and FARHAT [146].

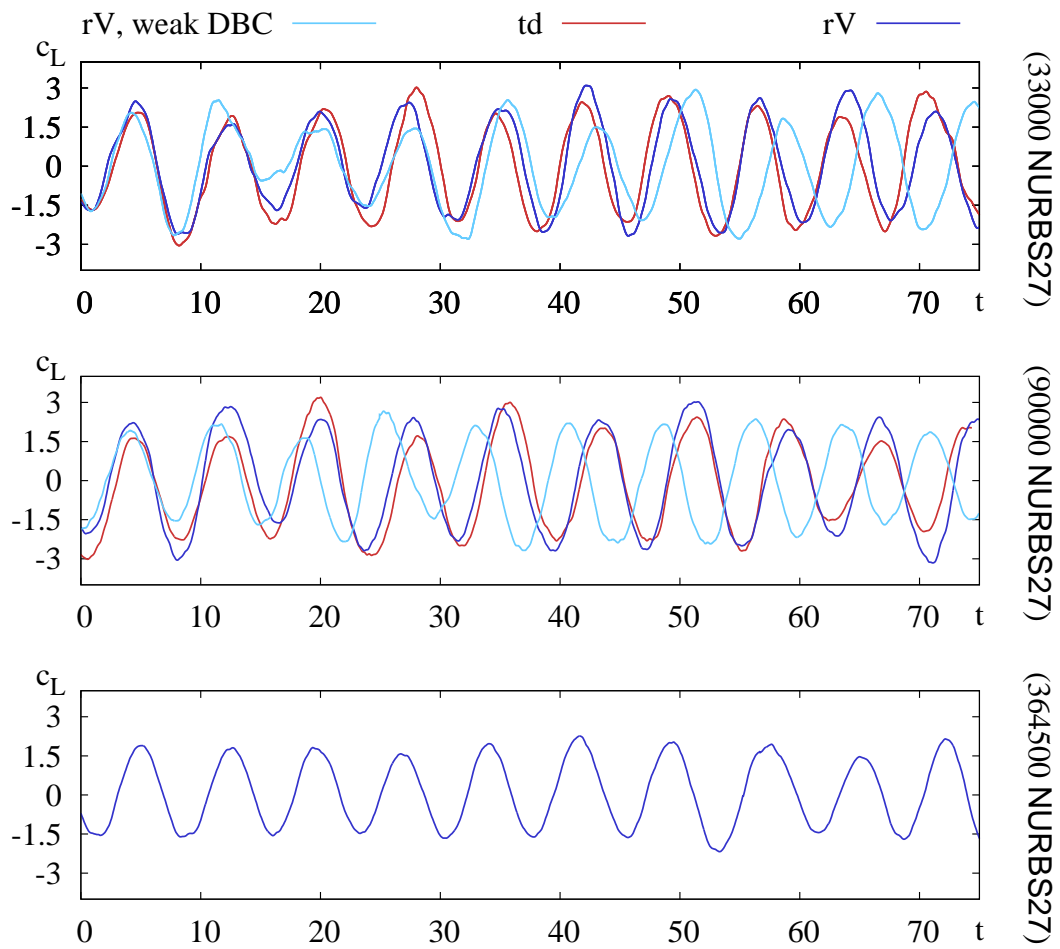


Figure 6.18: Oscillations in the lift coefficient for all computations investigated.

7 An isogeometric residual-based variational multiscale method for modelling turbulence in fluid-structure interaction

In addition to the numerical examples of chapters 5 and 6, which were mostly intended to validate the performance and to gain insight into the nature of the residual-based variational multiscale approach in the context of pure fluid problems, the current chapter will extend the range of use to applications in fluid-structure interaction. As already anticipated in section 2.1 by the statement of the governing equations of the fluid problem with respect to an ALE observer, the fluid-structure interaction approach used in this thesis will be based on a deforming-grid method. Fixed-grid approaches, as they are described for instance in WALL et al. [217], are not considered here. Additional solid and mesh subproblems required for the deforming-grid method will be described in section 7.1. The coupling of the subproblems as well as the coupled solution process will be reviewed very briefly in section 7.2. In order to validate the residual-based approach on a moving mesh, a simple test on a turbulent channel flow with prescribed deformation will be shown in section 7.3. Finally, in section 7.4, an example of a fluid-structure interaction simulation involving turbulent flow will be given.

7.1 Additional subproblems in fluid-structure interaction

In addition to the flow problem already discussed in detail, a fully coupled fluid-structure system consists of an additional structural and mesh motion subproblem. Solid and mesh motion subproblems are not in the main focus of this thesis, so they will be dealt with only very briefly in the current section.

7.1.1 Structure

The governing equations for the structural subproblem can be obtained by the same laws of continuum mechanics as the equations for the fluid problem. It is special about the structural equations that they are usually stated using a LAGRANGEan observer, i.e. the reference domain is chosen to equal the initial domain. This choice is equivalent to using a mesh mapping identical to the particle mapping $\Phi = \varphi$. With this choice, the differential version of the linear

momentum conservation equation in spatial representation (2.40) can be stated for the LAGRANGEan observer:

$$\begin{aligned} \rho_S|_{\mathbf{x}}(\mathbf{x}, t) \cdot \frac{\partial^2 (\mathbf{d}|_{\mathbf{x}})_k}{\partial t^2}(\varphi^{-1}(\mathbf{x}, t), t) &= \rho_S|_{\mathbf{x}}(\mathbf{x}, t) \cdot (\mathbf{b}|_{\mathbf{x}})_k(\mathbf{x}, t) + \\ &+ \sum_j \frac{\partial (\boldsymbol{\sigma}|_{\mathbf{x}})_{kj}}{\partial \mathbf{x}_j}(\mathbf{x}, t) \quad \text{for } k = 1, 2, 3 \end{aligned} \quad (7.1)$$

Here, $\rho_S|_{\mathbf{x}}$ is the spatial representation of the current structural density, $\mathbf{b}|_{\mathbf{x}}$ a body force per unit mass in spatial representation, $\boldsymbol{\sigma}|_{\mathbf{x}}$ the CAUCHY stress tensor in spatial representation and $\mathbf{d}|_{\mathbf{x}}$ the particle displacements in material representation introduced in equation (2.10). For structural problems, the material law providing a connection between deformation and occurring stresses is usually not stated for the CAUCHY stress tensor directly but rather for a pull-back of $\boldsymbol{\sigma}|_{\mathbf{x}}$, the so-called second PIOLA-KIRCHHOFF stress tensor

$$\mathbf{S}|_{\mathbf{X}}(\mathbf{X}, t) = \left[\det \left(\frac{\partial \varphi}{\partial \mathbf{X}} \right) (\mathbf{X}, t) \right] \cdot \left(\frac{\partial \varphi}{\partial \mathbf{X}} (\mathbf{X}, t) \right)^{-1} \cdot \boldsymbol{\sigma}|_{\mathbf{x}}(\varphi(\mathbf{X}, t), t) \cdot \left(\frac{\partial \varphi}{\partial \mathbf{X}} (\mathbf{X}, t) \right)^{-T}. \quad (7.2)$$

For simplicity, a SAINT-VENANT-KIRCHHOFF model

$$\mathbf{S}|_{\mathbf{X}}(\mathbf{X}, t) = \lambda_S \operatorname{tr}(\mathbf{E}|_{\mathbf{X}}(\mathbf{X}, t)) \cdot \mathbf{1} + 2\mu_S \cdot \mathbf{E}|_{\mathbf{X}}(\mathbf{X}, t) \quad (7.3)$$

which is valid in the small strain regime is assumed. It states a linear stress-strain relation based on the GREEN-LAGRANGE strain tensor

$$\mathbf{E}|_{\mathbf{X}}(\mathbf{X}, t) = \frac{1}{2} \left(\left(\frac{\partial \varphi}{\partial \mathbf{X}} (\mathbf{X}, t) \right)^T \left(\frac{\partial \varphi}{\partial \mathbf{X}} (\mathbf{X}, t) \right) - \mathbf{1} \right) \quad (7.4)$$

and two model parameters, the LAMÉ constants λ_S and μ_S . These parameters are often replaced by YOUNG'S modulus E_S and POISSON'S ratio ν_S ,

$$E_S = \frac{\mu_S (3\lambda_S + 2\mu_S)}{\lambda_S + \mu_S} \quad \text{and} \quad \nu_S = \frac{\lambda_S}{2(\lambda_S + \mu_S)}. \quad (7.5)$$

To sum up, the conservation equation of linear momentum in material representation using the second PIOLA-KIRCHHOFF stress tensor is given by

$$\begin{aligned} \rho_S^0|_{\mathbf{X}} \cdot \frac{\partial^2 (\mathbf{d}|_{\mathbf{X}})_k}{\partial t^2}(\mathbf{X}, t) &= \rho_S^0|_{\mathbf{X}} \cdot (\mathbf{b}|_{\mathbf{X}})_k(\mathbf{X}, t) + \\ &+ \sum_j \frac{\partial}{\partial \mathbf{X}_j} \left(\sum_l \frac{\partial \varphi_k}{\partial \mathbf{X}_l}(\mathbf{X}, t) \cdot (\mathbf{S}_{lj}|_{\mathbf{X}})(\mathbf{X}, t) \right) \quad \text{for } k = 1, 2, 3. \end{aligned} \quad (7.6)$$

The density $\rho_S^0|_{\mathbf{X}}$ in this equation is the material density. From equation (7.6), a weak form can be obtained which is discretised in time and space in analogy to what was described in chapter 3 for the fluid subproblem. For time discretisation, a generalised-alpha approach according to CHUNG and HULBERT [49] is a suitable choice. Spatial discretisation can be done

based on a GALERKIN approach. Thus, for structures which are not incompressible, the spatial discretisation process is simplified significantly compared to the process for incompressible fluids, which requires extra effort for convection induced and inf-sup-based instabilities as they were discussed in subsection 3.4.4. Nevertheless, due to the nonlinearity contained in the strain tensor for large deformations, the solution process for the unknown displacements still requires a similar predictor-corrector iteration. For more details, the reader is referred to the textbooks by BONET and WOOD [36], HUGHES [116] or ZIENKIEWICZ and TAYLOR [226].

7.1.2 Mesh motion

In fluid-structure interaction, the computational fluid domain has to deform according to the structural deformation. Strictly speaking, the structural deformation governs only the motion of the boundaries of the fluid domain. Its interior has to be deformed consistently with the boundaries, but otherwise it can be updated ‘arbitrarily’. Nevertheless, approaches ensuring a conservation of the element quality in the interior of the domain will be preferred in order to maintain the solution’s accuracy. Thus, desired properties of a mesh motion algorithm in the current setting are to keep element distortion as small as possible and to preserve boundary layer type meshes as they are common in turbulent flow applications.

The most intuitive choices to define the mesh motion are pseudo-structure approaches as they are discussed in WALL [215]. In these approaches, the computational fluid domain is treated as a solid which is deformed according to the prescribed deformation of the boundaries. Other options are structure analogies using spring models as described in FARHAT et al. [73, 72] or LAPLACE smoothers as they can be found in LÖHNER and YANG [157]. Furthermore, an extension to a hybrid fixed-grid/ALE method is also possible. This approach, which was proposed by GERSTENBERGER and WALL [92], is also promising but not considered here.

7.2 Fluid-structure interaction: coupled problem and solution methods

In fluid-structure interaction, spatially and temporally discretised subproblems amount to a coupled nonlinear problem. The coupling of these subproblems is strong, i.e. in general it is required to equilibrate the interactions between fluid and structure at the coupling interface in each time step. A loose coupling which abandons the exact equilibrium and rather treats the coupling explicit in time is problematic for incompressible flow in combination with light-weighted structures. This is due to the inherent instability related to the artificial added mass effect, see FÖRSTER et al. [80] for a discussion. Thus, although it would be feasible for instance in suitable applications in aeroelasticity, the weak coupling will not be considered here in more detail. Approaches which are more appropriate for the solution of the fluid-structure interaction problem under consideration will be listed below. For a more detailed overview and further references, the reader is referred to KÜTTLER [148].

The first category are nonlinearly coupled, DIRICHLET-NEUMANN partitioned approaches which are reviewed for instance by KÜTTLER and WALL [150]. In such methods, the fluid-structure interaction problem is split into two separate subproblems. The coupling takes place

based on an exchange of boundary data on the common boundary of fluid and structure subdomain. The coupling conditions are updated in a staggered, iterative manner involving nonlinear solutions on both subdomains in each step. A dynamically adapted relaxation procedure is usually employed in order to enhance robustness and rate of convergence. These approaches provide full flexibility with respect to the choice of the individual field solvers, but include an often costly iteration over the fields.

The second category are monolithic approaches which treat the nonlinearity of the whole coupled problem by a single NEWTON iteration. Such an approach in the context of isogeometric analysis is presented in BAZILEVS et al. [17]. The solution of the linear subproblems in this iteration can be done either by a partitioned linear approach involving a sequential solution of the linear subproblems or by a one-level solution of the linear system using a preconditioned KRYLOV method.

From this list of available coupling algorithms, the monolithic NEWTON-KRYLOV method turned out to be the most efficient solution approach for fluid-structure interaction problems involving turbulent incompressible flows and thus was selected as the most suitable method. In order to provide some more information on the chosen solution process, the degrees of freedom for each subproblem can be decomposed into interface degrees of freedom associated with an index Γ and remaining interior degrees of freedom denoted by an index I . For simplicity, matching fluid and structure meshes are assumed at the interface. For the monolithic approach, the kinematic coupling of fluid and structural degrees of freedom at the interface is given by

$$\frac{\mathbf{d}_{\Gamma}^{h,n+1} - \mathbf{d}_{\Gamma}^{h,n}}{\Delta t} = \frac{\mathbf{u}_{\Gamma}^{h,n+1} + \mathbf{u}_{\Gamma}^{h,n}}{2}. \quad (7.7)$$

Furthermore, the kinematic coupling for the mesh displacement at the interface is given by

$$\mathbf{d}_{\Gamma}^{h,n+1} = \mathbf{d}_{G,\Gamma}^{h,n+1}. \quad (7.8)$$

In addition to the kinematic coupling, a kinetic coupling at the interface has to hold, yielding a combined nonlinear equation system for all spatially and temporally discretised subproblems:

$$\underline{R}^{\text{FSI}} \left(\mathbf{d}^{h,n+1}, \mathbf{u}^{h,n+1}, p^{h,n+1}, \mathbf{d}_G^{h,n+1} \right) = \underline{0} \quad (7.9)$$

For matching grids, the kinematic coupling conditions at the interface reduce the actual unknowns in equation (7.9) for instance to the structural displacements $\mathbf{d}^{h,n+1}$, the interior fluid velocities $\mathbf{u}_I^{h,n+1}$, the fluid pressure $p^{h,n+1}$ and the mesh displacements in the interior of the fluid domain $\mathbf{d}_{G,I}^{h,n+1}$. The resulting linearised system in each NEWTON step is then solved for the increments of these unknowns using a block-preconditioned KRYLOV procedure as described in KÜTTLER [148], see also the references therein.

7.3 Preliminary study of residual-based variational multiscale modelling of turbulence on a deforming channel

For a three-scale variational multiscale model, RAJASEKHARAN and FARHAT [177] already reported successful applications to computations of turbulent flow on moving meshes. In order

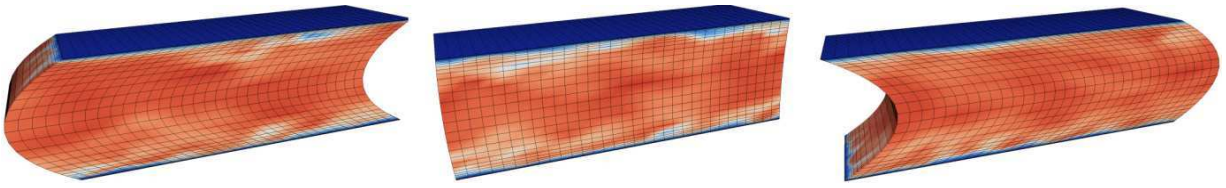


Figure 7.1: Test case for turbulent channel flow on a deforming grid.

to estimate the potential of residual-based variational multiscale modelling of turbulence for such applications, a preliminary study of the performance of this two-level approach will be done in this section. The study is based on a simulation of turbulent channel flow at $Re_\tau = 395$ on a deformable mesh. The initial mesh and all material parameters etc. are taken from the 32^3 HEX8 case from section 5.1. The applied mesh motion, defined as

$$\Phi(\boldsymbol{\xi}, t) = \boldsymbol{\xi} + 1.2 \cdot \sin(t) \cdot (1 - (\boldsymbol{\xi} \cdot \mathbf{e}_y)^2) \cdot \mathbf{e}_y, \quad (7.10)$$

leads to deformations as depicted in Figure 7.1. For simplicity, this mesh motion is chosen such that it preserves the distance between nodes and walls. This allows a simple spatial averaging in wall-parallel planes. The maximum of the grid velocity induced by Φ is approximately equal to the mean streamwise velocity. In Figure 7.2, results from the computation on a mesh deforming according to equation (7.10) are compared to results on a fixed mesh taken from BAZILEVS et al. [15]. For ease of comparison, the second order statistics of the ALE computations are

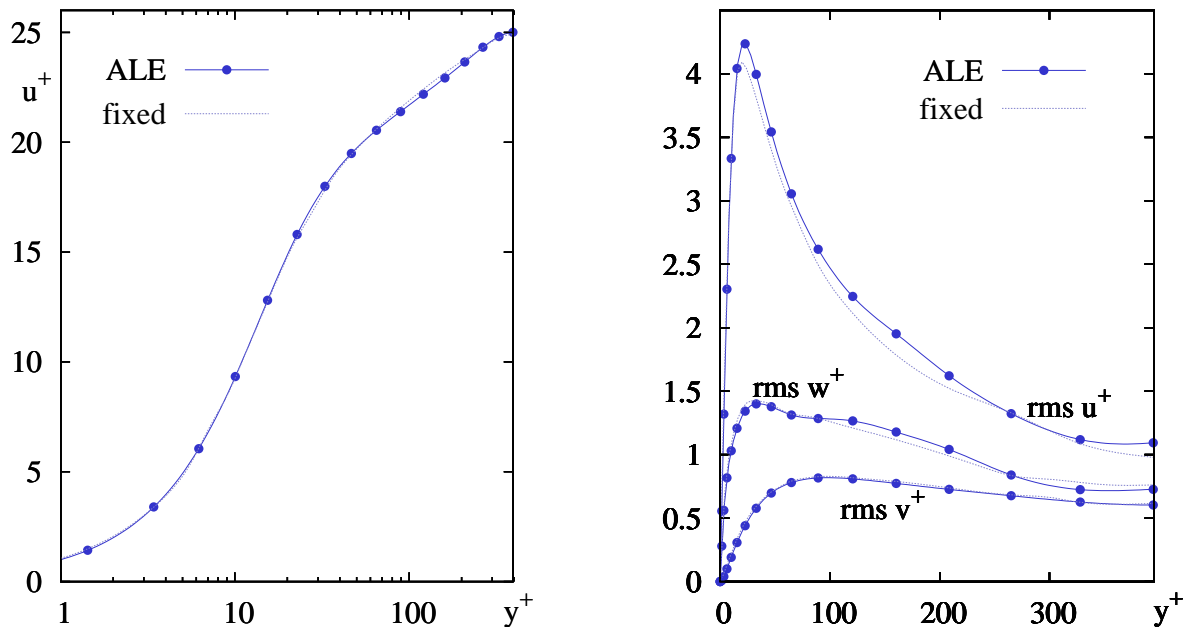


Figure 7.2: Results for turbulent channel flow computations on 32^3 trilinear elements at $Re_\tau = 395$. The solution on the deforming domain (ALE) is in excellent agreement with the solution on the EULERian grid (fixed) taken from BAZILEVS et al. [15].

based on pointwise spatial averaging, see section 5.2 for more details on the averaging process. Furthermore, the stabilisation parameter definitions used are the ones from equations (3.161) and (3.162). The results for the moving and fixed grid turned out to be almost identical. For future work, it will be very interesting to see how the results change with respect to a mesh motion which activates the divergence of grid velocity term from equation (4.61).

7.4 Fluid-structure interaction for a turbulent pipe flow with a flexible wall

The example that will be presented in this section is intended to demonstrate the applicability of residual-based variational multiscale modelling to fluid-structure interaction problems involving turbulent flows. The results of this section will combine all building blocks provided and validated in the previous chapters in the framework of a monolithic fluid-structure interaction (FSI) computation.

7.4.1 Computational setup

The geometry of the investigated circular pipe is defined in Figures 7.3 and 7.4. Its length is 5.0

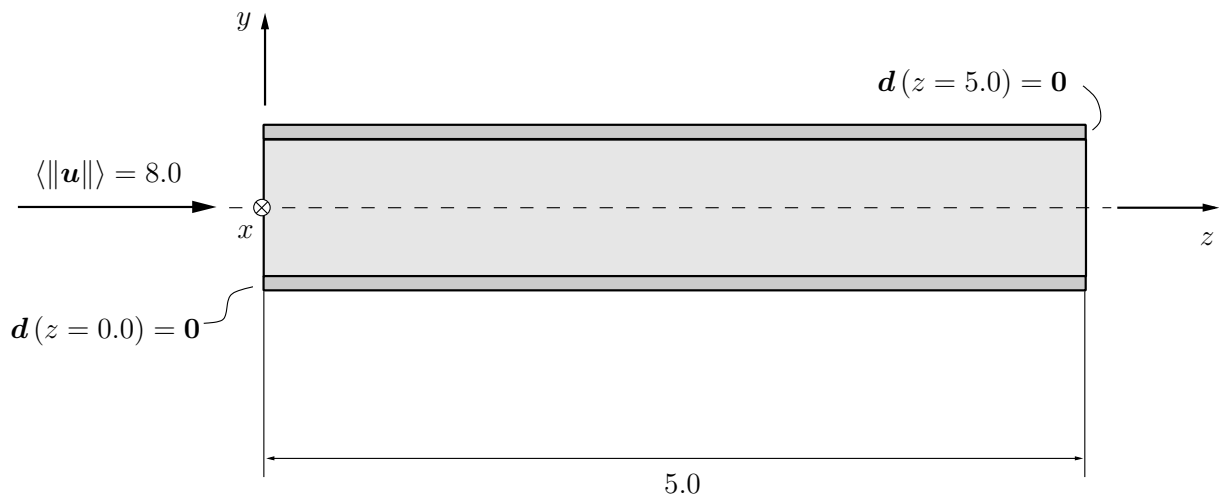


Figure 7.3: Pipe geometry and DIRICHLET boundary conditions. Another cut orthogonal to the z -axis is displayed in Figure 7.4.

and it has a diameter of 1.0. The pipe wall of thickness 0.1 consists of an elastic material. It is characterised by a material density $\rho_S^0 = 1.2$, a YOUNG'S modulus $E_S = 3 \cdot 10^6$ and a POISSON'S ratio $\nu_S = 0.3$. The structure is fixed by a DIRICHLET boundary condition at the beginning and end of the pipe segment. A fluid of density $\rho = 1.0$ and kinematic viscosity $\nu = 0.00015$ flows through the pipe at an averaged velocity of 8.0, corresponding to a REYNOLDS number of $Re = 5.3 \cdot 10^4$. The boundary condition on the inflow is of DIRICHLET type, the outflow boundary condition is of do-nothing NEUMANN type. The values for the turbulent inflow profile

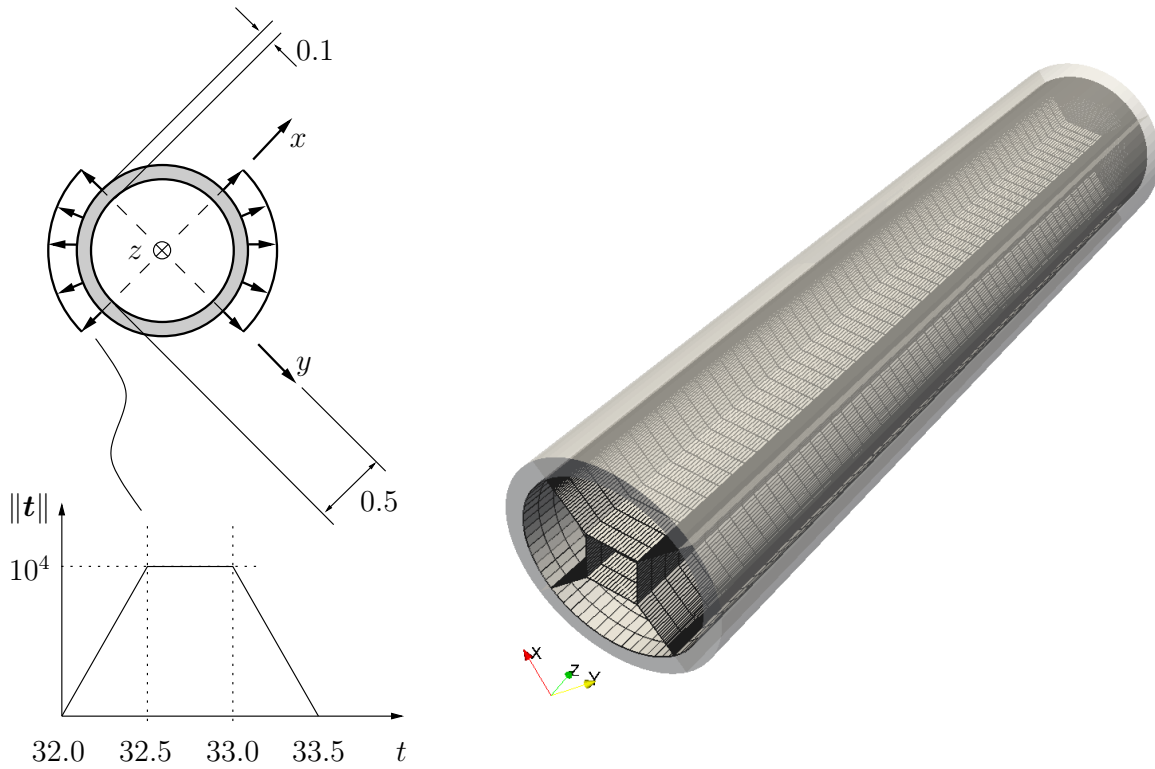


Figure 7.4: Pipe cross section defining pipe diameter, wall thickness and the surface-orthogonal loading t (left). Visualisation of the five fluid patches (right). The grid displayed corresponds to the visualisation cells used to post-process the NURBS solution, as usual.

are computed using a separate computation of turbulent pipe-flow on a periodic domain identical to the initial fluid domain described above. Starting from a randomly perturbed initial profile, the flow is computed for 32 time units until a turbulent flow profile has developed in the pipe. Afterwards, a surface-orthogonal loading following a time curve is applied to the outer surface of the structure as described in Figure 7.4.

Temporal discretisation on the fluid side is done based on the generalised-alpha approach using the same parameter setting as for all other examples in this thesis. On the structural side, the generalised-alpha parameters chosen are $\beta = 0.25$ and $\gamma = \alpha_F = \alpha_M = 0.5$. The computation is based on a time step size of $\Delta t = 0.01$. For spatial discretisation, the fluid domain is decomposed into five patches as it is indicated on the right side of Figure 7.4. For the structural domain, a matching discretisation composed of four patches is used. All patches of fluid and structure consist of second order isogeometric NURBS27 elements as it is shown in Table 7.1. In order to improve the boundary layer representation in the fluid domain, a hyperbolic mesh stretching based on a constant $C_{\text{stretch}} = 2.1$ was applied to the knot vector in surface-normal direction on the $20 \times 8 \times 25$ patches of the fluid domain.

Once more, the stabilisation parameter definitions used for the residual-based variational multiscale modelling are the ones from equations (3.161) and (3.162). The NEWTON-type linearisation scheme from subsection 4.5.3 was found to be appropriate for the fluid subproblem.

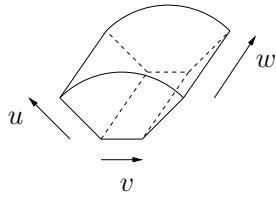
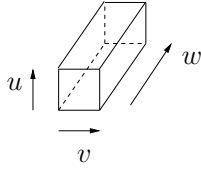
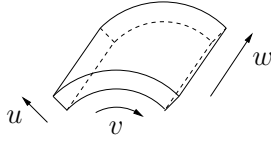
| fluid patches | | structure patches |
|---|---|--|
|  |  |  |
| $20 \times 8 \times 25$ | $8 \times 8 \times 25$ | $20 \times 8 \times 25$ |

Table 7.1: Number of elements in the patches of the discretisation for fluid and structure. The pseudo-structure approach used to compute the mesh deformation uses a mesh identical to the fluid discretisation.

7.4.2 Results

The applied external loading causes a deformation of the pipe as it is shown in the centre column of Figure 7.5. The pipe cross-section in the middle of the segment changes from an initial circular shape to an oblate ellipse at the peak of the external loading. As it can be already seen in the distribution of the absolute value of the fluid velocity on the right of Figure 7.5, this change of shape induces a separation of the flow on the part of the boundary which is curved towards the centre of the pipe. Note that even for the deformed state, the boundary is still smooth due to the NURBS representation. This ensures that for the separation caused by this deformation the break-off point is not determined by artificial kinks in the mesh. The separation is also shown in Figure 7.6, where absolute velocity distributions for three cross sections orthogonal to the z -axis are shown. The first cross section corresponds to the prescribed **DIRICHLET** values at the inflow of the pipe. The second cross section in the middle of the pipe segment is the one that exhibits the largest deformation. The last cross section at the outflow clearly shows the predominantly blue regions that correspond to the low-speed flow areas behind the separation point.

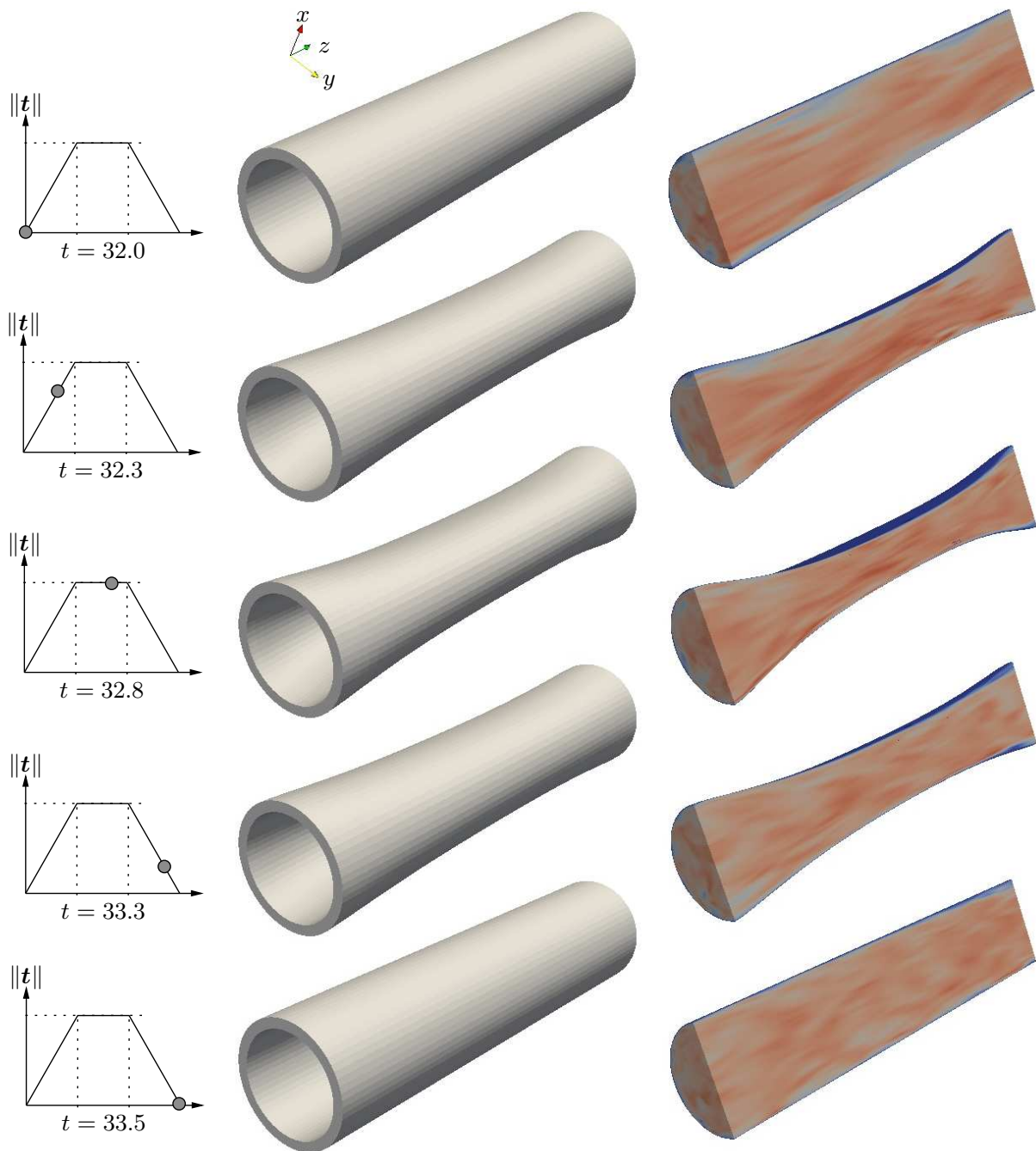


Figure 7.5: Unscaled deformation of the structural domain for five characteristic time steps during the load cycle $32.0 \leq t \leq 33.5$ (left). The corresponding distribution of the absolute value of fluid velocity on the deforming domain is given for a cross-section (right). A legend for the velocity values is contained in Figure 7.6.

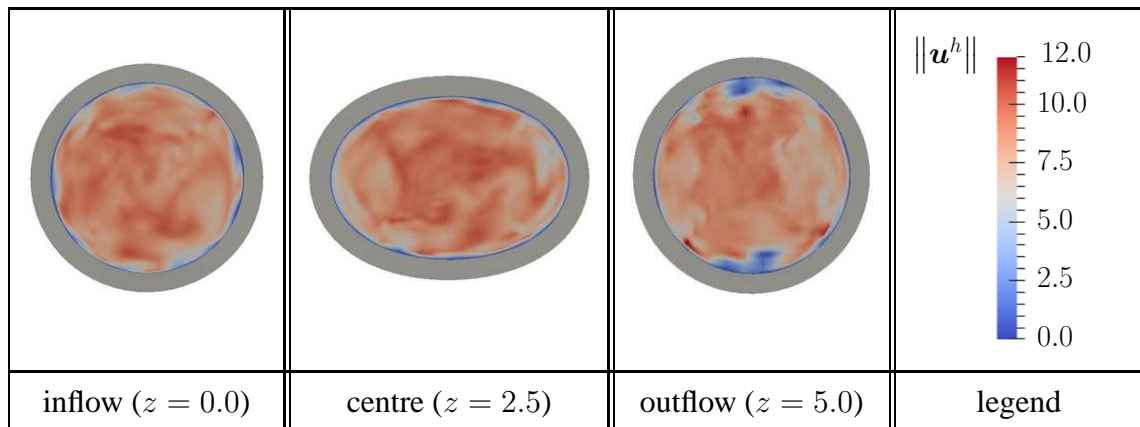


Figure 7.6: Distribution of the absolute velocity for three cuts through the deformed pipe at $t = 33.2$.

8 Summary and outlook

The ambition of this work was to combine several known methods and to extend them to a new range of applications. The time-dependent subgrid scales proposed by CODINA et al. [55] were successfully applied to residual-based variational multiscale modelling of fully turbulent flows. Furthermore, residual-based variational multiscale modelling of turbulence, CALO [45], and isogeometric fluid-structure interaction, BAZILEVS et al. [16], were combined to allow turbulent fluid-structure interaction computations in a monolithic framework according to KÜTTLER [148]. The first results obtained with this method are promising.

In order to reach these tasks, the residual-based variational multiscale framework was derived in an ALE framework. The subgrid models including the time-dependent subgrid approximation were included in a state-of-the-art generalised-alpha approach capable of treating time derivatives on deforming domains. The obtained algorithm was used for a detailed investigation of the nature of residual-based LES approaches. The time-dependent subgrid scales turned out not to be more accurate for the resolved-scale results in practice, which seems to be disappointing at first sight. Nevertheless, this is compensated by a more robust representation of unresolved-scale quantities and the fact that a lot more insight into the nature of residual-based approaches was gained with respect to the dissipation of the model terms, time dependency of the subgrid scales and their small-time-step behaviour. Furthermore, the impact of the isogeometric representation on the unresolved-scale quantities was studied, showing that the improved performance with respect to the resolved-scale results, see AKKERMAN et al. [3], comes along with a more pronounced representation of the unresolved scales.

There are several issues that will require further consideration in the future. The orthogonal subgrid-scale approach by CODINA [52] should be tested. For this approach, HUGHES and SANGALLI [125] predict a non-local GREEN's function, so a further assessment of its impact on the quality of the subgrid approximation will be mandatory. Nevertheless, the gains with respect to the reduced nonlinear character of the resulting equations would be significant and thus render the time-dependent approach more competitive to the conventional approach. The most valuable contribution of the time-dependent approach is that it eliminates the dependency of the conventional approach on the time step size. This will allow to pose the question for the 'optimal' stabilisation parameter or procedure independently of the chosen time step. In a very simplified way, this question was already dealt with in section 5.5 when looking for an optimal element-length definition close to the wall in boundary layer meshes. At the moment, since the time-dependent implementation introduces additional complexity and it did not improve the resolved-scale results in all test examples contained in this thesis, the conventional approach remains the recommended one for large-scale applications. Furthermore, the residual-based LES on meshes with pronounced volume change and distortion of elements should be investigated more closely. The investigations could be conducted on the basis of previous studies by FÖRSTER [78] on the performance of stabilised methods on distorted meshes. Very high REYNOLDS number applications are also a field that needs further consideration. The REYNOLDS stress term, which did

not provide a significant contribution to any of the energy budgets shown in this thesis, might play a more important role for these flows than the residual-based model could provide. It is possible that an additional subgrid viscosity or fine-scale subgrid viscosity term is capable of representing the effect of the REYNOLDS stress much better. Such a procedure is advocated by many researchers, in written form for instance by WANG and OBERAI [218] based on results from spectral analysis, and by GRAVEMEIER et al. [97], who are combining residual-based stabilisation with an additional subgrid term based on algebraic variational multiscale-multigrid modelling. A necessity to test the established fluid-structure interaction framework for more demanding settings, like thin structures in the wake of a cylinder, is also self-evident.

In addition to these straightforward enhancements and further investigations, several new research directions arise from the work presented in this thesis. The good performance of the weak DIRICHLET approach with respect to the computed lift and drag values in the turbulent flow around a square cylinder indicates that a lot of improvement can be made by a more elaborate treatment of boundary conditions at fluid-structure interfaces. Thus, in a first step, an incorporation of the weak DIRICHLET boundary conditions in the monolithic fluid-structure interaction framework can be considered. The weak DIRICHLET boundary condition formulation from BAZILEVS et al. [21] is based on an empirical, problem-specific near-wall model. The replacement of this model by a coupled URANS simulation in regions close to the walls would be perfectly in line with the idea of an improved treatment of the boundary conditions. Further investigations will be required, as for example concerning RANS modelling on moving meshes. Nevertheless, the approach seems to be extremely promising. The coupling of simulations on different fluid domains of different resolution, as they would for instance appear in hybrid methods, see GERSTENBERGER and WALL [92], is a well-known problem in LES. An investigation of this matter in the context of residual-based LES will also be interesting for future applications. A completely different future direction concerns the properties of iterative solvers and preconditioners. The good performance of the multilevel preconditioned GMRES, which was observed for the NURBS discretisation in comparison to a comparable serendipity discretisation, calls for a closer investigation of the relationship between elements and linear system. For instance, the uniformity and smoothness of the shape functions might be related to the good performance of the linear solver.

Finally, other multiphysics applications lie ahead. Combinations of isogeometric analysis, scalar transport, electrochemical processes and residual-based variational multiscale modelling of turbulence are planned, applications to turbulent combustion seem possible. The smoothness properties of the isogeometric approach, see COTTRELL et al. [57], are assumed to be very beneficial for other, non-fluid types of multiphysics applications as well. For instance, a combination of structures and optics, exploiting the smooth surface representations for the refraction of light in deforming lenses etc., is a very interesting area of research that did, at the best of my knowledge, not receive much attention up to now.

A Mathematical tools and proofs for the description of flows

In this appendix, several topics related to the governing equations will be addressed. Section A.1 provides the REYNOLDS transport theorem that was used in section 2.1 to derive the NAVIER-STOKES equations in ALE and EULERian formulation. The subsequent section A.2 provides a proof for the equivalence of the ALE mass conservation equation in reference and spatial representation. This property was used in section 2.1 to derive the spatial representation of the ALE form of the NAVIER-STOKES equations. In addition to these topics related to continuum mechanics, section A.3 is on the statistical description of turbulent flows. The material collected in that section will be useful for the derivation of the REYNOLDS-averaged NAVIER-STOKES equations and for the sampling procedures used in the numerical computations of chapter 5 and chapter 6. Section A.4 addresses a last topic. It is about fundamental function spaces and inner products required to convert the strong form of the equation into a weak, variational counterpart as it was done in section 3.2.

A.1 REYNOLDS transport theorem

Let $\Upsilon(\Xi, t)$ be an arbitrary motion mapping with a positive JACOBIAN determinant. Furthermore, let $V(t) := \Upsilon(V(t_0), t)$ be a ‘transported’ balance volume in the range of the motion mapping at time t and $\mathbf{v}|_{\Xi} := \frac{d\Upsilon}{dt}$ the velocity induced by the motion mapping. Then the substantial change of a physical quantity $\mathbf{f}|_{\chi}$ in this volume, i.e. the change of a quantity associated with the particles that are currently in the volume, is not only due to the local change of the quantity but also caused by a flux over the volume’s boundaries. Since the balance volume enclosing the particles which carry the physical quantity changes in time according to the motion mapping, the integral has to be transformed back to the initial domain using the transformation theorem to be able to interchange integration and time differentiation:

$$\begin{aligned} \frac{d}{dt} \int_{V(t)} \mathbf{f}|_{\chi}(\chi, t) d\chi &= \\ &= \frac{d}{dt} \int_{V(t_0)} \mathbf{f}|_{\chi}(\Upsilon(\Xi, t), t) \cdot \det \left(\frac{\partial \Upsilon}{\partial \Xi}(\Xi, t) \right) d\Xi = \\ &= \int_{V(t_0)} \frac{d}{dt} \left[\mathbf{f}|_{\chi}(\Upsilon(\Xi, t), t) \right] \cdot \det \left(\frac{\partial \Upsilon}{\partial \Xi}(\Xi, t) \right) + \\ &\quad + \mathbf{f}|_{\chi}(\Upsilon(\Xi, t), t) \cdot \frac{d}{dt} \left[\det \left(\frac{\partial \Upsilon}{\partial \Xi}(\Xi, t) \right) \right] d\Xi = \end{aligned}$$

$$\begin{aligned}
 &= \int_{V(t_0)} \left[\frac{\partial \mathbf{f}|_{\mathbf{x}}}{\partial t} (\boldsymbol{\Upsilon}(\boldsymbol{\Xi}, t), t) \right] \cdot \det \left(\frac{\partial \boldsymbol{\Upsilon}}{\partial \boldsymbol{\Xi}} (\boldsymbol{\Xi}, t) \right) + \\
 &\quad + \left[\sum_j \frac{\partial \mathbf{f}|_{\mathbf{x}}}{\partial \chi_j} (\boldsymbol{\Upsilon}(\boldsymbol{\Xi}, t), t) \cdot (\mathbf{v}|_{\boldsymbol{\Xi}})_j (\boldsymbol{\Xi}, t) \right] \cdot \det \left(\frac{\partial \boldsymbol{\Upsilon}}{\partial \boldsymbol{\Xi}} (\boldsymbol{\Xi}, t) \right) + \\
 &\quad + \mathbf{f}|_{\mathbf{x}} (\boldsymbol{\Upsilon}(\boldsymbol{\Xi}, t), t) \cdot \frac{d}{dt} \left[\det \left(\frac{\partial \boldsymbol{\Upsilon}}{\partial \boldsymbol{\Xi}} (\boldsymbol{\Xi}, t) \right) \right] d\boldsymbol{\Xi} \tag{A.1}
 \end{aligned}$$

The time derivative of a JACOBIAN determinant is given by the following equation, see for example the books by KÖNIGSBERGER [145] or CHORIN and MARSDEN [48]:

$$\frac{d}{dt} \det \left(\frac{\partial \boldsymbol{\Upsilon}}{\partial \boldsymbol{\Xi}} (\boldsymbol{\Xi}, t) \right) = \det \left(\frac{\partial \boldsymbol{\Upsilon}}{\partial \boldsymbol{\Xi}} (\boldsymbol{\Xi}, t) \right) \cdot \sum_{i,j} \frac{\partial \boldsymbol{\Upsilon}_i^{-1}}{\partial \chi_j} (\boldsymbol{\Upsilon}(\boldsymbol{\Xi}, t), t) \cdot \frac{\partial (\mathbf{v}|_{\boldsymbol{\Xi}})_j}{\partial \boldsymbol{\Xi}_i} (\boldsymbol{\Xi}, t) \tag{A.2}$$

Using this equation, the integral can be transformed back to the balance volume and yields the REYNOLDS transport theorem:

$$\begin{aligned}
 &\frac{d}{dt} \int_{V(t)} \mathbf{f}|_{\mathbf{x}} (\boldsymbol{\chi}, t) d\boldsymbol{\chi} = \\
 &\quad = \int_{V(t)} \left(\frac{\partial \mathbf{f}|_{\mathbf{x}}}{\partial t} (\boldsymbol{\chi}, t) + \sum_j (\mathbf{v}|_{\boldsymbol{\chi}})_j (\boldsymbol{\chi}, t) \cdot \frac{\partial \mathbf{f}|_{\mathbf{x}}}{\partial \chi_j} (\boldsymbol{\chi}, t) + \right. \\
 &\quad \quad \left. + \mathbf{f}|_{\mathbf{x}} (\boldsymbol{\chi}, t) \cdot \sum_j \frac{\partial (\mathbf{v}|_{\boldsymbol{\chi}})_j}{\partial \chi_j} (\boldsymbol{\chi}, t) \right) d\boldsymbol{\chi} = \\
 &\quad = \int_{V(t)} \left(\frac{\partial \mathbf{f}|_{\mathbf{x}}}{\partial t} (\boldsymbol{\chi}, t) + \sum_j \frac{\partial}{\partial \chi_j} \left((\mathbf{v}|_{\boldsymbol{\chi}})_j (\boldsymbol{\chi}, t) \cdot \mathbf{f}|_{\mathbf{x}} (\boldsymbol{\chi}, t) \right) \right) d\boldsymbol{\chi} \tag{A.3}
 \end{aligned}$$

The contribution from the local time derivative and from the flux term can be easily identified in the last line of equation (A.3).

A.2 ALE mass conservation in spatial representation — a proof

The point of departure for this proof is the ALE mass conservation equation in reference representation (2.26). In the beginning, the reference density in (2.26) has to be expressed in terms of the current density. For this purpose, equation (2.21) is rewritten as:

$$\rho^{\text{ref}}|_{\boldsymbol{\xi}} (\boldsymbol{\xi}, t) = \rho|_{\boldsymbol{\xi}} (\boldsymbol{\xi}, t) \cdot \det \left(\frac{\partial \boldsymbol{\Phi}}{\partial \boldsymbol{\xi}} \right) (\boldsymbol{\xi}, t) \tag{A.4}$$

Substituting this expression in the differential form of the ALE mass conservation equation in reference representation (2.26) requires the computation of several derivatives. The derivative

of the first term, related to the local change of the reference density, can be rephrased as follows using the time derivative of a JACOBIAN determinant similar to what has been used in the derivation of the REYNOLDS transport theorem:

$$\begin{aligned}
\frac{\partial \rho^{\text{ref}}|_{\xi}}{\partial t}(\xi, t) &= \frac{\partial \rho|_{\xi}}{\partial t}(\xi, t) \cdot \det\left(\frac{\partial \Phi}{\partial \xi}\right)(\xi, t) + \\
&+ \rho|_{\xi}(\xi, t) \cdot \frac{\partial}{\partial t}\left(\det\left(\frac{\partial \Phi}{\partial \xi}\right)\right)(\xi, t) = \\
&= \frac{\partial \rho|_{\xi}}{\partial t}(\xi, t) \cdot \det\left(\frac{\partial \Phi}{\partial \xi}\right)(\xi, t) + \\
&+ \rho|_{\xi}(\xi, t) \cdot \det\left(\frac{\partial \Phi}{\partial \xi}\right)(\xi, t) \cdot \sum_j \frac{\partial (\mathbf{u}_G|_x)_j}{\partial x_j}(\Phi(\xi, t), t)
\end{aligned} \tag{A.5}$$

Due to the product rule, three derivatives have to be computed for the flux term:

$$\begin{aligned}
\frac{\partial}{\partial \xi_j} \left(\rho^{\text{ref}}|_{\xi}(\xi, t) \cdot (\mathbf{w}|_{\xi})_j(\xi, t) \right) &= \\
&= \underbrace{\sum_j \frac{\partial \rho|_{\xi}}{\partial \xi_j}(\xi, t) \cdot (\mathbf{w}|_{\xi})_j(\xi, t) \cdot \det\left(\frac{\partial \Phi}{\partial \xi}\right)(\xi, t)}_{\square} + \\
&+ \underbrace{\rho|_{\xi}(\xi, t) \cdot \sum_j (\mathbf{w}|_{\xi})_j(\xi, t) \cdot \frac{\partial}{\partial \xi_j} \left(\det\left(\frac{\partial \Phi}{\partial \xi}\right) \right)(\xi, t)}_{\diamond} + \\
&+ \underbrace{\rho|_{\xi}(\xi, t) \cdot \sum_j \frac{\partial (\mathbf{w}|_{\xi})_j}{\partial \xi_j}(\xi, t) \cdot \det\left(\frac{\partial \Phi}{\partial \xi}\right)(\xi, t)}_{\triangleright}
\end{aligned} \tag{A.6}$$

The first term marked by \square can be rephrased in spatial representation using the ALE convective velocity (2.16) as follows

$$\begin{aligned}
\square &= \sum_j \frac{\partial \rho|_x(\Phi(\xi, t), t)}{\partial \xi_j} \cdot (\mathbf{w}|_{\xi})_j(\xi, t) = \\
&= \sum_{i,j} \frac{\partial \rho|_x}{\partial x_i}(\Phi(\xi, t), t) \cdot \frac{\partial \Phi_i}{\partial \xi_j}(\xi, t) \cdot (\mathbf{w}|_{\xi})_j(\xi, t) = \\
&= \sum_i \frac{\partial \rho|_x}{\partial x_i}(\Phi(\xi, t), t) \cdot (\mathbf{c}|_x)_i(\Phi(\xi, t), t)
\end{aligned} \tag{A.7}$$

For the second term marked by \diamond , the partial derivative of the JACOBIAN determinant in a given direction has to be computed. In analogy to equation (A.2), the partial derivative of this determ-

inant can be computed as

$$\begin{aligned}
 \frac{\partial}{\partial \xi_j} \left(\det \left(\frac{\partial \Phi}{\partial \xi} \right) \right) (\xi, t) &= \\
 &= \sum_{k,l} \frac{\partial \Phi_k^{-1}}{\partial x_l} (\Phi (\xi, t), t) \cdot \frac{\partial}{\partial \xi_j} \left(\frac{\partial \Phi_l}{\partial \xi_k} (\xi, t) \right) \cdot \det \left(\frac{\partial \Phi}{\partial \xi} \right) (\xi, t) = \\
 &= \sum_{k,l} \frac{\partial \Phi_k^{-1}}{\partial x_l} (\Phi (\xi, t), t) \cdot \frac{\partial}{\partial \xi_k} \left(\frac{\partial \Phi_l}{\partial \xi_j} (\xi, t) \right) \cdot \det \left(\frac{\partial \Phi}{\partial \xi} \right) (\xi, t) = \\
 &= \sum_l \frac{\partial}{\partial x_l} \left(\frac{\partial \Phi_l}{\partial \xi_j} (\Phi^{-1} (x, t), t) \right) (\Phi (\xi, t), t) \cdot \det \left(\frac{\partial \Phi}{\partial \xi} \right) (\xi, t). \quad (\text{A.8})
 \end{aligned}$$

From line two to line three, the sequence of partial differentiations was swapped and in the next line, the chain rule was applied. Using this identity, \diamond can be restated:

$$\diamond = \sum_{j,l} (\mathbf{w}|_x)_j (\Phi (\xi, t), t) \cdot \frac{\partial}{\partial x_l} \left(\frac{\partial \Phi_l}{\partial \xi_j} (\Phi^{-1} (x, t), t) \right) (\Phi (\xi, t), t) \cdot \det \left(\frac{\partial \Phi}{\partial \xi} \right) (\xi, t) \quad (\text{A.9})$$

A further simplification of this expression is possible in combination with term \triangleright . For this purpose, \triangleright is converted into

$$\triangleright = \sum_{j,l} \frac{\partial (\mathbf{w}|_x)_j}{\partial x_l} (\Phi (\xi, t), t) \cdot \frac{\partial \Phi_l}{\partial \xi_j} \underbrace{(\Phi^{-1} (\Phi (\xi, t), t), t)}_{(\xi, t)} \cdot \det \left(\frac{\partial \Phi}{\partial \xi} \right) (\xi, t) \quad (\text{A.10})$$

using the chain rule. The sum of the equations (A.9) and (A.10) allows for the application of the product rule

$$\begin{aligned}
 \triangleright + \diamond &= \sum_{j,l} \frac{\partial}{\partial x_l} \left((\mathbf{w}|_x)_j \cdot \left(\frac{\partial \Phi_l}{\partial \xi_j} (\Phi^{-1} (x, t), t) \right) \right) (\Phi (\xi, t), t) \cdot \det \left(\frac{\partial \Phi}{\partial \xi} \right) (\xi, t) = \\
 &= \sum_l \frac{\partial (\mathbf{c}|_x)_l}{\partial x_l} (\Phi (\xi, t), t) \cdot \det \left(\frac{\partial \Phi}{\partial \xi} \right) (\xi, t) \quad (\text{A.11})
 \end{aligned}$$

and thus completes the transformation to the spatial representation of the last missing terms. Finally, the intermediate results from the transformed local time derivative (A.5), the spatial derivatives (A.6) incorporating transformations (A.7) and (A.11) are inserted into the ALE mass conservation equation in reference representation (2.26). The resulting equation is divided by

the nonzero JACOBIan determinant and results in

$$\begin{aligned}
0 = & \frac{\partial \rho|_{\xi}}{\partial t} (\Phi^{-1}(\Phi(\xi, t), t), t) + \\
& + \rho|_{\mathbf{x}}(\Phi(\xi, t), t) \cdot \sum_j \frac{\partial (u_G|_{\mathbf{x}})_j}{\partial x_j}(\Phi(\xi, t), t) + \\
& + \sum_i \frac{\partial \rho|_{\mathbf{x}}}{\partial x_i}(\Phi(\xi, t), t) \cdot (c|_{\mathbf{x}})_i(\Phi(\xi, t), t) + \\
& + \rho|_{\mathbf{x}}(\Phi(\xi, t), t) \cdot \sum_l \frac{\partial (c|_{\mathbf{x}})_l}{\partial x_l}(\Phi(\xi, t), t). \tag{A.12}
\end{aligned}$$

Using equation (2.17), this can be rephrased as the ALE mass conservation equation in spatial representation (2.27) at point $\mathbf{x} = \Phi(\xi, t)$. \square

A.3 Statistical description of turbulent flows

Quantities like velocity or pressure in turbulent flows can be described using statistical tools. This implies that these quantities can be considered as random variables for a point \mathbf{x} and time t . More precisely, they can be associated with random processes since they are time-dependent and even more precisely they can be treated as random fields since they depend on time and position in space. The randomness results from the fact that turbulent motions exhibit an extreme sensitivity to perturbations in material parameters, initial and boundary conditions. Since such perturbations are unavoidable in practice, the exact state of a system sufficiently far in the future cannot be predicted. Nevertheless, statistical predictions of flow quantities can be made.

To clarify the meaning of the expression random variable, the following terms and definitions as they can be found in textbooks on stochastics as PAPOULIS and PILLAI [170] or CHUNG [50] are needed. An experimental outcome determined by the flow is called a sample. The set of all possible samples is called sample space S . Subsets E of the sample space are called event if they are elements of a σ -algebra Σ , i.e. elements of a set of sets which contains the sample space (A.13) and which is closed under countable unions of its elements (A.15) as well as under the complement operation of E in the sample space (A.14).

$$S \in \Sigma \tag{A.13}$$

$$E \in \Sigma \Rightarrow S \setminus E \in \Sigma \tag{A.14}$$

$$E_i \in \Sigma, i \in \mathbb{N} \Rightarrow \bigcup_{i=1}^{\infty} E_i \in \Sigma \tag{A.15}$$

The σ -algebra of all events is called event space. On the event space, a probability function P can be postulated. It associates each event with a nonnegative real number, the probability of the event.

$$P(E) \geq 0 \tag{A.16}$$

One can think of this probability as the probability that an arbitrary experimental outcome contained in the event is obtained. Hence, it is reasonable to postulate that the probability associated

with the sample space is one.

$$P(S) = 1 \quad (\text{A.17})$$

Furthermore, the probability of a countable union of pairwise disjoint events E_i is required to be equal to the sum of the probabilities of these events:

$$P\left(\bigcup_{i=1}^{\infty} E_i\right) = \sum_{i=1}^{\infty} P(E_i) \quad \text{if } E_i \cap E_j = \emptyset \text{ for } i \neq j \quad (\text{A.18})$$

This axiomatic definition of probability was introduced by KOLMOGOROV [142] in 1933, eight years before his pioneering work on turbulence [144, 143].

A vector valued random variable \mathbf{U} of dimension n is now defined as a function which maps the space of all samples to \mathbb{R}^n under the condition that for all $\mathbf{r} \in \mathbb{R}^n$ the sets

$$E_{\mathbf{r}} := \{s \in S \mid \mathbf{U}(s) \in]-\infty; r_1] \times \dots \times]-\infty; r_n]\} \quad (\text{A.19})$$

are elements of the event space. As a consequence, these CARTESIAN products of intervals, $]-\infty; r_1] \times \dots \times]-\infty; r_n]$, can be associated with a probability, namely with the probability of their preimage under the mapping of the random variable:

$$P_{\mathbf{U}}(\mathbf{r}) = P(E), \quad \mathbf{U}(E) =]-\infty; r_1] \times \dots \times]-\infty; r_n] \quad (\text{A.20})$$

The arising (cumulative) probability distribution $P_{\mathbf{U}}(\mathbf{r})$ completely determines the statistical properties of the random variable \mathbf{U} . If possible, it is convenient to introduce the nonnegative, integrable probability density function $p_{\mathbf{U}}$ by

$$p_{\mathbf{U}}(\mathbf{r}) = \frac{\partial P_{\mathbf{U}}}{\partial r_1 \dots \partial r_n}(\mathbf{r}) \quad \leftrightarrow \quad P_{\mathbf{U}}(\mathbf{r}) = \int_{-\infty}^{r_1} \dots \int_{-\infty}^{r_n} p_{\mathbf{U}}(\boldsymbol{\rho}) \, d\rho_1 \dots d\rho_n \quad (\text{A.21})$$

Random variables of this type are called continuous.

Having random variables and probability density functions at hand, first order moments as well as higher order moments can be introduced for $i = 1, \dots, n$:

$$\langle \mathbf{U}_i \rangle := \int_{\mathbb{R}^n} p_{\mathbf{U}}(\boldsymbol{\rho}) \cdot \mathbf{U}_i(\boldsymbol{\rho}) \, d\boldsymbol{\rho}, \quad (\text{A.22})$$

$$\langle \mathbf{U}_i^2 \rangle := \int_{\mathbb{R}^n} p_{\mathbf{U}}(\boldsymbol{\rho}) \cdot \mathbf{U}_i(\boldsymbol{\rho}) \cdot \mathbf{U}_i(\boldsymbol{\rho}) \, d\boldsymbol{\rho} \quad (\text{A.23})$$

...

The first order moments are usually referred to as means or expectations of the random variable. The expectation of a new random variable, defined by a function $f(\mathbf{U})$ of a random variable \mathbf{U} , can be computed in terms of the probability density function of the original random variable \mathbf{U} , see e.g. PAPOULIS and PILLAI [170]:

$$\langle f(\mathbf{U}) \rangle := \int_{\mathbb{R}^n} p_{\mathbf{U}}(\boldsymbol{\rho}) \cdot f(\mathbf{U}(\boldsymbol{\rho})) \, d\boldsymbol{\rho} \quad (\text{A.24})$$

Using this property, the expectations for products of fluctuations

$$\underline{U}_i \cdot \underline{U}_j := (\mathbf{U}_i - \langle \mathbf{U}_i \rangle) \cdot (\mathbf{U}_j - \langle \mathbf{U}_j \rangle), \quad i, j = 1, \dots, n \quad (\text{A.25})$$

can be studied. According to equation (A.24), these second order moments of fluctuations can be computed as follows:

$$\begin{aligned} \langle \underline{U}_i \cdot \underline{U}_j \rangle &= \int_{\mathbb{R}^n} p_U(\boldsymbol{\rho}) \cdot \underline{U}_i(\boldsymbol{\rho}) \cdot \underline{U}_j(\boldsymbol{\rho}) d\boldsymbol{\rho} = \\ &= \int_{\mathbb{R}^n} p_U(\boldsymbol{\rho}) \cdot (\mathbf{U}_i(\boldsymbol{\rho}) - \langle \mathbf{U}_i \rangle) \cdot (\mathbf{U}_j(\boldsymbol{\rho}) - \langle \mathbf{U}_j \rangle) d\boldsymbol{\rho} \end{aligned} \quad (\text{A.26})$$

For $i = j$ the resulting quantities are termed variances. They represent the average square deviation from the expectation.

$$\text{Var}(\mathbf{U}_i) := \langle \underline{U}_i^2 \rangle = \langle \mathbf{U}_i^2 \rangle - \langle \mathbf{U}_i \rangle^2, \quad (\text{A.27})$$

Similarly, for $i \neq j$, covariances are defined by

$$\text{Cov}(\mathbf{U}_i, \mathbf{U}_j) := \langle \underline{U}_i \cdot \underline{U}_j \rangle = \langle \mathbf{U}_i \cdot \mathbf{U}_j \rangle - \langle \mathbf{U}_i \rangle \cdot \langle \mathbf{U}_j \rangle. \quad (\text{A.28})$$

The covariance reflects the correlation between the two components \underline{U}_i and \underline{U}_j of the random variable of fluctuations. Mean values, variances and covariances are often used to characterise important properties of a probability distribution.

In practice, density functions as well as expectations and thus variances and covariances cannot be computed or measured but only be estimated. Let U^1, U^2, \dots be a series of independent identically distributed scalar random variables with unknown finite mean ϖ and variance σ^2 . One can think of U^i as a flow quantity observed in a turbulent flow experiment after a time t at a certain position \boldsymbol{x} . This experiment is independently repeated n times under the same conditions, giving rise to a whole series of measurements. The arithmetic mean

$$\bar{U}^n := \frac{1}{n} \sum_{i=1}^n U^i \quad (\text{A.29})$$

is called ensemble average over n repetitions. According to the strong law of large numbers it converges almost surely to the expected mean value ϖ :

$$P\left(\left\{s \mid \lim_{n \rightarrow \infty} \bar{U}^n(s) = \varpi\right\}\right) = 1, \quad \text{i.e.} \quad \lim_{n \rightarrow \infty} \bar{U}^n \xrightarrow{\text{a.s.}} \varpi \quad (\text{A.30})$$

Being able to estimate expectations, the central limit theorem provides further information on the unknown distribution of the ensemble average. Namely, the density function $p_{\bar{U}_{\text{std}}^n}$ of the standardised arithmetic mean,

$$\bar{U}_{\text{std}}^n := \frac{\frac{1}{n} \sum_{i=1}^n U^i - \varpi}{\sigma / \sqrt{n}}, \quad (\text{A.31})$$

converges towards the density $p_{\text{std}}(r)$ of a standardised GAUSSIAN distribution,

$$p_{\text{std}}(r) := \frac{1}{\sqrt{2\pi}} e^{-\frac{1}{2}r^2}. \quad (\text{A.32})$$

It should be emphasised that this is not a statement concerning the density function of the identically distributed random variables U^i but only a statement concerning the density function of the ensemble average. Turbulent flow quantities cannot be expected to be distributed GAUSSIAN, only their ensemble averages will approach a GAUSSIAN distribution for large n .

Computing the ensemble average in a practical application is often not feasible. Fortunately, many turbulent flow applications have additional properties which allow the estimation of mean values by ergodic processes. An important class are statistically stationary flows. For these flows, the statistical properties of the random processes describing the flow properties are invariant under a shift in time. This implies among other things that the first order density function of the random process at time t is independent of t . Hence, the expected value ϖ will be constant. Furthermore, the joint second order density function of the random variables at t_0 and $t_0 + t$ is independent of t_0 . For such flows, SLUTSKY's theorem, see e.g. PAPOULIS and PILLAI [170] or the book by FRISCH [84], can be applied ensuring that if the integral $\int_0^\infty C_t^{\text{stat}}(t) dt$ of the two-time covariance function

$$C_t^{\text{stat}}(t) = \langle (U(t_0) - \varpi) \cdot (U(t_0 + t) - \varpi) \rangle \quad (\text{A.33})$$

is finite, the time average of a single realisation converges to the expected value ϖ in the mean sense, i.e. their mean square deviation has zero expectation for $T \rightarrow \infty$

$$\varpi = \lim_{T \rightarrow \infty} \frac{1}{2T} \int_{-T}^T U(t) dt \quad (\text{in the mean sense}). \quad (\text{A.34})$$

Note that the averaging in equation (A.33) is based on the (joint) second order density function and that the definition of $C_t^{\text{stat}}(t)$ is independent of the actual choice of t_0 since we are dealing with a stationary process. A process is called mean-ergodic if (A.34) holds. The integral of the time correlation function introduces a correlation time

$$t_{\text{cor}} := \frac{\int_0^\infty C_t^{\text{stat}}(t) dt}{C_t^{\text{stat}}(0)}. \quad (\text{A.35})$$

For statistically stationary turbulent flow, it is an admissible assumption that t_{cor} is finite and hence that the processes are mean ergodic. Equation (A.34) is also applicable to second order moments which are stationary as well, allowing to estimate variances and correlations. Note that for these higher order moments, the correlation time is usually much higher than for first order means and thus the sampling period will have to be much longer to provide good estimates for higher order statistics. The concept of ergodicity in statistically stationary flows can be readily extended to statistically homogeneous random fields. Statistically homogeneous in direction x_{hom} means that all statistical quantities are independent of a shift in direction x_{hom} . Again, if the integral over the spatial two-point covariance,

$$C_x^{\text{hom}}(x_{\text{hom}}) = \langle (U(x_{\text{hom},0} - \varpi)) \cdot (U(x_{\text{hom},0} + x_{\text{hom}}) - \varpi) \rangle, \quad (\text{A.36})$$

is finite, the mean value can be estimated using spatial averaging:

$$\varpi = \lim_{X_{\text{hom}} \rightarrow \infty} \frac{1}{2X_{\text{hom}}} \int_{-X_{\text{hom}}}^{X_{\text{hom}}} U(x_{\text{hom}}) dx_{\text{hom}} \quad (\text{in the mean sense}) \quad (\text{A.37})$$

Similar to the correlation time in equation (A.35) an integral correlation length can be defined:

$$\ell_{\text{cor}} := \frac{\int_0^\infty C_x^{\text{hom}}(x_{\text{hom}}) dx_{\text{hom}}}{C_x^{\text{hom}}(0)}. \quad (\text{A.38})$$

This correlation length will be of importance when homogeneous flows are approximated on periodic domains, as it is done for example in turbulent channel flow computations. A choice of a periodic box too small compared to the correlation length will lead to a poor approximation of the ensemble average. A generalisation of these results to multiple homogeneous directions is possible.

This section will be concluded by a remark concerning the differentiation of expected values of random processes. For random processes associated with turbulent flows, it is a valid assumption that the time derivative of the expected value exists and that the mixed second derivative of the two-time covariance defined by

$$C_t(t_0, t) = \langle (U(t_0) - \varpi(t_0)) \cdot (U(t_0 + t) - \varpi(t_0 + t)) \rangle \quad (\text{A.39})$$

exists and is continuous. In this context, $\varpi(t_0)$ and $\varpi(t_0 + t)$ denote the expected values at time t_0 and $t_0 + t$ respectively. According to PARZEN [171], these conditions allow to compute the expected value of the derivative of a stochastic process as the time derivative of the expected value of the stochastic process, viz.

$$\frac{d \langle U \rangle}{dt} = \left\langle \frac{dU}{dt} \right\rangle. \quad (\text{A.40})$$

Similar statements are possible for spatial derivatives in random fields.

A.4 Fundamental function spaces

The space of square integrable functions is defined by

$$\mathcal{L}^2(\Omega(t^{n+1})) := \left\{ f : \Omega(t^{n+1}) \rightarrow \mathbb{R} \mid \int_{\Omega(t^{n+1})} f^2 d\mathbf{x} < \infty \right\}. \quad (\text{A.41})$$

By grouping functions which differ only on a set of measure 0, a HILBERT-space of equivalence classes, $L^2(\Omega(t^{n+1}))$, is derived from $\mathcal{L}^2(\Omega(t^{n+1}))$. The scalar product of this HILBERT-space is defined by

$$(f, g)_{\Omega(t^{n+1})} := \int_{\Omega(t^{n+1})} f \cdot g d\mathbf{x}. \quad (\text{A.42})$$

Extensions to product spaces of vector and tensor valued functions are straightforward. The respective scalar products are defined by

$$(\mathbf{f}; \mathbf{g})_{\Omega(t^{n+1})} := \sum_{i=1}^3 (f_i, g_i)_{\Omega(t^{n+1})} \quad (\text{A.43})$$

and

$$(\mathbf{f} : \mathbf{g})_{\Omega(t^{n+1})} := \sum_{i=1}^3 \sum_{j=1}^3 (f_{ij}, g_{ij})_{\Omega(t^{n+1})}. \quad (\text{A.44})$$

These scalar products immediately define integral norms in the usual way, for example

$$\|\cdot\|_{\mathbf{L}^2} := \sqrt{(\cdot, \cdot)_{\Omega(t^{n+1})}} \quad (\text{A.45})$$

on $\mathbf{L}^2(\Omega(t^{n+1}))$. To be able to state the weak form, the introduction of a further space, the SOBOLEV-space $\mathbf{H}^1(\Omega(t^{n+1}))$ is necessary:

$$\mathbf{H}^1(\Omega(t^{n+1})) := \left\{ f \in \mathbf{L}^2(\Omega(t^{n+1})) \mid \frac{\partial f}{\partial x_i} \in \mathbf{L}^2(\Omega(t^{n+1})), i = 1, 2, 3 \right\} \quad (\text{A.46})$$

This space is equipped with a scalar product

$$(f, g)_{\mathbf{H}^1(\Omega(t^{n+1}))} := \int_{\Omega(t^{n+1})} \left(f \cdot g + \sum_{i=1}^3 \frac{\partial f}{\partial x_i} \cdot \frac{\partial g}{\partial x_i} \right) d\mathbf{x}, \quad (\text{A.47})$$

defining a norm $\|\cdot\|_{\mathbf{H}^1}$ in the usual way. Again, a generalisation of this HILBERT-space for vector and tensor-valued functions is straightforward based on CARTESIAN product spaces, e.g.

$$[\mathbf{H}^1(\Omega(t^{n+1}))]^3 := \mathbf{H}^1(\Omega(t^{n+1})) \times \mathbf{H}^1(\Omega(t^{n+1})) \times \mathbf{H}^1(\Omega(t^{n+1})). \quad (\text{A.48})$$

When introducing boundary conditions, a further space required is the trace space

$$\Gamma^{-\frac{1}{2}}(t^{n+1}) := \left\{ \mathbf{g} \in [\mathbf{L}^2(\partial\Omega(t^{n+1}))]^3 \mid \mathbf{g} = \mathbf{f}|_{\partial\Omega(t^{n+1})} \right. \\ \left. \text{for a } \mathbf{f} \in [\mathbf{H}^1(\Omega(t^{n+1}))]^3 \right\}. \quad (\text{A.49})$$

In this definition, the restriction of a solution to the domain boundary $\partial\Omega(t^{n+1})$ has to be understood in the sense of a trace operator, see for instance KNABNER and ANGERMANN [141].

B Additional information on non-uniform rational B-splines

This appendix covers a number of topics related to B-splines. In section B.1, knot insertion and order elevation processes will be presented which can be used for h -, p - and k -refinement in isogeometric analysis. Furthermore, section B.2 contains an example for the construction of a NURBS curve describing a segment of a circle by projective transformation of a B-spline curve.

B.1 Knot insertion and order elevation for B-splines

Let

$$C^{\text{B-spline}}(u) := \sum_{i=1}^l B_i^p(u) \cdot \mathbf{X}_i^{\text{B}} \quad (\text{B.1})$$

be a B-spline curve of order p with l control points $\mathbf{X}_i^{\text{B}} \in \mathbb{R}^n$ defined on the knot vector

$$\mathbf{u} = (u_1, u_2, \dots, u_{l+p+1}). \quad (\text{B.2})$$

Several refinement strategies for this B-spline curve will now be described. Naturally, these strategies can as well be applied to surfaces and volumes of B-splines and NURBS.

Knot insertion

First, the process of knot insertion without changing a curve geometrically or parametrically will be explained. The new knot $\bar{u} \in [u_i; u_{i+1}[$ is inserted into the initial knot vector to provide a new, extended knot vector

$$\bar{\mathbf{u}} = (u_1, \dots, u_i, \bar{u}, u_{i+1}, \dots, u_{l+p+1}). \quad (\text{B.3})$$

This extended knot vector generates $l+1$ basis functions with corresponding control points $\bar{\mathbf{X}}_i^{\text{B}}$. In order to maintain geometry and parametrisation, i.e. to fulfil

$$C^{\text{B-spline}}(u) = \sum_{i=1}^{l+1} \bar{B}_i^p(u) \cdot \bar{\mathbf{X}}_i^{\text{B}}, \quad (\text{B.4})$$

the new control points are defined according to the rule

$$\bar{\mathbf{X}}_j^{\text{B}} = \alpha_j \cdot \mathbf{X}_j^{\text{B}} + (1 - \alpha_j) \cdot \mathbf{X}_{j-1}^{\text{B}} \quad (\text{B.5})$$

with parameters

$$\alpha_j = \begin{cases} 1 & 1 \leq j \leq i - p \\ \frac{\bar{u} - u_j}{u_{j+p} - u_j} & i - p + 1 \leq j \leq i \\ 0 & i + 1 \leq j \leq l + 1 \end{cases} \quad (\text{B.6})$$

The knot insertion process preserves $l - p + 1$ control points. p control point values are new or modified. Figures B.1 and B.2 show an example of a quadratic B-spline curve with initial knot vector $\mathbf{u} = (0, 0, 0, 0.5, 0.7, 1, 1, 1)$ and newly inserted knot at $\bar{u} = 0.3$.

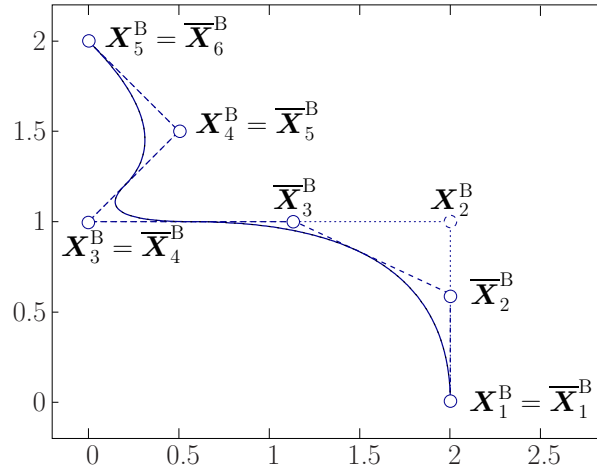


Figure B.1: Knot insertion. B-spline curves and control polygons with and without the inserted knot.

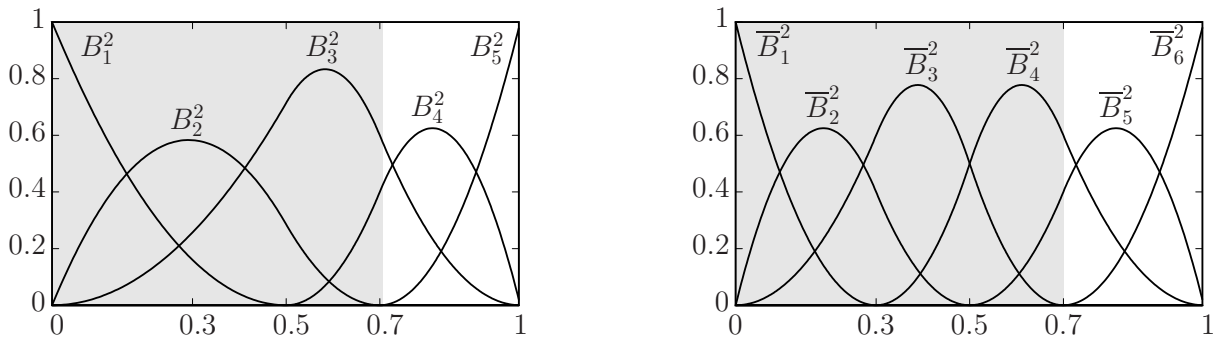


Figure B.2: Knot insertion, impact on basis functions. The basis functions in the white area are untouched by the knot insertion, and so are the corresponding control point values in Figure B.1.

A special application of knot insertion is to decompose a B-spline curve into piecewise BÉZIER segments. This is done by inserting each inner knot until it has multiplicity p . The resulting curve can be split at the interpolated points into BÉZIER segments which consist of open knot vectors of length $2p + 2$. For the curve from Figures B.1 and B.2, the split into BÉZIER segments is visualised in Figures B.3 and B.4.

Note that if a B-spline curve can be constructed from another curve by knot insertion, the respective knots can be deleted from the curve without changing the curve's geometry. This is done simply by inversion of the process described above and can be used for order elevation of B-spline curves as it will be described below.

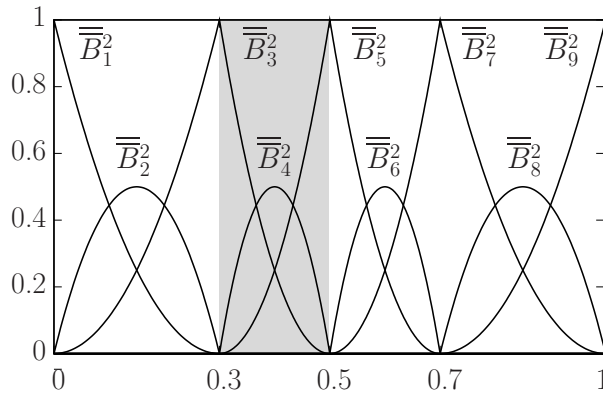


Figure B.3: Split of B-spline curve into BÉZIER segments by knot insertion, corresponding basis functions. The segment associated with the part of the curve marked by the grey colour corresponds to a knot vector $(0.3, 0.3, 0.3, 0.5, 0.5, 0.5)$ of length $2p + 2 = 6$.

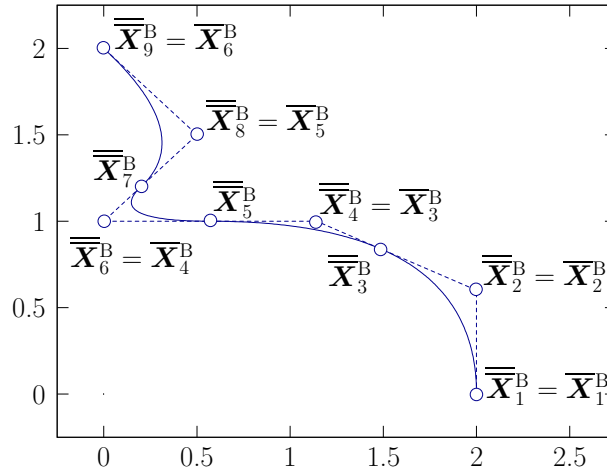


Figure B.4: The B-spline curve from Figure B.1 is split into four BÉZIER segments by three additional knot insertions.

Order elevation

For a BÉZIER segment, order elevation can be done simply by increasing the multiplicity of the two knot values by one and by computing the new control point values according to the formula

$$\begin{aligned} \bar{X}_0^B &= X_0^B \\ \bar{X}_i^B &= \left(1 - \frac{i}{p+1}\right) \cdot X_i^B + \frac{i}{p+1} \cdot X_{i-1}^B \quad \text{for } i = 1, \dots, p \\ \bar{X}_{p+1}^B &= X_p^B. \end{aligned} \tag{B.7}$$

This equation is derived using basic properties of BERNSTEIN polynomials which generate the BÉZIER spline. Thus, for an order elevation of a B-spline curve, the curve has to be split into a set of BÉZIER segments as it was described above. The single segments can be order elevated

according to equation (B.7) and afterwards be reassembled into a single curve. Redundant knots stemming from the decomposition into BÉZIER segments can be finally removed by the knot deletion procedure mentioned above. For the example curve, the results of the order elevation process are illustrated in Figures B.5 and B.6.

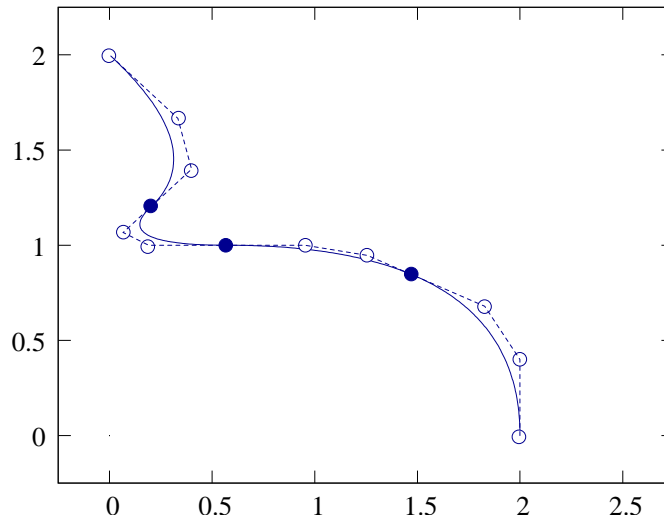


Figure B.5: Order elevated example curve from Figure B.1. The filled control points correspond to the removable control points associated with the BÉZIER segments required for order elevation. The remaining control points define the order elevated B-spline curve.

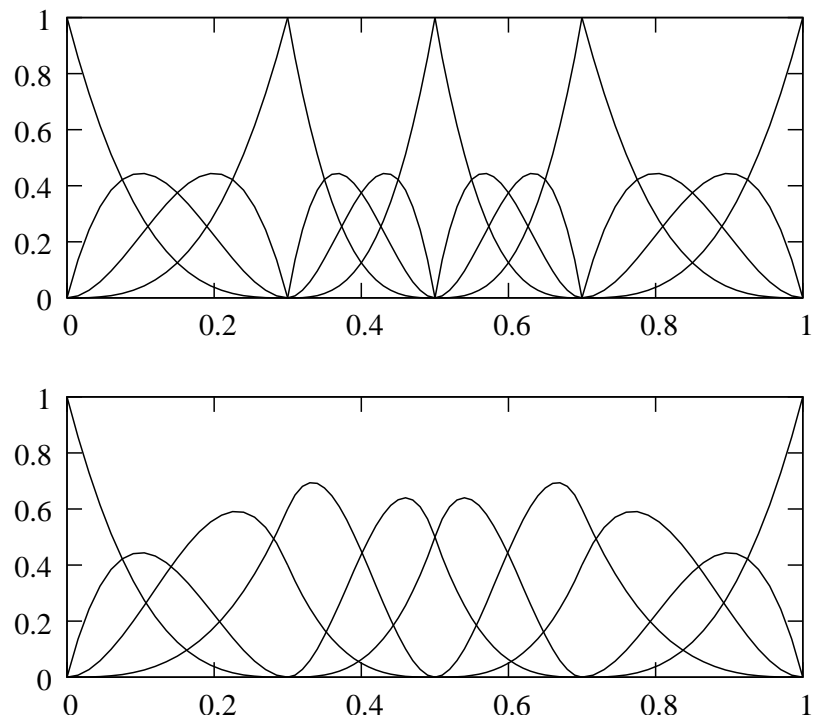


Figure B.6: Basis functions corresponding to the piecewise order elevated BÉZIER (top) and B-spline curve (bottom) from Figure B.5.

k-refinement

The process to perform order elevation prior to knot insertion is known as k -refinement. The order of these operations is important since they do not commute. Performing order elevation first and knot insertion afterwards preserves a higher degree of continuity, see the illustrations in Figure B.7. The number of basis functions generated by knot insertion followed by order elevation is higher compared to what is obtained in the case of k -refinement.

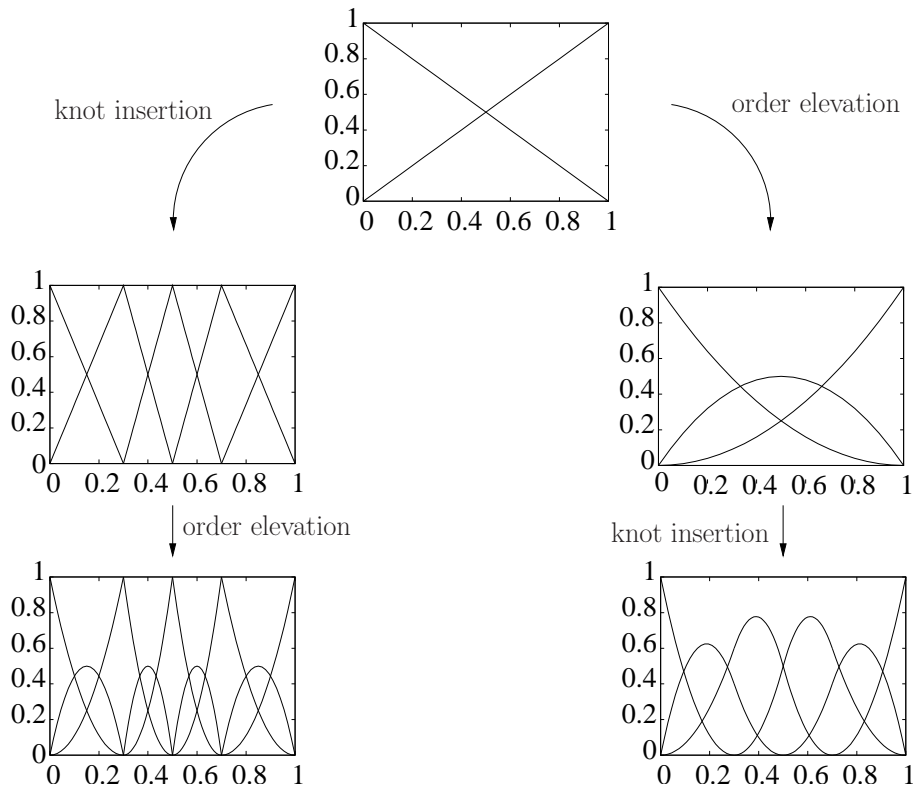


Figure B.7: Two linear B-spline basis functions are refined using knot insertion of three knots 0.3, 0.5, 0.7 and order elevation of one degree in k -refinement (right) and reverse order (left).

B.2 Construction of a circle segment using NURBS — an example

Segments of circles in the two-dimensional xy -space can be exactly represented using projections of quadratic B-spline polynomials in three-dimensional xyz -space. This will be done here for a quarter of a circle of radius 0.5 around the origin. The generating B-spline curve in this example is defined using quadratic B-spline, in this case BÉZIER, basis functions on an open knot vector $\mathbf{u} = (0, 0, 0, 1, 1, 1)$ with the three control points

$$\mathbf{X}_1^B = \begin{pmatrix} \frac{1}{2} \\ 0 \\ 1 \end{pmatrix}, \quad \mathbf{X}_2^B = \begin{pmatrix} \frac{1}{2\sqrt{2}} \\ \frac{1}{2\sqrt{2}} \\ \frac{1}{\sqrt{2}} \end{pmatrix} \quad \text{and} \quad \mathbf{X}_3^B = \begin{pmatrix} 0 \\ \frac{1}{2} \\ 1 \end{pmatrix}. \quad (\text{B.8})$$

As it is shown in Figure B.8, the generating curve defines a cone with the apex in the origin.

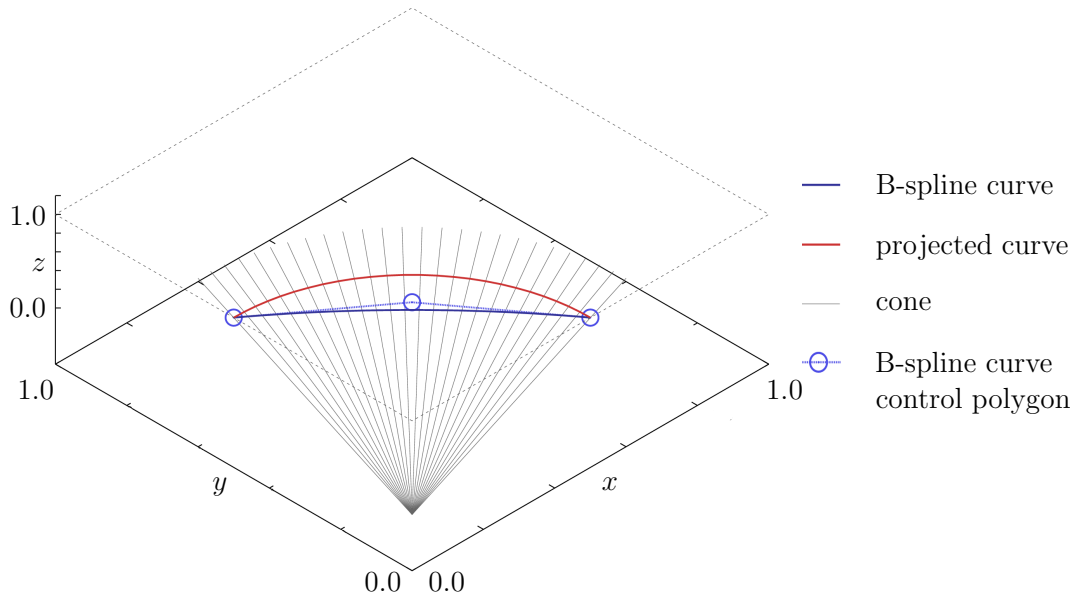


Figure B.8: Cone generated by a B-spline. The red line is the intersection between cone and an xy -parallel plane at $z = 1$.

Based on the definition of the NURBS curve as the projection of the generating B-spline curve according to equation (3.76), it is defined as the intersection of the cone and a plane orthogonal to the z -axis at $z = 1$. This intersection is visualised as the red line in Figures B.8 and B.9. A view along the z -axis, as it is depicted in Figure B.10, clearly shows the generated quarter of a circle with radius 0.5 around the origin.

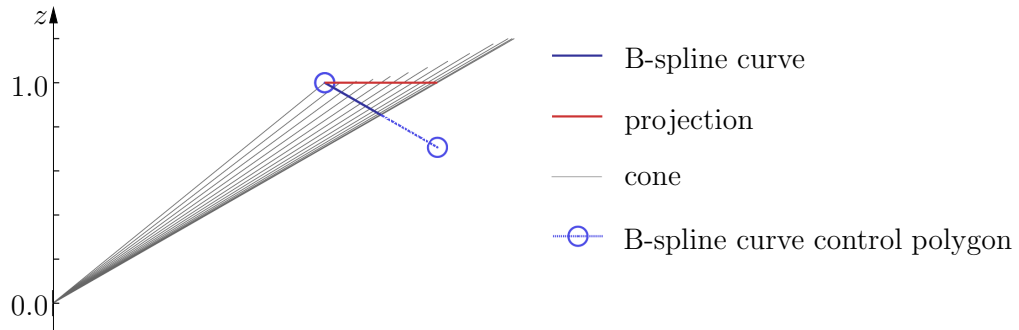


Figure B.9: Side view for the cone from Figure B.8.

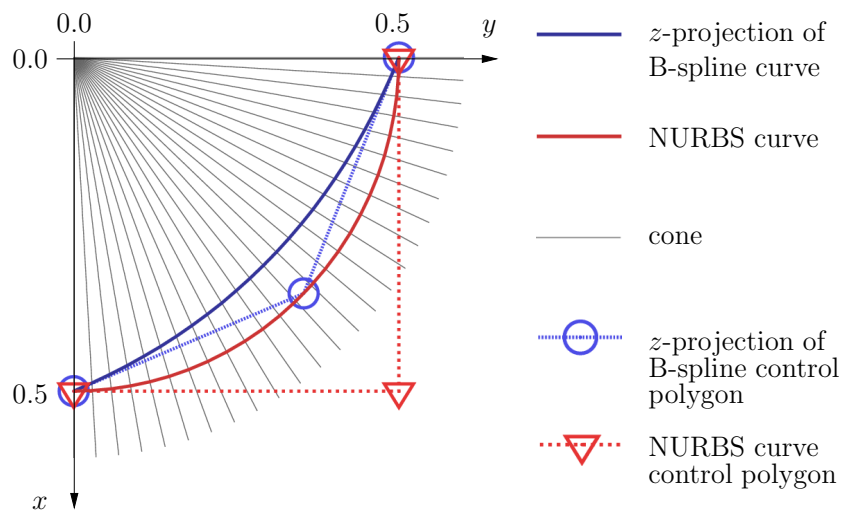


Figure B.10: Visualisation of the NURBS circle generated from the B-spline curve in Figures B.8 and B.9.

C A dynamic SMAGORINSKY implementation for comparison

In chapter 5 of this thesis, results from residual-based variational multiscale modelling of turbulence are compared to results obtained using a dynamic SMAGORINSKY model. Some fundamentals of this ‘classical’, filter-based LES model are presented in section C.1. The employed finite element implementation is provided afterwards in section C.2. Finally, some results highlighting basic properties of the method are shown in section C.3.

C.1 The (dynamic) SMAGORINSKY model

First a short introduction to eddy-viscosity subgrid models will be given in subsection C.1.1, including a brief discussion of the constant coefficient SMAGORINSKY model and its shortcomings for wall-bounded flows. Afterwards, in subsection C.1.2, the extension to the dynamic approach will be presented.

C.1.1 Eddy-viscosity subgrid models

One of the important characteristics of turbulent flows listed in subsection 2.2.1 is their diffusivity. Eddy-viscosity subgrid models are based on the assumption that the effect of unresolved scales onto resolved scales can be represented by an increased molecular diffusion. Accordingly, the residual stress in equation (4.16) is assumed to equal

$$\boldsymbol{\tau}_{\Delta}^{\text{res,dev}} = -2\nu_{\text{S,tur}}\boldsymbol{\varepsilon}(\bar{\mathbf{u}}) . \quad (\text{C.1})$$

It is always deviatoric according to the incompressibility condition which implies a trace-free filtered strain rate tensor. In contrast to the turbulent viscosity defined in (4.3), the subgrid viscosity $\nu_{\text{S,tur}}$ accounts only for effects of unresolved, small scales. Assumption (C.1) allows to restate equation (4.16) based on an updated ‘effective’ viscosity

$$\nu_{\text{eff}} = \nu + \nu_{\text{S,tur}} , \quad (\text{C.2})$$

viz.

$$\frac{\partial \bar{\mathbf{u}}}{\partial t} + \nabla \cdot \left(\bar{\mathbf{u}} \otimes \bar{\mathbf{u}} + \frac{\bar{p}^{\text{dev}}}{\rho} \mathbf{1} - 2\nu_{\text{eff}} \boldsymbol{\varepsilon}(\bar{\mathbf{u}}) \right) = \bar{\mathbf{b}} \\ \nabla \cdot \bar{\mathbf{u}} = 0 . \quad (\text{C.3})$$

Eddy-viscosity models are a functional modelling approach. Although the residual stress approximation (C.1) is usually of poor quality, they can provide a sufficient amount of model dissipation to describe the energetic action of the unresolved scales.

The best known eddy-viscosity approach is the constant coefficient SMAGORINSKY model [191]. It determines the turbulent subgrid viscosity based on an analogon to PRANDTL's mixing length hypothesis (4.6), i.e.

$$\nu_{S,tur} = \ell_{S,mix}^2 \|\boldsymbol{\varepsilon}(\bar{\mathbf{u}})\| = (C_{Smag} \cdot \bar{\Delta})^2 \|\boldsymbol{\varepsilon}(\bar{\mathbf{u}})\| \quad (C.4)$$

and accordingly

$$\tau_{\bar{\Delta}}^{res,dev} / \rho = -2 (C_{Smag} \cdot \bar{\Delta})^2 \|\boldsymbol{\varepsilon}(\bar{\mathbf{u}})\| \boldsymbol{\varepsilon}(\bar{\mathbf{u}}) . \quad (C.5)$$

The norm of the filtered strain rate tensor used in definitions (C.4), (C.5) can be evaluated as

$$\|\boldsymbol{\varepsilon}(\bar{\mathbf{u}})\| = \sqrt{2 \cdot \sum_{i=1}^3 \sum_{j=1}^3 \boldsymbol{\varepsilon}(\bar{\mathbf{u}})_{ij} \boldsymbol{\varepsilon}(\bar{\mathbf{u}})_{ij}} . \quad (C.6)$$

In equations (C.4) and (C.5), the counterpart to the mixing length is the SMAGORINSKY length scale $\ell_{S,mix}$. It is assumed to scale linearly with the filter width $\bar{\Delta}$ of the applied filter:

$$\ell_{S,mix} = C_{Smag} \cdot \bar{\Delta} \quad (C.7)$$

The proportionality factor is the SMAGORINSKY constant C_{Smag} . A value for this constant can be derived from the LILLY analysis for homogeneous isotropic turbulence. Assuming that the filter width is contained in the inertial subrange, a filter-dependent value for C_{Smag} can be obtained, see the book by POPE [174]. The sharp spectral cutoff filter, for example, corresponds to a value of $C_{Smag} = 0.17$. This value often turns out to be too large in practice, so the constant is adjusted within one order of magnitude to improve the results. By definition, the classical SMAGORINSKY model does not allow negative values for turbulent dissipation. A representation of backscatter, i.e. of energy transfer from unresolved to resolved scales is not possible within this model.

The constant coefficient SMAGORINSKY model is developed for filter widths in the inertial range of high REYNOLDS number turbulence. This requirement is not met in the viscous sub-region in wall-bounded flows. Here, the constant coefficient SMAGORINSKY model leads to an incorrect nonzero turbulent subgrid viscosity and thus to an artificial shear stress close to the wall. In order to avoid this inconsistency, the SMAGORINSKY length scale can be damped in the viscous near wall region using a VAN DRIEST damping function

$$\ell_{S,mix} = C_{Smag} \cdot \bar{\Delta} \cdot \left(1 - e^{-\frac{y^+}{A^+}}\right) . \quad (C.8)$$

In this equation, $A^+ = 26$ is a constant parameter and y^+ denotes the distance from the wall in wall units as it was introduced in subsection 2.2.5. In the following subsection, a dynamic variant of the SMAGORINSKY model will be described. This extension is capable of automatically determining an appropriate local SMAGORINSKY coefficient even in the near-wall flow regime.

C.1.2 GERMANO model

The dynamic SMAGORINSKY model was introduced by GERMANO et al. [91]. It will be presented in this subsection in the modified version by LILLY [155]. The GERMANO model uses a

second, coarser filter \widehat{G} associated with a filter width $\widehat{\Delta}$. This second filter is applied to the already filtered equation (4.12) yielding

$$\begin{aligned} \frac{\partial \widehat{\mathbf{u}}}{\partial t} + \nabla \cdot \left(\widehat{\overline{\mathbf{u} \otimes \mathbf{u}}} + \frac{\widehat{p}}{\rho} \cdot \mathbf{1} - 2\nu \varepsilon(\widehat{\mathbf{u}}) \right) &= \widehat{\mathbf{b}} \\ \nabla \cdot \widehat{\mathbf{u}} &= 0. \end{aligned} \quad (\text{C.9})$$

The successive application of the filters \overline{G} and \widehat{G} in this equation can be interpreted as a combined filter $\widehat{\overline{G}}$ with filter width $\widehat{\Delta}$. The main idea of the GERMANO approach is that a part of the unresolved, modelled scales associated with the combined filter $\widehat{\overline{G}}$ is actually resolved by the finer filter \overline{G} . This resolved part of the modelled scales is then used to determine the model parameter in the SMAGORINSKY approach dynamically.

In the following, this process will be described in more detail. It starts by rewriting the nonlinear convective term filtered by the combined filter in two ways. The first version is a split into resolved and residual stresses corresponding to the combined filter in analogy to equations (4.14) and (4.15):

$$\rho \cdot \widehat{\overline{\mathbf{u} \otimes \mathbf{u}}} = \rho \cdot \widehat{\mathbf{u}} \otimes \widehat{\mathbf{u}} + \rho \cdot \left(\widehat{\overline{\mathbf{u} \otimes \mathbf{u}}} - \widehat{\mathbf{u}} \otimes \widehat{\mathbf{u}} \right) = \rho \cdot \widehat{\mathbf{u}} \otimes \widehat{\mathbf{u}} + \tau_{\widehat{\Delta}}^{\text{res}} \quad (\text{C.10})$$

In addition to this representation, the nonlinear convective stresses can also be split with respect to the filter \overline{G} , obtaining a \widehat{G} -filtered version of equation (4.14):

$$\rho \cdot \widehat{\overline{\mathbf{u} \otimes \mathbf{u}}} = \rho \cdot \widehat{\overline{\mathbf{u}}} \otimes \widehat{\overline{\mathbf{u}}} + \rho \cdot \left(\widehat{\overline{\mathbf{u} \otimes \mathbf{u}}} - \widehat{\overline{\mathbf{u}}} \otimes \widehat{\overline{\mathbf{u}}} \right) = \rho \cdot \widehat{\overline{\mathbf{u}}} \otimes \widehat{\overline{\mathbf{u}}} + \widehat{\tau}_{\widehat{\Delta}}^{\text{res}} \quad (\text{C.11})$$

By a combination of equations (C.10) and (C.11), the difference between the residual stress $\tau_{\widehat{\Delta}}^{\text{res}}$ and the filtered residual stress $\widehat{\tau}_{\widehat{\Delta}}^{\text{res}}$ can be expressed in terms of filtered, resolved-scale quantities:

$$\tau_{\widehat{\Delta}}^{\text{res}} - \widehat{\tau}_{\widehat{\Delta}}^{\text{res}} = \rho \cdot \widehat{\overline{\mathbf{u}}} \otimes \widehat{\overline{\mathbf{u}}} - \rho \cdot \widehat{\mathbf{u}} \otimes \widehat{\mathbf{u}} \quad (\text{C.12})$$

This equation is often termed GERMANO identity. It expresses the resolved part of the turbulent stress $\tau_{\widehat{\Delta}}^{\text{res}}$ in terms of known, \widehat{G} -filtered, resolved-scale quantities which are commonly associated with the tensor

$$\mathbf{L} = \widehat{\overline{\mathbf{u}}} \otimes \widehat{\overline{\mathbf{u}}} - \widehat{\mathbf{u}} \otimes \widehat{\mathbf{u}}. \quad (\text{C.13})$$

The total unresolved stresses for both resolutions are unknown and have to be modelled. In the GERMANO approach, this is done using the same SMAGORINSKY model for both resolutions:

$$\tau_{\widehat{\Delta}}^{\text{res,dev}} / \rho = -2C_{\text{Dyn}} \widehat{\Delta}^2 \left\| \varepsilon(\widehat{\mathbf{u}}) \right\| \varepsilon(\widehat{\mathbf{u}}) \quad (\text{C.14})$$

$$\widehat{\tau}_{\widehat{\Delta}}^{\text{res,dev}} / \rho = -2C_{\text{Dyn}} \overline{\Delta}^2 \left\| \varepsilon(\overline{\mathbf{u}}) \right\| \varepsilon(\overline{\mathbf{u}}) \quad (\text{C.15})$$

The parameter C_{Dyn} , which corresponds to C_{Smag}^2 in the standard approach, will be determined locally. Nevertheless, it is assumed that it can be treated as a constant for the application of the filter \widehat{G} , resulting in

$$\widehat{\tau}_{\widehat{\Delta}}^{\text{res,dev}} / \rho = -2C_{\text{Dyn}} \overline{\Delta}^2 \left\| \varepsilon(\widehat{\overline{\mathbf{u}}}) \right\| \varepsilon(\widehat{\overline{\mathbf{u}}}). \quad (\text{C.16})$$

Using equations (C.14) and (C.16), the deviatoric part of the left side of equation (C.12) corresponds to

$$\begin{aligned} & \tau_{\widehat{\Delta}}^{\text{res,dev}} / \rho - \widehat{\tau_{\widehat{\Delta}}^{\text{res,dev}}} / \rho = \\ & = 2C_{\text{Dyn}}\overline{\Delta}^2 \left(\|\varepsilon(\widehat{\mathbf{u}})\| \varepsilon(\widehat{\mathbf{u}}) - \left(\frac{\widehat{\Delta}}{\overline{\Delta}} \right)^2 \cdot \|\varepsilon(\widehat{\mathbf{u}})\| \varepsilon(\widehat{\mathbf{u}}) \right). \end{aligned} \quad (\text{C.17})$$

Normalising this part of the modelled stress by $2C_{\text{Dyn}}\overline{\Delta}^2$ yields the tensor

$$\mathbf{M} = \|\varepsilon(\widehat{\mathbf{u}})\| \varepsilon(\widehat{\mathbf{u}}) - \left(\frac{\widehat{\Delta}}{\overline{\Delta}} \right)^2 \cdot \|\varepsilon(\widehat{\mathbf{u}})\| \varepsilon(\widehat{\mathbf{u}}). \quad (\text{C.18})$$

This tensor \mathbf{M} is deviatoric, a property inherited from the filtered strain rate $\varepsilon(\widehat{\mathbf{u}})$. Thus, it allows to reexpress the contraction of \mathbf{L} with \mathbf{M} by the contraction of \mathbf{L}^{dev} with \mathbf{M} :

$$\begin{aligned} \mathbf{L} : \mathbf{M} &= \sum_{i=1}^3 \sum_{j=1}^3 (\mathbf{L}_{ij} \cdot \mathbf{M}_{ij}) = \\ &= \sum_{i=1}^3 \sum_{j=1}^3 (\mathbf{L}_{ij}^{\text{dev}} \cdot \mathbf{M}_{ij}) + \sum_{i=1}^3 \sum_{j=1}^3 \left(\left(\frac{1}{3} \sum_{k=1}^3 \mathbf{L}_{kk} \right) \mathbf{1}_{ij} \cdot \mathbf{M}_{ij} \right) = \\ &= \sum_{i=1}^3 \sum_{j=1}^3 (\mathbf{L}_{ij}^{\text{dev}} \cdot \mathbf{M}_{ij}) = \mathbf{L}^{\text{dev}} : \mathbf{M} \end{aligned} \quad (\text{C.19})$$

Based on the model for the unresolved stresses,

$$\mathbf{L}^{\text{dev}} = \tau_{\widehat{\Delta}}^{\text{res,dev}} / \rho - \widehat{\tau_{\widehat{\Delta}}^{\text{res,dev}}} / \rho = 2C_{\text{Dyn}}\overline{\Delta}^2 \mathbf{M}, \quad (\text{C.20})$$

this equation can be used to determine the ‘constant’ C_{Dyn} according to

$$C_{\text{Dyn}}\overline{\Delta}^2 = - \frac{\sum_{i=1}^3 \sum_{j=1}^3 (\mathbf{L}_{ij} \cdot \mathbf{M}_{ij})}{2 \cdot \sum_{i=1}^3 \sum_{j=1}^3 (\mathbf{M}_{ij} \cdot \mathbf{M}_{ij})}. \quad (\text{C.21})$$

The GERMANO model has a single parameter, the filter width ratio

$$\alpha_{\Delta} = \frac{\widehat{\Delta}}{\overline{\Delta}} \quad (\text{C.22})$$

included in the definition of \mathbf{M} . It has to be provided by the user, see the discussion in the next subsection. The dynamic SMAGORINSKY model is consistent in the sense that the subgrid viscosity vanishes in laminar regions.

C.2 Finite element implementation

The implementation used in chapter 5 is based on the work of TEJADA-MARTÍNEZ [199]. It employs trilinear hexahedral elements for both pressure and velocity. Included stabilisation terms are of PSPG, SUPG and LSIC type as they are described in section 3.5.

In the finite element context, the filter \widehat{G} corresponds to the implicit grid filter associated with the stabilised GALERKIN approach. On the contrary, the second filter \widehat{G} is applied as an explicit discrete spatial test filter based on quadrature of the box filter. Let \underline{x}^h be a given node-based scalar quantity and ι the index of a node in the interior of the computational domain with $n_{e,\text{adj}}(\iota)$ adjacent elements with element indices $e_1, \dots, e_{n_{e,\text{adj}}(\iota)}$. Then the filtered value for this node is obtained as the volume average over all adjacent elements:

$$\widehat{\underline{x}}_\iota = \frac{1}{\text{vol}_\iota} \cdot \sum_{i=1}^{n_{e,\text{adj}}(\iota)} \int_{\Omega_{e_i}} x^h(\mathbf{x}) d\mathbf{x} \quad (\text{C.23})$$

As usual in finite elements, the integration of x^h involved in this equation is performed element-wise by quadrature and assembled into node-based global vectors for $\widehat{\underline{x}}_\iota$. For this approach, the volume of the support of the box filter,

$$\text{vol}_\iota = \sum_{i=1}^{n_{e,\text{adj}}(\iota)} \int_{\Omega_{e_i}} 1 d\mathbf{x}, \quad (\text{C.24})$$

has to be precomputed for all nodes. Values of $\widehat{\underline{x}}_\iota$ on no-slip boundaries are set to zero. For a more thorough discussion of these filters, the reader is referred to TEJADA-MARTÍNEZ and JANSEN [200].

The required filtered quantities for the GERMANO approach are all components of the expressions given in the following table:

| filtered quantity | $\widehat{\underline{u}}^h$ | $\widehat{\underline{u}}^h \otimes \widehat{\underline{u}}^h$ | $\ \widehat{\boldsymbol{\varepsilon}}(\widehat{\underline{u}}^h)\ \boldsymbol{\varepsilon}(\widehat{\underline{u}}^h)$ |
|---|-----------------------------|---|---|
| number of vectors of size n_{np} | 3 | 9 | 9 |

(C.25)

Given these nodal quantities, the tensors

$$\mathbf{L} = \widehat{\underline{u}}^h \otimes \widehat{\underline{u}}^h - \widehat{\underline{u}}^h \otimes \widehat{\underline{u}}^h \quad (\text{C.26})$$

and

$$\mathbf{M} = \|\widehat{\boldsymbol{\varepsilon}}(\widehat{\underline{u}}^h)\| \boldsymbol{\varepsilon}(\widehat{\underline{u}}^h) - \alpha_\Delta \cdot \|\boldsymbol{\varepsilon}(\widehat{\underline{u}}^h)\| \boldsymbol{\varepsilon}(\widehat{\underline{u}}^h) \quad (\text{C.27})$$

can be obtained on each element's centre by interpolation of the node-based filtered quantities (C.25) using the standard element shape functions. The filter width ratio in equation (C.27) was chosen to

$$\alpha_\Delta = \sqrt{3}. \quad (\text{C.28})$$

As described in TEJADA-MARTÍNEZ and JANSEN [201], α_Δ could also be determined dynamically but the fixed value is kept here for simplicity. Based on the tensors (C.26) and (C.27), a value $C_{\text{Dyn}}\overline{\Delta}^2$ can be obtained for each element according to equation (C.21). For channel flow problems, this equation is modified by an additional averaging of numerator and denominator in wall-parallel plains:

$$C_{\text{Dyn}}\overline{\Delta}^2 = \frac{\langle \mathbf{L} : \mathbf{M} \rangle_{\text{plane}}}{2 \langle \mathbf{M} : \mathbf{M} \rangle_{\text{plane}}} \quad (\text{C.29})$$

Furthermore, as in VREMAN et al. [214], a clipping of negative values is performed.

$$\frac{C_{\text{Dyn}}\overline{\Delta}^2 + |C_{\text{Dyn}}\overline{\Delta}^2|}{2} \rightarrow C_{\text{Dyn}}\overline{\Delta}^2 \quad (\text{C.30})$$

This averaging and clipping is done in order to avoid numerical instabilities by eliminating negative values of $C_{\text{Dyn}}\overline{\Delta}^2$. From the physical point of view, this procedure is equivalent to a complete elimination of backscatter.

For every element, the value $C_{\text{Dyn}}\overline{\Delta}^2$ allows to determine a modified viscosity. This effective viscosity is used in the computation of system matrix and residual contributions of the respective element during the set-up of the linear system (3.127). Here, it does not only have an impact on the viscous GALERKIN term but also on stabilisation terms via the residual and the stabilisation parameter. An example for the distribution of the averaged effective viscosity in a turbulent channel flow can be found in section C.3.

It is important to remark that there is an interaction between dynamic model dissipation and numerical dissipation arising from the stabilised finite element approach. This fact was studied in detail by TEJADA-MARTÍNEZ and JANSEN [202]. They also proposed a modification of the dynamic model in order to account for this interaction. The implementation used in this thesis does not include such a modification.

C.3 Averaged distribution of effective viscosity in a turbulent channel flow

Here, some basic properties of the dynamic SMAGORINSKY approach are highlighted and it is verified that the filtering process implemented is able to produce reasonable distributions of the effective viscosity. For this purpose, distributions of important quantities are shown for a turbulent channel flow computation. The setup for this computation can be found in section 5.1. The distributions correspond to a channel flow simulated at $\text{Re}_\tau = 180$ on 32^3 HEX8 elements.

Figure C.1 contains the averaged distribution of the effective SMAGORINSKY constant $\sqrt{C_{\text{Dyn}}}$ along the channel height. As one can see in Figure C.1, the dynamic approach is able to detect the viscous sublayer region close to the wall, yielding a damping of the effective SMAGORINSKY constant similar to a VAN DRIEST damping. Accordingly, the extra turbulent viscosity displayed on the right of Figure C.1 is decreasing to zero at the wall, explaining the superiority of a dynamic SMAGORINSKY approach in comparison to a simple constant coefficient model.

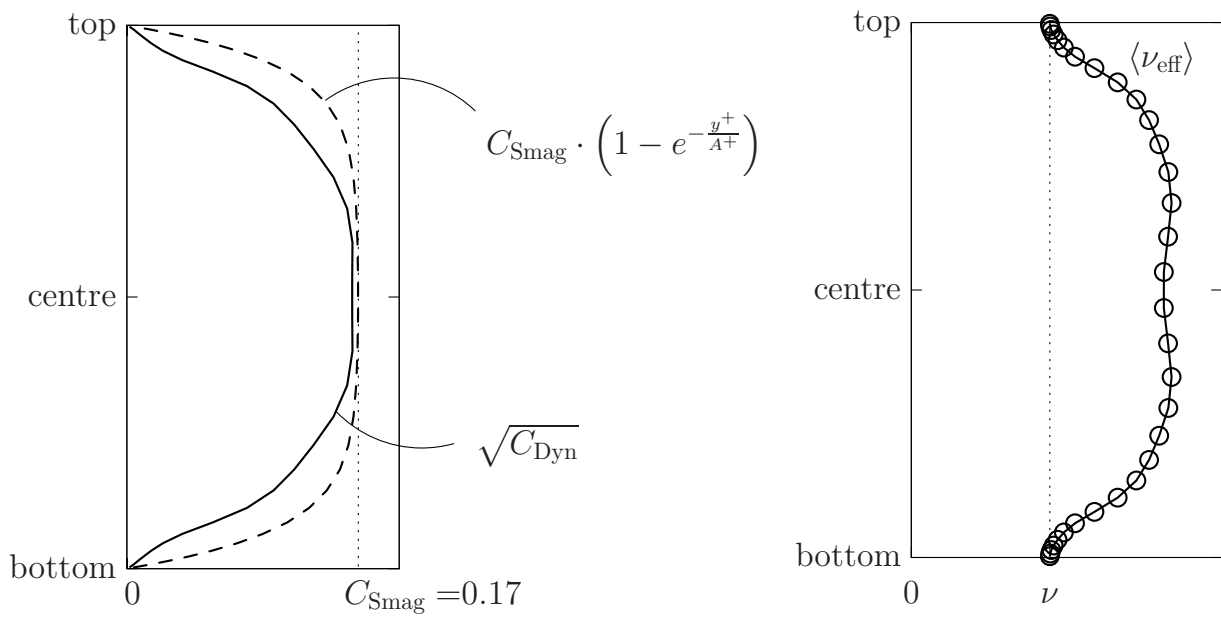


Figure C.1: Distribution of the parameter $\sqrt{C_{\text{Dyn}}}$ and for comparison the distribution of the SMAGORINSKY constant multiplied by a VAN DRIEST damping function (left). Distribution of averaged effective viscosity over the channel height (right). The circles indicate positions of element centres. The extra turbulent viscosity corresponds to the difference between effective and kinematic viscosity.

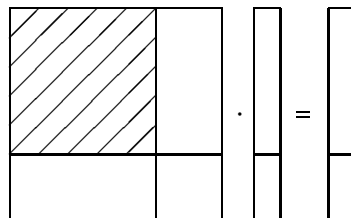
D Linearisation schemes for residual-based VMM

This appendix is designated to provide a detailed listing of the linearisation terms used for the minimal (M), fixed-point-like (F) and NEWTON-like (N) linearisation schemes introduced in subsection 4.4.6. For easy reading, every matrix block is preceded by a picture which specifies its position in the matrix system (3.127). All contributions will be listed with one entry per line. They are connected to the lines of a table which indicates by a symbol \times whether a term is active in the respective linearisation scheme or not. In the simplified linearisation schemes (M) and (F), the nonlinearity introduced by cross and REYNOLDS stress terms can often be treated completely without a contribution to the tangent matrix. The symbol \otimes indicates that in this case it is an option to include these terms only on the right hand side and thus to neglect the respective linearisations. The definition of the constants required for the linearisations always follow the listing of the block terms in a separate small table. These tables contain the constants for the time-dependent subgrid approximation (td) on the left and for the conventional subgrid closure (rV) on the right. Linearisations for the quasi-static subgrid closure can always be derived from the conventional subgrid closure by replacing the stabilisation parameter $\tau_M^{\text{VX}\oplus\Delta t}$ by its counterpart $\tau_M^{\text{VX}\ominus\Delta t}$. For ease of notation, some abbreviations for the current iteration values of subgrid and resolved-scale velocity, ALE convective velocity and JACOBIan of the resolved-scale velocity are introduced:

| | |
|--|--|
| $\tilde{\mathbf{u}} = \tilde{\mathbf{u}}_{(i)}^{n+\alpha_F}$ | $\mathbf{u} = \mathbf{u}_{(i)}^{h,n+\alpha_F}$ |
| $\mathbf{c} = \mathbf{c}_{(i)}^{h,n+\alpha_F}$ | $J = \nabla \mathbf{u}_{(i)}^{h,n+\alpha_F}$ |

D.1 Convective ALE form

Linearisations of the momentum equation with respect to velocities



The first terms to appear on the velocity block of the momentum-equation part of the matrix are the GALERKIN terms. If a time-dependent subgrid approximation is used, all GALERKIN terms

which have not been integrated by parts are rescaled and an additional linearisation of a viscous term stemming from the subgrid acceleration term appears.

$$\begin{aligned}
 & \left[\left(\frac{\partial R_{\mathbf{u}}}{\partial \mathbf{a}^{h,n+1}} \right)_{(i)} \right]_{3 \cdot (A-1) + k, 3 \cdot (B-1) + l} \\
 = & C_{\text{saccGal,I}} \delta_{kl} (N_B, N_A)_{\Omega(t^{n+1})} \\
 & + C_{\text{saccGal,C}} \delta_{kl} ((\mathbf{c} \cdot \nabla) N_B, N_A)_{\Omega(t^{n+1})} \\
 & + C_{\text{saccGal,C}} (N_B J_{kl}, N_A)_{\Omega(t^{n+1})} \\
 & + C_{\text{Gal,D}} \delta_{kl} (\nabla N_B; \nabla N_A)_{\Omega(t^{n+1})} \\
 & + C_{\text{Gal,D}} ((\nabla N_B \cdot \mathbf{e}_k), (\nabla N_A \cdot \mathbf{e}_l))_{\Omega(t^{n+1})} \\
 & + C_{\text{sacc,D}} \left(\frac{\partial^2 N_B}{\partial x_k \partial x_l}, N_A \right)_{\Omega(t^{n+1})} \\
 & + C_{\text{sacc,D}} \delta_{kl} \left(\sum_j \frac{\partial^2 N_B}{\partial x_j^2}, N_A \right)_{\Omega(t^{n+1})}
 \end{aligned}
 \begin{array}{|c|c|c|}
 \hline
 \text{M} & \text{F} & \text{N} \\
 \hline
 \times & \times & \times \\
 \hline
 \times & \times & \times \\
 \hline
 & & \times \\
 \hline
 \times & \times & \times \\
 \hline
 \times & \times & \times \\
 \hline
 & \times & \times \\
 \hline
 & \times & \times \\
 \hline
 \end{array} \quad (\text{D.1})$$

The required constants are:

| | td | rV |
|------------------------|---|--------------------------------|
| $C_{\text{saccGal,I}}$ | $\alpha_M \cdot \frac{\alpha_F \gamma \Delta t}{\alpha_M \tau_M^{\text{vX}\ominus\Delta t} + \alpha_F \gamma \Delta t}$ | α_M |
| $C_{\text{saccGal,C}}$ | $\alpha_F \gamma \Delta t \cdot \frac{\alpha_F \gamma \Delta t}{\alpha_M \tau_M^{\text{vX}\ominus\Delta t} + \alpha_F \gamma \Delta t}$ | $\alpha_F \gamma \Delta t$ |
| $C_{\text{Gal,D}}$ | $\nu \alpha_F \gamma \Delta t$ | $\nu \alpha_F \gamma \Delta t$ |
| $C_{\text{sacc,D}}$ | $\nu \alpha_M \alpha_F \gamma \Delta t \cdot \frac{\tau_M^{\text{vX}\ominus\Delta t}}{\alpha_M \tau_M^{\text{vX}\ominus\Delta t} + \alpha_F \gamma \Delta t}$ | / |

(D.2)

The LSIC (grad-div) stabilisation acts on the same matrix block.

$$\begin{aligned}
 & \left[\left(\frac{\partial R_{\mathbf{u}}}{\partial \mathbf{a}^{h,n+1}} \right)_{(i)} \right]_{3 \cdot (A-1) + k, 3 \cdot (B-1) + l} \\
 + & C_{\text{LSIC}} ((\nabla N_B \cdot \mathbf{e}_l), (\nabla N_A \cdot \mathbf{e}_k))_{\Omega(t^{n+1})}
 \end{aligned}
 \begin{array}{|c|c|c|}
 \hline
 \text{M} & \text{F} & \text{N} \\
 \hline
 \times & \times & \times \\
 \hline
 \end{array} \quad (\text{D.3})$$

It is essentially the same in the conventional and time-dependent approach.

| | td | rV |
|-------------------|---|--|
| C_{LSIC} | $\gamma \Delta t \cdot \tau_C^{\text{vX}\ominus\Delta t}$ | $\gamma \Delta t \cdot \tau_C^{\text{vX}\oplus\Delta t}$ |

(D.4)

Further contributions to the first matrix block arise from SUPG stabilisation.

$$\begin{aligned}
 & \left[\left(\frac{\partial R_{\mathbf{u}}}{\partial \underline{\mathbf{a}}^{h,n+1}} \right) \right]_{(i)}^{3 \cdot (A-1) + k, 3 \cdot (B-1) + l} \\
 + = & C_{\text{SUPG,I}} \delta_{kl} (N_B, (\mathbf{c} \cdot \nabla) N_A)_{\Omega(t^{n+1})} \\
 & + C_{\text{SUPG,C}} \delta_{kl} ((\mathbf{c} \cdot \nabla) N_B, (\mathbf{c} \cdot \nabla) N_A)_{\Omega(t^{n+1})} \\
 & + C_{\text{SUPG,C}} (N_B J_{kl}, (\mathbf{c} \cdot \nabla) N_A)_{\Omega(t^{n+1})} \\
 & - C_{\text{SUPG,D}} \left(\frac{\partial^2 N_B}{\partial x_k \partial x_l}, (\mathbf{c} \cdot \nabla) N_A \right)_{\Omega(t^{n+1})} \\
 & - C_{\text{SUPG,D}} \delta_{kl} \left(\sum_j \frac{\partial^2 N_B}{\partial x_j^2}, (\mathbf{c} \cdot \nabla) N_A \right)_{\Omega(t^{n+1})} \\
 & - C_{\text{SUPG,T}} (\tilde{\mathbf{u}}_k, N_B (\nabla N_A \cdot \mathbf{e}_l))_{\Omega(t^{n+1})}
 \end{aligned}
 \begin{array}{|c|c|c|}
 \hline
 \text{M} & \text{F} & \text{N} \\
 \hline
 \times & \times & \times \\
 \hline
 \times & \times & \times \\
 \hline
 & & \times \\
 \hline
 & \times & \times \\
 \hline
 & \times & \times \\
 \hline
 & & \times \\
 \hline
 \end{array}
 \tag{D.5}$$

The required constants are collected in the following table.

| | td | rV |
|---------------------|---|---|
| $C_{\text{SUPG,I}}$ | $\alpha_M \cdot \frac{\alpha_F \gamma \Delta t \cdot \tau_M^{\text{VX} \oplus \Delta t}}{\alpha_M \tau_M^{\text{VX} \oplus \Delta t} + \alpha_F \gamma \Delta t}$ | $\alpha_M \cdot \tau_M^{\text{VX} \oplus \Delta t}$ |
| $C_{\text{SUPG,C}}$ | $\alpha_F \gamma \Delta t \cdot \frac{\alpha_F \gamma \Delta t \cdot \tau_M^{\text{VX} \oplus \Delta t}}{\alpha_M \tau_M^{\text{VX} \oplus \Delta t} + \alpha_F \gamma \Delta t}$ | $\alpha_F \gamma \Delta t \cdot \tau_M^{\text{VX} \oplus \Delta t}$ |
| $C_{\text{SUPG,D}}$ | $\nu \alpha_F \gamma \Delta t \cdot \frac{\alpha_F \gamma \Delta t \cdot \tau_M^{\text{VX} \oplus \Delta t}}{\alpha_M \tau_M^{\text{VX} \oplus \Delta t} + \alpha_F \gamma \Delta t}$ | $\nu \alpha_F \gamma \Delta t \cdot \tau_M^{\text{VX} \oplus \Delta t}$ |
| $C_{\text{SUPG,T}}$ | $\alpha_F \gamma \Delta t$ | $\alpha_F \gamma \Delta t$ |

(D.6)

Note that for the time-dependent approach, the stabilisation parameter $\tau_M^{\text{VX} \oplus \Delta t}$ of the conventional approach is simply replaced by the quotient

$$\frac{\alpha_F \gamma \Delta t \cdot \tau_M^{\text{VX} \oplus \Delta t}}{\alpha_M \tau_M^{\text{VX} \oplus \Delta t} + \alpha_F \gamma \Delta t}
 \tag{D.7}$$

which has the same asymptotic behaviour. The first half of the linearisation of the REYNOLDS stress term is of a similar form.

$$\begin{aligned}
 & \left[\left(\frac{\partial R_{\mathbf{u}}}{\partial \underline{\mathbf{a}}^{h,n+1}} \right) \right]_{(i)}^{3 \cdot (A-1) + k, 3 \cdot (B-1) + l} \\
 + = & C_{\text{Rey,I}} \delta_{kl} (N_B, (\tilde{\mathbf{u}} \cdot \nabla) N_A)_{\Omega(t^{n+1})} \\
 & + C_{\text{Rey,C}} \delta_{kl} ((\mathbf{c} \cdot \nabla) N_B, (\tilde{\mathbf{u}} \cdot \nabla) N_A)_{\Omega(t^{n+1})} \\
 & + C_{\text{Rey,C}} (N_B J_{kl}, (\tilde{\mathbf{u}} \cdot \nabla) N_A)_{\Omega(t^{n+1})} \\
 & - C_{\text{Rey,D}} \left(\frac{\partial^2 N_B}{\partial x_k \partial x_l}, (\tilde{\mathbf{u}} \cdot \nabla) N_A \right)_{\Omega(t^{n+1})} \\
 & - C_{\text{Rey,D}} \delta_{kl} \left(\sum_j \frac{\partial^2 N_B}{\partial x_j^2}, (\tilde{\mathbf{u}} \cdot \nabla) N_A \right)_{\Omega(t^{n+1})}
 \end{aligned}
 \begin{array}{|c|c|c|}
 \hline
 \text{M} & \text{F} & \text{N} \\
 \hline
 \otimes & \otimes & \times \\
 \hline
 \otimes & \otimes & \times \\
 \hline
 & & \times \\
 \hline
 & \otimes & \times \\
 \hline
 & \otimes & \times \\
 \hline
 \end{array}
 \tag{D.8}$$

It can be implemented easily using an enriched SUPG test function

$$((\mathbf{c} + \tilde{\mathbf{u}}) \cdot \nabla) N_A. \quad (\text{D.9})$$

The remaining terms are:

$$\left[\left(\frac{\partial R_{\mathbf{u}}}{\partial \mathbf{a}^{h,n+1}} \right) \right]_{(i)_{3 \cdot (A-1) + k, 3 \cdot (B-1) + l}} + = C_{\text{Rey,I}} \quad (\tilde{\mathbf{u}}_k, N_B (\nabla N_A \cdot \mathbf{e}_l))_{\Omega(t^{n+1})}$$

$$+ C_{\text{Rey,C}} \quad (\tilde{\mathbf{u}}_k, ((\mathbf{u} \cdot \nabla) N_B) \cdot (\nabla N_A \cdot \mathbf{e}_l))_{\Omega(t^{n+1})}$$

$$+ C_{\text{Rey,C}} \quad (\tilde{\mathbf{u}}_k, N_B \cdot \left(\sum_j J_{jl} \cdot (\nabla N_A \cdot \mathbf{e}_j) \right))_{\Omega(t^{n+1})}$$

$$- C_{\text{Rey,D}} \quad (\tilde{\mathbf{u}}_k, \left(\sum_j \frac{\partial^2 N_B}{\partial x_j \partial x_i} \cdot (\nabla N_A \cdot \mathbf{e}_j) \right))_{\Omega(t^{n+1})}$$

$$- C_{\text{Rey,D}} \quad (\tilde{\mathbf{u}}_k, \left(\sum_j \frac{\partial^2 N_B}{\partial x_j^2} \right) \cdot (\nabla N_A \cdot \mathbf{e}_l))_{\Omega(t^{n+1})}$$

| M | F | N |
|---|---|---|
| ⊗ | ⊗ | × |
| ⊗ | ⊗ | × |
| | | × |
| | ⊗ | × |
| | ⊗ | × |

(D.10)

All constants in that equation are equivalent to the corresponding constants of the SUPG linearisation terms.

| | td | rV |
|--------------------|---|---|
| $C_{\text{Rey,I}}$ | $\alpha_M \cdot \frac{\alpha_F \gamma \Delta t \cdot \tau_M^{\text{VX} \oplus \Delta t}}{\alpha_M \tau_M^{\text{VX} \oplus \Delta t} + \alpha_F \gamma \Delta t}$ | $\alpha_M \cdot \tau_M^{\text{VX} \oplus \Delta t}$ |
| $C_{\text{Rey,C}}$ | $\alpha_F \gamma \Delta t \cdot \frac{\alpha_F \gamma \Delta t \cdot \tau_M^{\text{VX} \oplus \Delta t}}{\alpha_M \tau_M^{\text{VX} \oplus \Delta t} + \alpha_F \gamma \Delta t}$ | $\alpha_F \gamma \Delta t \cdot \tau_M^{\text{VX} \oplus \Delta t}$ |
| $C_{\text{Rey,D}}$ | $\nu \alpha_F \gamma \Delta t \cdot \frac{\alpha_F \gamma \Delta t \cdot \tau_M^{\text{VX} \oplus \Delta t}}{\alpha_M \tau_M^{\text{VX} \oplus \Delta t} + \alpha_F \gamma \Delta t}$ | $\nu \alpha_F \gamma \Delta t \cdot \tau_M^{\text{VX} \oplus \Delta t}$ |

(D.11)

Linearisations of the cross stress terms are given in the following.

$$\left[\left(\frac{\partial R_{\mathbf{u}}}{\partial \mathbf{a}^{h,n+1}} \right) \right]_{(i)_{3 \cdot (A-1) + k, 3 \cdot (B-1) + l}} + = C_{\text{cross,GT}} \quad \delta_{kl} ((\tilde{\mathbf{u}} \cdot \nabla) N_B, N_A)_{\Omega(t^{n+1})}$$

$$- C_{\text{cross,I}} \quad (J_{kl} N_B, N_A)_{\Omega(t^{n+1})}$$

$$- C_{\text{cross,C}} \quad (J_{kl} (\mathbf{u} \cdot \nabla) N_B, N_A)_{\Omega(t^{n+1})}$$

$$- C_{\text{cross,C}} \quad (N_B (\sum_m J_{ml} \cdot J_{km}), N_A)_{\Omega(t^{n+1})}$$

$$+ C_{\text{cross,D}} \quad \left(\left(\sum_m \frac{\partial^2 N_B}{\partial x_m^2} \right) \cdot J_{kl}, N_A \right)_{\Omega(t^{n+1})}$$

$$+ C_{\text{cross,D}} \quad \left(\left(\sum_m \frac{\partial^2 N_B}{\partial x_m \partial x_l} \right) \cdot J_{km}, N_A \right)_{\Omega(t^{n+1})}$$

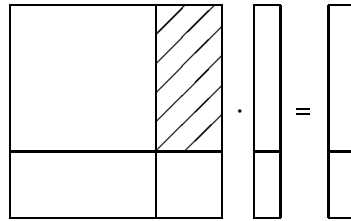
| M | F | N |
|---|---|---|
| ⊗ | ⊗ | × |
| ⊗ | ⊗ | × |
| ⊗ | ⊗ | × |
| | | × |
| | ⊗ | × |
| | ⊗ | × |

(D.12)

Again, the constants equal the values from the SUPG terms.

| | td | rV | |
|-----------------------|---|---|--------|
| $C_{\text{cross,GT}}$ | $\alpha_F \gamma \Delta t$ | $\alpha_F \gamma \Delta t$ | |
| $C_{\text{cross,I}}$ | $\alpha_M \cdot \frac{\alpha_F \gamma \Delta t \cdot \tau_M^{\text{VX} \oplus \Delta t}}{\alpha_M \tau_M^{\text{VX} \oplus \Delta t} + \alpha_F \gamma \Delta t}$ | $\alpha_M \cdot \tau_M^{\text{VX} \oplus \Delta t}$ | (D.13) |
| $C_{\text{cross,C}}$ | $\alpha_F \gamma \Delta t \cdot \frac{\alpha_F \gamma \Delta t \cdot \tau_M^{\text{VX} \oplus \Delta t}}{\alpha_M \tau_M^{\text{VX} \oplus \Delta t} + \alpha_F \gamma \Delta t}$ | $\alpha_F \gamma \Delta t \cdot \tau_M^{\text{VX} \oplus \Delta t}$ | |
| $C_{\text{cross,D}}$ | $\nu \alpha_F \gamma \Delta t \cdot \frac{\alpha_F \gamma \Delta t \cdot \tau_M^{\text{VX} \oplus \Delta t}}{\alpha_M \tau_M^{\text{VX} \oplus \Delta t} + \alpha_F \gamma \Delta t}$ | $\nu \alpha_F \gamma \Delta t \cdot \tau_M^{\text{VX} \oplus \Delta t}$ | |

Linearisations of the momentum equation with respect to pressure



The terms to appear in the pressure block of the linearisation of the momentum equation are given by

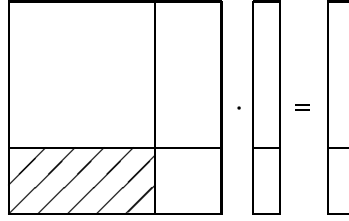
$$\begin{aligned}
 & \left[\left(\frac{\partial R_{\underline{u}}}{\partial \underline{p}^{h,n+1}} \right)_{(i)} \right]_{3 \cdot (A-1) + k, B} \\
 = & -C_{G,P} \quad (N_B, (\nabla N_A \cdot \mathbf{e}_k))_{\Omega(t^{n+1})} \\
 & -C_{\text{sacc},P} \quad ((\nabla N_B \cdot \mathbf{e}_k), N_A)_{\Omega(t^{n+1})} \\
 & +C_{\text{SUPG},P} \quad ((\nabla N_B \cdot \mathbf{e}_k), (\mathbf{c} \cdot \nabla) N_A)_{\Omega(t^{n+1})} \\
 & -C_{\text{cross},P} \quad (\sum_m (\nabla N_B \cdot \mathbf{e}_m) J_{km}, N_A)_{\Omega(t^{n+1})} \\
 & +C_{\text{Rey},P} \quad ((\nabla N_B \cdot \mathbf{e}_k), (\tilde{\mathbf{u}} \cdot \nabla) N_A)_{\Omega(t^{n+1})} \\
 & +C_{\text{Rey},P} \quad (\tilde{\mathbf{u}}_k, (\nabla N_B \cdot \nabla N_A))_{\Omega(t^{n+1})}
 \end{aligned}
 \begin{array}{|c|c|c|}
 \hline
 \text{M} & \text{F} & \text{N} \\
 \hline
 \times & \times & \times \\
 \hline
 \times & \times & \times \\
 \hline
 \times & \times & \times \\
 \hline
 \otimes & \otimes & \times \\
 \hline
 \otimes & \otimes & \times \\
 \hline
 \otimes & \otimes & \times
 \end{array}
 \quad (D.14)$$

Constants are given by

| | td | rV |
|----------------------|--|-----------------------------|
| $C_{G,P}$ | 1 | 1 |
| $C_{\text{sacc},P}$ | $\alpha_M \cdot \frac{\tau_M^{VX\oplus\Delta t}}{\alpha_M \tau_M^{VX\oplus\Delta t} + \alpha_F \gamma \Delta t}$ | / |
| $C_{\text{SUPG},P}$ | $\frac{\alpha_F \gamma \Delta t \cdot \tau_M^{VX\oplus\Delta t}}{\alpha_M \tau_M^{VX\oplus\Delta t} + \alpha_F \gamma \Delta t}$ | $\tau_M^{VX\oplus\Delta t}$ |
| $C_{\text{cross},P}$ | $\frac{\alpha_F \gamma \Delta t \cdot \tau_M^{VX\oplus\Delta t}}{\alpha_M \tau_M^{VX\oplus\Delta t} + \alpha_F \gamma \Delta t}$ | $\tau_M^{VX\oplus\Delta t}$ |
| $C_{\text{Rey},P}$ | $\frac{\alpha_F \gamma \Delta t \cdot \tau_M^{VX\oplus\Delta t}}{\alpha_M \tau_M^{VX\oplus\Delta t} + \alpha_F \gamma \Delta t}$ | $\tau_M^{VX\oplus\Delta t}$ |

(D.15)

Linearisations of the continuity equation with respect to velocities



The linearisation of the continuity equation with respect to velocities yields

$$\begin{aligned}
 & \left[\left(\frac{\partial R_p}{\partial \underline{u}^{h,n+1}} \right)_{(i)} \right]_{A,3 \cdot (B-1) + l} \\
 = & C_{G,\text{cont}} \quad (\nabla N_B \cdot \mathbf{e}_l, N_A)_{\Omega(t^{n+1})} \\
 & + C_{\text{PSPG},I} \quad (N_B; (\nabla N_A \cdot \mathbf{e}_l))_{\Omega(t^{n+1})} \\
 & + C_{\text{PSPG},C} \quad ((\mathbf{c} \cdot \nabla) N_B, \nabla N_A \cdot \mathbf{e}_l)_{\Omega(t^{n+1})} \\
 & + C_{\text{PSPG},C} \quad (N_B (\sum_m J_{ml}); \nabla N_A)_{\Omega(t^{n+1})} \\
 & - C_{\text{PSPG},D} \quad \left(\left(\sum_j \frac{\partial^2 N_B}{\partial x_j^2} \right); \nabla N_A \cdot \mathbf{e}_l \right)_{\Omega(t^{n+1})} \\
 & - C_{\text{PSPG},D} \quad \sum_j \left(\frac{\partial^2 N_B}{\partial x_j \partial x_l}, (\nabla N_A \cdot \mathbf{e}_j) \right)_{\Omega(t^{n+1})}
 \end{aligned}$$

| | M | F | N |
|----------------------|---|---|---|
| $C_{G,\text{cont}}$ | × | × | × |
| $C_{\text{PSPG},I}$ | × | × | × |
| $C_{\text{PSPG},C}$ | × | × | × |
| $C_{\text{PSPG},C}$ | | | × |
| $-C_{\text{PSPG},D}$ | | × | × |
| $-C_{\text{PSPG},D}$ | | × | × |

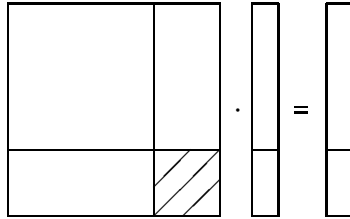
(D.16)

with constants

| | td | rV |
|---------------------|--|--|
| $C_{G,\text{cont}}$ | $\gamma \Delta t$ | $\gamma \Delta t$ |
| $C_{\text{PSPG},I}$ | $\alpha_M \cdot \frac{\gamma \Delta t \cdot \tau_M^{VX\oplus\Delta t}}{\alpha_M \tau_M^{VX\oplus\Delta t} + \alpha_F \gamma \Delta t}$ | $\alpha_M \cdot \tau_M^{VX\oplus\Delta t}$ |
| $C_{\text{PSPG},C}$ | $\alpha_F \gamma \Delta t \cdot \frac{\gamma \Delta t \cdot \tau_M^{VX\oplus\Delta t}}{\alpha_M \tau_M^{VX\oplus\Delta t} + \alpha_F \gamma \Delta t}$ | $\alpha_F \gamma \Delta t \cdot \tau_M^{VX\oplus\Delta t}$ |
| $C_{\text{PSPG},D}$ | $\nu \alpha_F \gamma \Delta t \cdot \frac{\gamma \Delta t \cdot \tau_M^{VX\oplus\Delta t}}{\alpha_M \tau_M^{VX\oplus\Delta t} + \alpha_F \gamma \Delta t}$ | $\nu \alpha_F \gamma \Delta t \cdot \tau_M^{VX\oplus\Delta t}$ |

(D.17)

Linearisations of the continuity equation with respect to pressure



The system matrix is completed by the linearisation of the continuity part with respect to the pressure.

$$\begin{aligned}
 & \left[\left(\frac{\partial R_p}{\partial \underline{p}^{h,n+1}} \right)_{(i) A,B} \right] \begin{array}{|c|c|c|} \hline \text{M} & \text{F} & \text{N} \\ \hline \times & \times & \times \\ \hline \end{array} \\
 & = C_{\text{PSPG,P}} (\nabla N_B; \nabla N_A)_{\Omega(t^{n+1})}
 \end{aligned} \tag{D.18}$$

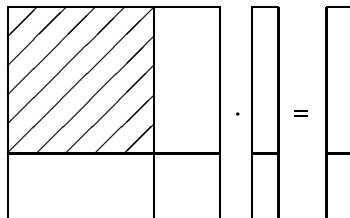
This part is related only to the PSPG stabilisation. The respective constant reads

$$C_{\text{PSPG,P}} \begin{array}{|c|c|} \hline \text{td} & \text{rV} \\ \hline \frac{\gamma \Delta t \cdot \tau_M^{\text{vX} \oplus \Delta t}}{\alpha_M \tau_M^{\text{vX} \oplus \Delta t} + \alpha_F \gamma \Delta t} & \tau_M^{\text{vX} \oplus \Delta t} \\ \hline \end{array} \cdot \tag{D.19}$$

D.2 Conservative EULERian form

The conservative form differs from the convective form only in a slight modification of the weak form of the momentum equation, see subsections 4.4.5 and 4.4.3. Thus, linearisation terms related to the continuity equation do not change with respect to the expressions given in section D.1. They can simply be taken from that section and will not be repeated here again. Linearisation terms for the momentum part in the conservative form are defined in the following.

Linearisations of the momentum equation with respect to velocities



The first terms to appear on the velocity block of the momentum-equation part of the matrix are of GALERKIN type. If a time-dependent subgrid approximation is used, only the inertia term can be treated by a rescaling, all other terms have been integrated by parts and do now appear with a

GALERKIN and a subgrid acceleration contribution.

$$\begin{aligned}
 & \left[\left(\frac{\partial R_{\underline{\mathbf{u}}}}{\partial \underline{\mathbf{a}}^{h,n+1}} \right)_{(i)} \right]_{3 \cdot (A-1) + k, 3 \cdot (B-1) + l} \\
 = & C_{\text{saccGal,I}} \delta_{kl} (N_B, N_A)_{\Omega(t^{n+1})} \\
 & - C_{\text{Gal,C}} \delta_{kl} (N_B, (\mathbf{u} \cdot \nabla) N_A)_{\Omega(t^{n+1})} \\
 & - C_{\text{Gal,C}} ((\mathbf{u} \cdot \mathbf{e}_k), N_B (\nabla N_A \cdot \mathbf{e}_l))_{\Omega(t^{n+1})} \\
 & - C_{\text{sacc,C}} \delta_{kl} ((\mathbf{u} \cdot \nabla) N_B, N_A)_{\Omega(t^{n+1})} \\
 & - C_{\text{sacc,C}} (N_B J_{kl}, N_A)_{\Omega(t^{n+1})} \\
 & + C_{\text{Gal,D}} \delta_{kl} (\nabla N_B; \nabla N_A)_{\Omega(t^{n+1})} \\
 & + C_{\text{Gal,D}} ((\nabla N_B \cdot \mathbf{e}_k), (\nabla N_A \cdot \mathbf{e}_l))_{\Omega(t^{n+1})} \\
 & + C_{\text{sacc,D}} \left(\frac{\partial^2 N_B}{\partial x_k \partial x_l}, N_A \right)_{\Omega(t^{n+1})} \\
 & + C_{\text{sacc,D}} \delta_{kl} \left(\sum_j \frac{\partial^2 N_B}{\partial x_j^2}, N_A \right)_{\Omega(t^{n+1})}
 \end{aligned}
 \begin{array}{|c|c|c|}
 \hline
 \mathbf{M} & \mathbf{F} & \mathbf{N} \\
 \hline
 \times & \times & \times \\
 \hline
 \times & \times & \times \\
 \hline
 & & \times \\
 \hline
 \times & \times & \times \\
 \hline
 & & \times \\
 \hline
 \times & \times & \times \\
 \hline
 \times & \times & \times \\
 \hline
 & \times & \times \\
 \hline
 & \times & \times \\
 \hline
 \end{array} \tag{D.20}$$

Constants are given in the following table:

| | td | rV |
|------------------------|---|--------------------------------|
| $C_{\text{saccGal,I}}$ | $\alpha_M \cdot \frac{\alpha_F \gamma \Delta t}{\alpha_M \tau_M^{\text{vx} \oplus \Delta t} + \alpha_F \gamma \Delta t}$ | α_M |
| $C_{\text{Gal,C}}$ | $\alpha_F \gamma \Delta t$ | $\alpha_F \gamma \Delta t$ |
| $C_{\text{sacc,C}}$ | $\alpha_F \gamma \Delta t \cdot \frac{\alpha_M \tau_M^{\text{vx} \oplus \Delta t}}{\alpha_M \tau_M^{\text{vx} \oplus \Delta t} + \alpha_F \gamma \Delta t}$ | / |
| $C_{\text{Gal,D}}$ | $\nu \alpha_F \gamma \Delta t$ | $\nu \alpha_F \gamma \Delta t$ |
| $C_{\text{sacc,D}}$ | $\nu \alpha_M \alpha_F \gamma \Delta t \cdot \frac{\tau_M^{\text{vx} \oplus \Delta t}}{\alpha_M \tau_M^{\text{vx} \oplus \Delta t} + \alpha_F \gamma \Delta t}$ | / |

The LSIC (grad-div) stabilisation is the same as for the convective case.

$$\begin{aligned}
 & \left[\left(\frac{\partial R_{\underline{\mathbf{u}}}}{\partial \underline{\mathbf{a}}^{h,n+1}} \right)_{(i)} \right]_{3 \cdot (A-1) + k, 3 \cdot (B-1) + l} \\
 + = & C_{\text{LSIC}} ((\nabla N_B \cdot \mathbf{e}_l), (\nabla N_A \cdot \mathbf{e}_k))_{\Omega(t^{n+1})}
 \end{aligned}
 \begin{array}{|c|c|c|}
 \hline
 \mathbf{M} & \mathbf{F} & \mathbf{N} \\
 \hline
 \times & \times & \times \\
 \hline
 \end{array} \tag{D.22}$$

The required constant is essentially the same in the conventional and time-dependent approach.

| | td | rV |
|-------------------|--|--|
| C_{LSIC} | $\gamma \Delta t \cdot \tau_C^{\text{vx} \oplus \Delta t}$ | $\gamma \Delta t \cdot \tau_C^{\text{vx} \oplus \Delta t}$ |

Further contributions to the first matrix block arise from SUPG stabilisation.

$$\begin{aligned}
 & \left[\left(\frac{\partial R_{\underline{u}}}{\partial \underline{a}^{h,n+1}} \right)_{(i)} \right]_{3 \cdot (A-1) + k, 3 \cdot (B-1) + l} \\
 + & = C_{\text{SUPG,I}} \delta_{kl} (N_B, (\mathbf{u} \cdot \nabla) N_A)_{\Omega(t^{n+1})} \\
 & + C_{\text{SUPG,C}} \delta_{kl} ((\mathbf{u} \cdot \nabla) N_B, (\mathbf{u} \cdot \nabla) N_A)_{\Omega(t^{n+1})} \\
 & + C_{\text{SUPG,C}} (N_B J_{kl}, (\mathbf{u} \cdot \nabla) N_A)_{\Omega(t^{n+1})} \\
 - & C_{\text{SUPG,D}} \left(\frac{\partial^2 N_B}{\partial x_k \partial x_l}, (\mathbf{u} \cdot \nabla) N_A \right)_{\Omega(t^{n+1})} \\
 - & C_{\text{SUPG,D}} \delta_{kl} \left(\sum_j \frac{\partial^2 N_B}{\partial x_j^2}, (\mathbf{u} \cdot \nabla) N_A \right)_{\Omega(t^{n+1})} \\
 - & C_{\text{SUPG,T}} (\tilde{\mathbf{u}}_k, N_B (\nabla N_A \cdot \mathbf{e}_l))_{\Omega(t^{n+1})}
 \end{aligned}
 \quad
 \begin{array}{|c|c|c|}
 \hline
 & \text{M} & \text{F} & \text{N} \\
 \hline
 & \times & \times & \times \\
 \hline
 & \times & \times & \times \\
 \hline
 & & & \times \\
 \hline
 & & \times & \times \\
 \hline
 & & \times & \times \\
 \hline
 & & & \times \\
 \hline
 \end{array}
 \quad (\text{D.24})$$

They and the following REYNOLDS stress terms are equivalent to the terms in the convective approach. The required constants are collected in the following table.

| | td | rV |
|---------------------|---|---|
| $C_{\text{SUPG,I}}$ | $\alpha_M \cdot \frac{\alpha_F \gamma \Delta t \cdot \tau_M^{\text{VX} \ominus \Delta t}}{\alpha_M \tau_M^{\text{VX} \ominus \Delta t} + \alpha_F \gamma \Delta t}$ | $\alpha_M \cdot \tau_M^{\text{VX} \oplus \Delta t}$ |
| $C_{\text{SUPG,C}}$ | $\alpha_F \gamma \Delta t \cdot \frac{\alpha_F \gamma \Delta t \cdot \tau_M^{\text{VX} \oplus \Delta t}}{\alpha_M \tau_M^{\text{VX} \oplus \Delta t} + \alpha_F \gamma \Delta t}$ | $\alpha_F \gamma \Delta t \cdot \tau_M^{\text{VX} \oplus \Delta t}$ |
| $C_{\text{SUPG,D}}$ | $\nu \alpha_F \gamma \Delta t \cdot \frac{\alpha_F \gamma \Delta t \cdot \tau_M^{\text{VX} \oplus \Delta t}}{\alpha_M \tau_M^{\text{VX} \oplus \Delta t} + \alpha_F \gamma \Delta t}$ | $\nu \alpha_F \gamma \Delta t \cdot \tau_M^{\text{VX} \oplus \Delta t}$ |
| $C_{\text{SUPG,T}}$ | $\alpha_F \gamma \Delta t$ | $\alpha_F \gamma \Delta t$ |

(D.25)

The first half of the linearisation of the REYNOLDS stress term is

$$\begin{aligned}
 & \left[\left(\frac{\partial R_{\underline{u}}}{\partial \underline{a}^{h,n+1}} \right)_{(i)} \right]_{3 \cdot (A-1) + k, 3 \cdot (B-1) + l} \\
 + & = C_{\text{Rey,I}} \delta_{kl} (N_B, (\tilde{\mathbf{u}} \cdot \nabla) N_A)_{\Omega(t^{n+1})} \\
 & + C_{\text{Rey,C}} \delta_{kl} ((\mathbf{c} \cdot \nabla) N_B, (\tilde{\mathbf{u}} \cdot \nabla) N_A)_{\Omega(t^{n+1})} \\
 & + C_{\text{Rey,C}} (N_B J_{kl}, (\tilde{\mathbf{u}} \cdot \nabla) N_A)_{\Omega(t^{n+1})} \\
 - & C_{\text{Rey,D}} \left(\frac{\partial^2 N_B}{\partial x_k \partial x_l}, (\tilde{\mathbf{u}} \cdot \nabla) N_A \right)_{\Omega(t^{n+1})} \\
 - & C_{\text{Rey,D}} \delta_{kl} \left(\sum_j \frac{\partial^2 N_B}{\partial x_j^2}, (\tilde{\mathbf{u}} \cdot \nabla) N_A \right)_{\Omega(t^{n+1})}
 \end{aligned}
 \quad
 \begin{array}{|c|c|c|}
 \hline
 & \text{M} & \text{F} & \text{N} \\
 \hline
 & \otimes & \otimes & \times \\
 \hline
 & \otimes & \otimes & \times \\
 \hline
 & & & \times \\
 \hline
 & & \otimes & \times \\
 \hline
 & & \otimes & \times \\
 \hline
 \end{array}
 \quad (\text{D.26})$$

The remaining terms are

$$\begin{aligned}
 & \left[\left(\frac{\partial R_{\mathbf{u}}}{\partial \underline{\mathbf{a}}^{h,n+1}} \right) \right]_{(i)}^{3 \cdot (A-1) + k, 3 \cdot (B-1) + l} \\
 + & C_{\text{Rey,I}} \quad \left(\tilde{\mathbf{u}}_k, N_B (\nabla N_A \cdot \mathbf{e}_l) \right)_{\Omega(t^{n+1})} \\
 + & C_{\text{Rey,C}} \quad \left(\tilde{\mathbf{u}}_k, ((\mathbf{u} \cdot \nabla) N_B) \cdot (\nabla N_A \cdot \mathbf{e}_l) \right)_{\Omega(t^{n+1})} \\
 + & C_{\text{Rey,C}} \quad \left(\tilde{\mathbf{u}}_k, N_B \cdot \left(\sum_j J_{jl} \cdot (\nabla N_A \cdot \mathbf{e}_j) \right) \right)_{\Omega(t^{n+1})} \\
 - & C_{\text{Rey,D}} \quad \left(\tilde{\mathbf{u}}_k, \left(\sum_j \frac{\partial^2 N_B}{\partial x_j \partial x_l} \cdot (\nabla N_A \cdot \mathbf{e}_j) \right) \right)_{\Omega(t^{n+1})} \\
 - & C_{\text{Rey,D}} \quad \left(\tilde{\mathbf{u}}_k, \left(\sum_j \frac{\partial^2 N_B}{\partial x_j^2} \right) \cdot (\nabla N_A \cdot \mathbf{e}_l) \right)_{\Omega(t^{n+1})}
 \end{aligned}
 \begin{array}{|c|c|c|}
 \hline
 \text{M} & \text{F} & \text{N} \\
 \hline
 \otimes & \otimes & \times \\
 \hline
 \otimes & \otimes & \times \\
 \hline
 & & \times \\
 \hline
 & \otimes & \times \\
 \hline
 & \otimes & \times
 \end{array} \quad (\text{D.27})$$

Required constants are equivalent to the constants of the SUPG linearisation terms, as usual.

| | td | rV |
|--------------------|---|---|
| $C_{\text{Rey,I}}$ | $\alpha_M \cdot \frac{\alpha_F \gamma \Delta t \cdot \tau_M^{\text{VX} \ominus \Delta t}}{\alpha_M \tau_M^{\text{VX} \ominus \Delta t} + \alpha_F \gamma \Delta t}$ | $\alpha_M \cdot \tau_M^{\text{VX} \oplus \Delta t}$ |
| $C_{\text{Rey,C}}$ | $\alpha_F \gamma \Delta t \cdot \frac{\alpha_F \gamma \Delta t \cdot \tau_M^{\text{VX} \ominus \Delta t}}{\alpha_M \tau_M^{\text{VX} \ominus \Delta t} + \alpha_F \gamma \Delta t}$ | $\alpha_F \gamma \Delta t \cdot \tau_M^{\text{VX} \oplus \Delta t}$ |
| $C_{\text{Rey,D}}$ | $\nu \alpha_F \gamma \Delta t \cdot \frac{\alpha_F \gamma \Delta t \cdot \tau_M^{\text{VX} \ominus \Delta t}}{\alpha_M \tau_M^{\text{VX} \ominus \Delta t} + \alpha_F \gamma \Delta t}$ | $\nu \alpha_F \gamma \Delta t \cdot \tau_M^{\text{VX} \oplus \Delta t}$ |

(D.28)

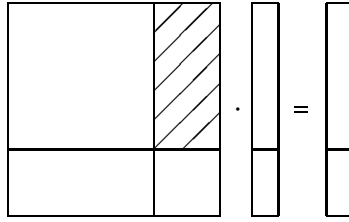
Linearisations of the cross stress terms have changed and are given in the following:

$$\begin{aligned}
 & \left[\left(\frac{\partial R_{\mathbf{u}}}{\partial \underline{\mathbf{a}}^{h,n+1}} \right) \right]_{(i)}^{3 \cdot (A-1) + k, 3 \cdot (B-1) + l} \\
 + & -C_{\text{cross,GT}} \quad \delta_{kl} \quad (N_B, (\tilde{\mathbf{u}} \cdot \nabla) N_A)_{\Omega(t^{n+1})} \\
 + & C_{\text{cross,I}} \quad (\mathbf{u}_k, N_B (\nabla N_A \cdot \mathbf{e}_l))_{\Omega(t^{n+1})} \\
 + & C_{\text{cross,C}} \quad (\mathbf{u}_k, (\mathbf{u} \cdot \nabla N_B) (\nabla N_A \cdot \mathbf{e}_l))_{\Omega(t^{n+1})} \\
 + & C_{\text{cross,C}} \quad \left(\mathbf{u}_k, N_B \left(\sum_m J_{ml} \frac{\partial N_A}{\partial x_m} \right) \right)_{\Omega(t^{n+1})} \\
 - & C_{\text{cross,D}} \quad \left(\mathbf{u}_k, \sum_m \frac{\partial^2 N_B}{\partial x_m \partial x_l} \frac{\partial N_A}{\partial x_m} \right)_{\Omega(t^{n+1})} \\
 - & C_{\text{cross,D}} \quad \left(\mathbf{u}_k, \left(\sum_m \frac{\partial^2 N_B}{\partial x_m^2} \right) \left(\frac{\partial N_A}{\partial x_l} \right) \right)_{\Omega(t^{n+1})}
 \end{aligned}
 \begin{array}{|c|c|c|}
 \hline
 \text{M} & \text{F} & \text{N} \\
 \hline
 \otimes & \otimes & \times \\
 \hline
 \otimes & \otimes & \times \\
 \hline
 \otimes & \otimes & \times \\
 \hline
 & & \times \\
 \hline
 & \otimes & \times \\
 \hline
 & \otimes & \times
 \end{array} \quad (\text{D.29})$$

Once more, the constants equal the values from the SUPG terms.

| | td | rV | |
|-----------------------|---|---|--------|
| $C_{\text{cross,GT}}$ | $\alpha_F \gamma \Delta t$ | $\alpha_F \gamma \Delta t$ | |
| $C_{\text{cross,I}}$ | $\alpha_M \cdot \frac{\alpha_F \gamma \Delta t \cdot \tau_M^{\text{VX}\ominus\Delta t}}{\alpha_M \tau_M^{\text{VX}\ominus\Delta t} + \alpha_F \gamma \Delta t}$ | $\alpha_M \cdot \tau_M^{\text{VX}\oplus\Delta t}$ | (D.30) |
| $C_{\text{cross,C}}$ | $\alpha_F \gamma \Delta t \cdot \frac{\alpha_F \gamma \Delta t \cdot \tau_M^{\text{VX}\ominus\Delta t}}{\alpha_M \tau_M^{\text{VX}\ominus\Delta t} + \alpha_F \gamma \Delta t}$ | $\alpha_F \gamma \Delta t \cdot \tau_M^{\text{VX}\oplus\Delta t}$ | |
| $C_{\text{cross,D}}$ | $\nu \alpha_F \gamma \Delta t \cdot \frac{\alpha_F \gamma \Delta t \cdot \tau_M^{\text{VX}\ominus\Delta t}}{\alpha_M \tau_M^{\text{VX}\ominus\Delta t} + \alpha_F \gamma \Delta t}$ | $\nu \alpha_F \gamma \Delta t \cdot \tau_M^{\text{VX}\oplus\Delta t}$ | |

Linearisations of the momentum equation with respect to pressure



The terms to appear in the pressure part of the linearisation of the conservative form of the momentum equation are given by

$$\begin{aligned}
 & \left[\left(\frac{\partial R_{\underline{u}}}{\partial p^{h,n+1}} \right)_{(i)} \right]_{3 \cdot (A-1) + k, B} \\
 = & -C_{\text{G,P}} \quad (N_B, (\nabla N_A \cdot \mathbf{e}_k))_{\Omega(t^{n+1})} \\
 & -C_{\text{sacc,P}} \quad ((\nabla N_B \cdot \mathbf{e}_k), N_A)_{\Omega(t^{n+1})} \\
 & +C_{\text{SUPG,P}} \quad ((\nabla N_B \cdot \mathbf{e}_k), (\mathbf{u} \cdot \nabla) N_A)_{\Omega(t^{n+1})} \\
 & +C_{\text{cross,P}} \quad ((\mathbf{u} \cdot \mathbf{e}_k), (\nabla N_B \cdot \nabla) N_A)_{\Omega(t^{n+1})} \\
 & +C_{\text{Rey,P}} \quad ((\nabla N_B \cdot \mathbf{e}_k), (\tilde{\mathbf{u}} \cdot \nabla) N_A)_{\Omega(t^{n+1})} \\
 & +C_{\text{Rey,P}} \quad (\tilde{\mathbf{u}}_k, (\nabla N_B \cdot \nabla) N_A)_{\Omega(t^{n+1})}
 \end{aligned}$$

| | M | F | N |
|-----------|-----------|-----------|----------|
| \times | \times | \times | \times |
| \times | \times | \times | \times |
| \times | \times | \times | \times |
| \otimes | \otimes | \otimes | \times |
| \otimes | \otimes | \otimes | \times |
| \otimes | \otimes | \otimes | \times |

(D.31)

The only modified contribution is the one connected to the cross stress term. Constants are given by

| | td | rV |
|----------------------|--|-----------------------------|
| $C_{G,P}$ | 1 | 1 |
| $C_{\text{sacc},P}$ | $\alpha_M \cdot \frac{\tau_M^{VX\ominus\Delta t}}{\alpha_M \tau_M^{VX\ominus\Delta t} + \alpha_F \gamma \Delta t}$ | / |
| $C_{\text{SUPG},P}$ | $\frac{\alpha_F \gamma \Delta t \cdot \tau_M^{VX\ominus\Delta t}}{\alpha_M \tau_M^{VX\ominus\Delta t} + \alpha_F \gamma \Delta t}$ | $\tau_M^{VX\oplus\Delta t}$ |
| $C_{\text{cross},P}$ | $\frac{\alpha_F \gamma \Delta t \cdot \tau_M^{VX\ominus\Delta t}}{\alpha_M \tau_M^{VX\ominus\Delta t} + \alpha_F \gamma \Delta t}$ | $\tau_M^{VX\oplus\Delta t}$ |
| $C_{\text{Rey},P}$ | $\frac{\alpha_F \gamma \Delta t \cdot \tau_M^{VX\ominus\Delta t}}{\alpha_M \tau_M^{VX\ominus\Delta t} + \alpha_F \gamma \Delta t}$ | $\tau_M^{VX\oplus\Delta t}$ |

(D.32)

as before.

E Iterative solution of the linear problem

A central part of the finite element approximation process of a fluid problem is the solution of the linear system (3.127). Although this linear system is sparse, it is usually very large. An efficient way to compute solutions for such problems is to use iterative solvers in combination with suitable preconditioners. An overview of contemporary iterative solution procedures can be found in SAAD and VAN DER VORST [185].

The iterative method used for the solution of nonsymmetric problems within this work is a KRYLOV subspace method, the generalised minimal residual approach (GMRES) by SAAD and SCHULTZ [184]. Compared to other methods, like the bi-conjugate gradient stabilised method (Bi-CGSTAB) by VAN DER VOST [213], the GMRES approach has certain disadvantages concerning memory consumption and computational cost. Nevertheless, it provides a more robust method and thus is preferred for applications as they are considered in this thesis. Section E.1 will provide a short introduction to the GMRES approach.

An obvious requirement for the applicability of a conventional GMRES method is that the linear system (3.127) is not singular. Unfortunately, for purely DIRICHLET bounded problems as they are discussed in chapter 5 and section 6.1, this will not be the case using the standard choice for \mathcal{S}_p^h according to equations (3.108) and (3.109). In the same way as the continuous pressure, the discrete pressure increment will be defined only up to a constant. Nevertheless, as already noted in section 3.2, the continuous pressure is uniquely defined on a factor space for the pressure as given in (3.54). On its discrete counterpart $\mathcal{S}_p^{h,\text{restricted}}$, the equivalence class of the discrete pressure is also defined uniquely, and thus the projection of the linear equation system into the corresponding factor space of $\mathbb{R}^{\bar{n}^{\text{dof}}}$ has full rank. In section E.2, a modified preconditioned GMRES procedure for the iterative solution of the projection of the linear system (3.127) will be described. The solution procedure is based on the fact that the kernel of the system matrix is known to be spanned by the vector

$$(\underline{e})_\kappa = \begin{cases} 0 & \text{for } 1 \leq \kappa \leq \bar{n}_u^{\text{dof}} \\ 1 & \text{for } \bar{n}_u^{\text{dof}} + 1 \leq \kappa \leq \bar{n}_u^{\text{dof}} + n_p^{\text{dof}} \end{cases} \quad (\text{E.1})$$

The basis vector in equation (E.1) is one only for pressure degrees of freedom and zero for all other degrees of freedom. The modifications to the standard iterative solution procedure are encouraged by a paper by BOCHEV and LEHOUCQ [31] on the solution of the pure NEUMANN problem. Modified iterative solvers of this type are applicable not only to this special class of fluid problems, but also for instance to insufficiently supported static structural problems. The main advantage of this approach is that the effective condition number of the nonsingular projected system is smaller than the condition number of a corresponding problem with the singularity removed by the imposition of a DIRICHLET condition on the pressure in one point. See the comments in the reference given above and the results in subsection 6.1.2.

E.1 A preconditioned GMRES procedure

In this section, a short overview of the basic principles of the preconditioned GMRES method will be given. This overview is not meant to be complete, it is only intended to provide the necessary information to understand the modifications that will be described in the following section. The exact preconditioned GMRES implementation used in the computations presented in this thesis is the one from the AZTEC package [212] in combination with preconditioning procedures provided by the ML package [89].

The following explanations will refer to a generic, nonsymmetric, linear system in residual form,

$$\mathbf{r} = \mathbf{b} - \mathbf{A} \cdot \mathbf{x} = \mathbf{0}. \quad (\text{E.2})$$

For the moment, the system matrix \mathbf{A} of size $N \times N$ is assumed to be nonsingular. For an initial estimate of the solution \mathbf{x}_0 , a corresponding initial residual

$$\mathbf{r}_0 = \mathbf{b} - \mathbf{A} \cdot \mathbf{x}_0 \quad (\text{E.3})$$

can be computed. Based on this initial residual, a series of successive KRYLOV subspaces

$$K^i = \text{span} \{ \mathbf{r}_0, \mathbf{A} \mathbf{r}_0, \dots, \mathbf{A}^{i-1} \mathbf{r}_0 \} \quad (\text{E.4})$$

can be defined.

E.1.1 The GMRES method

The iterative GMRES method determines the approximate solution $\mathbf{x}_i = \mathbf{x}_0 + \mathbf{z}_i$ in iteration step i such that the increment \mathbf{z}_i minimises the norm of the residual $\mathbf{r}_i = \mathbf{b} - \mathbf{A} \cdot \mathbf{x}_i$ on the i -th KRYLOV subspace, i.e. \mathbf{z}_i is determined as the minimum of the optimisation problem

$$\min_{\mathbf{z}_i \in K^i} \|\mathbf{r}_i\|^2 = \min_{\mathbf{z}_i \in K^i} \|\mathbf{r}_0 - \mathbf{A} \mathbf{z}_i\|^2. \quad (\text{E.5})$$

In the GMRES approach, the optimisation problem (E.5) is restated as an equivalent minimisation problem on \mathbb{R}^i using an appropriate basis representation of K^i . This basis representation is successively generated by an orthonormalisation process usually referred to as ARNOLDI's method. The process is started with

$$\mathbf{v}_1 = \frac{\mathbf{r}_0}{\|\mathbf{r}_0\|}. \quad (\text{E.6})$$

Given a KRYLOV subspace K^i with orthonormal basis $\mathbf{v}_1, \dots, \mathbf{v}_i$, the new basis vector is determined according to

$$\hat{\mathbf{v}}_{i+1} = \mathbf{A} \mathbf{v}_i - \sum_{j=1}^i (\mathbf{v}_j^T \mathbf{A} \mathbf{v}_i) \mathbf{v}_j, \quad \mathbf{v}_{i+1} = \frac{\hat{\mathbf{v}}_{i+1}}{\|\hat{\mathbf{v}}_{i+1}\|}. \quad (\text{E.7})$$

The coefficients $(\mathbf{H}^i)_{j,k} = \mathbf{v}_j^T \mathbf{A} \mathbf{v}_k$ define an $i \times i$ matrix. Due to the orthonormal construction of the basis $\mathbf{v}_1, \dots, \mathbf{v}_i$ and the definition of the KRYLOV subspace (E.4), $(\mathbf{H}^i)_{j,k} = 0$ holds for

$j > k + 1$, i.e. the matrix \mathbf{H}^i is of HESSENBERG type. Moreover, due to the orthonormality of the basis functions, the scalar product of equation (E.7) with the new basis vector $\underline{\mathbf{v}}_{i+1}$ yields the identity

$$\|\hat{\underline{\mathbf{v}}}_{i+1}\| = \underline{\mathbf{v}}_{i+1}^T \mathbf{A} \underline{\mathbf{v}}_i = (\mathbf{H}^{i+1})_{i+1,i}. \quad (\text{E.8})$$

A hierarchy for the HESSENBERG matrices \mathbf{H}^i and the definition of an extended HESSENBERG matrix $\hat{\mathbf{H}}^i$ can be found in Figure E.1. In every iteration, the orthonormal basis can be further-

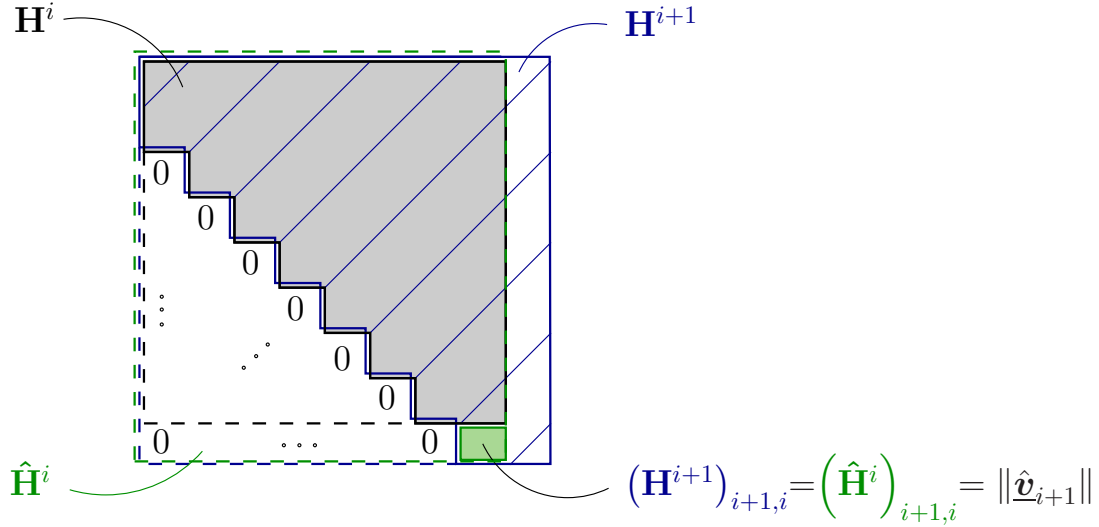


Figure E.1: The HESSENBERG matrix \mathbf{H}^i of iteration i enlarged with an extra row containing the only nonzero entry $\|\hat{\underline{\mathbf{v}}}_{i+1}\|$ is called the extended HESSENBERG $\hat{\mathbf{H}}^i$. It constitutes the first i columns of \mathbf{H}^{i+1} .

more gathered in a matrix

$$\mathbf{V}^i = \left(\begin{array}{c|c|c|c} \underline{\mathbf{v}}_1 & \underline{\mathbf{v}}_2 & \dots & \underline{\mathbf{v}}_i \end{array} \right) \in \mathbb{R}^{N \times i} \quad (\text{E.9})$$

and every $\underline{\mathbf{z}}_i \in K^i$ can be reexpressed using this basis and a coordinate representation $\mathbf{y}_i \in \mathbb{R}^i$:

$$\underline{\mathbf{z}}_i = \mathbf{V}^i \mathbf{y}_i \quad (\text{E.10})$$

The optimisation problem (E.5) can now be restated as a least-squares problem for the coordinates with respect to the orthonormal basis in the form

$$\min_{\mathbf{y}_i \in \mathbb{R}^i} \|\|\underline{\mathbf{r}}_0\| \cdot \underline{\mathbf{v}}_1 - \mathbf{A} \mathbf{V}^i \mathbf{y}_i\|^2. \quad (\text{E.11})$$

Using the matrix-equivalent to equation (E.7),

$$\mathbf{A} \mathbf{V}^i = \mathbf{V}^{i+1} \hat{\mathbf{H}}^i, \quad (\text{E.12})$$

and the notation

$$\|\underline{\mathbf{r}}_0\| \cdot \underline{\mathbf{v}}_1 = \|\underline{\mathbf{r}}_0\| \cdot \mathbf{V}^{i+1} \mathbf{e}_1, \quad (\text{E.13})$$

with the vector \mathbf{e}_1 defined as the first column of the $(i+1) \times (i+1)$ identity matrix $\mathbf{I}^{(i+1) \times (i+1)}$, equation (E.11) is furthermore equivalent to

$$\min_{\mathbf{y}_i \in \mathbb{R}^i} \left\| \|\underline{\mathbf{r}}_0\| \cdot \mathbf{e}_1 - \hat{\mathbf{H}}^i \mathbf{y}_i \right\|^2. \quad (\text{E.14})$$

Here, the orthonormality of the basis functions was used once more in the form

$$(\mathbf{V}^{i+1})^T \mathbf{V}^{i+1} = \mathbf{I}^{(i+1) \times (i+1)}. \quad (\text{E.15})$$

System (E.14) can be solved very efficiently by orthogonal transformation using GIVENS rotations. These rotations do not alter the norm of the expression to be minimised, but allow to eliminate the entries of $\hat{\mathbf{H}}^i$ below the diagonal of \mathbf{H}^i , so that the minimal solution can be determined by a simple backward substitution. See for instance SCHWARZ [188] for an algorithm. From \mathbf{y}_i , the increment $\underline{\mathbf{z}}_i$ and finally $\underline{\mathbf{x}}_i$ can be recovered.

One of the drawbacks of the GMRES method which was already mentioned in the beginning is the requirement to store the KRYLOV basis vectors \mathbf{V}^i , a process which is quite costly in terms of memory. Furthermore, the computational cost for set-up and solution of the least-squares problem increases with the number of basis vectors, and at the same time, the quality of the orthonormalisation generated by ARNOLDI's method diminishes due to round-off problems. Thus, in practice, it is reasonable to limit the admissible size of the KRYLOV subspace to a small number of about 25–125. When reaching this iteration count, the current KRYLOV subspace is dropped and rebuilt on the residual of the last iteration value. This procedure is known as restarted GMRES. It decreases the robustness of the method, but nevertheless it is required to limit the memory consumption of the algorithm. For these small dimensions of the KRYLOV subspace, the computational costs for the matrix-vector multiplications involved in the computation of the basis vectors and the determination of the HESSENBERG entries will be significant.

The GMRES method without a restart is guaranteed to terminate after N steps. Important for practical application is that if \mathbf{A} possesses an appropriate eigenvalue spectrum, a sufficient convergence can be obtained in very few steps.

E.1.2 Preconditioned version

In order to improve the speed of convergence of the iterative procedure, the system can be transformed into an equivalent system with a more favourable eigenvalue spectrum using a linear preconditioning operator \mathbf{M} . Based on a RICHARDSON iteration with relaxation factor ω_{relax} , this preconditioner is sufficient for the construction of a stand-alone, iterative solver:

$$\underline{\mathbf{x}}_{k+1} = \underline{\mathbf{x}}_k + \omega_{\text{relax}} \mathbf{M}^{-1} (\underline{\mathbf{b}} - \mathbf{A} \underline{\mathbf{x}}_k) \quad (\text{E.16})$$

Thus, the combination of preconditioning and the GMRES method can not only be understood as an accelerated version of the GMRES procedure but also as an accelerated version of this preconditioner-based solution process.

The following explanations are restricted to the case of right preconditioning, the case that is used in the computations of chapters 5–7. The right preconditioned system corresponding to equation (E.2) reads

$$(\mathbf{A} \mathbf{M}^{-1}) \hat{\underline{x}} = \underline{b} \quad \text{or equivalently} \quad \underline{r} = \underline{b} - (\mathbf{A} \mathbf{M}^{-1}) \hat{\underline{x}} = \underline{0}. \quad (\text{E.17})$$

The solution \underline{x} can be recovered from the solution $\hat{\underline{x}}$ of equation (E.17) by the application of the inverse preconditioner, i.e.

$$\underline{x} = \mathbf{M}^{-1} \hat{\underline{x}}. \quad (\text{E.18})$$

In general, a preconditioner \mathbf{M} can be considered as an approximation to the system matrix \mathbf{A} , for which the application of its inverse \mathbf{M}^{-1} to a vector can easily be computed. A survey of some preconditioning techniques for large linear systems, including incomplete factorisations, can be found for instance in BENZI [28]. For high performance preconditioners, techniques like incomplete factorisations or GAUSS-SEIDEL procedures are often employed as smoothers in the framework of an algebraic multigrid preconditioner. For a basic introduction to algebraic multigrid, the reader might consult FALGOUT [71], and for further explanations and references KÜTTLER [148].

Concerning the GMRES algorithm described above, the changes introduced by the preconditioning are very local. For the right-preconditioned system, the KRYLOV subspaces are now built using $\mathbf{A} \mathbf{M}^{-1}$ instead of \mathbf{A} , resulting in

$$K^i = \text{span} \left\{ \underline{r}_0, (\mathbf{A} \mathbf{M}^{-1}) \underline{r}_0, \dots, (\mathbf{A} \mathbf{M}^{-1})^{i-1} \underline{r}_0 \right\}. \quad (\text{E.19})$$

This definition is based on the initial residual

$$\underline{r}_0 = \underline{b} - (\mathbf{A} \mathbf{M}^{-1}) \hat{\underline{x}}_0. \quad (\text{E.20})$$

Throughout the whole iterative KRYLOV procedure, only the inverse of the preconditioner is required. This holds true for the whole ARNOLDI process (E.7) as well as for the recovery of \underline{x} from equation (E.18). Although the inverse preconditioner has a matrix representation, it is usually not evaluated explicitly. The complete preconditioned algorithm is summarised in Figure E.2.

E.2 Treatment of singular systems with known kernel

As indicated before, the variational problem based on a finite dimensional solution subspace $\mathcal{S}_u^h \times \mathcal{S}_p^{h,\text{restricted}}$ corresponds to an equivalent problem on $\mathbb{R}^{\overline{n}^{\text{dof}}} / \text{span} \{ \underline{c} \}$. The basis vector \underline{c} is required to satisfy the kernel property

$$\mathbf{A} \underline{c} = \underline{0}. \quad (\text{E.21})$$

Furthermore, the right hand side of the system, which can be associated with a forcing, is assumed to be orthogonal to the kernel

$$\underline{c}^T \underline{b} = 0. \quad (\text{E.22})$$

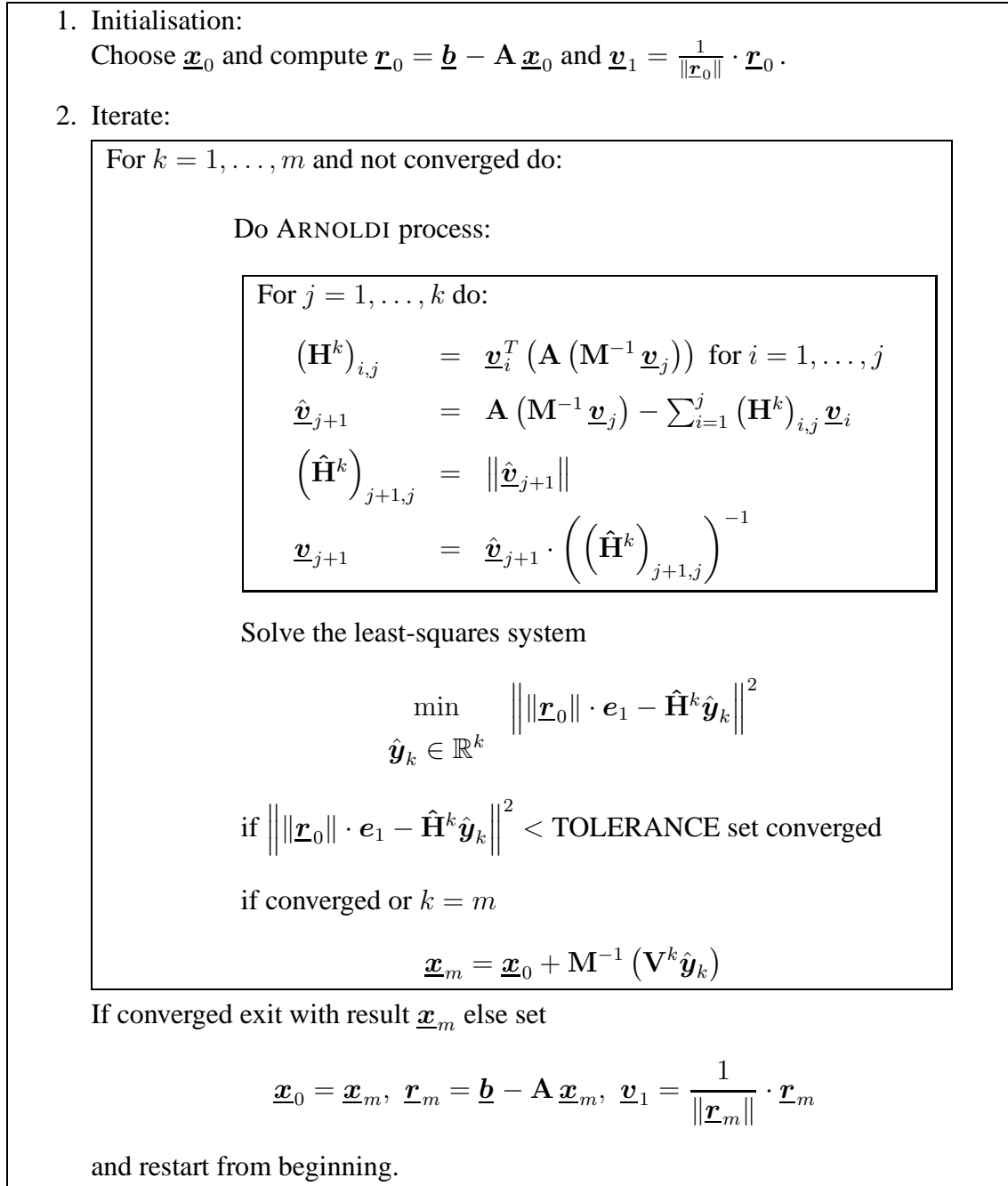


Figure E.2: Restarted GMRES algorithm. Note that the ARNOLDI process can be simplified according to the hierarchy described in Figure E.1.

The matrix and inverse preconditioner applications in the GMRES procedure above will now be modified such that the algorithm computes a representative of the equivalence class that solves the variational problem on $\mathcal{S}_u^h \times \mathcal{S}_p^{h,\text{restricted}}$. This representative is selected such that the pressure

satisfies a certain algebraic condition, i.e.

$$\underline{\mathbf{x}}^T \underline{\mathbf{w}} = \left((\underline{\mathbf{u}}^h)^T, (\underline{\mathbf{p}}^h)^T \right) \underline{\mathbf{w}} = 0. \quad (\text{E.23})$$

The weight vector $\underline{\mathbf{w}}$ in this condition is nonzero only for pressure degrees of freedom, and it is required to satisfy

$$\underline{\mathbf{c}}^T \underline{\mathbf{w}} \neq 0. \quad (\text{E.24})$$

Possible choices for the weight vector $\underline{\mathbf{w}}$ will be discussed below. Equation (E.23) is a linear equality constraint on the pressure. An overview of potential iterative solution methods for this kind of problem can be found in SAINT-GEORGES et al. [187]. The method that is preferred in this work is to solve the system in an unconstrained setting using a subspace projection method.

E.2.1 Choices for the weight vector

Equation (E.23) can be interpreted as a zero mean pressure condition. The weight vector specifies the way this mean is evaluated. Several options are given below.

- One possibility to define the weight vector is to define its pressure components as the integral of the pressure basis functions over the complete domain:

$$(\underline{\mathbf{w}})_\kappa = \begin{cases} 0 & \text{for } 1 \leq \kappa \leq \bar{n}_u^{\text{dof}} \\ \int_{\Omega(t^{n+1})} N_{\kappa - \bar{n}_u^{\text{dof}}}^{S_p^h}(\mathbf{x}) d\mathbf{x} & \text{for } \bar{n}_u^{\text{dof}} + 1 \leq \kappa \leq \bar{n}_u^{\text{dof}} + n_p^{\text{dof}} \end{cases} \quad (\text{E.25})$$

Due to the local support of the basis functions, the vector $\underline{\mathbf{w}}$ can be evaluated and assembled element-wise as it is usually done in finite elements. This choice of the weight vector constrains the integral mean of the discrete pressure to zero:

$$\begin{aligned} 0 &= \underline{\mathbf{x}}^T \underline{\mathbf{w}} = \left((\underline{\mathbf{u}}^h)^T, (\underline{\mathbf{p}}^h)^T \right) \underline{\mathbf{w}} = \\ &= \sum_{\iota=1}^{n_p^{\text{dof}}} \left(\int_{\Omega(t^{n+1})} N_\iota^{S_p^h}(\mathbf{x}) d\mathbf{x} \right) \cdot (\underline{\mathbf{p}}^h)_\iota = \\ &= \int_{\Omega(t^{n+1})} \left(\sum_{\iota=1}^{n_p^{\text{dof}}} N_\iota^{S_p^h}(\mathbf{x}) \cdot (\underline{\mathbf{p}}^h)_\iota \right) d\mathbf{x} = \int_{\Omega(t^{n+1})} p^h(\mathbf{x}) d\mathbf{x} \end{aligned} \quad (\text{E.26})$$

- Another possibility to define the weight vector is to choose it identical to the kernel basis vector, i.e. to set

$$\underline{\mathbf{w}} = \underline{\mathbf{c}}. \quad (\text{E.27})$$

This leads to point-based component averaging of the pressure vector:

$$0 = \underline{\mathbf{x}}^T \underline{\mathbf{w}} = \left((\underline{\mathbf{u}}^h)^T, (\underline{\mathbf{p}}^h)^T \right) \underline{\mathbf{c}} = \sum_{\iota=1}^{n_p^{\text{dof}}} (\underline{\mathbf{p}}^h)_\iota \quad (\text{E.28})$$

- A further option is to allow exactly one nonzero entry in the weight vector:

$$(\underline{\mathbf{w}})_\kappa = \begin{cases} 1 & \text{for one } \kappa \text{ with } \bar{n}_u^{\text{dof}} + 1 \leq \kappa \leq \bar{n}_u^{\text{dof}} + n_p^{\text{dof}} \\ 0 & \text{else} \end{cases} \quad (\text{E.29})$$

For this choice, the value at the corresponding node is set to zero:

$$0 = \underline{\mathbf{x}}^T \underline{\mathbf{w}} = \left((\underline{\mathbf{u}}^h)^T, (\underline{\mathbf{p}}^h)^T \right) \underline{\mathbf{c}} = (\underline{\mathbf{p}}^h)_{\kappa - \bar{n}_u^{\text{dof}}} \quad (\text{E.30})$$

Although this condition is identical to the imposition of a zero DIRICHLET condition in that point, it is still imposed within the subspace projection method and thus inherits the advantages of this approach.

E.2.2 Projector definitions

The required discrete projectors are defined by

$$\mathbf{P}(\underline{\mathbf{x}}) = \underline{\mathbf{x}} - \frac{\underline{\mathbf{x}}^T \underline{\mathbf{w}}}{(\underline{\mathbf{c}}^T \underline{\mathbf{w}})} \underline{\mathbf{c}} \quad (\text{E.31})$$

and

$$\mathbf{P}^T(\underline{\mathbf{x}}) = \underline{\mathbf{x}} - \frac{\underline{\mathbf{c}}^T \underline{\mathbf{x}}}{(\underline{\mathbf{c}}^T \underline{\mathbf{w}})} \underline{\mathbf{w}}. \quad (\text{E.32})$$

Important properties of these projectors (E.31) and (E.32) are:

- $\underline{\mathbf{c}}$ defines the kernel of the projector \mathbf{P} ,

$$\mathbf{P}(\underline{\mathbf{c}}) = \underline{\mathbf{c}} - \frac{\underline{\mathbf{c}}^T \underline{\mathbf{w}}}{(\underline{\mathbf{c}}^T \underline{\mathbf{w}})} \underline{\mathbf{c}} = \underline{\mathbf{c}} - \underline{\mathbf{c}} = \underline{\mathbf{0}}, \quad (\text{E.33})$$

and thus \mathbf{P} projects out the kernel of matrix \mathbf{A} .

- The space spanned by $\mathbf{P} \underline{\mathbf{x}}$ is orthogonal to the weight vector $\underline{\mathbf{w}}$, i.e.

$$\underline{\mathbf{w}}^T (\mathbf{P}(\underline{\mathbf{x}})) = \underline{\mathbf{w}}^T \left(\underline{\mathbf{x}} - \frac{\underline{\mathbf{x}}^T \underline{\mathbf{w}}}{(\underline{\mathbf{c}}^T \underline{\mathbf{w}})} \underline{\mathbf{c}} \right) = \underline{\mathbf{w}}^T \underline{\mathbf{x}} - \frac{\underline{\mathbf{x}}^T \underline{\mathbf{w}}}{(\underline{\mathbf{c}}^T \underline{\mathbf{w}})} \underline{\mathbf{w}}^T \underline{\mathbf{c}} = 0. \quad (\text{E.34})$$

In other words, if the projector is applied to a vector $\underline{\mathbf{x}}$, the result automatically satisfies the linear algebraic constraint (E.23).

- $\underline{\mathbf{w}}$ defines the kernel of the projector \mathbf{P}^T ,

$$\mathbf{P}^T(\underline{\mathbf{w}}) = \underline{\mathbf{w}} - \frac{\underline{\mathbf{c}}^T \underline{\mathbf{w}}}{(\underline{\mathbf{c}}^T \underline{\mathbf{w}})} \underline{\mathbf{w}} = \underline{\mathbf{0}}. \quad (\text{E.35})$$

- The space spanned by $\mathbf{P}^T \underline{\mathbf{x}}$ is orthogonal to the kernel vector $\underline{\mathbf{c}}$, i.e.

$$\underline{\mathbf{c}}^T (\mathbf{P}^T(\underline{\mathbf{x}})) = \underline{\mathbf{c}}^T \underline{\mathbf{x}} - \frac{\underline{\mathbf{c}}^T \underline{\mathbf{x}}}{(\underline{\mathbf{c}}^T \underline{\mathbf{w}})} \underline{\mathbf{c}}^T \underline{\mathbf{w}} = 0. \quad (\text{E.36})$$

E.2.3 Projected system of equations

Using these projectors, the projected version of the unpreconditioned system can be stated:

$$\mathbf{P}^T \mathbf{A} \mathbf{P} \underline{\mathbf{x}} = \mathbf{P}^T \underline{\mathbf{b}}. \quad (\text{E.37})$$

The structure of this equation is very similar to a left and right preconditioning of the original linear system. This allows to include the projector and the transposed projector very easily in the framework of a preconditioned GMRES method by a modification of the preconditioner and matrix call. The ‘forcing’ on the right hand side of the projected equation is orthogonalised to the kernel according to projector property (E.36). Furthermore, applying \mathbf{P} before \mathbf{A} makes sure that $\mathbf{P}^T \mathbf{A} \mathbf{P} \underline{\mathbf{c}} = \underline{\mathbf{0}}$ according to property (E.33). These properties restore consistency even in cases in which the exact satisfaction of $\mathbf{A} \underline{\mathbf{c}} = \underline{\mathbf{0}}$ and $\underline{\mathbf{b}}^T \underline{\mathbf{c}} = 0$ is not provided due to numerical problems in the set-up of \mathbf{A} and $\underline{\mathbf{b}}$.

The corresponding preconditioned equivalent to the projected equation reads

$$\mathbf{P}^T \underline{\mathbf{r}} = \mathbf{P}^T \underline{\mathbf{b}} - (\mathbf{P}^T \mathbf{A} \mathbf{P} \mathbf{M}^{-1}) \hat{\underline{\mathbf{x}}} = \underline{\mathbf{0}} \quad (\text{E.38})$$

with

$$\underline{\mathbf{x}} = \mathbf{P} \mathbf{M}^{-1} \hat{\underline{\mathbf{x}}}. \quad (\text{E.39})$$

The projector in (E.39) in combination with property (E.34) ensures that the result computed by the preconditioned algorithm satisfies the linear equality constraint (E.23). For the projected system (E.38), the KRYLOV subspaces are constructed based on the projected preconditioned matrix, i.e.

$$K^i = \text{span} \left\{ \mathbf{P}^T \underline{\mathbf{r}}_0, (\mathbf{P}^T \mathbf{A} \mathbf{P} \mathbf{M}^{-1}) \mathbf{P}^T \underline{\mathbf{r}}_0, \dots, \dots, (\mathbf{P}^T \mathbf{A} \mathbf{P} \mathbf{M}^{-1})^{i-1} \mathbf{P}^T \underline{\mathbf{r}}_0 \right\}. \quad (\text{E.40})$$

This causes every vector in the KRYLOV subspaces to be orthogonal to the kernel span $\{\underline{\mathbf{c}}\}$ of \mathbf{A} according to property (E.36). Thus, the minimisation problems (E.5) and (E.14) are well-defined and have a unique solution for the projected system even though the matrix \mathbf{A} is singular.

To sum up, the preconditioned GMRES procedure can be used to determine a unique solution of the projected problem as it is shown in Figure E.3. The solution will be characterised by the linear constraint (E.23). In a post-processing step, the obtained pressure can be shifted by an arbitrary constant to obtain any other member of the respective equivalence class. For an implementation, it is convenient to associate the application of the projector \mathbf{P} with the application of the inverse preconditioner \mathbf{M}^{-1} and the application of the transposed projector \mathbf{P}^T with the application of the matrix \mathbf{A} . Although both projectors have a matrix representation, it is advisable to apply them as series of scalar products and vector sums as indicated in equations (E.31) and (E.32).

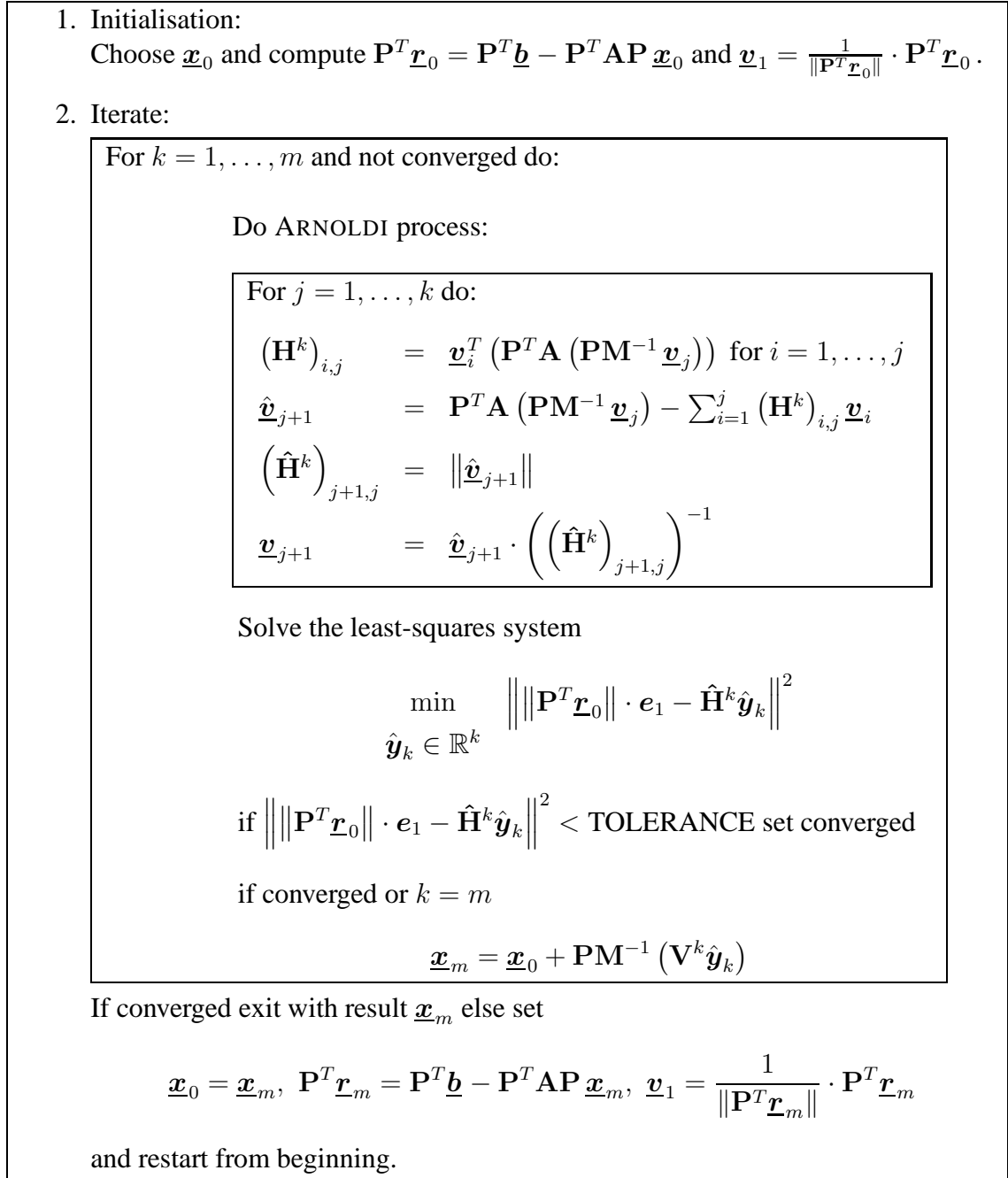


Figure E.3: Restarted GMRES algorithm for the solution of the projected problem. Again, the ARNOLDI process can be simplified according to the hierarchy described in Figure E.1.

Bibliography

- [1] N.A. ADAMS, S. HICKEL, S. FRANZ, *Implicit subgrid-scale modeling by adaptive deconvolution*, Journal of Computational Physics **200** (2004) 412–431.
- [2] AGARD, *A selection of test cases for the validation of large-eddy simulations of turbulent flows*, Tech. Rep. AGARD-AR-345, The Advisory Group for Aerospace Research and Development (1998).
- [3] I. AKKERMAN, Y. BAZILEVS, V.M. CALO, T.J.R. HUGHES, S. HULSHOFF, *The role of continuity in residual-based variational multiscale modeling of turbulence*, Computational Mechanics **41** (2008) 371–378.
- [4] G. ALFONSI, *Reynolds-averaged Navier-Stokes equations for turbulence modeling*, Applied Mechanics Reviews **62** (2009) 040802.
- [5] I. BABUŠKA, *The finite element method with Lagrangian multipliers*, Numerische Mathematik **20** (1973) 179–192.
- [6] S. BADIA, R. CODINA, *Analysis of a stabilized finite element approximation of the transient convection-diffusion equation using an ALE framework*, SIAM Journal on Numerical Analysis **44** (2006) 2159–2197.
- [7] J. BARDINA, J.H. FERZIGER, W.C. REYNOLDS, *Improved turbulence models based on LES of homogeneous incompressible turbulent flows*, Tech. Rep. TF-19, Department of Mechanical Engineering, Stanford University (1984).
- [8] G.R. BARRENECHEA, F. VALENTIN, *An unusual stabilized finite element method for a generalized Stokes problem*, Numerische Mathematik **92** (2002) 652–677.
- [9] F. BASSI, S. REBAY, *High-order accurate discontinuous finite element solution of the 2D Euler equations*, Journal of Computational Physics **138** (1997) 251–285.
- [10] G.K. BATCHELOR, *An introduction to fluid dynamics*, Cambridge University Press, 2000.
- [11] J. BAZILEVS, *Isogeometric analysis of turbulence and fluid-structure interaction*, Ph.D. thesis, The University of Texas at Austin (2006).
- [12] Y. BAZILEVS, I. AKKERMAN, *Large eddy simulation of turbulent Taylor-Couette flow using isogeometric analysis and the residual-based variational multiscale method*, Journal of Computational Physics **229** (2010) 3402–3414.

- [13] Y. BAZILEVS, L. BEIRAO DA VEIGA, J.A. COTTRELL, T.J.R. HUGHES, G. SANGALLI, *Isogeometric analysis: approximation, stability and error estimates for h-refined meshes*, *Mathematical Models and Methods in Applied Sciences* **16** (2006) 1031–1090.
- [14] Y. BAZILEVS, V.M. CALO, J.A. COTTRELL, J.A. EVANS, T.J.R. HUGHES, S. LIPTON, M.A. SCOTT, T.W. SEDERBERG, *Isogeometric analysis using T-splines*, *Computer Methods in Applied Mechanics and Engineering* **199** (2010) 229–263.
- [15] Y. BAZILEVS, V.M. CALO, J.A. COTTRELL, T.J.R. HUGHES, A. REALI, G. SCOVAZZI, *Variational multiscale residual-based turbulence modeling for large eddy simulation of incompressible flows*, *Computer Methods in Applied Mechanics and Engineering* **197** (2007) 173–201.
- [16] Y. BAZILEVS, V.M. CALO, Y. ZHANG, T.J.R. HUGHES, *Isogeometric fluid-structure interaction analysis with applications to arterial blood flow*, *Computational Mechanics* **38** (2006) 310–322.
- [17] Y. BAZILEVS, V.M. CALO, Y. ZHANG, T.J.R. HUGHES, *Isogeometric fluid-structure interaction: Theory, algorithms and computations*, *Computational Mechanics* **43** (2008) 3–37.
- [18] Y. BAZILEVS, J.R. GOHEAN, T.J.R. HUGHES, R.D. MOSER, Y. ZHANG, *Patient-specific isogeometric fluid-structure interaction analysis of thoracic aortic blood flow due to implantation of the Jarvik 2000 left ventricular assist device*, *Computer Methods in Applied Mechanics and Engineering* **198** (2009) 3534–3550.
- [19] Y. BAZILEVS, T.J.R. HUGHES, *Weak imposition of Dirichlet boundary conditions in fluid mechanics*, *Computers and Fluids* **36** (2007) 12 – 26.
- [20] Y. BAZILEVS, T.J.R. HUGHES, *NURBS-based isogeometric analysis for the computation of flows about rotating components*, *Computational Mechanics* **43** (2008) 143–150.
- [21] Y. BAZILEVS, C. MICHLER, V.M. CALO, T.J.R. HUGHES, *Weak Dirichlet boundary conditions for wall-bounded turbulent flows*, *Computer Methods in Applied Mechanics and Engineering* **196** (2007) 4853–4862.
- [22] Y. BAZILEVS, C. MICHLER, V.M. CALO, T.J.R. HUGHES, *Isogeometric variational multiscale modeling of wall-bounded turbulent flows with weakly enforced boundary conditions on unstretched meshes*, *Computer Methods in Applied Mechanics and Engineering* **199** (2010) 780–790.
- [23] P.W. BEARMAN, E.D. OBASAJU, *An experimental study of pressure fluctuations on fixed and oscillating square section cylinders*, *Journal of Fluid Mechanics* **119** (1982) 297–321.
- [24] M. BEHR, *Stabilized finite element methods for incompressible flows with emphasis on moving boundaries and interfaces*, Ph.D. thesis, University of Minnesota (1992).

-
- [25] T. BELYTSCHKO, J.M. KENNEDY, D.F. SCHOEBERLE, *Quasi-Eulerian finite element formulation for fluid structure interaction*, Journal of Pressure Vessel Technology **102** (1980) 62–69.
- [26] T. BELYTSCHKO, Y.Y. LU, L. GU, *Element-free Galerkin methods*, International Journal for Numerical Methods in Engineering **37** (1994) 229–256.
- [27] D.J. BENSON, Y. BAZILEVS, M.C. HSU, T.J.R. HUGHES, *Isogeometric shell analysis: The Reissner-Mindlin shell*, Computer Methods in Applied Mechanics and Engineering **199** (2010) 276–289.
- [28] M. BENZI, *Preconditioning techniques for large linear systems: A survey*, Journal of Computational Physics **182** (2002) 418–477.
- [29] M. BENZI, G.H. GOLUB, J. LIESEN, *Numerical solution of saddle point problems*, Acta Numerica **14** (2005) 1–137.
- [30] B.R. BIRD, J.M. WIEST, *Constitutive equations for polymeric liquids*, Annual Review of Fluid Mechanics **27** (1995) 169–193.
- [31] P. BOCHEV, R.B. LEHOUCQ, *On the finite element solution of the pure Neumann problem*, SIAM Review **47** (2005) 50–66.
- [32] P.B. BOCHEV, M.D. GUNZBURGER, R.B. LEHOUCQ, *On stabilized finite element methods for the Stokes problem in the small time step limit*, International Journal for Numerical Methods in Fluids **53** (2007) 573–597.
- [33] P.B. BOCHEV, M.D. GUNZBURGER, J.N. SHADID, *On inf-sup stabilized finite element methods for transient problems*, Computer Methods in Applied Mechanics and Engineering **193** (2004) 1471–1489.
- [34] P.B. BOCHEV, M.D. GUNZBURGER, J.N. SHADID, *Stability of the SUPG finite element method for transient advection-diffusion problems*, Computer Methods in Applied Mechanics and Engineering **193** (2004) 2301–2323.
- [35] G. BÖHME, *Strömungsmechanik nichtnewtonscher Fluide*, 2nd ed., Teubner, 2002.
- [36] J. BONET, R.D. WOOD, *Nonlinear continuum mechanics for finite element analysis*, 2nd ed., Cambridge University Press, 2008.
- [37] J.P. BORIS, F.F. GRINSTEIN, E.S. ORAN, R.L. KOLBE, *New insights into large eddy simulation*, Fluid Dynamics Research **10** (1992) 199–228.
- [38] B. BORNEMANN, *Time integration algorithms for the steady states of dissipative nonlinear dynamic systems*, Ph.D. thesis, Imperial College London (2003).
- [39] M. BRAACK, E. BURMAN, V. JOHN, G. LUBE, *Stabilized finite element methods for the generalized Oseen problem*, Computer Methods in Applied Mechanics and Engineering **196** (2007) 853–866.

- [40] D. BRAESS, *Finite Elemente, Theorie, schnelle Löser und Anwendungen in der Elastizitätstheorie*, 3rd ed., Springer, 2003.
- [41] S.C. BRENNER, L.R. SCOTT, *The mathematical theory of finite element methods*, vol. 15 of Springer series texts in applied mathematics, 2nd ed., Springer, 2002.
- [42] F. BREZZI, M. FORTIN, *Mixed and hybrid finite element methods*, Springer series in computational mathematics, Springer, 2002.
- [43] A.N. BROOKS, T.J.R. HUGHES, *Streamline upwind/Petrov-Galerkin formulations for convection dominated flows with particular emphasis on the incompressible Navier-Stokes equation*, *Computer Methods in Applied Mechanics and Engineering* **32** (1982) 199–259.
- [44] M.H. BUSCHMANN, M. GAD-EL HAK, *Recent developments in scaling of wall-bounded flows*, *Progress in Aerospace Sciences* **42** (2006) 419–467.
- [45] V.M. CALO, *Residual-based multiscale turbulence modeling: Finite volume simulations of bypass transition*, Ph.D. thesis, Stanford University (2005).
- [46] C. CANUTO, M.Y. HUSSAINI, A. QUARTERONI, T.A. ZANG, *Spectral methods — fundamentals in single domains*, 1st ed., Springer, 2006.
- [47] H. CHOI, P. MOIN, *Effects of the computational time step on numerical solutions of turbulent flow*, *Journal of Computational Physics*, **113** (1994) 1–4.
- [48] A.J. CHORIN, J.E. MARSDEN, *A mathematical introduction to fluid mechanics*, 3rd ed., Springer, 1993.
- [49] J. CHUNG, G.M. HULBERT, *Time integration algorithm for structural dynamics with improved numerical dissipation: the generalized-alpha method*, *Journal of Applied Mechanics* **60** (1993) 371–375.
- [50] K.L. CHUNG, *A course in probability theory*, 3rd ed., Academic Press, 2001.
- [51] B. COCKBURN, G.E. KARNIADAKIS, C.W. SHU (eds.), *The development of discontinuous Galerkin methods*, vol. 11 of Springer series lecture notes in computational science and engineering, Springer, 2000.
- [52] R. CODINA, *Stabilization of incompressibility and convection through orthogonal subscales in finite element methods*, *Computer Methods in Applied Mechanics and Engineering* **190** (2000) 1579–1599.
- [53] R. CODINA, *Stabilized finite element approximation of transient incompressible flows using orthogonal subscales*, *Computer Methods in Applied Mechanics and Engineering* **191** (2002) 4295–4321.
- [54] R. CODINA, J. PRINCIPE, *Dynamic subscales in the finite element approximation of thermally coupled incompressible flows*, *International Journal for Numerical Methods in Fluids* **54** (2007) 707–730.

-
- [55] R. CODINA, J. PRINCIPE, O. GUASCH, S. BADIA, *Time dependent subscales in the stabilized finite element approximation of incompressible flow problems*, *Computer Methods in Applied Mechanics and Engineering* **196** (2007) 2413–2430.
- [56] S.S. COLLIS, *Monitoring unresolved scales in multiscale turbulence modeling*, *Physics of Fluids* **13** (2001) 1800–1806.
- [57] J.A. COTTRELL, T.J.R. HUGHES, Y. BAZILEVS, *Isogeometric analysis: toward integration of CAD and FEA*, 1st ed., Wiley-Blackwell, 2009.
- [58] J.A. COTTRELL, A. REALI, Y. BAZILEVS, T.J.R. HUGHES, *Isogeometric analysis of structural vibrations*, *Computer Methods in Applied Mechanics and Engineering* **195** (2006) 5257–5296.
- [59] R. COURANT, K. FRIEDRICHS, H. LEWY, *Über die partiellen Differenzengleichungen der mathematischen Physik*, *Mathematische Annalen* **100** (1928) 32–74.
- [60] C.F. CURTISS, J.O. HIRSCHFELDER, *Integration of stiff equations*, *Proceedings of the National Academy of Sciences of the United States of America* **38** (1952) 235–243.
- [61] W. DETTMER, D. PERIC, *An analysis of the time integration algorithms for the finite element solutions of incompressible Navier-Stokes equations based on a stabilised formulation*, *Computer Methods in Applied Mechanics and Engineering* **192** (2003) 1177–1226.
- [62] P. DEUFLHARD, F. BORNEMANN, *Numerische Mathematik II — Integration gewöhnlicher Differentialgleichungen*, 2nd ed., de Gruyter, 1994.
- [63] C.R. DOERING, *The 3D Navier-Stokes problem*, *Annual Review of Fluid Mechanics* **41** (2009) 109–128.
- [64] J. DONEA, A. HUERTA, *Finite element methods for flow problems*, Wiley, 2003.
- [65] J. DONEA, A. HUERTA, J.P. PONTOT, A. RODRÍGUEZ-FERRAN, *Arbitrary Lagrangian-Eulerian methods*, in: E. STEIN, R. DE BORST, T.J.R. HUGHES (eds.), *Encyclopedia of computational mechanics — fundamentals*, vol. 1, Wiley, 2004.
- [66] S. DONG, *Direct numerical simulation of turbulent Taylor-Couette flow*, *Journal of Fluid Mechanics* **587** (2007) 373–393.
- [67] M.R. DÖRFEL, B. JÜTTLER, B. SIMEON, *Adaptive isogeometric analysis by local h-refinement with T-splines*, *Computer Methods in Applied Mechanics and Engineering* **199** (2010) 264–275.
- [68] H. ELMAN, D. SILVESTER, A. WATHEN, *Finite elements and fast iterative solvers: with applications in incompressible fluid dynamics*, Oxford University Press, 2005.
- [69] G. ENGEL, K. GARIKIPATI, T.J.R. HUGHES, M.G. LARSON, L. MAZZEI, R.L. TAYLOR, *Continuous/discontinuous finite element approximations of fourth-order elliptic problems in structural and continuum mechanics with applications to thin beams and*

- plates, and strain gradient elasticity*, Computer Methods in Applied Mechanics and Engineering **191** (2002) 3669–3750.
- [70] C. ESKILSSON, S.J. SHERWIN, *Spectral/hp discontinuous Galerkin methods for modeling 2D Boussinesq equations*, Journal of Computational Physics **212** (2006) 566–589.
- [71] R.D. FALGOUT, *An introduction to algebraic multigrid*, Computing in Science and Engineering **8** (2006) 24–33.
- [72] C. FARHAT, C. DEGAND, *A three-dimensional torsional spring analogy method for unstructured dynamic meshes*, Computers and Structures **80** (2002) 305–316.
- [73] C. FARHAT, C. DEGAND, B. KOOBUS, M. LESOINNE, *Torsional springs for two-dimensional dynamic unstructured fluid meshes*, Computer Methods in Applied Mechanics and Engineering **163** (1998) 231–245.
- [74] G.E. FARIN, *NURBS: From projective geometry to practical use*, A.K. Peters, Ltd., 1999.
- [75] S. FERNÁNDEZ-MÉNDEZ, A. HUERTA, *Imposing essential boundary conditions in mesh-free methods*, Computer Methods in Applied Mechanics and Engineering **193** (2004) 1257–1275.
- [76] J.H. FERZIGER, M. PERIC, *Computational methods for fluid dynamics*, 2nd ed., Springer, 1999.
- [77] C.A.J. FLECHTER, *Computational techniques for fluid dynamics 2, specific techniques for different flow categories*, Springer series scientific computation, 2nd ed., Springer, 1996.
- [78] C. FÖRSTER, *Robust methods for fluid-structure interaction with stabilised finite elements*, Ph.D. thesis, Universität Stuttgart (2007).
- [79] C. FÖRSTER, W.A. WALL, E. RAMM, *On the geometric conservation law in transient flow calculations on deforming domains*, International Journal for Numerical Methods in Fluids **50** (2006) 1369–1379.
- [80] C. FÖRSTER, W.A. WALL, E. RAMM, *Artificial added mass instabilities in sequential staggered coupling of nonlinear structures and incompressible viscous flows*, Computer Methods in Applied Mechanics and Engineering **196** (2007) 1278–1293.
- [81] C. FÖRSTER, W.A. WALL, E. RAMM, *Stabilized finite element formulation for incompressible flow on distorted meshes*, International Journal for Numerical Methods in Fluids **60** (2009) 1103–1126.
- [82] L.P. FRANCA, S.L. FREY, *Stabilized finite element methods: II. The incompressible Navier-Stokes equations*, Computer Methods in Applied Mechanics and Engineering **99** (1992) 209–233.

-
- [83] L.P. FRANCA, F. VALENTIN, *On an improved unusual stabilized finite element method for the advective-reactive-diffusive equation*, Computer Methods in Applied Mechanics and Engineering **190** (2000) 1785–1800.
- [84] U. FRISCH, *Turbulence — the legacy of A.N. Kolmogorov*, Cambridge University Press, 1995.
- [85] P. GAMNITZER, V. GRAVEMEIER, W.A. WALL, *Time-dependent subgrid scales in residual-based large eddy simulation of turbulent channel flow*, Computer Methods in Applied Mechanics and Engineering **199** (2010) 819–827.
- [86] P. GAMNITZER, V. GRAVEMEIER, W.A. WALL, *Advances in variational multiscale methods for turbulent flows*, Springer series lecture notes in applied and computational mechanics, Springer, to appear.
- [87] P. GAMNITZER, W.A. WALL, *An ALE-Chimera method for large deformation fluid structure interaction*, in: P. WESSELING, E. OÑATE, J. PÉRIAUX (eds.), Proceedings of the European conference on computational fluid dynamics ECCOMAS CFD, 2006.
- [88] C.W. GEAR, *Numerical initial value problems in ordinary differential equations*, Prentice-Hall, 1971.
- [89] M.W. GEE, C.M. SIEFERT, J.J. HU, R.S. TUMINARO, M.G. SALA, *ML 5.0 smoothed aggregation user's guide*, Tech. Rep. SAND2006-2649, Sandia National Laboratories (2006).
- [90] K. GERDES, D. SCHÖTZAU, *hp-finite element simulations for Stokes flow — stable and stabilized*, Finite Elements in Analysis and Design **33** (1999) 143–165.
- [91] M. GERMANO, U. PIOMELLI, P. MOIN, W.H. CABOT, *A dynamic subgrid-scale eddy viscosity model*, Physics of Fluids A **3** (1991) 1760–1765.
- [92] A. GERSTENBERGER, W.A. WALL, *Enhancement of fixed-grid methods towards complex fluid-structure interaction applications*, International Journal for Numerical Methods in Fluids **57** (2008) 1227–1248.
- [93] R.A. GRANGER, *Fluid mechanics*, Dover Publications, 1996.
- [94] V. GRAVEMEIER, *The variational multiscale method for laminar and turbulent incompressible flows*, Ph.D. thesis, Universität Stuttgart (2003).
- [95] V. GRAVEMEIER, *Scale-separating operators for variational multiscale large eddy simulation of turbulent flows*, Journal of Computational Physics **212** (2006) 400–435.
- [96] V. GRAVEMEIER, *The variational multiscale method for laminar and turbulent flow*, Archives of Computational Methods in Engineering — State of the Art Reviews **13** (2006) 249–324.

- [97] V. GRAVEMEIER, M.W. GEE, M. KRONBICHLER, W.A. WALL, *An algebraic variational multiscale-multigrid method for large eddy simulation of turbulent flow*, Computer Methods in Applied Mechanics and Engineering **199** (2010) 853–864.
- [98] V. GRAVEMEIER, S. LENZ, W.A. WALL, *Variational multiscale methods for incompressible flows*, International Journal of Computing Science and Mathematics **1** (2007) 444–466.
- [99] V. GRAVEMEIER, S. LENZ, W.A. WALL, *Towards a taxonomy for multiscale methods in computational mechanics: Building blocks of existing methods*, Computational Mechanics **41** (2008) 279–291.
- [100] V. GRAVEMEIER, W.A. WALL, E. RAMM, *A three-level finite element method for the instationary, incompressible Navier-Stokes equations*, Computer Methods in Applied Mechanics and Engineering **193** (2004) 1323–1366.
- [101] V. GRAVEMEIER, W.A. WALL, E. RAMM, *Large eddy simulation of turbulent incompressible flows by a three-level finite element method*, International Journal for Numerical Methods in Fluids **48** (2005) 1067–1099.
- [102] P. GRESHO, R. SANI, *Incompressible flow and the finite element method, advection-diffusion*, vol. 1, Wiley, 2000.
- [103] P. GRESHO, R. SANI, *Incompressible flow and the finite element method, isothermal laminar flow*, vol. 2, Wiley, 2000.
- [104] M. GRIEBEL, M.A. SCHWEITZER, *A particle-partition of unity method. Part V: Boundary conditions*, in: S. HILDEBRANDT, H. KARCHER (eds.), Geometric Analysis and Nonlinear Partial Differential Equations, Springer, 2002.
- [105] M.E. GURTIN, *An introduction to continuum mechanics*, vol. 158 of mathematics in science and engineering, Academic Press, 1981.
- [106] E. HAIRER, S.P. NØRSETT, G. WANNER, *Solving ordinary differential equations I, non-stiff problems*, Springer series in computational mathematics, 2nd ed., Springer, 2000.
- [107] E. HAIRER, G. WANNER, *Solving ordinary differential equations II, stiff and differential-algebraic problems*, Springer series in computational mathematics, 2nd ed., Springer, 2004.
- [108] P. HANSBO, J. HERMANSSON, T. SVEDBERG, *Nitsche’s method combined with space-time finite elements for ALE fluid-structure interaction problems*, Computer Methods in Applied Mechanics and Engineering **193** (2004) 4195–4206.
- [109] P. HANSBO, A. SZEPESSY, *A velocity-pressure streamline diffusion finite element method for the incompressible Navier-Stokes equations*, Computer Methods in Applied Mechanics and Engineering **84** (1990) 175–192.

-
- [110] I. HARARI, T.J.R. HUGHES, *What are C and h ?: Inequalities for the analysis and design of finite element methods*, Computer Methods in Applied Mechanics and Engineering **97** (1992) 157–192.
- [111] C. HÄRTEL, L. KLEISER, F. UNGER, R. FRIEDRICH, *Subgrid-scale energy transfer in the near-wall region of turbulent flows*, Physics of Fluids **6** (1994) 3130–3143.
- [112] S. HICKEL, N.A. ADAMS, J.A. DOMARADZKI, *An adaptive local deconvolution method for implicit LES*, Journal of Computational Physics **213** (2006) 413–436.
- [113] C.W. HIRT, A.A. AMSDEN, J.L. COOK, *An Arbitrary Lagrangian-Eulerian computing method for all flow speeds*, Journal of Computational Physics **14** (1974) 227–253.
- [114] M.C. HSU, Y. BAZILEVS, V.M. CALO, T.E. TEZDUYAR, T.J.R. HUGHES, *Improving stability of stabilized and multiscale formulations in flow simulations at small time steps*, Computer Methods in Applied Mechanics and Engineering **199** (2010) 828–840.
- [115] T.J.R. HUGHES, *Multiscale phenomena: Green’s functions, the Dirichlet-to-Neumann formulation, subgrid scale models, bubbles and the origins of stabilized methods*, Computer Methods in Applied Mechanics and Engineering **127** (1995) 387–401.
- [116] T.J.R. HUGHES, *The finite element method linear static and dynamic finite element analysis*, Dover Publications, 2000.
- [117] T.J.R. HUGHES, J.A. COTTRELL, Y. BAZILEVS, *Isogeometric analysis: CAD, finite elements, NURBS, exact geometry and mesh refinement*, Computer Methods in Applied Mechanics and Engineering **194** (2005) 4135–4195.
- [118] T.J.R. HUGHES, G. ENGEL, L. MAZZEI, M.G. LARSON, *The continuous Galerkin method is locally conservative*, Journal of Computational Physics **163** (2000) 467–488.
- [119] T.J.R. HUGHES, G. FEIJÓO, L. MAZZEI, J.B. QUINCY, *The variational multiscale method — a paradigm for computational mechanics*, Computer Methods in Applied Mechanics and Engineering, **166** (1998) 3–24.
- [120] T.J.R. HUGHES, L.P. FRANCA, M. BALESTRA, *A new finite element formulation for computational fluid dynamics: V. Circumventing the Babuska-Brezzi condition: A stable Petrov-Galerkin formulation of the Stokes problem accommodating equal-order interpolation*, Computer Methods in Applied Mechanics and Engineering **59** (1986) 85–99.
- [121] T.J.R. HUGHES, L. MAZZEI, K.E. JANSEN, *Large eddy simulation and the variational multiscale method*, Computing and Visualization in Science **3** (2000) 47–59.
- [122] T.J.R. HUGHES, L. MAZZEI, A.A. OBERAI, A.A. WRAY, *The multiscale formulation of large eddy simulation: Decay of homogeneous isotropic turbulence*, Physics of Fluids **13** (2001) 505–512.
- [123] T.J.R. HUGHES, A.A. OBERAI, L. MAZZEI, *Large eddy simulation of turbulent channel flows by the variational multiscale method*, Physics of Fluids **13** (2001) 1784–1799.

- [124] T.J.R. HUGHES, A. REALI, G. SANGALLI, *Efficient quadrature for NURBS-based isogeometric analysis*, Computer Methods in Applied Mechanics and Engineering **199** (2010) 301–313.
- [125] T.J.R. HUGHES, G. SANGALLI, *Variational multiscale analysis: the fine-scale Green's function, projection, optimization, localization, and stabilized methods*, SIAM Journal on Numerical Analysis **45** (2007) 539–557.
- [126] T.J.R. HUGHES, G. SCOVAZZI, L.P. FRANCA, *Multiscale and stabilized methods*, in: E. STEIN, R.D. BORST, T.J.R. HUGHES (eds.), Encyclopedia of computational mechanics — computational fluid dynamics, vol. 3, Wiley, 2004.
- [127] T.J.R. HUGHES, G.N. WELLS, *Conservation properties for the Galerkin and stabilised forms of the advection-diffusion and incompressible Navier-Stokes equations*, Computer Methods in Applied Mechanics and Engineering **194** (2005) 1141–1159.
- [128] G. IACCARINO, A. OOI, P.A. DURBIN, M. BEHNIA, *Reynolds averaged simulation of unsteady separated flow*, International Journal of Heat and Fluid Flow **24** (2003) 147–156.
- [129] P. JAMET, R. BONNEROT, *Numerical solution of the Eulerian equations of compressible flow by a finite element method which follows the free boundary and the interfaces*, Journal of Computational Physics **18** (1975) 21–45.
- [130] P. JAMET, R. BONNEROT, *Numerical computation of the free boundary for the two-dimensional Stefan problem by space-time finite elements*, Journal of Computational Physics **25** (1977) 163–181.
- [131] K.E. JANSEN, S.S. COLLIS, C. WHITING, F. SHAKIB, *A better consistency for low-order stabilized finite element methods*, Computer Methods in Applied Mechanics and Engineering **174** (1999) 154–170.
- [132] K.E. JANSEN, C.H. WHITING, G.M. HULBERT, *A generalized- α method for integrating the filtered Navier-Stokes equations with a stabilized finite element method*, Computer Methods in Applied Mechanics and Engineering **190** (2000) 305–319.
- [133] V. JOHN, *On large eddy simulation and variational multiscale methods in the numerical simulation of turbulent incompressible flows*, Applications of Mathematics **51** (2006) 321–353.
- [134] V. JOHN, S. KAYA, *A finite element variational multiscale method for the Navier-Stokes equations*, SIAM Journal on Scientific Computing **26** (2005) 1485–1503.
- [135] V. JOHN, A. KINDL, *Variants of projection-based finite element variational multiscale methods for the simulation of turbulent flows*, International Journal for Numerical Methods in Fluids **56** (2008) 1321–1328.
- [136] V. JOHN, M. ROLAND, *Simulations of the turbulent channel flow at $Re_\tau = 180$ with projection-based finite element variational multiscale methods*, International Journal for Numerical Methods in Fluids **55** (2007) 407–429.

-
- [137] P. KAGAN, A. FISCHER, P.Z. BAR-YOSEPH, *New B-Spline finite element approach for geometrical design and mechanical analysis*, International Journal for Numerical Methods in Engineering **41** (1998) 435–458.
- [138] P. KAGAN, A. FISCHER, P.Z. BAR-YOSEPH, *Mechanically based models: Adaptive refinement for B-spline finite element*, International Journal for Numerical Methods in Engineering **57** (2003) 1145–1175.
- [139] G. KARYPIS, K. SCHLOEGEL, V. KUMAR, *PARMETIS — parallel graph partitioning and sparse matrix ordering library — version 3.1*, Tech. rep., University of Minnesota, Department of Computer Science and Engineering (2003).
- [140] J. KIENDL, K.U. BLETZINGER, J. LINHARD, R. WÜCHNER, *Isogeometric shell analysis with Kirchhoff-Love elements*, Computer Methods in Applied Mechanics and Engineering **198** (2009) 3902–3914.
- [141] P. KNABNER, L. ANGERMANN, *Numerik partieller Differentialgleichungen. Eine anwendungsorientierte Einführung*, Springer, 2000.
- [142] A.N. KOLMOGOROV, *Grundlagen der Wahrscheinlichkeitsrechnung*, Springer, 1933.
- [143] A.N. KOLMOGOROV, *Dissipation of energy in the locally isotropic turbulence*, Proceedings: Mathematical and Physical Sciences **434** (1991) 15–17.
- [144] A.N. KOLMOGOROV, *The local structure of turbulence in incompressible viscous fluid for very large Reynolds numbers*, Proceedings: Mathematical and Physical Sciences **434** (1991) 9–13.
- [145] K. KÖNIGSBERGER, *Analysis 2*, 2nd ed., Springer, 1997.
- [146] B. KOOBUS, C. FARHAT, *A variational multiscale method for the large eddy simulation of compressible turbulent flows on unstructured meshes — application to vortex shedding*, Computer Methods in Applied Mechanics and Engineering **193** (2004) 1367–1383.
- [147] L. KRIVODONOVA, M. BERGER, *High-order accurate implementation of solid wall boundary conditions in curved geometries*, Journal of Computational Physics **211** (2006) 492–512.
- [148] U. KÜTTLER, *Effiziente Lösungsverfahren für Fluid-Struktur-Interaktions-Probleme*, Ph.D. thesis, Technische Universität München (2009).
- [149] U. KÜTTLER, M.W. GEE, C. FÖRSTER, A. COMERFORD, W.A. WALL, *Coupling strategies for biomedical fluid-structure interaction problems*, International Journal for Numerical Methods in Biomedical Engineering **26** (2010) 305–321.
- [150] U. KÜTTLER, W.A. WALL, *Fixed-point fluid structure interaction solvers with dynamic relaxation*, Computational Mechanics **43** (2008) 61–72.

- [151] O.A. LADYZHENSKAYA, V.A. SOLONNIKOV, *Unique solvability of an initial- and boundary-value problem for viscous incompressible nonhomogeneous fluids*, Journal of Mathematical Sciences **9** (1978) 697–749.
- [152] L.D. LANDAU, E.M. LIFSCHITZ, *Lehrbuch der theoretischen Physik, Band 6: Hydrodynamik*, 5th ed., Akademie Verlag, 1991.
- [153] B.E. LEE, *The effect of turbulence on the surface pressure field of square prisms*, Journal of Fluid Mechanics **69** (1975) 263–282.
- [154] M. LESIEUR, O. MÉTAIS, *New trends in large-eddy simulation of turbulence*, Annual Review of Fluid Mechanics **28** (1996) 45–82.
- [155] D.K. LILLY, *A proposed modification of the Germano subgrid-scale closure method*, Physics of Fluids A **4** (1992) 633–635.
- [156] A. LINKE, *Collision in a cross-shaped domain — a steady 2D Navier-Stokes example demonstrating the importance of mass conservation in CFD*, Computer Methods in Applied Mechanics and Engineering **198** (2009) 3278–3286.
- [157] R. LÖHNER, C. YANG, *Improved ALE mesh velocities for moving bodies*, Communications in Numerical Methods in Engineering **12** (1996) 599–608.
- [158] J.E. MARSDEN, T.J.R. HUGHES, *Mathematical foundations of elasticity*, Dover Publications, 1994.
- [159] J. MATHIEU, J. SCOTT, *An introduction to turbulent flow*, Cambridge University Press, 2000.
- [160] C. MENEVEAU, J. KATZ, *Scale-invariance and turbulence models for large-eddy simulation*, Annual Review of Fluid Mechanics **32** (2000) 1–32.
- [161] S. MITTAL, *On the performance of high aspect ratio elements for incompressible flows*, Computer Methods in Applied Mechanics and Engineering **188** (2000) 269–287.
- [162] P. MOIN, K. MAHESH, *Direct numerical simulation: A tool in turbulence research*, Annual Review of Fluid Mechanics **30** (1998) 539–578.
- [163] R.D. MOSER, J. KIM, N.N. MANSOUR, *Direct numerical simulation of turbulent channel flow up to $Re_\tau=590$* , Physics of Fluids **11** (1999) 943–945.
- [164] B. NAYROLES, G. TOUZOT, P. VILLON, *Generalizing the finite element method: Diffuse approximation and diffuse elements*, Journal Computational Mechanics **10** (1992) 307–318.
- [165] J. NITSCHKE, *Über ein Variationsprinzip zur Lösung von Dirichlet-Problemen bei Verwendung von Teilräumen, die keinen Randbedingungen unterworfen sind*, Abhandlungen aus dem Mathematischen Seminar der Universität Hamburg **36** (1971) 9–15.

-
- [166] J. NOCEDAL, S.J. WRIGHT, *Numerical optimization*, Springer series in operations research, Springer, 2000.
- [167] A.A. OBERAI, J. WANDERER, *A dynamic approach for evaluating parameters in a numerical method*, International Journal for Numerical Methods in Engineering **62** (2005) 50–71.
- [168] M. OLSHANSKII, G. LUBE, T. HEISTER, J. LÖWE, *Grad-div stabilization and subgrid pressure models for the incompressible Navier-Stokes equations*, Computer Methods in Applied Mechanics and Engineering **198** (2009) 3975–3988.
- [169] R.L. PANTON, *Incompressible flow*, 3rd ed., Wiley, 2005.
- [170] A. PAPOULIS, S.U. PILLAI, *Probability, random variables and stochastic processes*, 4th ed., Mc-Graw Hill, 2002.
- [171] E. PARZEN, *Stochastic processes*, SIAM, 1999.
- [172] R. PEYRET, *Spectral methods for incompressible viscous flow*, Springer, 2002.
- [173] L. PIEGL, W. TILLER, *The NURBS book*, Springer series monographs in visual communication, 2nd ed., Springer, 1997.
- [174] S.B. POPE, *Turbulent flows*, Cambridge University Press, 2000.
- [175] L. PRANDTL, *Bericht über die Untersuchungen zur ausgebildeten Turbulenz*, Zeitschrift für angewandte Mathematik und Mechanik **5** (1925) 136–139.
- [176] J. PRINCIPE, R. CODINA, F. HENKE, *The dissipative structure of variational multiscale methods for incompressible flows*, Computer Methods in Applied Mechanics and Engineering **199** (2010) 791–801.
- [177] A. RAJASEKHARAN, C. FARHAT, *Application of a variational multiscale method for large eddy simulation of turbulent flows on moving/deforming unstructured grids*, Finite Elements in Analysis and Design **45** (2009) 272–279.
- [178] R. RANNACHER, *On the numerical solution of the incompressible Navier-Stokes equations*, ZAMM — Journal of Applied Mathematics and Mechanics / Zeitschrift für Angewandte Mathematik und Mechanik **73** (1993) 203–216.
- [179] L.F. RICHARDSON, *Weather prediction by numerical process*, Cambridge University Press, 1922.
- [180] W. RODI, *Comparison of LES and RANS calculations of the flow around bluff bodies*, Journal of Wind Engineering and Industrial Aerodynamics **69–71** (1997) 55–75.
- [181] W. RODI, J.H. FERZIGER, M. BREUER, M. POURQUIÉ, *Status of large eddy simulation: Results of a workshop*, Journal of Fluids Engineering **119** (1997) 248–262.

- [182] D.F. ROGERS, *An introduction to NURBS. With historical perspective*, Morgan Kaufmann Publishers, 2000.
- [183] E. ROTHE, *Zweidimensionale parabolische Randwertaufgaben als Grenzfall eindimensionaler Randwertaufgaben*, *Mathematische Annalen* **102** (1930) 650–670.
- [184] Y. SAAD, M.H. SCHULTZ, *GMRES: A generalized minimal residual algorithm for solving nonsymmetric linear systems*, *SIAM Journal on Scientific and Statistical Computing* **7** (1986) 856–869.
- [185] Y. SAAD, H.A. VAN DER VORST, *Iterative solution of linear systems in the 20th century*, *Journal of Computational and Applied Mathematics* **123** (2000) 1–33.
- [186] P. SAGAUT, *Large eddy simulation for incompressible flows: An introduction*, Springer, 2006.
- [187] P. SAINT-GEORGES, Y. NOTAY, G. WARZÉE, *Efficient iterative solution of constrained finite element analyses*, *Computer Methods in Applied Mechanics and Engineering* **160** (1998) 101–114.
- [188] H.R. SCHWARZ, *Numerische Mathematik*, 4th ed., Teubner, 1997.
- [189] R. SEVILLA, S. FERNÁNDEZ-MÉNDEZ, A. HUERTA, *NURBS-enhanced finite element method (NEFEM)*, *International Journal for Numerical Methods in Engineering* **76** (2008) 56–83.
- [190] C.W. SHU, *High order weighted essentially nonoscillatory schemes for convection dominated problems*, *SIAM Review* **51** (2009) 82–126.
- [191] J. SMAGORINSKY, *General circulation experiments with the primitive equations: I. The basic experiment*, *Monthly Weather Review* **91** (1963) 99–164.
- [192] A. SOHANKAR, L. DAVIDSON, C. NORBERG, *Large eddy simulation of flow past a square cylinder: Comparison of different subgrid scale models*, *Journal of Fluids Engineering* **122** (2000) 39–47.
- [193] D.B. SPALDING, *A single formula for the law of the wall*, *Journal of Applied Mechanics* **28** (1961) 444–458.
- [194] R. STENBERG, *On some techniques for approximating boundary conditions in the finite element method*, *Journal of Computational and Applied Mathematics* **63** (1995) 139–148.
- [195] S. STOLZ, N.A. ADAMS, *An approximate deconvolution procedure for large-eddy simulation*, *Physics of Fluids* **11** (1999) 1699–1701.
- [196] G. STRANG, G.J. FIX, *An analysis of the finite element method*, Wellesley-Cambridge Press, 1997.
- [197] A.M. STUART, A.R. HUMPHRIES, *Dynamical systems and numerical analysis*, Cambridge University Press, 1998.

-
- [198] C.A. TAYLOR, T.J.R. HUGHES, C.K. ZARINS, *Finite element modeling of blood flow in arteries*, Computer Methods in Applied Mechanics and Engineering **158** (1998) 155–196.
- [199] A.E. TEJADA-MARTÍNEZ, *Dynamic subgrid-scale modeling for large-eddy simulation of turbulent flows with a stabilized finite element method*, Ph.D. thesis, Rensselaer Polytechnic Institute (2002).
- [200] A.E. TEJADA-MARTÍNEZ, K.E. JANSEN, *Spatial test filters for dynamic model large-eddy simulation with finite elements*, Communications in Numerical Methods in Engineering **19** (2003) 205–213.
- [201] A.E. TEJADA-MARTÍNEZ, K.E. JANSEN, *A dynamic Smagorinsky model with dynamic determination of the filter width ratio*, Physics of Fluids **16** (2004) 2514–2528.
- [202] A.E. TEJADA-MARTÍNEZ, K.E. JANSEN, *On the interaction between dynamic model dissipation and numerical dissipation due to streamline upwind/Petrov-Galerkin stabilization*, Computer Methods in Applied Mechanics and Engineering **194** (2005) 1225–1248.
- [203] R. TEMAM, *Navier-Stokes equations and nonlinear functional analysis*, CBMS-NSF regional conference series in applied mathematics, 2nd ed., SIAM, 1995.
- [204] H. TENNEKES, J.L. LUMLEY, *A first course in turbulence*, MIT Press, 1972.
- [205] T.E. TEZDUYAR, M. BEHR, , S. MITTAL, J. LIU, *A new strategy for finite element computations involving moving boundaries and interfaces — the deforming-spatial-domain/space-time procedure: II. Computation of free-surface flows, two-liquid flows, and flows with drifting cylinders*, Computer Methods in Applied Mechanics and Engineering **94** (1992) 353–371.
- [206] T.E. TEZDUYAR, M. BEHR, J. LIU, *A new strategy for finite element computations involving moving boundaries and interfaces — the deforming-spatial-domain/space-time procedure: I. The concept and the preliminary numerical tests*, Computer Methods in Applied Mechanics and Engineering **94** (1992) 339–351.
- [207] T.E. TEZDUYAR, S. MITTAL, S.E. RAY, R. SHIH, *Incompressible flow computations with stabilized bilinear and linear equal-order-interpolation velocity-pressure elements*, Computer Methods in Applied Mechanics and Engineering **95** (1992) 221–242.
- [208] T.E. TEZDUYAR, Y. OSAWA, *Finite element stabilization parameters computed from element matrices and vectors*, Computer Methods in Applied Mechanics and Engineering **190** (2000) 411–430.
- [209] A.V. TROFIMOVA, A.E. TEJADA-MARTÍNEZ, K.E. JANSEN, R.T. LAHEY JR., *Direct numerical simulation of turbulent channel flows using a stabilized finite element method*, Computers and Fluids **38** (2009) 924–938.
- [210] C. TRUESDELL, W. NOLL, *The non-linear field theories of mechanics*, 3rd ed., Springer, 2004.

- [211] C. TRUESDELL, K.R. RAJAGOPAL, *An introduction to the mechanics of fluids*, Birkhäuser, 2000.
- [212] R.S. TUMINARO, M. HEROUX, S.A. HUTCHINSON, J.N. SHADID, *Official Aztec user's guide: Version 2.1*, Tech. Rep. SAND99-8801J, Sandia National Laboratories (1999).
- [213] H.A. VAN DER VORST, *Bi-CGSTAB: A fast and smoothly converging variant of Bi-CG for the solution of nonsymmetric linear systems*, SIAM Journal on Scientific and Statistical Computing **13** (1992) 631–644.
- [214] B. VREMAN, B. GEURTS, H. KUERTEN, *Large-eddy simulation of the turbulent mixing layer*, Journal of Fluid Mechanics **339** (1997) 357–390.
- [215] W.A. WALL, *Fluid-Struktur-Interaktion mit stabilisierten Finiten Elementen*, Ph.D. thesis, Universität Stuttgart (1999).
- [216] W.A. WALL, M.A. FRENZEL, C. CYRON, *Isogeometric structural shape optimization*, Computer Methods in Applied Mechanics and Engineering **197** (2008) 2976–2988.
- [217] W.A. WALL, P. GAMNITZER, A. GERSTENBERGER, *Fluid-structure interaction approaches on fixed grids based on two different domain decomposition ideas*, International Journal of Computational Fluid Dynamics **22** (2008) 411–427.
- [218] Z. WANG, A.A. OBERAI, *Spectral analysis of the dissipation of the residual-based variational multiscale method*, Computer Methods in Applied Mechanics and Engineering **199** (2010) 810–818.
- [219] P. WESSELING, *Principles of computational fluid dynamics*, vol. 29 of Springer series computational mathematics, Springer, 2001.
- [220] C.H. WHITING, *Stabilized finite element methods for fluid dynamics using a hierarchical basis*, Ph.D. thesis, Rensselaer Polytechnic Institute (1999).
- [221] C.H. WHITING, K.E. JANSEN, *A stabilized finite element method for the incompressible Navier-Stokes equations using a hierarchical basis*, International Journal for Numerical Methods in Fluids **35** (2001) 93–116.
- [222] D.C. WILCOX, *Turbulence modeling for CFD*, 2nd ed., DCW Industries, 2002.
- [223] M. WOSNIK, L. CASTILLO, W.K. GEORGE, *A theory for turbulent pipe and channel flows*, Journal of Fluid Mechanics **421** (2000) 115–145.
- [224] P. WRIGGERS, *Computational contact mechanics*, Wiley, 2002.
- [225] R.L. ZIENKIEWICZ, R.L. TAYLOR, *The finite element method, Vol. 1 — the basis*, 5th ed., Butterworth-Heinemann, 2000.
- [226] R.L. ZIENKIEWICZ, R.L. TAYLOR, *The finite element method, Vol. 2 — solid mechanics*, 5th ed., Butterworth-Heinemann, 2000.

- [227] R.L. ZIENKIEWICZ, R.L. TAYLOR, *The finite element method, Vol. 3 — fluid dynamics*, 5th ed., Butterworth-Heinemann, 2000.